2004

Cohesive zone model for facesheet -core interface delamination in honeycomb FRP sandwich panels

Weiqiao Wang
West Virginia University

Recommended Citation

Wang, Weiqiao, "Cohesive zone model for facesheet -core interface delamination in honeycomb FRP sandwich panels" (2004). *Graduate Theses, Dissertations, and Problem Reports*. 2578.
https://researchrepository.wvu.edu/etd/2578

Cohesive Zone Model for Facesheet-Core Interface Delamination in Honeycomb FRP Sandwich Panels

by

Weiqiao Wang

Dissertation submitted to the
College of Engineering and Mineral Resources
at West Virginia University
in partial fulfillment of the requirements
for the degree of

Doctor of Philosophy
in
Civil Engineering

Approved by

Julio F. Davalos, Ph.D., Chair
Jacky C. Prucz, Ph.D.
Bruce Kang, Ph.D.
Pizhong Qiao, Ph.D.
Indrajit Ray, Ph.D.

Department of Civil and Environmental Engineering
Morgantown, West Virginia
2004

Keywords: Delamination, Fracture, Sandwich Structure, Cohesive Zone Model

Cohesive Zone Model for Facesheet-Core Interface Delamination in Honeycomb FRP Sandwich Panels

Weiqiao Wang

Advisor: Dr. Julio F. Davalos

Abstract:

The focus of this dissertation is on developing efficient modeling techniques to study facesheet-core interface delamination in honeycomb fiber-reinforced polymer (HFRP) sandwich panels. Delamination problems are usually treated from a fracture mechanics point of view. However, interface delamination is generally very complex in nature and difficult to solve, because it involves not only geometric and material discontinuities, but also the inherently coupled Mode I, II and III fracture in layered material systems attributed to the well-known oscillatory singularity nature of the stress and displacement field in the vicinity of the delamination crack tip. One of the key issues in this research is to determine the best way to characterize interface delamination within the framework of continuum mechanics rather than using ad hoc methods just to facilitate numerical implementations, such as springs across a crack in the finite element method.

The usual requirement of defining an initial crack and assuming self-similar progression of a crack, make traditional fracture mechanics approaches inefficient for modeling interface delamination. To circumvent these difficulties, five most relevant nonlinear crack models are reviewed and compared. It is concluded that by unifying strength-based crack initiation and fracture-based crack progression, the cohesive crack modeling approach has distinct advantages compared to other global methods.

In this study, a cohesive zone model (CZM) with linear-exponential irreversible softening traction-separation law, satisfying empirical mixed-mode fracture criteria, is proposed to represent progressive damage occurring within the interface during the fracture process. The CZM is implemented as a cohesive interface element through a user-defined element subroutine within the general purpose finite element code ABAQUS. The framework and formulation of a three dimensional interface element are presented. Two sets of parameters are required for application of the developed interface element, namely, interfacial strength and fracture toughness. The initiation of fracture is determined by the interfacial strength and the progression of fracture is determined by the interface fracture toughness. The surface-like interface element consists of an upper and a lower face with initially zero thickness in the undeformed configuration. In the finite element modeling, these interface elements are positioned within the interface where potential delamination propagation is expected. A contact-type interface element is also developed to simulate contact behavior in the delaminated region.

Verification examples applying the developed interface element are presented with numerical simulations of standard fracture test configurations, namely double cantilever beam (DCB) and mixed-mode bending (MMB) specimens, under Mode I, Mode II, or mixed-mode loading conditions. For all the simulations, the present finite element solutions are in good agreement with either the linear elastic fracture mechanics analytical solutions or experimental data available in the literature. Non-self-similar delamination growth or a curved delamination front due to anticlastic bending effect in the DCB specimen is captured numerically. To test the robustness of the CZM in simulating delamination coupled with highly nonlinear structural response, delamination buckling of a laminated composite plate under in-plane compression is simulated; in order to lessen the burden of using a fine mesh, a slight modification of the formulation of the interface element was made resulting in a more brittle fracture behavior within the interface.

Delamination in composite sandwich structures is an important failure mode. Although the problem of a facesheet delaminated from a solid core has been extensively investigated, the failure mechanism of delamination of a facesheet from a honeycomb core is far from fully understood. Application of the CZM to study facesheet-core interface delamination of honeycomb sandwich structures is rare. In this study, facesheet delamination in HFRP sandwich panels is addressed with the developed cohesive interface element.

The interfacial properties of strength and fracture toughness are obtained through a systematic experimental program. The effects of such parameters as facesheet bonding layers and core-wall thickness are investigated, and although more tests are needed before a definite conclusion can be drawn from the current experimental data, some preliminary observations are provided regarding their effects on interface fracture response. It is shown that the response of the HFRP sandwich panel involving facesheet-core interface delamination propagation is mainly controlled by the interface fracture toughness, while the interfacial strength has a relatively small effect. As such, the interfacial strength value need not be measured precisely.

Simulation of the contoured double cantilever beam (CDCB) specimen with vertical core elements, used to obtain fracture toughness values, is successfully performed with the measured interfacial properties. It is verified that in this test the Mode II contribution is negligible, showing the validity of using the CDCB specimen for measurement of Mode I interface fracture toughness. A peeling delamination test of an HFRP sandwich panel is successfully modeled, demonstrating the predictive capability of the developed CZM to simulate the facesheet-core interface delamination propagation in actual HFRP sandwich panels with sinusoidal wave core configuration. Finally, a simulation of a four-point bending test of an actual HFRP sandwich panel is conducted, and without assuming an initial delamination, the cohesive zone modeling approach with the present interface element successfully predicted the delaminated region observed in the experiment.

Acknowledgments

I would like to express my gratitude and appreciation to my advisor Dr. Julio F. Davalos, for his continuing assistance, support and encouragement through the inspiring guidance of this research. Special thanks to the committee members, Dr. J. Prucz, Dr. B. Kang, Dr. P. Qiao and Dr. I. Ray for their academic collaboration and valuable suggestions for this dissertation.

Thanks are also owed to Kansas Structural Composites Inc. for generously providing all the test samples. Laboratory assistance of Mr. Raabal El-Amine, Mr. Justin Robinson and Mr. Avinash Vantaram should be acknowledged. I also want to thank my colleagues Mr. An Chen and Mr. Chuanyu Feng for helpful discussions.

At last but not least, I want to express deepest thanks to my lovely and beautiful wife Jieming for her endless support and forbearance throughout my academic career. I also must thank my parents and family for their everlasting support and blessings in my life.

This research is supported by NSF Partnerships for Innovation program.

Table of Contents

List of Figures

i

List of Tables

Nomenclature

(H)FRP	(Honeycomb) Fiber-Reinforced Polymer
CZM(s)	Cohesive Zone Model(s)
SERR	Strain Energy Release Rate
(C)DCB	(Contoured) Double Cantilever Beam
FWT	Flatwise Tension
LEFM	Linear Elastic Fracture Mechanics
SIF(s)	Stress Intensity Factor(s)
EPFM	Elastic-Plastic Fracture Mechanics
COD	Crack Opening Displacement
CTOD	Crack Tip Opening Displacement
BIFM	Bi-material Interface Fracture Mechanics
SED	Strain Energy Density
FPZ	Fracture Process Zone
R.C.T.	Real Crack Tip
F.C.T.	Fictitious Crack Tip
PBI	Pseudo Boundary Integral
FE(M)	Finite Element (Method)
XFEM	eXtended Finite Element Method
BEM	Boundary Element Method
SF	Singular Field
CTE	Crack Tip Element
NSF	Non-Singular Field
ELS	End Load Split
ENF	End Notch Flexure
ECT	Edge-Cracked Torsion
MMB	Mixed-Mode Bending
VCCT	Virtual Crack Closure Technique
CSB	Cracked Sandwich Beam

HSAPT	high-order sandwich plate theory
DLS	Double-Line-Search
SLS	Single-Line-Search
RVE	Representative Volume Element
ChopSM	Chopped Strand Mat
LVL	Laminated Veneer Lumber
MTS	Mechanical Testing System
ASTM	American Society for Testing and Materials
LVDT	Linear Variable Differential Transformer

Chapter 1

Introduction

1.1 Sandwich Structures

Sandwich structure concept arose many years ago with the credit usually attributed to Fairbairn (1849) who first came up with this idea. Due to their many advantages, sandwich structures are gaining increasing applications in aeronautical, marine, automotive and civil engineering. Typically, a sandwich structure consists of two thin, stiff and strong facesheets of dense material separated by a thick core made of low density material which may also be much less stiff and strong (Figure 1.1 a). Such a structure provides an analogy to an I-beam where the facesheets are equivalent to the flanges, and the core acts as the web. Obviously by adjusting the height of the core, the bending stiffness of this arrangement could be very much greater than that of a single solid plate of the same total weight made of the same material as the facesheets.

The facesheets carry in-plane and bending loads, while the primary function of the core is to resist transverse shear loads. The core should be stiff enough in the direction perpendicular to the facesheets to ensure that they maintain the correct distance apart while not sliding with respect to each other in order to ensure composite action. Also, the core must be stiff enough to keep the facesheets as flat as possible to prevent them from local buckling (wrinkling) under in-plane compressive loads.

Facesheets materials include metals and fiber reinforced composites, the latter being used mostly in advanced applications due to their high strength-to-weight ratios. A variety of core shapes have been used which may fall into three categories: foam or solid core, honeycomb core, and corrugated or truss core. The ‘solid’ core is relatively inexpensive and can consist of perforated chipboard, balsa wood, plastics, low density foams, lightweight concrete, or clay products, etc. (Figure 1.1a). Since World War II, honeycomb core architectures have been widely used. It is typically formed from strips of thin aluminum alloy or steel foil deformed and joined together (Figure 1.1b). The corrugated core is a fluted metal sheet attached alternately to the upper and lower facesheets (Figure 1.1c). Non-metallic honeycomb and corrugated cores are becoming increasingly popular due to their light weight and flexibility in the manufacturing process.

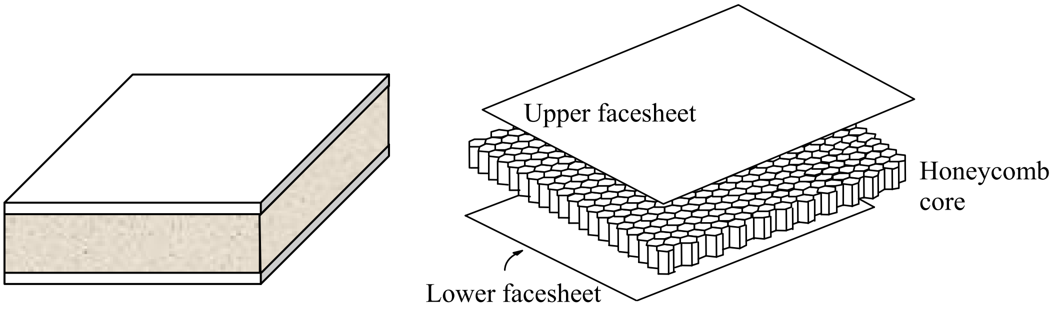

(a) foam core (b) honeycomb core

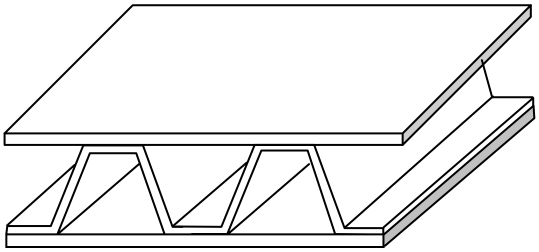

(c) corrugated core

Figure 1.1 Sandwich panels with various core configurations.

The proper design of sandwich structure is very important in order to achieve its expected load-bearing capability. It involves such details as nature of the edge members, splices and joints in the cores and facesheets, stiffeners and inserts to distribute concentrated loads, type of adhesive, method of fabrication and so on. A detailed description of sandwich structures design and analysis can be found in the books by Plantema (1966), Allen (1969), Zenkert (1995) and Vinson (1999).

1.2 HFRP sandwich panels

Developments in new cores continue to be of primary interest. Recently, growing interests have arisen in composite materials for civil infrastructure rehabilitation. The concept of lightweight and heavy-duty honeycomb fiber-reinforced polymer (HFRP) sandwich panels, with sinusoidal wave core configuration in the plane extending vertically between face laminates, was developed for highway bridge decks by Kansas Structural Composites Inc. Stiffness characterizations for these panels have already been completed by Davalos et al. (2001).

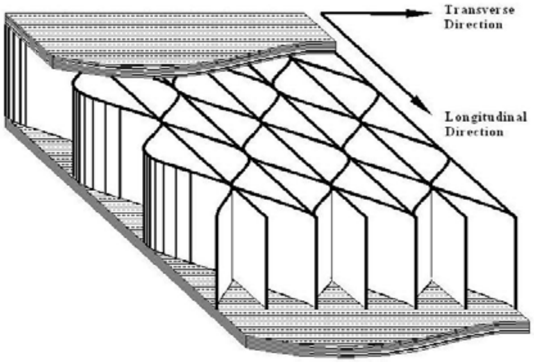

Figure 1.2 Configuration of the HFRP sandwich panel.

HFRP panels consist of a sinusoidal honeycomb core attached to two facesheets with bonding layers of polymer resin (Figure 1.2). Each component may fail in a distinct way, e.g. facesheet wrinkling, core shear, or facesheet-core debonding (Figure 1.3), which will degrade the structural performance of the sandwich panel or even lead to its sudden overall failure.

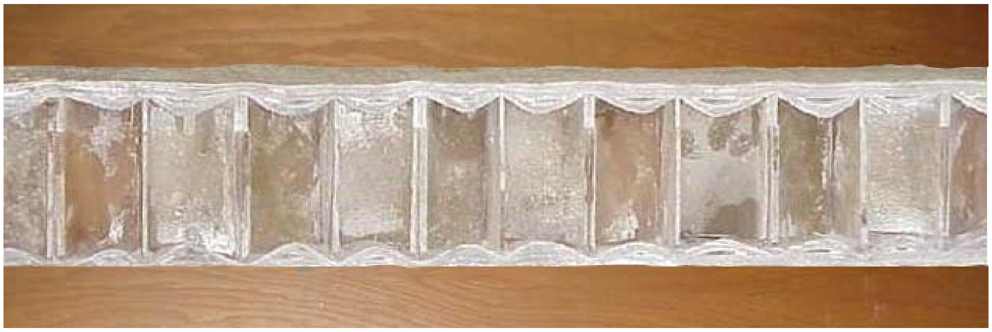

(a) facesheet wrinkling

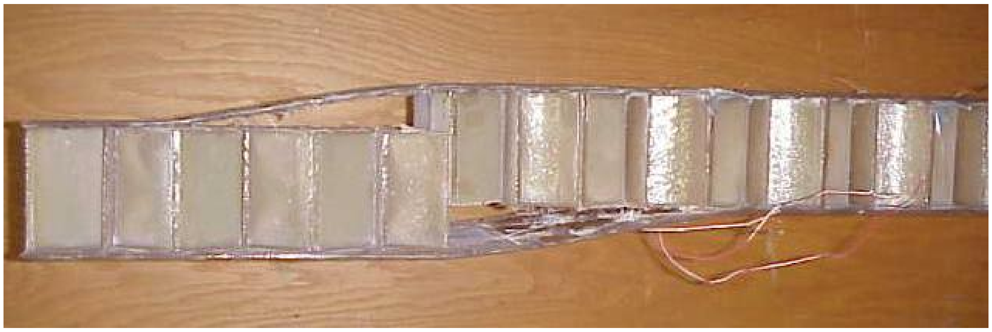

(b) core shear

(c) facesheet-core debonding

Figure 1.3 Failure types of HFRP sandwich panels.

1.2.1 Delamination: An Important Failure Mode

Among the aforementioned modes of failure, facesheet-core interface debonding or delamination is of major importance because of its frequent occurrence and adverse effects. It is critical that the interface bond between the facesheets and the core remain intact for the panel to perform its task. However, quite often manufacturing defects, in-service loading conditions, impact of foreign objects, or high stress concentrations in the area of geometric or material discontinuities can cause an initial debonding at the interface. In the debonded region, the facesheet will lose its support from the core and it results in the loss of I-beam effect of the sandwich panel. Under compression or shear loads, it may cause the facesheet buckling and further delamination propagation, which can lead to catastrophic collapse of the structure.

From the point of view of prediction and numerical simulation, the delamination failure in laminated composite and sandwich structures poses many challenges for engineers. Delamination can be conveniently treated as a problem of fracture mechanics. However, traditional methods in fracture mechanics such as the virtual crack closure integral assume an initial delaminated area and self-similar crack growth. Generally, delamination growth is non-self-similar, and thus renders the existing methodologies impractical. Furthermore, the facesheet-core delamination involves all the complications of the elastic bi-material fracture mechanics, especially the lack of rationally based procedures for the determination of mode components of strain energy release rates (SERR), G_{I}, G_{II}, and G_{III} in bi-material crack problems.

1.3 Objective and Scope

The primary objective of this thesis is to investigate the feasibility of applying the cohesive zone model (CZM) for simulating delamination propagation of the HFRP sandwich panels. This model is not based on classical fracture mechanics which is heavily concerned with crack tip singular stress fields. In bi-material interface delamination problems, it is usually assumed that the interface is much weaker than the surrounding bulk materials and the crack path is known a priori along the interface. A cohesive layer is then interposed at the interface and the model is governed essentially by the critical values of the SERR (G_c) and strength (σ_c) of the interface as determined experimentally. The model unifies strength-based crack initiation and fracture-based crack propagation. The initiation of fracture is determined by σ_c and the progression of fracture is determined by G_c. A variety of CZMs have been used to address many kinds of problems in the literature. In the current study, a linear-exponential form of CZM is proposed and implemented into a general purpose finite element code as a special 3D interface element capable of dealing with mixed-mode crack situations. As opposed to traditional one-parameter (G_c) fracture mechanics methods, the two-parameter (G_c and σ_c) CZM has many advantages such as robustness, simplicity and the ability to account for contact of the delaminated surfaces.

The secondary objective is to determine the interfacial properties, i.e. G_c and σ_c, of the HFRP sandwich panels. Contoured Double Cantilever Beam (CDCB) specimens are used for the Mode I interfacial fracture toughness G_{cI}. Interfacial tensile and shear strength σ_{cI}, σ_{cII} (or σ_{cIII}) are determined by flatwise tension (FWT) and shear tests, respectively. The influence of varying bonding layers and core thickness are investigated for the purpose of optimized practical application.

The developed CZM is applied to many problems with delamination or debonding involved. Although the method is initially intended for study of delamination propagation in HFRP sandwich panels, it also provides an efficient approach to predict and track the delamination growth in laminated composite structures. Within the context of fracture mechanics, the primary emphasis here is slow stable crack growth, sub-critical and quasi-static. Dynamic crack propagation is beyond the current version of the interface element formulation. Standard fracture test configurations loaded under Mode I, Mode II, and mixed-mode loading are simulated to verify the predictive capability of the developed CZM. For the modeling of HFRP sandwich panels, a CDCB specimen is first simulated, followed by modeling of a peeling test and a bending test of sandwich panels. Compressively loaded laminated composite plates containing initial delaminations will first undergo delamination buckling before experiencing delamination growth. In these cases, contact or loss of contact between the delaminated surfaces can be an important factor in the prediction of structural collapse or dictating the mode of delamination growth. Interface element with contact detecting capability is applied to address this problem. Composite plates containing through-the-width delaminations and subjected to compression are simulated.

1.4 Organization of the Dissertation

The remainder of this dissertation is organized into six chapters.

Chapter 2 is intended to provide background materials related to the topic to be investigated in the subsequent chapters. It contains a brief review of fracture mechanics with emphasis on the bi-material interfacial fracture problem followed by an introduction to five popular nonlinear crack models for nonmetallic materials.

Chapter 3 focuses on modeling of delamination in layered composite laminates and composite sandwich structures. A comprehensive literature review is undertaken of previous work by other researchers in this field. Traditional modeling techniques are discussed, however preference is given to cohesive crack modeling via interface elements.

In Chapter 4, the framework and formulation of a three dimensional cohesive interface finite element are described. A mixed-mode linear-exponential softening traction-separation law is proposed to represent progressive damage occurring in the interface during the fracture process. Typical nonlinear solution methods are also discussed.

In Chapter 5, verification examples applying the developed interface element are presented with numerical simulations of standard fracture test configurations and buckling driven delamination in a laminated composite plate loaded with in-plane compression. Typical computational issues related to modeling with interface elements are discussed.

Chapter 6 is exclusively devoted to modeling of facesheet-core interface delamination in HFRP sandwich panels. A systematic experimental program is carried out to investigate interfacial properties as required in the application of the CZM. Using the measured properties, simulations are performed for three cases: a CDCB specimen, a peeling delamination test, and a four-point bending test.

In the last chapter, major conclusions are summarized and suggestions for future work are given.

Chapter 2

Fracture Mechanics and Nonlinear Crack Models

The life of a structural component is limited by its ability to resist the effects of its usage history, which may consist of cyclic loads, fluctuations in temperature, or a corrosive environment. With the increasing cost of developing advanced structures, engineers find it more economical to refurbish and maintain the existing structures than to build new ones. The damage tolerance design method has become widely accepted in the industry to extend the life of a structural component. Allowing for the presence of sub-critical cracks that will not grow to critical length between periodic inspections, this method provides quantitative guidance for the balancing of the cost of repair or replacement of a damaged component against the possibility that continued service could lead to failure. This design method is primarily based upon fracture mechanics to ensure sufficient strength and structural integrity to sustain major damage and to avoid catastrophic failure.

In this chapter, a brief review of fracture mechanics will be given with emphasis on the bi-material interfacial fracture mechanics. An introduction is then made to five nonlinear crack models for nonmetallic materials which are widely adopted in the literature for numerical modeling of crack initiation and propagation within materials or in the material interfaces.

2.1 Linear Elastic Fracture Mechanics (LEFM)

The origin of contemporary fracture mechanics is Griffith's work on the fracture of glass (Griffith, 1920). The basic idea put forward by Griffith is an energy balance equation that relates the rate of change of internal and external energy due to crack propagation to the surface tension corresponding to the newly created surfaces. An expression for the necessary condition for fracture propagation of a crack with surface area A, can be stated as

$$\frac{d}{dA}(U - V) = 2\gamma \tag{2.1}$$

where V and U refer to the work of the external forces and internal strain energy, respectively, and γ is the specific surface energy of the solid.

Griffith's work was largely ignored by the engineering community until the late 1940's when Irwin (1948) and Orowan (1948) investigated brittle fracture of metallic structures and found that in the energy balance equation, the rate of plastic work, at the crack front, must also be considered as a component of the dissipated energy. Irwin concluded that if the characteristic size of the zone of plastic deformations is very small compared to the length of the crack, the energy flow into the fracture zone will come from the elastic bulk of the solid. Therefore, it will not be critically dependent on the details of the stress state very near the crack tip. In addition, the stress in the elastic bulk of the solid will not differ significantly from the purely elastic solution. This work led to the generalization of Griffith's equation to

$$\frac{d}{dA}(U-V)=G \tag{2.2}$$

where G is the energy release rate for crack propagation and incorporates the effects of small scale yielding at the crack tip. Because of this significant observation, under certain conditions, one can now justify calculating the energy available for crack propagation from a purely elastic analysis. This idea is the fundamental underpinning of linear elastic fracture mechanics (LEFM).

Irwin's second important contribution was to provide a quantitative relation between the sometimes mathematically awkward strain energy release rate (SERR), a global parameter, and the stress-intensity factor (SIF), a local crack-tip parameter. He was able to do this by recognizing the universality of the asymptotic stress and displacement fields around the crack-tip for linear elastic materials. The asymptotic stress fields for different configurations differ only by scalar coefficients, i.e. the stress-intensity factors (SIFs), K's. Imaging that the crack has extended by a small amount, Irwin calculated the work required to close it up to its original length which can be equated to the product of the energy release rate and the crack extension increment. By using the cracked body solutions of Westergaard (1939), he showed that the stresses and displacements near a crack tip in a linear elastic solid subjected to general loading conditions may be expressed in terms of three SIFs K_{I}, K_{II}, and K_{III}, corresponding to the three fundamental modes of fracture, i.e. opening, sliding, and shearing or tearing modes, respectively, as illustrated in Figure 2.1.

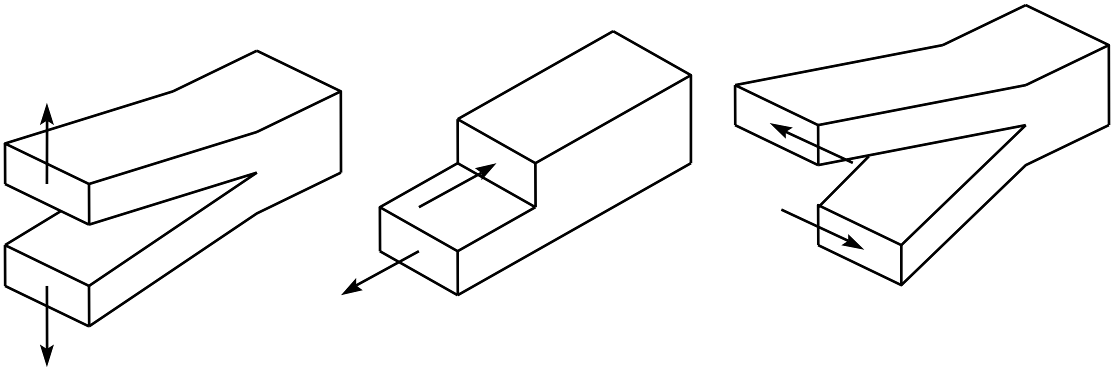

(a) Mode I (Opening) (b) Mode II (Sliding) (c) Mode III (Shearing)

Figure 2.1 The three fundamental modes of fracture.

The SIFs quantify the effects of geometry and boundary conditions on the near-tip stress and strain fields. In the vicinity of an ideally sharp crack tip in a linear elastic and isotropic material (Figure 2.2), the stresses can be expressed in the following form referenced to the polar coordinates (r, θ)

$$\sigma_{ij} = \frac{K}{\sqrt{2\pi r}} f_{ij}(\theta) \tag{2.3}$$

where K is one of the three SIFs, and $f_{ij}(\theta)$ is a function of θ. The SIFs can be used to determine whether or not the crack would grow. An alternative measure of the tendency for crack propagation is the SERR, G and its components G_{I}, G_{II}, and G_{III}, which are easily related to K's as

$$G_I = \frac{K_I^2}{E}, G_{II} = \frac{K_{II}^2}{E} \tag{2.4}$$

in plane stress problems in isotropic materials.

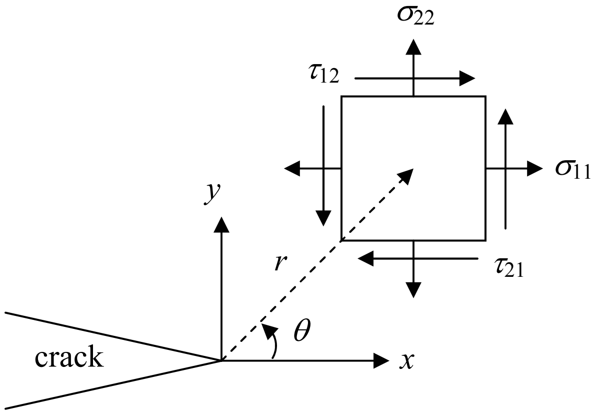

Figure 2.2 Stresses in a plane crack-tip.

2.2 Elastic-Plastic Fracture Mechanics (EPFM)

LEFM predicts impractical infinite stress at the crack tip, and it is limited by the small-scale yielding condition that the plastic zone near the crack tip be small compared to the size of the *K*-dominant region and any relevant geometric dimension. Irwin (1958) estimated the size of the plastic zone, r_y, at a crack tip in a material with yield strength of σ_Y as

$$r_y = \frac{K^2}{n\pi\sigma_Y^2} \tag{2.5}$$

where n = 1 for plane stress and n = 3 for plane strain. If r_y is relatively small, LEFM could still be used provided that an effective crack length equal to $r_y/2$ was added to the actual crack length. However, for high toughness, low strength materials which generally undergo extensive plastic deformation and crack-tip blunting prior to initiation of crack growth, LEFM cannot predict accurately the load carrying capacity of a degraded component made from these materials. To overcome this difficulty, there have been large advances in the development of elastic-plastic fracture mechanics (EPFM).

Wells (1961) introduced the crack opening displacement (COD) concept, later called crack tip opening displacement (CTOD), δ, to model fracture under general yielding conditions. By assuming that δ will be directly proportional to overall tensile strain e after general yield has been reached, Wells suggested the following fracture criterion for the post-yield region

$$\frac{\delta}{2\pi e_Y a} = \frac{e}{e_Y} \tag{2.6}$$

where $e_Y = \sigma_Y / E$ is the uniaxial yield strain. This set the basis for the widely used COD method. In 1960, Dugdale developed an important closed-form solution of plastic zone size applicable for plane stress condition. This key paper largely advanced the COD concept. Using method of complex variable theory of elasticity developed by Mushkhelishvili (1954), Dugdale supposed that for a thin sheet loaded in tension, the yielding will be confined to a narrow band lying along the crack line. Mathematically, this idea is identical to placing internal stresses on the portions of the (mathematical) crack face near its tips; the physical crack being the remaining stress-free length. In Dugdale's model, the magnitude of the internal stresses are taken to be equal to the yield stress of the material, while the crack tip stress singularity was abolished. For a crack of length $2a$ in an infinite medium under uniform tension σ (Figure 2.3), the length of the plastic zone at the crack tip is given by Dugdale as

$$d = 2a\sin^2\left(\frac{\pi}{4}\frac{\sigma}{\sigma_Y}\right) \tag{2.7}$$

Based on the Dugdale model, Goodier and Field (1963) first obtained the explicit relation of δ as follows

$$\delta = \frac{8}{\pi}\frac{a\sigma_Y}{E}\log\left[\sec\left(\frac{\pi}{2}\frac{\sigma}{\sigma_Y}\right)\right] \tag{2.8}$$

Burdekin and Stone (1966) obtained this key result independently, and demonstrated that fracture could be governed by the critical value of COD, δ_c. Their work provided the basis for the well-known semi-empirical "COD Design Curve" approach.

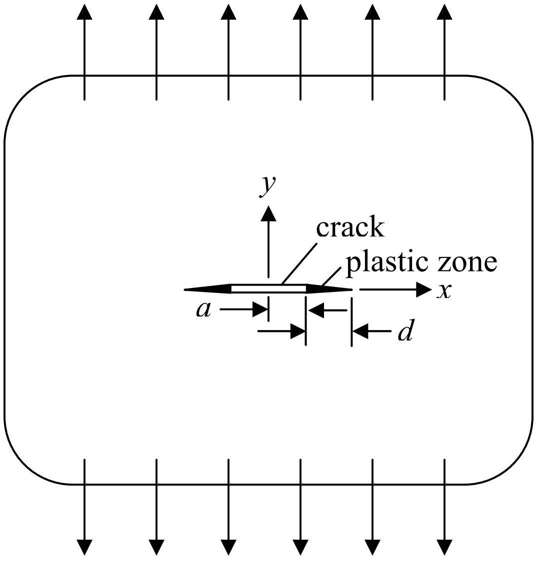

Figure 2.3 The Dugdale model.

As an alternative to the COD design curve, Rice (1968) developed a path independent integral, *J*-integral, and Hutchinson (1968) showed how such a concept could be used to obviate the need for a direct description of the discrete and nonlinear events involved in crack extension. The basic equation is

$$J = \int_{\Gamma} w dy - \mathbf{T}\frac{\partial \mathbf{u}}{\partial x} ds \tag{2.9}$$

where Γ is the a curve that surrounds the crack-tip, **T** is the traction vector, **u** is the displacement vector, *w* is the strain energy density and the *y* direction is taken normal to the crack line. The path independent of the *J*-integral arises because deformation plasticity (i.e. nonlinear elastic behavior) is used. Begley and Landes (1972) recognized that *J* provides three distinct attractive features: 1) for linear elastic behavior it is identical to *G*, 2) for elastic-plastic behavior it characterizes the crack-tip region and, hence, would be expected to be equally valid under nonlinear conditions, and 3) it can be conveniently evaluated experimentally. The interpretation of *J* as the rate of change of the potential energy for nonlinear constitutive behavior plays a key role for the analysis of fracture in elastic-plastic conditions. Hutchinson and Paris (1979) have shown that outside a core of non-proportional loading the deformation is nearly proportional. Provided the region of non-proportional loading is well contained within the region dominated by the *J*-singularity there exists an annular region where the HRR (Hutchinson, 1968; Rice and Rosengren, 1968) field holds (Figure 2.4). If fracture process zone size R is small compared to the *J*-dominant region D, the initiation and growth of a crack can be expected to be governed by a critical value of *J*.

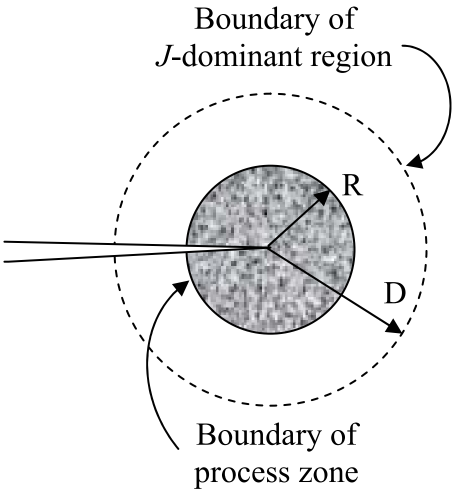

Figure 2.4 Basis for J-integral EPFM.

2.3 Bi-material Interface Fracture Mechanics (BIFM)

Despite the fact that LEFM techniques have been very successful for assessing defects in metals, limited success has been achieved so far for composite materials mainly due to their heterogeneous nature. Delamination in laminated composite and sandwich structures essentially involves cracking between materials of different properties. In this section, concepts of bi-material interface fracture mechanics (BIFM) will be briefly reviewed.

Although long-standing problems of adhesion mechanics have required consideration of failure and fracture at and near interfaces, it was only the advent of composite materials and the improved understanding of fracture in non-monolithic solids that motivated a widespread interest in interfacial fracture studies. The interface crack problem was first studied by Williams (1959) who showed that the stresses near the crack tip exhibit an oscillatory character of the type $r^{-1/2+i\varepsilon}$ where ε is a bi-material constant.

This result has also been confirmed by other researchers (Rice and Sih, 1965; Erdogan, 1965). The oscillatory stress singularity leads to physical absurdity of crack surface interpenetration or overlapping, as pointed out by England (1965) and Malyshev and Salganik (1965). Various ways have been proposed to resolve this problem: some have eliminated the oscillatory term by postulating a frictionless contact zone (Comminou, 1977a, 1977b; Gautesen and Dundurs, 1987, 1988), by relinquishing the hypotheses of infinitesimal deformations (Knowles and Sternberg, 1983; Ravichandran and Knauss, 1989; Hermann, 1989) or by introducing a transition layer (Yang and Shih, 1990). Others (Shih and Asaro, 1988, 1989; Shih, 1991) have used a numerical plasticity model to compute the detailed stress and deformation fields at the crack-tip. But the more widely used approach to deal with this problem is the concept of small-scale contact (Rice, 1988) which essentially ignores its presence on the basis of its usually small size.

Unlike homogeneous materials, bi-material interface crack exhibits a coupling of tensile and shear effects. In a 2-D problem, both opening and shearing modes are induced even when the geometry and loading are symmetric with respect to the crack plane. The oscillatory singular stress field is characterized by a complex stress-intensity factor, **K**, together with the bi-material constant ε, relating the elastic properties of the two materials.

Consider two isotropic elastic materials bonded along the x_1-axis as shown in Figure 2.5. Let E_i, v_i and μ_i denote the Young's modulus, the Poisson's ratio and the shear modulus of the ith material, respectively. Dundurs (1969) defined the following mismatch parameters

$$\alpha = \frac{\mu_1(k_2+1)-\mu_2(k_1+1)}{\mu_1(k_2+1)+\mu_2(k_1+1)} = \frac{E_1^{'}-E_2^{'}}{E_1^{'}+E_2^{'}} \tag{2.10a}$$

$$\beta = \frac{\mu_1(k_2-1)-\mu_2(k_1-1)}{\mu_1(k_2+1)+\mu_2(k_1+1)} \tag{2.10b}$$

where subscripts 1 and 2 refer to the materials above and below the interface, respectively; $E' = E$ in plane stress and $E/(1-v^2)$ in plane strain, $k = (3-v)/(1+v)$ in plane stress and $3-4v$ in plane strain.

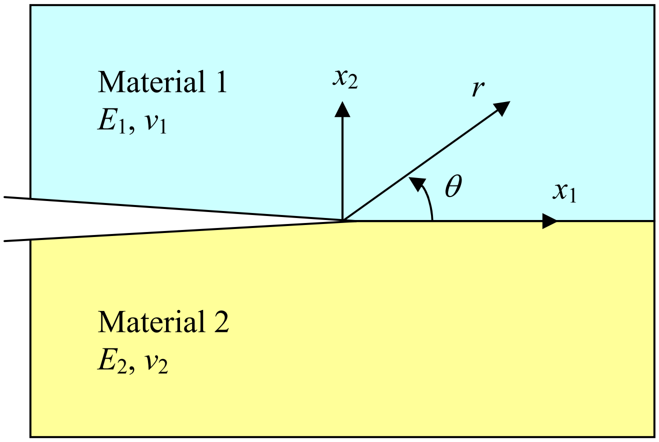

Figure 2.5 Interface crack between two dissimilar materials.

Both α and β vanish when the elastic properties of the two materials are the same and they change sign when the materials are interchanged. The bi-material constant ε can then be defined as

$$\varepsilon = \frac{1}{2\pi}\ln\frac{(1-\beta)}{(1+\beta)} \tag{2.11}$$

The complex stress-intensity factor, **K,** is defined as

$$\mathbf{K} = K_1 + iK_2 \tag{2.12}$$

where $i = \sqrt{-1}$. The notations K_1 and K_2 instead of K_{I} and K_{II} are commonly adopted for a bi-material system.

The stresses on the interface directly ahead of the tip, at $\theta = 0$, are given by

$$\boldsymbol{\sigma} = \sigma_{22} + i\sigma_{12} = \frac{K_1 + iK_2}{\sqrt{2\pi r}} r^{i\varepsilon} \tag{2.13}$$

where $r^{i\varepsilon}$ is the so-called oscillatory singularity which causes complications that are not present in the elastic fracture mechanics of homogeneous materials.

The corresponding crack flank displacements at a distance r behind the tip, $\theta = \pi$, are given by

$$\boldsymbol{\delta} = \delta_2 + i\delta_1 = \frac{8(K_1 + iK_2)}{(1+2i\varepsilon)\cosh(\pi\varepsilon)}\sqrt{\frac{r}{2\pi}}\frac{r^{i\varepsilon}}{E^*} \tag{2.14}$$

with

$$\frac{1}{E^*} = \frac{1}{2}\left(\frac{1}{\overline{E}_1} + \frac{1}{\overline{E}_2}\right) \tag{2.15}$$

where $\overline{E}_i = E_i$ in plane stress and $\overline{E}_i = E_i / \left(1 - v_i^2\right)$ in plane strain.

An alternative characterization of the near-tip stress field involves the energy release rate, G, together with the loading phase angle, Ψ. The interface energy release rate G is related to the stress-intensity factors by

$$G = \frac{|\mathbf{K}|^2}{\cosh^2(\pi\varepsilon)E^*} \tag{2.16}$$

and the phase angle is

$$\Psi = \tan^{-1}\left[\frac{\mathrm{Im}\left(KL^{i\varepsilon}\right)}{\mathrm{Re}\left(KL^{i\varepsilon}\right)}\right] \tag{2.17}$$

where L is an arbitrary length parameter. Hutchinson and Suo (1992) suggested taking L as a measurement of the crack tip process zone, for example. The phase angle, indicating the mode mixity, measures the ratio between the shear stress and normal stress at the interface in front of the crack tip.

Of the two non-dimensional parameters, α and β, measuring the dissimilarity in material elastic properties, α is more important. For most material systems, the influence of β is small and negligible (He and Hutchinson, 1989). Taking $\beta = 0$, thus $\varepsilon = 0$, equations (1.16) and (1.17) become

$$G = \frac{K_1^2 + K_2^2}{E^*} \tag{2.18}$$

$$\Psi = \tan^{-1}\frac{K_2}{K_1} \tag{2.19}$$

The criterion for initiation of crack growth in the interface when crack tip is loaded in mixed mode characterized by Ψ is

$$G = G_c(\Psi) \tag{2.20}$$

The relationship between the loading phase angle, Ψ, and the interface toughness, G_c, is a property of the type of material on either side of the interface and the nature of the bonding. Usually, G_c is determined by experiment (Charalambides et al., 1989) although

Hutchinson (1989) proposed the following analytical expression to describe interface toughness variations

$$G_c = G_{c0}\left(1 + \tan^2 \Psi\right) \tag{2.21}$$

where G_{c0} is the toughness when the shear loading is zero.

2.4 Nonlinear Crack Models for Nonmetallic Materials

In brittle-matrix fiber-reinforced composites and quasibrittle materials (like concrete, rocks, ceramics, polymers, high-strength metallic alloys), nonlinear mechanical effects generally occur at the tip of macrocracks. Such local effects as, for example, plastic deformation, yielding, strain-hardening, strain-softening, mechanical damage, matrix microcracking, aggregate debonding, fiber bridging, fiber slippage, crazing, and so on, should be properly described through different simplified models. Excluding the metallic alloys, for which the bulk behavior cannot always be modeled as linear elastic, all the other structural materials may be studied through nonlinear crack models, where nonlinearity is concentrated only in the crack tip region. In this section, five most relevant nonlinear crack models are reviewed and compared.

2.4.1 Damage Crack Model

In this model, the strain energy density (SED) theory of Sih (1973, 1974) is applied to predict the failure modes. According to this theory, outside a core region of radius r_0 (a minimum distance below which it is meaningless to study the mechanical behavior of the material from a continuum-mechanics point of view), the SED field can always be described by the following general relationship

$$\frac{\mathrm{d}W}{\mathrm{d}V} = \frac{S(\theta)}{r} \tag{2.22}$$

All the material elements ahead of the crack tip will fail and induce crack growth when the SED is higher than a critical value S_c which is a material property and can be related to the SIF.

Based on the SED theory, the rate of change of the strain energy density factor dS with respect to the crack growth rate da remains constant for each loading increment, i.e. $\mathrm{d}S/\mathrm{d}a$ = constant. The straight line relationship S versus a rotates in a counterclockwise direction around a common point as the loading increment is increased. According to a model based on damage, the stress and strain fields in the whole body are reevaluated during the crack propagation, and the effective elastic modulus is reduced incrementally to reflect the degree of damage (Figure 2.6). The fracture strain ε_f is a sensitive parameter with $\varepsilon_f \to \infty$ to represent an elastic-perfectly plastic material and $\varepsilon_f \to \varepsilon_u$ (ultimate strain) to represent an elastic-perfectly brittle material. For mixed mode problems, the trajectory of the crack is determined assuming the crack will propagate in a direction normal to the maximum principal tensile stress by a length given by the SED criterion.

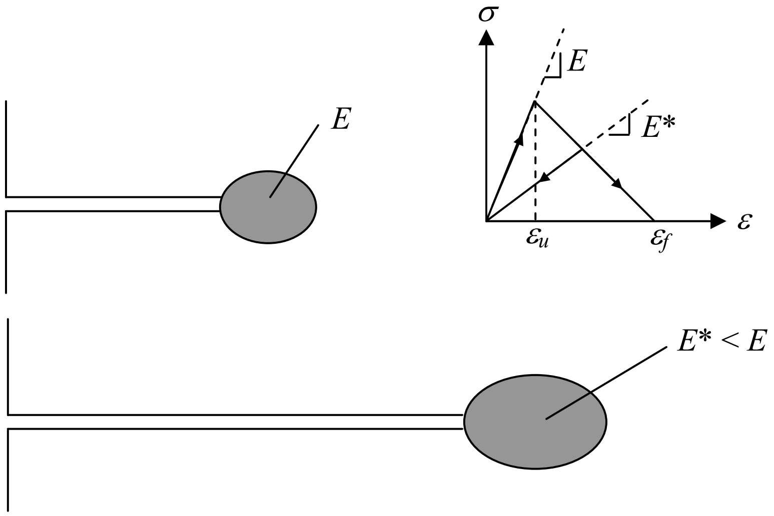

Figure 2.6 Damage crack model.

2.4.2 Cohesive Crack Model

In many quasibrittle materials, it is common that the global structural behavior exhibits strain softening, i.e., a negative slope of the stress-strain diagram, due to micro-cracking and localization of the deformation in a narrow band, called fracture process zone (FPZ), where energy dissipation occurs. The behavior of the material outside this band is still linear elastic. The fully developed fracture process zone (FPZ) is usually large compared to the crack length or other dimensions of a specimen, which renders LEFM inapplicable. The FPZ can be described by two simplified approaches: 1) the entire FPZ is lumped into the crack line and is characterized in the form of a stress-displacement law which exhibits softening; 2) the inelastic deformations in the FPZ are smeared over a band of a certain width, imaged to exist in front of the main crack. In this subsection, we will focus on the first approach which is usually referred to as cohesive crack model (also called fictitious crack model, Dugdale-Barenblatt model). The second approach, called the crack band model, will be illustrated in the next subsection.

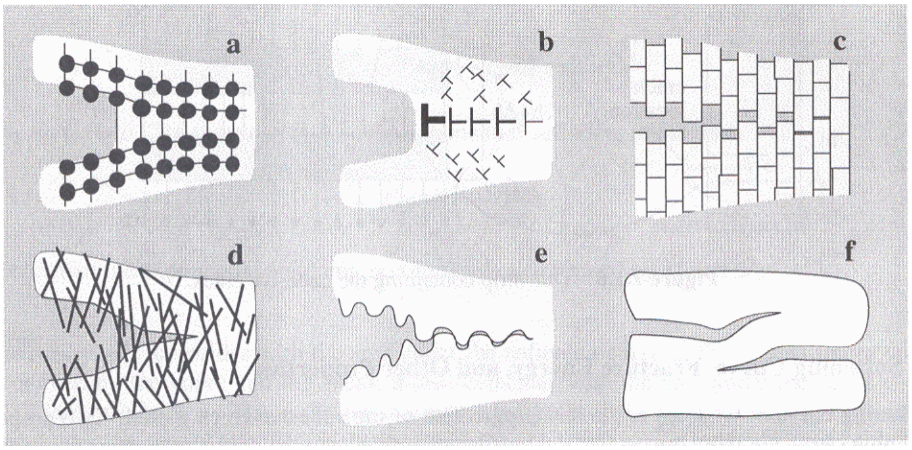

Figure 2.7 Various physical sources of cohesive cracks: a) atomic bonds, b) yield (dislocation) strip, c) grain bridging, d) fiber bridging, e) aggregate frictional interlock, and f) crack overlap (Bažant and Planas, p. 161, 1997).

Cohesive crack models came into being in the early 1960's to account for the basic aspects of the nonlinear material behavior ahead of the tip of a pre-existent crack. In these models, the crack is assumed to extend and to open while still transferring stress from one face to the other. The first cohesive model was proposed by Barenblatt (1962) to study the nonlinear behavior of the atomic bonds breaking during crack propagation (Figure 2.7a). Barenblatt simulated the interatomic forces by introducing distributed cohesive stresses on the newly formed crack surfaces, depending on the separation between the crack faces. His analysis showed that the cohesive zone could relieve the unrealistic crack tip singularity of LEFM. The fracture energy G_f was related to the atomic binding energy. Simultaneously, Dugdale (1960) proposed a relatively simple model to deal with plasticity at a crack tip, as previously mentioned in 2.2. The stress on the crack line ahead of the crack tip was assumed to be limited by the yield strength and the plastic deformation was concentrated along the crack line, thus generating a displacement discontinuity similar to a crack. This approximation can be justified based on flow of dislocations that combine and concentrate on the crack line (Figure 2.7b).

Since the pioneering studies of Barenblatt and Dugdale, cohesive crack models have frequently been used to describe the nonlinear behavior near the crack tip in metals, polymers, ceramics, and geomaterials. Many distinct micromechanisms with scales ranging from nanometers to centimeters, as shown in Figure 2.7, have been successfully treated using these models.

In the late 1970's, Hillerborg, Modéer and Petersson (1976) extended the concept of cohesive crack for concrete, called fictitious crack model. This model can not only be used to describe the behavior of a pre-existing crack, but by including crack initiation rules, it can also be applied to initially uncracked structures and describe all the fracture processes from no crack at all to complete structural breakage. The fictitious crack model provides a continuous link between the classical strength-based analysis of structures and the energy-based classical fracture mechanics: cohesive cracks start to open as dictated by a strength criterion that naturally and smoothly evolves towards an energy criterion for large cracks. As this model forms the basis of many other cohesive models developed later, its basic concepts will be introduced next.

The basic assumption is the formation, as an extension of the real crack, of a fictitious crack, referred to as the process zone, where the material, although damaged, is still able to transfer stresses (Figure 2.8). The point separating the stress-free area, i.e., the real crack, from the process zone, is called the Real Crack Tip (R.C.T.), while the point separating the process zone from the uncracked material is referred to as the Fictitious Crack Tip (F.C.T.).

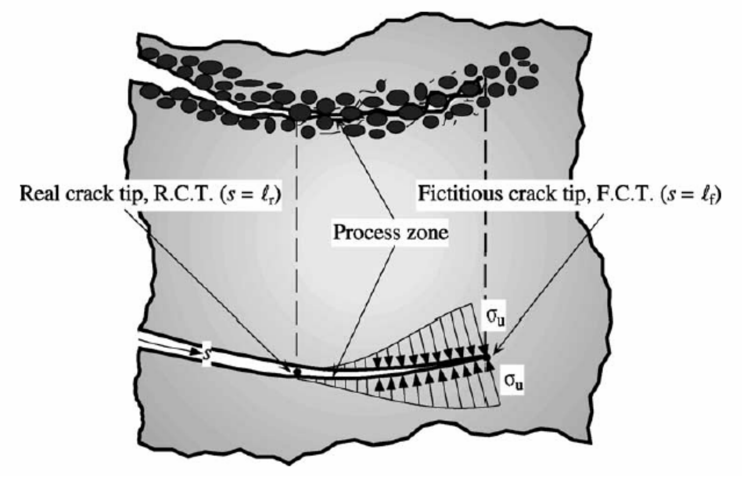

Figure 2.8 Fictitious crack model (Carpinteri et al., 2003).

In the process zone, the crack will propagate when stress at the crack tip reaches the material's ultimate tensile strength σ_u. During crack propagation, the stresses transferred by the material are some form of decreasing functions of the crack separation (Figure 2.9b). It is assumed that all the energy dissipation takes place in the process zone, while the bulk material remains linear elastic (Figure 2.9a). At the F.C.T., the stress will always be equal to the ultimate tensile strength, thus eliminating stress singularities. The area under the curve of stress versus crack separation represents the fracture energy, G, which together with σ_u, characterizes the two-parameter fracture model.

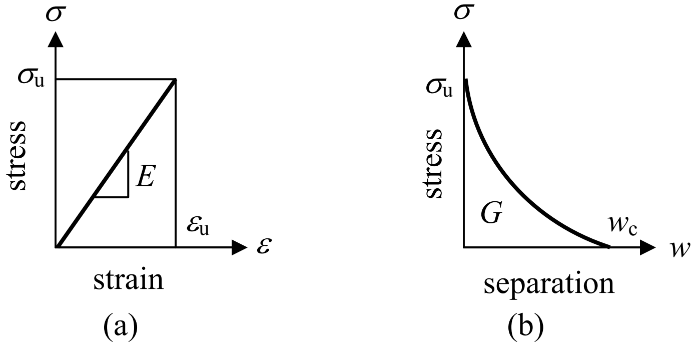

Figure 2.9 Constitutive laws: (a) undamaged material, (b) process zone.

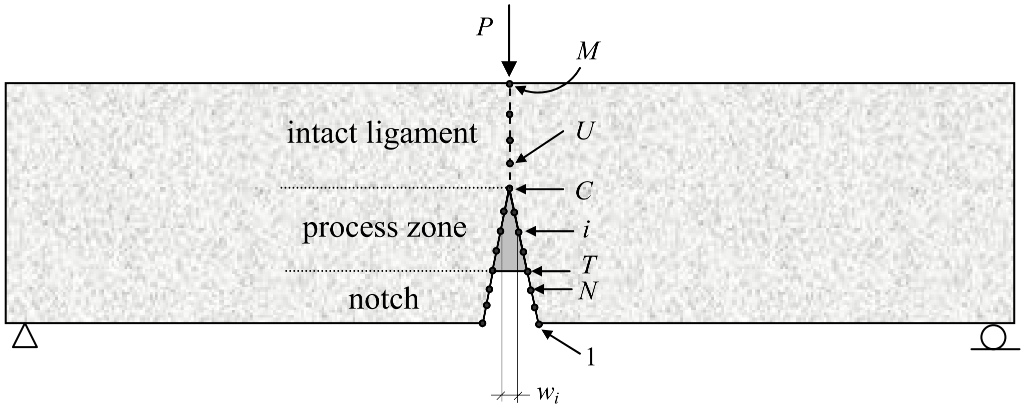

Figure 2.10 Three-point bending concrete specimen for PBI methods.

The cohesive crack models find a lot of applications for numerical modeling of crack propagation in materials exhibiting strain softening, for example, in concrete structures. Figure 2.10 shows a three-point bending test of a concrete beam. A mode I problem is considered since the crack trajectory is known along the middle span of the beam due to symmetry. The pseudo-boundary-integral (PBI) methods can be efficiently applied to this case. They are similar to boundary integral methods, but the kernel of the integral equation is discretized *a priori* typically using the finite element method (FEM). The cohesive crack problem will be reduced to solving a system of equations defined on the cracked cross-section. A FE mesh is created with M pairs of nodes arranged along the crack path. We assume, in general, that the structure has an initial notch spanning the nodes $1,\cdots,N$, and that the process zone has extended from the node at the initial R.C.T. node $T = N + 1$ to the F.C.T. node C; the nodes from $U = C + 1$ on pertain to the uncracked ligament. In the process zone, the cohesive forces σ_i are related to the crack opening w_i according to a constitutive law $f(w_i)$. The governing equations of the problem are written in terms of the nodal values as

$$\sigma_i = 0 \qquad \text{for } i = 1,\cdots,N \tag{2.23a}$$

$$\sigma_i = f(w_i) \qquad \text{for } i = T,\cdots, C \tag{2.23b}$$

$$w_i = 0 \qquad \text{for } i \geq C \tag{2.23c}$$

In this system, σ_i and w_i are explicit unknowns, and the load P is an implicit unknown. The PBI methods use elastic relations to link σ_i, w_i and P. The solution can be sought by various methods, such as, the influence method (Petersson, 1981; Planas and Elices, 1991), the smeared-tip method (Planas and Elices, 1992; Bažant, 1990).

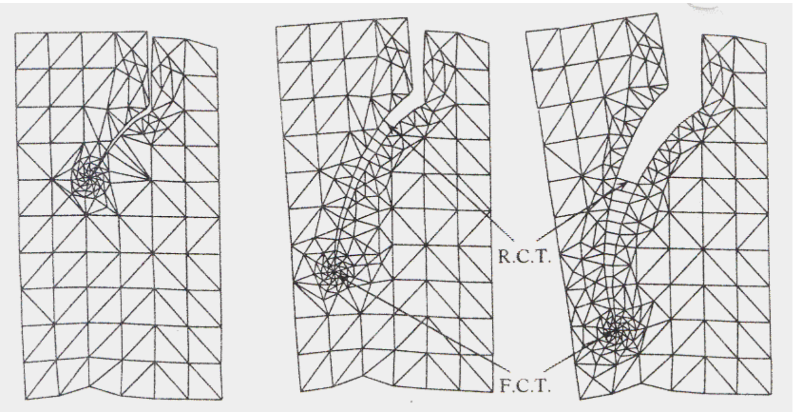

Figure 2.11 Discrete interelement crack approach applied to mixed-mode crack growth (Carpinteri, p.85, 1998).

The PBI methods are very powerful for the analysis of repetitive geometries of various sizes and different material properties, which are particularly suited for determining the size effect for a wide range of sizes. However, they are not intended to solve a single particular case, especially for mixed-mode loading problems, because the time savings in computing the crack growth cannot compensate for the computation of the influence matrices. In a mixed-mode problem, the crack path is unknown before the analysis, and the growth of a cohesive crack is a highly nonlinear process which usually requires complex numerical procedures. In the last two decades, a considerable amount of computational effort has been devoted to deal with cohesive cracks using FEM. Among them, three main approaches have been used: 1) discrete interelement crack approach, 2) smeared crack approach, 3) discrete intraelement crack approach.

In the discrete interelement crack approach, the crack extends between elements as shown in Figure 2.11. The softening behavior in the process zone is simulated using interface elements connecting the nodes on both sides of the crack. The FE mesh must be modified at each step of crack propagation. Automatic adaptive mesh generation and analysis program is needed to reduce the complexities involved. A number of special programs have been developed for such purpose, for example, C.CRA.P. (Carpinteri, 1998), FRANC (Ingraffea, 2003), MERLIN (Saouma, 2003). In the smeared crack approach, conventional FE formulations are used with element-dependent stress-strain relations obtained by smearing the crack opening displacement in the element intersected by the crack. It has the advantage that the mesh topology is unchanged during crack growth. Such concept is very close to the crack-band model which will be introduced in the next subsection. Recently, a new robust discrete intraelement crack approach has been developed in which the crack runs through elements. This method is called the eXtended Finite Element Method (XFEM) by the developers (Belytschko and Black, 1999; Moës, Dolbow and Belytschko, 1999). In XFEM, the standard displacement-based finite element approximation is enriched near a crack by incorporating both the discontinuous field and the singular asymptotic crack tip field. Figure 2.12 shows a typical XFEM mesh with a curved crack of two tips. With such enrichment, the FE mesh can be considerably coarse near the crack tip and the elements need not to conform to the crack geometry. For growing cracks, no remeshing is necessary. In principle, this technique can be applied to problems with arbitrary discontinuities and singularities demonstrated by several applications (Sukumar *et al.*, 2000, 2003a, 2003b; Belytschko *et al.*, 2001; Huang *et al.*, 2003; Patzák and Jirásek, 2003). Extension of this method to cohesive crack models are reported by Wells and Sluys (2001) and Moës and Belytschko (2002). Due to absence of a stress singularity, no special enrichments around the crack tip are needed.

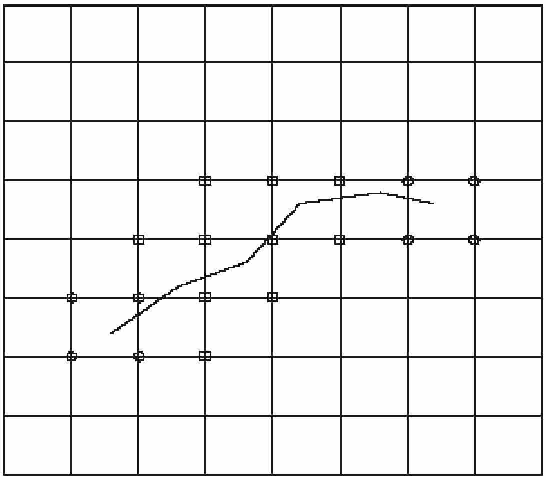

Figure 2.12 A typical XFEM mesh with a curved crack of two tips. The squared nodes are enriched with the Heaviside function, and the circled nodes are enriched with the near-tip asymptotic field.

The aforementioned formulation of the cohesive crack model is its simplest version. Five possible extensions of this model were discussed in Bažant and Planas (1997): 1) extend the formulation to include cohesive crack tip singularity using a softening curve consisting of an initial spike with large strength, which is suitable for describing fracture of fiber-reinforced materials; 2) accept a behavior other than isotropic linear elastic in the bulk material around the crack; 3) introduce dependence on stress triaxiality; 4) introduce a fully consistent mixed-mode formulation; 5) introduce time-dependence in the cracking behavior and in the bulk material. Due to these flexibilities, cohesive crack models are widely used and continually developed recently. Application of these models to study delamination in composite structures will be discussed in Chapter 3, and a mixed-mode cohesive zone model will be implemented and applied in the subsequent chapters.

2.4.3 Crack Band Model

Smeared cracking approach has gained wide popularity in finite element analysis, particularly, of concrete structures. Instead of modeling fracture by discrete line cracks, in this approach, cracks are represented in a smeared manner, as was first introduced by Rashid (1968), that infinite number of parallel cracks of infinitely small opening are imaged to be continuously distributed (smeared) over the finite element. This can be conveniently modeled by reducing the material stiffness and strength in the direction normal to the cracks after the peak strength of the material has been reached. Such changes of the stiffness matrix can be easily implemented in a finite element code, which is the appealing feature of this method.

The smeared cracking with strain softening, however, leads to certain numerical difficulties, such as, localization instabilities and spurious mesh sensitivities. In order to prevent localization of smeared cracking into arbitrarily small regions, some mathematical concepts, called localization limiter, were introduced. One of such concepts is the crack band model, which is rather simple and also popular. This model was developed by Bažant and co-workers (Bažant, 1976; Bažant and Cedolin, 1979, 1980, 1983). The basic attribute of this model is that the given constitutive relation with strain softening must be associated with a certain width h_c of the crack band, which represents a reference width and is treated as a material property to be determined experimentally.

There is a close similarity between the crack band model and the cohesive crack model in terms of the softening constitutive law. This can be illustrated in Figure 2.13 for a uniaxial case. The only difference results from the strain and displacement distribution. Figure 2.14a and b show the comparison of the axial displacement distribution in a bar for a cohesive crack model and a crack band model. Figure 2.14c and d show the corresponding strain distributions. The difference could be nil for most engineering problems since it is almost invariably true that $h_c << L$ (bar length) in practical situations.

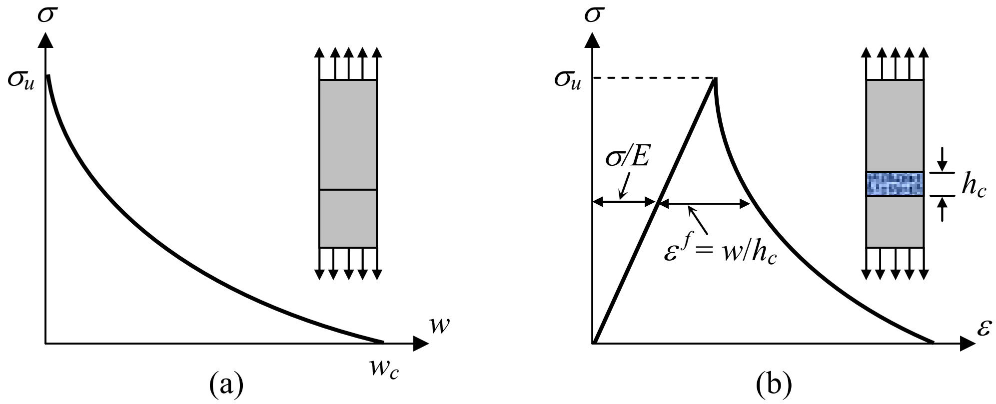

(a) (b)

Figure 2.13 Correspondence between the softening curve of the cohesive crack model (a), and the stress-strain curve of the crack band model (b).

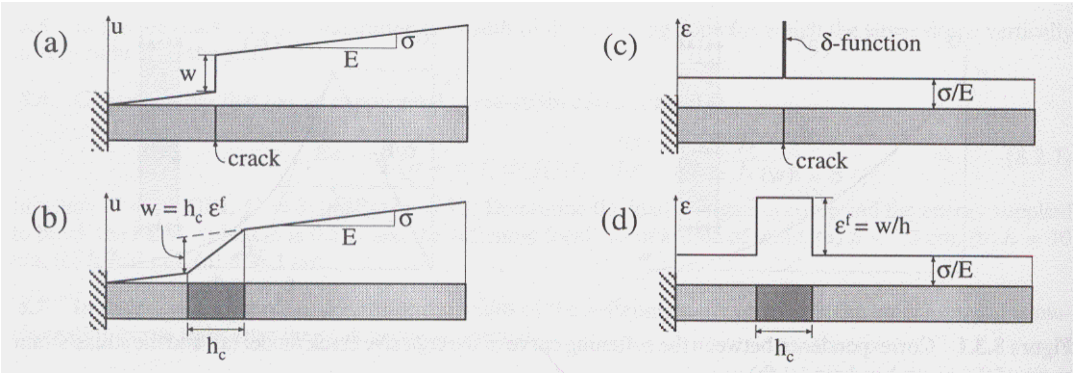

Figure 2.14 Comparison of the distributions of axial displacement and of strain in a bar for the cohesive crack model (a, c) and the crack band model (b, d) (Bažant and Planas, p. 222, 1997).

2.4.4 Bridged Crack Model

The fracture process zone in quasi-brittle materials typically consists of a microcracking region, near the tip of the macrocracks, and a bridging region, along the wake of the macrocracks. Microcracks initiate and propagate at nearby pre-existing flaws and secondary phases (e.g. grains, aggregates, fibers and particles); these secondary phases can restrain the macrocrack from opening by their bridging action. In normal concrete and various cementitious composites, for instance, the bridging and the microcracking regions often coexist on the same scale. In many composites the fracture process essentially involves the brittle growth of a single crack bridged by reinforcing elements.

The bridged crack model is intended to describe the toughening mechanisms of load transfer from the reinforcements to the surrounding material. Similar to the cohesive crack model, it is also originated from Barenblatt's or Dugdale's model. The only difference between them regards the crack tip stress field, which is assumed to be singular for the bridged crack or finite for the cohesive crack (Figure 2.15). The condition $K_I = 0$ provides smooth closure of crack faces of the cohesive crack (Figure 2.15b), instead of the parabolic shape consistent with $K_I \neq 0$ for the bridged crack (Figure 2.15a). In this model, the crack growth is governed by the toughness of the matrix, and the bridging tractions, which control crack opening, are governed by the properties of the reinforcing phase and by its interaction with the matrix. Various bridged crack models are proposed in the literature. A distinction between them regards distribution of the closing tractions, which may be continuous or discontinuous depending on distributions of the reinforcements in the material.

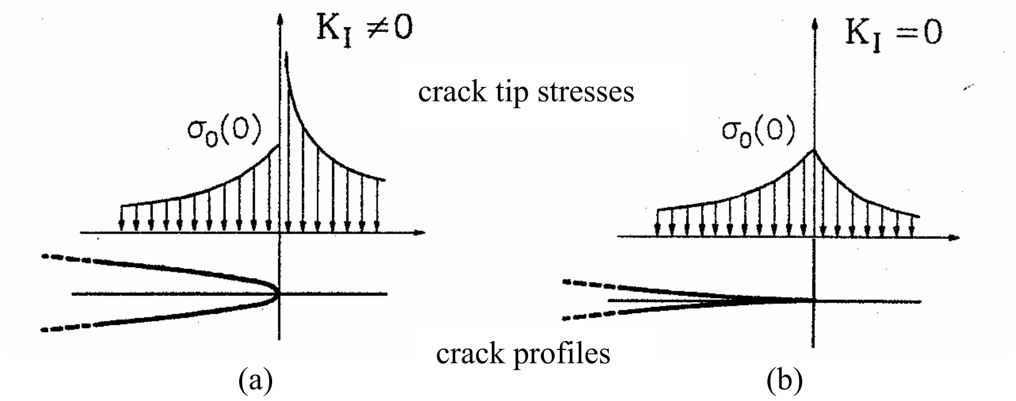

(a) (b)

Figure 2.15 Conditions at the crack tip: (a) bridged crack model; (b) cohesive crack model (Carpinteri, p.144, 1998).

2.4.5 Microcrack Interacting Model

Experimental evidences show that quasi-brittle materials undergo profuse microcracking during evolution of fracture process. Macrocracks are developed as a consequence of growth and coalescence of a large number of microcracks due to the changes of material internal microstructures and the related damage mechanisms. It was observed that microcracking could greatly enhance the material fracture toughness. This toughening effect can be attributed to several possible mechanisms which involve both extrinsic and intrinsic mechanisms. Extrinsic mechanisms are active in the damaged area lying on the two sides of the crack, in which bridging effects are dominant and can be described using bridged crack models as introduced previously. Intrinsic mechanisms are to be found ahead and around the crack tips, where the interaction effects between the macrocrack and the microcracks, and between the microcracks themselves, are the major factors leading to the toughening mechanism, i.e. shielding effects.

Based on displacement or stress discontinuities, or both, various boundary element methods (BEMs) have been developed to account for the microcrack-macrocrack interactions. The main drawback of the BEMs is that the coefficient matrix of the algebraic system is full and the presence of special parabolic tip elements makes the matrix non symmetric, so that the solution is a time consuming process. A small-scale microcracking approach is admissible for those rocks and ceramic composites, where microcracks are detectable at a scale where the resolution is still at least one order of magnitude higher than the typical microstructural dimension. Microcracks are distributed with appropriate saturated density around the macrocrack tip to represent the damage level, while the influences of microcracks located in very far areas can be neglected. This approach has been used as the basis of some phenomenological models, where the dilatant behavior of a tensile crack is considered for deriving the constitutive equations of the material. Microcracking can also be studied using statistical approaches. The microcracks are randomly distributed with a certain statistical law according to the material microstructures, and their effects on the macrocrack are analyzed with LEFM resulting in a statistical population of SIFs at the main crack tip.

2.4.6 Comparisons

The physical reality in the crack tip region is often very complex and can hardly be described through a single simplified theoretical model, where only some of the peculiarities of the system are contained. Different models can be applied alternatively to describe the fracture phenomena in practical situations. For the same crack tip process zone, we could use the damage crack model for meso-scale analyses, as well as the microcrack interacting model for micro-scale analyses. When the process zone is particularly elongated, we can utilize the cohesive crack model, whereas the bridged crack model has to be considered when the matrix is particularly brittle or the reinforcements show a discrete disposition.

The damage crack model is equivalent to the cohesive crack model for particular values of the fracture strain ε_f. On the other hand, the bridged crack model is equivalent to the cohesive crack model when the matrix is relatively ductile. For composite materials whose matrices can be approximately as being perfectly brittle (e.g. fibrous ceramic-matrix composites or fiber-reinforced mortar), the bridged crack model proves to be the most appropriate approach since it separately examines the toughening mechanisms of the different phases. For composites with quasi-brittle matrices (e.g. fiber-reinforce concrete), which are characterized by peculiar bridging or microcracking mechanisms, the cohesive crack model is the best approach since it allows the definition of a cohesive law representing all the toughening mechanisms of the composite. The crack band model is equivalent to the cohesive crack model in that they yield very similar results if the fracture energy equivalence is preserved. The choice of a discrete cohesive crack or crack band seems to be a matter of computational effectiveness and convenience of analysis. In the cases where boundary integral methods can be applied, the use of the cohesive crack model can be computationally more efficient. When the general FEM is used, the programming of the crack band model is much easier since no remeshing is required. The microcrack interacting model can deal with mutual crack interactions of a macrocrack in the proximity of a cloud of microcracks. It can be applied to describe the onset of propagation and the early stages of fracture. However, a satisfactory simulation of fracture phenomena needs an evolutive analysis by means of a discrete crack model, to take into account the influence of microcracks on the trajectory of the main crack.

The selection of the most consistent and suitable model depends on the morphological and phenomenological characteristics of the process zone. In general, the guidelines below should be followed:

- When the mechanical damage is smeared in a uniform way, without irregularities or discontinuities, the damage crack model should be used;
- When the mechanical damage is confined into a narrow band along the strain-softening crack line, the use of the cohesive crack model or the crack band model is suggested;
- When the mechanical damage is confined into a narrow band where the bridging and restraining forces of the reinforcements are active, the bridged crack model is most appropriate;
- When the mechanical damage ahead of the crack tip is represented by a cloud of microcracks, the microcrack interacting model is best suited.

2.5 Summary

This chapter serves as a brief introduction to basic fracture mechanics concepts within isotropic materials and on bi-material interfaces. To represent the nonlinear mechanical effects occurring at the tip of macrocracks in brittle or quasibrittle materials, five important nonlinear crack models are introduced and compared.

Chapter 3

Delamination and Cohesive Crack Modeling

For HFRP sandwich panels, facesheet delamination occurs when manufacturing defects or loading cause a section of the facesheet to detach from the core. The delaminated region may grow, potentially leading to catastrophic failure under certain loading conditions. The goal of the present study is to model efficiently and accurately the facesheet delamination initiation and propagation under various loading cases.

3.1 Delamination in Composite Materials

To begin the study, considering the similarity of facesheet delamination to interlaminar fracture or delamination in layered composite materials, a comprehensive literature search was performed to study previous work by other researchers in the field of delamination of composites.

Failure analysis of fiber-reinforced laminated composites has steadily gained importance with increasing use of such materials in high-performance structures. Considerable inhomogeneity and anisotropy, in its fracture toughness, as well as in the stiffness and strength properties, are largely the results of material property mismatching in a composite. Elementary events, such as matrix cracking, interface debonding and fiber-breaking, are coupled in a complicated way to cause damage growth and fracture (Liu et al., 1993). One major obstacle to achieving the full weight-saving potential of advanced composite materials in large, highly strained structures is the tendency of these materials to delaminate as a result of impact or manufacturing defect. Delamination, or a debond between the plies of such a laminate, represents one of the weakest failure modes in a laminated composite (Armanios et al. 1991). The stress gradients that occur near geometric discontinuities such as ply drop-offs, stiffener terminations and flanges, bonded and bolted joints, and access holes promote delamination initiation, trigger interlaminar damage mechanisms, and may cause a significant loss of structural integrity. Numerous researchers have investigated this problem by means of analytical, numerical and experimental methods, which is reflected by abundant articles published in this area. In fact, several books cover this topic exclusively, including those written or edited by Johnson (1985), Kachanov (1988), Pagano (1989).

3.1.1 G-based approaches

Due to the similarity of a delamination to an embedded or through width crack, most researchers evaluated delamination between the layers of the composite from a fracture mechanics point of view. Delamination problems is generally very complex in nature and difficult to solve, because it involves not only geometric and material discontinuities, but also the inherently coupled Mode I, II and III fracture in layered material systems attributed to the well-known oscillatory singularity nature of the stress and displacement field in the vicinity of the delamination crack tip (Erdogan and Gupta, 1971). In order to eliminate the singularity, a variety of singular field (SF)-based approaches have been proposed, including the conventional finite crack extension approach (Sun and Manoharan, 1989; Hwu and Hu, 1992a), the modified finite crack extension approach (Beuth, 1996), the $\beta = 0$ approach (Davidson, 1995; Davidson et al. 1995a), and the resin interlayer approach (Raju et al., 1988). In these procedures, components of energy release rate (ERR), G, are obtained using classical LEFM, which is valid providing that there exists a ‘singular zone’ or ‘zone of K-dominance’. However, for some composite materials, the damage zone is large compared to the radius of the singular field, invalidating the definition of a K-dominance zone. In these cases, decomposing G into individual components using these methods will lead to inconsistent results. As an alternative, using a crack tip element (CTE) analysis (Davidson et al. 1995a) along with a non-singular field (NSF) definition of mode mix, the ‘CTE/NSF’ approach was developed by Davidson et al. (1997). Its accuracy of predicting delamination growth in unidirectional and multidirectional laminated composites was evaluated by Davidson et al. (2000). The ‘CTE/NSF’ approach was found to be superior to the previous SF-based approaches in that it yielded the material toughness as a single-valued function of mode mix.

In interfacial fracture modeling of composite delamination, despite the difficulty in dealing with the crack tip oscillatory singularity, it was shown (Wang, 1983; Sun and Jih, 1987; Rice, 1988) that SIFs may not have the usual significance attached as in the isotropic crack case, however, based on Irwin’s virtual crack extension concept (1957), the ERR and its components are well defined quantities. Realistic values of mode components can be obtained if the extremely small oscillatory region close to the crack tip were simply ignored. Hence, the growth and propagation of an existing delamination is often modeled as being governed by the values of *G* around the delamination front. For instance, Bottega (1983) used a variational principle to derive a growth law based on the energy released during the growth of a delamination, where the delamination edge was considered as a moving intermediate boundary. Williams et al. (1981) used an energy criterion in predicting crack propagation and arrest in DCB fiber composite specimens.

Mode mix is typically specified in terms of the ERR. However, other near-tip quantities can be used to designate mode mix, such as, stress intensity factors, stresses ahead of the crack tip and crack face displacements. Narayan and Beuth (1998) showed that use of different quantities to designate mode mix can give significantly different results in matching composite applications to mixed-mode toughness tests, due to the practice of using G_c data from toughness tests on 0^0 laminates to predict delamination resistance in applications involving debonding between off-axis plies. It is suggested that practitioners consider the differences in failure load predictions that would result if different near-tip quantities were used to relate composite applications to measured toughness. To this end, methods are provided for converting mode mix designation in terms of the ERR into designations in terms of other fracture quantities.

3.1.2 Mixed-Mode Delamination Growth Criterion

Delamination in composite materials is inherently mixed-mode. It is important that relative contributions of different modes should be carefully addressed. Several researchers studied this topic, including Chatterjee et al. (1986) who performed a general analysis. Other researchers discuss specific modes in more depth, for instance, Cui and Wisnom (1993) used an interface model consisting of spring elements to study mode II delamination. Meanwhile, Davidson et al. (1995b) evaluated the contributions of mode II and III to the total ERR in delamination problems. They also studied the effect of stacking sequence and ply orientation in laminate debonding. König et al. (1995) define a critical ERR based upon mixed-mode delamination and correlate this critical value to buckling induced delamination under cyclic loading.

Interlaminar fracture toughness in Mode I (G_{Ic}), Mode II (G_{IIc}) and Mode III (G_{IIIc}) can be obtained experimentally using different specimens. As a common practice, G_{Ic} is measured by the double cantilever beam (DCB) specimen (Robinson and Song, 1992; O'Brien, 1998a; ASTM, 2000), G_{IIc} by the end load split (ELS) or the end notch flexure (ENF) specimen (Davidson, et al. 1995b; O'Brien, 1998b; Martin and Davidson, 1999). Although several specimens have been suggested for the measurement of G_{IIIc} (Lee, 1993; Martin, 1991; Robinson and Song, 1994; Trakas and Kortschot, 1997), an interaction criterion incorporating Mode III, however, has not yet been established. The edge-cracked torsion test (ECT) appears to be the most likely candidate for standardization (Li, et al. 1997). In order to predict delamination onset or growth for two-dimensional problems, the calculated total ERR, G_{T}, and its components are compared to interlaminar fracture toughness properties measured over a range of mode mixities from pure Mode I loading to pure Mode II loading. A quasi-static mixed-mode fracture criterion is determined by plotting the interlaminar fracture toughness, G_c, versus the mixed-mode ratio, $G_{\mathrm{II}}/G_{\mathrm{T}}$, determined from data generated using pure Mode I DCB, pure Mode II 4ENF, and mixed-mode bending (MMB) tests of varying ratios as shown in Figure 3.1. A curve fit of these data is performed to determine a mathematical relationship between G_c and $G_{\mathrm{II}}/G_{\mathrm{T}}$. According to the total ERR criterion, $G_{\mathrm{T}} = G_c$, failure is expected when, for a given mixed mode ratio G_{II}/G_T, the calculated total ERR, G_T, exceeds the interlaminar fracture toughness, G_c. In order to predict delamination onset or growth for three-dimensional problems the entire failure surface $G_c = G_c(G_I, G_{II}, G_{III})$ as shown in Figure 3.2 is required.

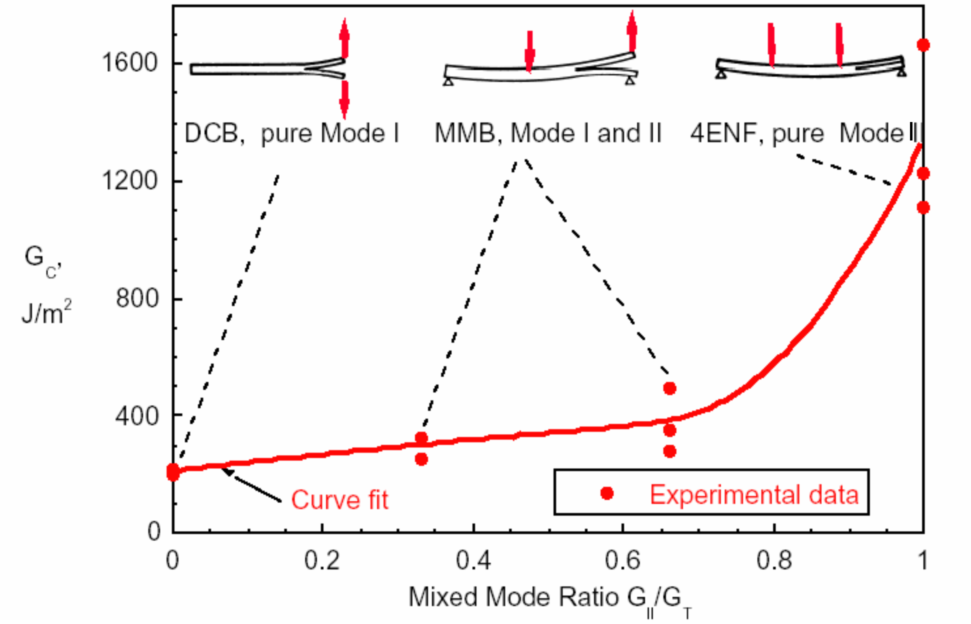

Figure 3.1 Mixed-Mode I, II failure criterion for IM7/8552 (Krueger et al. 2003).

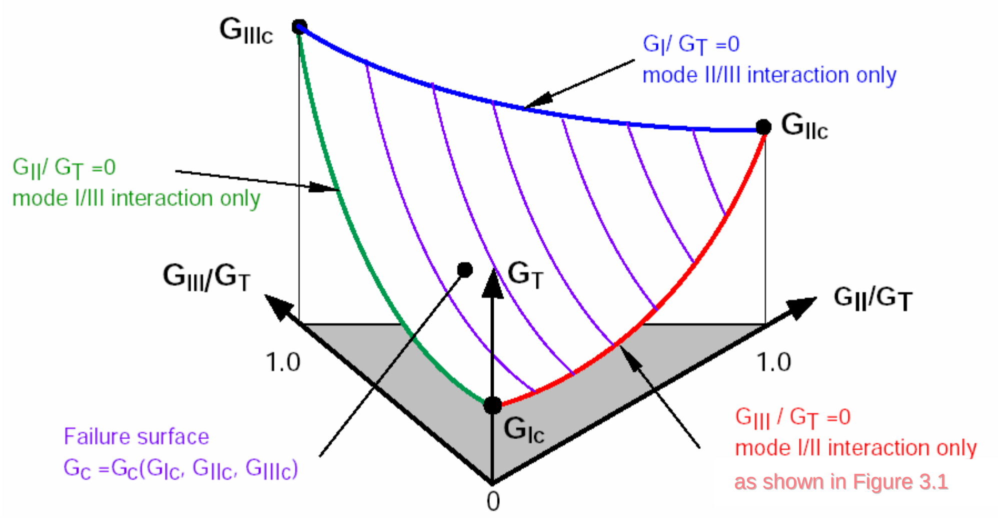

Figure 3.2 Mixed-Mode failure criterion for Modes I, II and III (Krueger et al. 2003).

In realistic structural applications, appropriate failure criteria should be chosen to account for the relative contributions of the different modes. The development of a criterion requires an extensive test program that is often prohibitive to conduct. In the absence of such test data in the mixed-mode range, the analyst must rely on empirical expressions. A variety of empirical delamination growth criteria have been proposed in the literature (e.g. Garg, 1988; Suo and Hutchinson, 1989). Reeder (1992, 1993) performed a comprehensive study of failure criteria for mixed-mode delamination in brittle graphite/epoxy, toughened graphite/epoxy and tough graphite/thermoplastic composites under the full mixed-mode range. The criteria evaluated included:

1) Linear Criterion

$$\left(\frac{G_I}{G_{Ic}}\right)+\left(\frac{G_{II}}{G_{IIc}}\right)=1 \tag{3.1}$$

2) Power Law Criterion

$$\left(\frac{G_I}{G_{Ic}}\right)^{\alpha}+\left(\frac{G_{II}}{G_{IIc}}\right)^{\beta}=1 \tag{3.2}$$

3) Bilinear Criterion

$$G_I=\xi G_{II}+G_{Ic} \tag{3.3}$$

MMB tests were used to measure the mixed-mode delamination toughness of the above composites, providing experimental data to assess the criteria. It was concluded that the linear criterion appears to be the most suited to predict failure of thermoplastic PEEK matrix composites, while it is inaccurate for predicting the response of epoxy composites. The relatively simple bilinear criterion was found to yield the best results when simulating epoxy matrix composites. The power law criterion provided a reasonable fit to the test data for the three different composite materials. In addition, it was found that $\alpha = \beta = 1$, i.e. the linear criterion, could yield good fit to the experimental results (Johnson and Mangalagiri, 1987; Jurf and Pipes, 1982), although Donaldson (1987) and Hwu et al. (1995) suggested differing values of α and β.

3.1.3 Virtual Crack Closure Technique

In composite materials, due to their inherent complications, it is almost impossible to derive exact closed form expressions for the energy release rates. Therefore, numerical methods are broadly used based on LEFM. Although boundary element method (BEM) can also be utilized to study interface crack problems (Cho et al. 1992a, b), most researchers employed FEM in their investigations. ERR components can be extracted from a fracture FE model using the virtual crack closure technique (VCCT) (Rybicki and Kanninen, 1977; O’Brien, 1982; Raju, 1987). A recent overview of the VCCT has been given by Krueger (2002). This technique has been used almost exclusively in the analysis of composite delamination because it does not require knowledge of the near-crack-tip fields, which are complicated in form and have only recently been determined (Suo, 1990; Qu and Bassani, 1993). The global nature of the ERR helps in obtaining a numerical value as there is no need for an very refined mesh near the crack tip. A mesh can be chosen so that it is sufficiently coarse as not to be influenced by the oscillatory nature of stresses but fine enough to capture the broad features of the crack tip stress distribution.

The theory behind VCCT is that if a crack with an initial length a extends by a small amount Δ, the energy absorbed in the process is equal to the work required to close the crack to its original length (Figure 3.3.a). This work can be computed as

$$W = \frac{1}{2}\int_0^{\Delta} \delta(r)\sigma(\Delta - r)dr \tag{3.4}$$

where δ(r) is the crack opening or sliding displacement at a distance r behind the crack tip at (a+Δ); σ is the associated stress distribution ahead of the crack tip at a. It is postulated that the crack front does not change shape for a very small increment of crack growth. Therefore, the opening displacement immediately behind the crack tip at a is the same as that behind the crack tip at (a+Δ), when Δ is infinitesimal. By using Equation (3.4), only one finite element analysis (for a crack of length a) needs to be done in order to calculate the ERR, which is expressed as

$$G = \lim_{\Delta \to 0} \frac{W}{t\Delta} \tag{3.5}$$

where t is the thickness of the material.

In the finite element analysis, considering models with 4-node quadrilateral elements (Figure 3.3.b), the expressions for G_{I} and G_{II} are

$$\begin{aligned} G_I &= \frac{1}{2t\Delta}\{F_x(v_a - v_b)\} \\ G_{II} &= \frac{1}{2t\Delta}\{F_y(u_a - u_b)\} \end{aligned} \tag{3.6}$$

The forces at the crack tip can be obtained by placing very stiff springs between coincident nodes c and d and evaluating the forces in these springs. For geometric nonlinear analysis where large deformations may occur, both forces and displacements obtained in the global coordinate system need to be transformed into a local coordinate system which originates at the crack tip. The growth of the delamination is simulated by releasing the node for which the computed ERR reaches its critical value based on a mixed-mode interaction law as discussed previously.

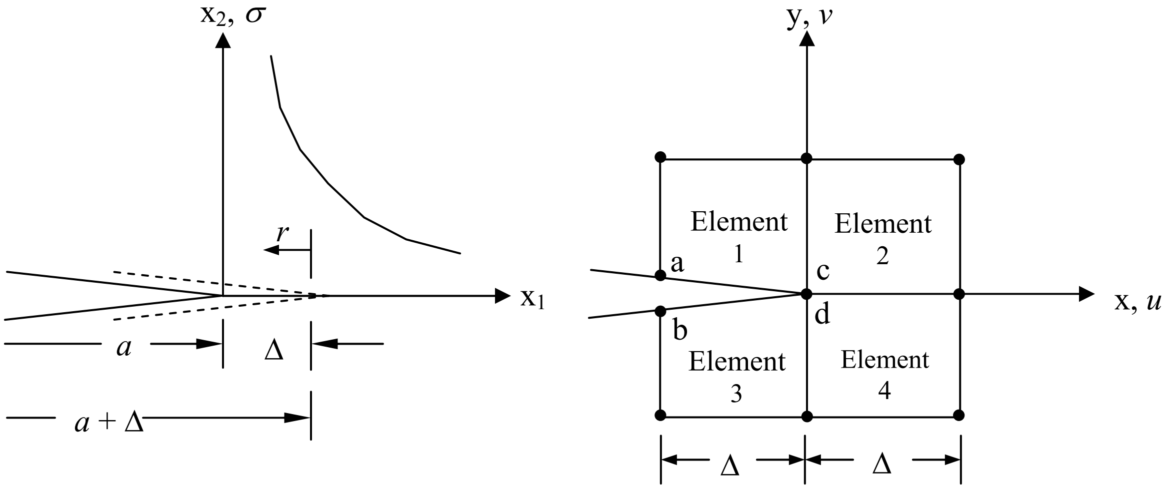

(a) Normal stress distribution ahead of the crack

(b) Finite-element nodes near crack tip

Figure 3.3 Virtual crack closure technique.

The VCCT is very useful in dealing with cracks in heterogeneous materials since no assumption of isotropy or homogeneity around the crack tip is necessary. Thus, it has been widely used to simulate delamination in composite structures. For example, based on a three-dimensional FE model, Mukherjee et al. (1994) used it to calculate the energy release rates around a delamination in a layered composite. A frictionless contact theory was developed to prevent interpenetration between the faces of the delamination, which was revealed to be crucial for the correct simulation of the growing delamination under various loadings. Köning et al. (1995) employed the VCCT to predict delamination growth in plates containing a circular delamination loaded in tension and compression. A three-dimensional layered element was used and the Mode I, Mode II, and Mode III energy release rates were computed along the delamination front. The location of the maximum predicted energy release rates, and hence the delamination growth, were in good agreement with experimental results.

For laminated composite structures, the use of three-dimensional model to predict delamination using the VCCT can be computationally intensive. In order to minimize the cost, Krueger and O'Brien (2001) developed a modeling technique that combines shell elements and three dimensional elements. In this approach, a local three-dimensional solid finite element model is only used in the immediate vicinity of the delamination front. Multi-point constraints provided a kinematically compatible interface between the local three-dimensional model and the global structural model meshed with plate or shell finite elements. It was shown that this technique is relatively efficient since it reduces the number of degrees of freedom compared to a full three-dimensional model.

3.1.3 Buckling Driven Delamination

When a delaminated composite plate is subjected to in-plane compression, local buckling of the delaminated region or mixed-mode buckling, which is a combination of local and global buckling, may occur before global buckling, as shown in Figure 3.4. Localized buckling of delaminated plies in a composite laminate can reduce its ability to resist compressive loads and precipitate rapid delamination growth leading to structural collapse (Simitses et al., 1985; Yin et al., 1986). A large amount of research has been performed on this subject. Some representative work will be reviewed next. For a more detailed description, one is referred to the works of Kachanov (1988) and Kutlu (1991).

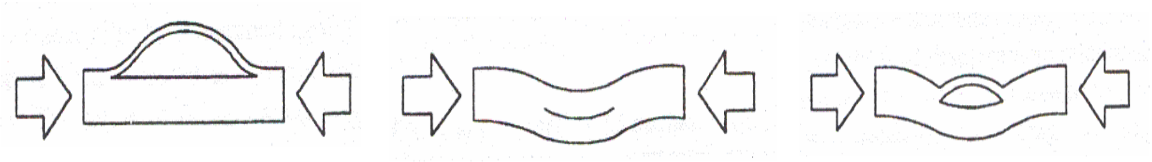

(a) Local buckling (b) Global buckling (c) Mixed-mode buckling

Figure 3.4 Three types of buckling mode shape.

Various analytical methods have been developed to analyze a composite plate containing a single delamination. When the delamination is near surface and the unbuckled portion of the laminated composite plate could be considered infinitely thick compared to the thickness of the delamination, the ‘thin film’ model can be used to predict the local buckling loads (Kachanov, 1976). More general cases including thick surface delamination and mixed-mode buckling were studied by Chai and co-workers (1981, 1985) using one- and two-dimensional models. The parameters controlling the growth or arrest of the delamination damage were identified as the fracture energy, disbond depth and elastic properties of the materials from both sides of the delamination interface. Bottega and Maewal (1983) modeled the penny-shaped delamination in circular plates as a one-dimensional problem and used the energy method and asymptotic analysis to obtain the buckling loads and postbuckling load-displacement relation. Vizzini and Lagace (1987) studied the buckling of a delaminated sublaminate on an elastic foundation by Rayleigh-Ritz energy method. Kardomateas (1993) applied a perturbation method to investigate the initial stage of postbuckling behavior. Wang et al. (1995) presented a continuous analysis method for determining the local buckling loads of delaminated beams and plates. Transverse shear effects on delamination buckling and postbuckling of delaminated plates were examined by Chen (1993), Chattopadhyay and Gu (1994) and Kyoung and Kim (1995).

In cases of a delamination of arbitrary shape or multiple delaminations, FE analysis is required for accurate characterization of the buckling and postbuckling behavior of the delaminated composite plate. Based on a geometrically nonlinear FE analysis, Whitcomb (1981) performed a parametric study of postbuckled through-width delaminations in laminated plates. It was found that energy release rates G_{I} and G_{II} were very sensitive to delamination length, delamination depth, and load level. In addition, delamination growth was dominated by G_{I}. In 1989, he extended this work to three-dimensional cases and later contact effects were also included (Whitcomb, 1992). In both of these latter works, a postbuckled embedded delamination was investigated and it was pointed out that the problem is definitely mixed-mode, although Mode III effect was negligible for all cases considered. Mukherjee et al. (1991) combined the FEM and asymptotic expansion method in their analyses of the buckling of delaminated plates. Yeh and Tan (1994) conducted nonlinear FE analyses to predict the buckling loads of elliptically delaminated composite plates. Klug (1994) used the VCCT based on plate theory to model postbuckling delamination growth. From an FE nonlinear buckling analysis, Hwang and Mao (2001) studied the buckling loads, buckling modes, postbuckling behavior, and critical loads of delamination growth for delaminated unidirectional carbon/epoxy composites. In order to predict the delamination growth loads, the total ERR criterion, the ERR component criterion, and the interlaminar stress criterion (Brewer and Lagace, 1988) were used. Analyzing the response of laminated composites containing multiple delaminations is more complicated and difficult than dealing with a single delamination. The interface conditions of multiple delaminations involve strong interactions between the delamination surfaces. To study the problem of multiple delaminations, several models have been developed (Kutlu and Chang, 1992, 1995a, 1995b; Adan et al., 1994; Wang et al. 1997).

3.2 Delamination in Composite Sandwich Structures

In spite of the fruitful research activity in the area of delamination in composite materials, little is mentioned about the problem of interest, delamination of a facesheet from a honeycomb core. However, much effort has been devoted to the problem of a facesheet debonding from a solid core.

3.2.1 Solid Core Sandwich Structures

Carlsson et al. (1991) proposed the use of a cracked sandwich beam (CSB) test to analyze debond between facesheet and core due to shear stress. The strain energy release rate for Mode II can be determined from this test based upon the rate of change in beam compliance to crack extension. They performed extensive testing with glass/polyester facesheets on balsa core. Furthermore, Carlsson (1991) discussed issues related to the appropriate design of the CSB specimen in order to achieve debonding failure prior to core crush or core shear failure. Frostig et al. (1992) and Frostig and Baruch (1992) developed a general high-order sandwich plate theory (HSAPT) for the analysis of sandwich panels and plates. In this theory, the high order and the localized effects are results of the closed form solution of the mathematical model and no presumptions are imposed on the distribution of the deformations through the thickness of the core. The theory accounts for the vertical flexibility of the core along with its shear flexibility, and it is valid for a broad range of sandwich structures. Based on the HSAPT, rigorous analyses of the bending behavior of delaminated sandwich beams and circular sandwich plates were performed (Frostig, 1992; Rabinovitch and Frostig, 2002). Behavior of sandwich plates with general construction and a transversely flexible core under general loading conditions could be effectively described with or without considering contact. Investigation of more localized effects at the edge of the delaminated region using fracture mechanics criteria based on FE analysis was presented by Falk (1994). This study revealed the stress concentrations that arise in the close vicinity of the edge of the delaminated region and demonstrates their crucial influence on the safety of the structural members. Triantafillou and Gibson (1989) determined critical disbond sizes between the core and facesheets using an energy approach. It was revealed that debonding occurs only if there are relatively large pre-existing delaminations at the interface; otherwise it is preceded by other modes of failure, such as, face yielding, face wrinkling and core shearing. Triantafillou and Gibson (1987) developed failure mode maps for foam core sandwich beams, from which the dominant failure mode can be predicted for every possible beam design. Applying the boundary collocation method, Razi et al. (1999) determined the stress distribution in sandwich panels with multiple-site arbitrarily located delaminations caused by impact.

As with the delamination driven by buckling in layered composites, the debonded sandwich panels are very susceptible to buckling under in-plane compressive loads, which may lead to the propagation of delamination, and/or core and facesheet failure. Although the general principles are similar, differences arise in the behavior of delamination buckling and postbuckling within a sandwich structure from that of a laminated composite structure; the substrate in a delaminated sandwich structure includes a much different kind of material, namely a transversely flexible core made of foam or low strength honeycomb. Hence, the contribution of the shear stresses and shear deformation of the core are expected to be noteworthy in the buckling analysis of a delaminated sandwich structure. Using a perturbation procedure, Kardomateas and Huang (1993) studied the buckling and initial postbuckling behavior of facesheet delamination or facesheet/core debonds based on the nonlinear beam theory with transverse shear deformation. Somers et al. (1991), Kim and Dharan (1992), and Hwu and Hu (1992b) derived closed-form solutions of the critical buckling load. The effects of core, facesheet, delamination length on the buckling load, the delamination growth, and the ultimate axial load capacity were discussed. Sleight and Wang (1995) modeled the debonded facesheet as a beam on a Winkler elastic foundation. They employed the Rayleigh-Ritz and finite difference method to predict the buckling loads, and compared them with plane strain finite element analysis. It was concluded that FE analysis is necessary in order to predict the buckling loads accurately. Chen et al. (1997) presented a continuous analysis to predict the local delamination buckling load of sandwich beams. The procedure allows direct determination of the buckling load by considering the entire beam without separating it into regions with and without delaminations.

3.2.2 Honeycomb Core Sandwich Structures

Information regarding delamination problems in sandwich structures with honeycomb core is very sparse, and only quite a few articles were found.

Detailed FE models were used by Burton and Noor (1997) to examine the effect of the adhesive joint between the square-cell honeycomb core and the facesheets on the load transfer and static response of sandwich panels. The adhesive strain energy was used to investigate the effect of adhesive joint characteristics (thickness and adhesive joint fillet size) as well as the core cell size and wall thickness on the load transfer in the core/facesheet joint. Extensive in-plane compression tests of Nomex hexagonal honeycomb core sandwich panels were carried out by Avery (1998) and Avery and Sankar (2000) to investigate the effects of core and facesheet properties, and delamination length on the compression strength of debonded sandwich composites. FE analysis was also performed using equivalent solid core (Narayanan, 1999; Sankar et al. 1999).

Extensive research on the behavior of hexagonal honeycomb core sandwich panels applied to aircraft industry has been reported by the Cornell Fracture Group (Ingraffea et al. 1997; Ural et al., 1999). In their study, various modeling approaches were attempted using the program FRANC3D/STAGS. Explicit models were firstly used, in which all cell walls in the core were modeled explicitly with shell elements. With improvement of STAGS, sandwich elements were available to efficiently represent both facesheets and a homogenized core. The adhesive layer was initially modeled with spring elements, and later was represented with cohesive elements which largely enhanced the capability of predicting delamination growth. Using a computational fracture mechanics approach, TerMaath et al. (1999) applied the VCCT combined with FE analysis to study disbond growth in honeycomb sandwich structures. Using the explicit model, the across-the-width edge peel-off case was effectively simulated. It was indicated that among various parameters, facesheet thickness and stiffness appear to display the greatest influence on the disbond growth. Han et al. (2002) proposed the cohesive element approach to simulate delamination propagation in honeycomb core composite panels. The cohesive constitutive model was applied to reproduce traction-separation behavior between the facesheet and core. Detailed description of the cohesive crack modeling approach will be presented in the next subsection.

3.3 Cohesive Crack Modeling

LEFM based methods have limitations that an initial delamination must be assumed, the initial position of the delamination front needs to be known *a priori*, and the delamination growth is assumed to be self-similar. These necessitate the use of very small elements at the delamination front and pose essential difficulties where a curved delamination front develops due to spatially varying ERRs. Raju et al. (1988) have shown that the total ERR converges with mesh refinement, while the individual components of the ERR do not converge when the ratio of the size of delamination tip element to the ply thickness decreases. This is due to the oscillatory stress singularity occurring near the interface crack tip of dissimilar media. Finite elements with certain size limits should be used in order to get acceptably accurate numerical results. On the other hand, although providing valuable information concerning onset and stability of delamination growth, the use of VCCT to simulate delamination growth requires complex moving mesh techniques (Rinderknecht and Kröplin, 1994) to advance the crack front, especially when dealing with multiple delaminations in three-dimensional problems.

In order to overcome the above limitations associated with the LEFM and VCCT, the continuum damage mechanics could be applied to model the interfacial damage growth occurring in delamination problems. For example, to simulate sublaminate buckling and delamination of composite plates, using both fracture and damage mechanics, Rinderknecht and Kröplin (1995) developed a finite element called 'delamination process element' incorporating the sublaminate and baselaminate as well as the resin-rich layer (a so-called process layer with very thin thickness), in which the connection between sublaminate and baselaminate can be fixed or controlled by either continuity or damage parameters. Sprenger et al. (2000) and Wagner et al. (2001) presented an FEM to simulate growing delaminations in composite structures. Using an inelastic material law with softening, the delamination process was assumed to take place within an interface layer having a small but non-vanishing thickness. In addition, to avoid mesh-dependent solutions, a regularization technique was applied. El-Sayed and Sridharan (2001, 2002) proposed a cohesive layer model in terms of stresses and strains of the material of the interface layer having small thickness. Provided appropriate properties of the cohesive layer are defined, this model was demonstrated to be efficient for predicting delamination growth in composites and sandwich structures.

An alternative approach is the use of the cohesive interface elements placed between the composite laminae or at the interface of sandwich facesheet/core to represent the behavior of the resin-rich bonding layer. Instead of considering the interfacial material layer as a continuum, it is generally postulated that this layer is so thin compared to the thickness of the adjacent bulk material that it could be assumed to approach zero. Thus, the cohesive interface elements have zero thickness in the undeformed configuration. With this approximation, the information of the stress distribution through the thickness in the interfacial layer is lost, since it is modeled as uniform.

The concept of cohesive interface elements is based on a Dugdale-Barenblatt type cohesive zone model (CZM) as mentioned in Chapter 2. Since Hilleborg et al. (1976) applied the fictitious crack model to the analysis of concrete cracking, CZM concept has been gaining increasing popularity in describing fracture and failure behavior in a wide variety of material systems. With the crack path known *a priori* in the interface, CZM is particularly appealing when interfacial strength are relatively weak compared with the adjoining materials (Needleman, 1987), as in the case of composite laminae and sandwich facesheet/core interface.

The CZM, characterized by a softening traction-separation law which provides a phenomenological mechanical relation between the interfacial tractions and separations, is an idealized description of the real physical fracture process as shown schematically in Figure 3.5 (a). As opposed to the LEFM, a non-singular stress field is thereby resulted at the crack tip. The choice of the law is basically free as there is no unequivocal correlation between the softening constitutive law and the result of the analysis. The bilinear cohesive law shown in Figure 3.5 (b) is usually used to describe fracture behavior in quasibrittle materials. Typical failure process is gone through from point *a* to *f* in Figure 3.5 (a)-(b): at point *a* the tractions are small; around point *b*, large but finite tractions exist to resist separation; maximum tractions are reached at point *c*; material degradation occurs but still transfer loads at point *d*; tractions approach zero at point *e* and vanish thereafter as the result of complete debonding. The material characterization parameters of the softening constitutive law are the interfacial strength σ_c and the fracture toughness G_c of the material. Combining a strength-based formulation with a fracture mechanics-based formulation, initiation and non-self-similar growth of cracks could be simulated efficiently via CZM. In fact, a crack is initiated when the interface traction attains the interfacial strength, and the crack is advanced when the work of fracture equals to the material's resistance to crack propagation. The softening portion of the constitutive law accounts for the complex mechanisms occurring in the volume of material ahead of the crack tip by which large amounts of energy are absorbed in the fracture process. The complex fracture mechanisms range from void nucleation, void growth, and coalescence of microcavities to macrocrack formation as shown in Figure 3.5 (a).

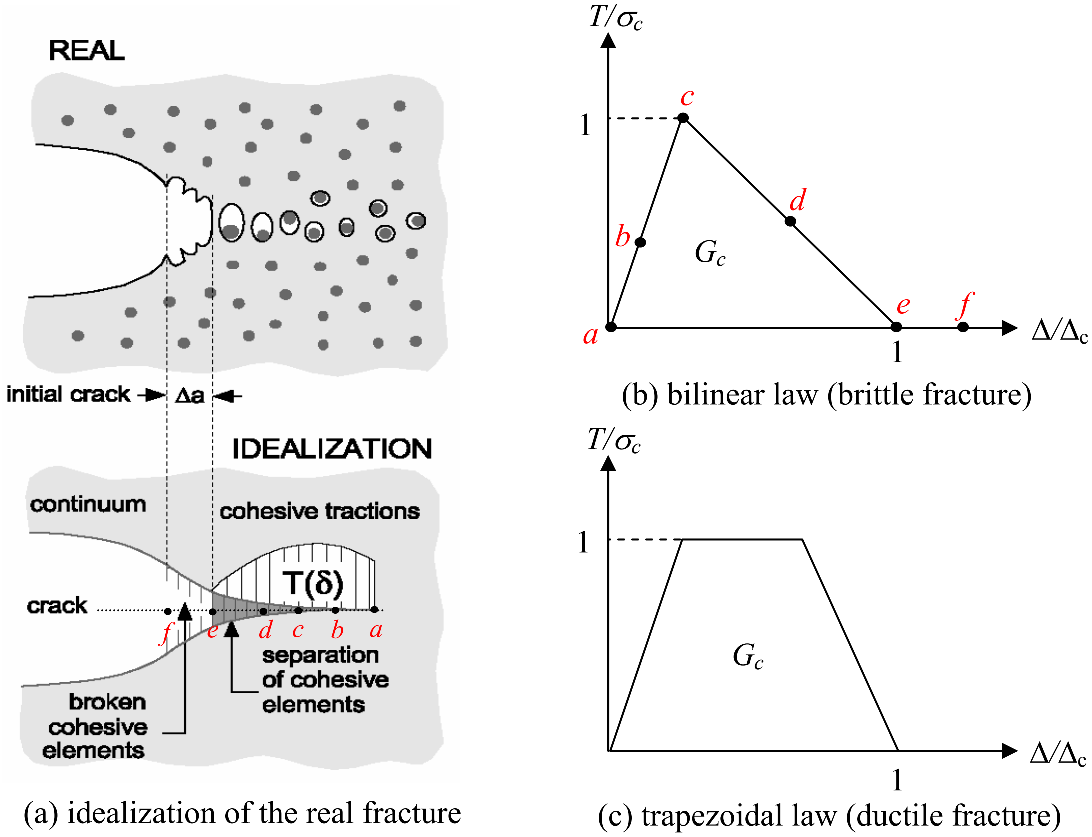

(a) idealization of the real fracture process with CZM

(b) bilinear law (brittle fracture)

(c) trapezoidal law (ductile fracture)

Figure 3.5 Representation of the fracture process via the CZM.

3.3.1 Constitutive Laws

One of the key problems in the application of CZM is the choice of an appropriate constitutive traction-separation law for the studied material within the cohesive zone. For instance, if the fracture in ductile materials is to be modeled, the trapezoidal cohesive law (Figure 3.5 (c)) is better than the bilinear one (Figure 3.5 (b)). A variety of such constitutive equations have been proposed in the literature. Several investigations dealt with the effect of the shape of the traction–separation function on the resulting fracture behavior (Elices et al., 2002; Tijssens et al., 2000; Needleman, 1990; Tvergaard and Hutchinson, 1992, 1994). Although it is generally recognized that the exact mathematical form of the interfacial constitutive law is less important than its capability to represent the interfacial strength and critical fracture energy, Chandra et al. (2002) demonstrated that, apart from these two parameters, CZM should include the shape of traction-separation law in order to accurately simulate the interface and reproduce the macroscopic mechanical behavior of composites. In their work, two different forms of CZMs (exponential and bilinear) were used to evaluate the response of interfaces in titanium matrix composites reinforced by silicon carbide (SCS-6) fibers. The computational results were then compared to thin slice push-out experimental data. It was observed that the bilinear CZM reproduced the macroscopic mechanical response and the failure process while the exponential form failed to do so. Hence, when using CZMs to model separation in a given material system, an appropriate shape, depending on the type of material system and the inelastic micromechanical processes, should be used.

In addition to the bilinear cohesive laws mentioned above, the exponential form of traction-separation law is also widely used. The exponential form mimics the physics involved in atomic separation (Rose et al., 1981). Needleman (1987) was one of the first to use it to simulate particle debonding in metal matrices. Xu and Needleman (1993, 1994, 1995) further used the above models to study the void nucleation at the interface between particle and matrix, fast crack growth in brittle materials under dynamic loading, and dynamic crack growth at the interface of bimaterials. The constitutive laws relate the normal and shear traction components to the crack opening and sliding. Mixed mode crack propagation can be simulated, since the crack separations are coupled in the constitutive equations. Xu-Needleman's constitutive laws are restricted to two dimensional plane problems. Rahul-Kumar et al. (1999) extended Xu-Needleman's exponential constitutive law to predict normal and shear interfacial fracture in a three dimensional space. Later (2000), they augmented Xu-Needleman's constitutive law to offer resistance to interpenetration of the surfaces of the interfacial material.

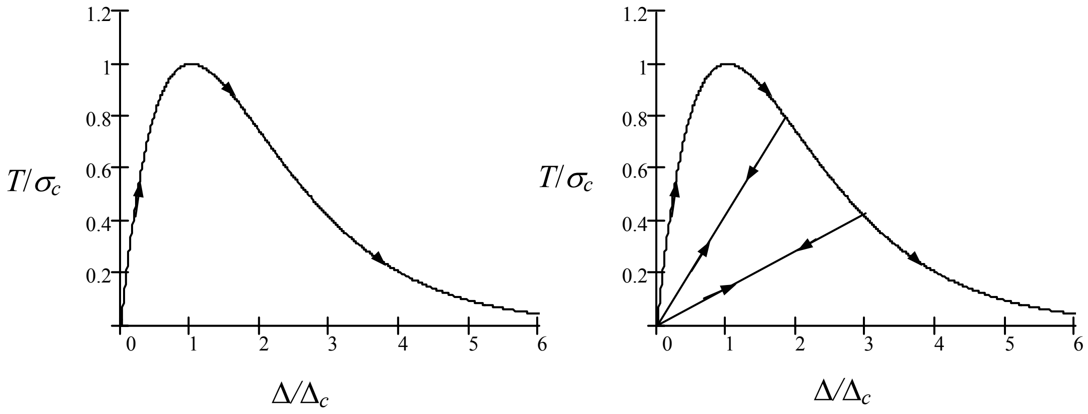

(a) Reversible law (b) Irreversible law

Figure 3.6 Softening traction-separation constitutive law.

Many cohesive fracture laws are irreversible and history-dependent. It is presumed that the cohesive tractions exactly retrace the loading traction-separation curve upon unloading such that the consumed local surface fracture energy is fully recovered (Figure 3.6. (a)). While this is rigorously correct when fracture occurs at the atomistic level, where cohesion directly arises from the atomic bonds, most macroscopic decohesion processes may be expected to entail some degree of irreversibility since stresses may internally redistribute upon external loading in such a way that cracks arrest and cracks faces close. This requires the formulation of irreversible cohesive laws such as proposed by Camacho and Ortiz (1996). Ortiz and Pandolfi (1999) extended this formulation to three dimensions. In their model, cohesive surfaces are assumed to unload to the origin (Figure 3.6. (b)). This procedure seems reasonable since the interfacial stiffness when reloading is lower than the original (undamaged) stiffness. Such a procedure simulates the effects of the damage mechanisms that occurred along the interface. Other authors (Chaboche et al., 1997; Petrossian and Wisnom, 1998) have proposed an unloading curve with a slope equal to that of the traction-separation curve at zero separation. Such a procedure, typically used in the formulation of plasticity problems, would lead to the use of the same stiffness when reloading, and to residual relative displacements along the interface when the load reverts to zero.

A shortcoming of Ortiz-Pandolfi's constitutive law is that the interfacial strength and the fracture toughness associated with Mode I, Mode II and Mode III fracture cannot be specified separately. In their modeling, mode coupling is accounted for by introducing an effective scalar opening displacement and the mode ratio is one of the input parameters, which are inappropriate since the mode mixity is unknown *a priori* in different loading conditions. Although Xu-Needleman's constitutive law does not have this limitation since it separates the work of peel and shear, it does not satisfy empirical mixed-mode fracture criteria as discussed in Section 3.1.2.

An objective of this dissertation is to propose a linear-exponential irreversible constitutive law that incorporates mixed-mode fracture criteria using material characterization data to predict the initiation and subsequent growth of delamination in composite laminates and honeycomb sandwich structures. Material characterization test data of Mode I, Mode II, and Mode III are used to define the fracture toughness and interfacial strength for each failure mode.

3.3.2 Nonlinear Finite Element Formulations

The concept of applying CZM to simulate crack growth is usually implemented by means of interface elements located in the potential crack path. The fracture process is characterized by the nonlinear, traction-separation law described previously. An appealing feature of this method is that it does not presume a particular type of constitutive response in the bulk of the material, and successive crack growth is a natural outcome of the analyses.

Cohesive interface elements can be divided into two main groups: point interface elements and continuous interface elements. Point interface elements are identical to spring elements connecting nodes. Several types of continuous interface elements have been proposed, including two dimensional line interface elements, three dimensional interface elements with or without initial thickness.

Spring interface elements have been used by Yang et al. (2001) for fatigue crack growth in quasibrittle materials. The softening material in the cohesive zone was modeled to be internal singular surfaces in the elastic body. The interactions of the singular surfaces were described in a cohesive force law. Damage in the interface was modeled to accumulate not only along the damage locus but also along an unloading path underneath it. With this formulation, subcritical fatigue crack growth due to cyclic loading within the cohesive zone could be modeled. Such point interface elements were also used by Cui and Wisnom (1993) and Shahwan and Waas (1997) for predicting delamination in composites.

Since Needleman's pioneering work (1987), two dimensional interface elements have been widely adopted in studies on void nucleation (Tvergaard, 1990; Xu and Needleman, 1993), quasi-static crack growth (Needleman, 1990; Tvergaard and Hutchinson, 1992), stability of the separation process (Suo et al., 1992; Levy, 1994), reinforcement cracking in metal matrix composites (Finot et al., 1994), dynamic crack growth (Xu and Needleman, 1994; Siegmund and Needleman, 1997), fracture at interfaces (Xu and Needleman, 1996;), and impact damage in brittle materials (Camacho and Ortiz,1996).

Despite its apparent versatility, extension of cohesive interface elements to three dimensions has been much less explored. Beer (1985) developed a general isoparametric joint element applicable to three-dimensional solid finite elements and two-dimensional shell finite elements. de Moura et al. (1996) developed an 18-node interface finite element for three-dimensional crack propagation. These works did not consider interfacial geometric nonlinearities.

de-Andres et al. (1999) and Ortiz and Pandolfi (1999) considered the finite deformation of the interfacial surface material, and kept the geometric terms in the consistent tangent stiffness matrix required in the finite element formulation. Although Allix and Corigliano (1999) kept geometric terms in the tangent stiffness matrix, the rotation tensor and the Jacobian of transformation of the interfacial surface material were approximated for simplicity. These approximations were made consistent with the von Karman plate theory assumptions for the bulk material. Qiu et al. (2001) presented a co-rotational formulation applied to interface elements for two dimensional crack propagation. By including the interfacial geometric nonlinearity, large displacements and rotations with small strains were taken into account.

The aforementioned three dimensional interface elements are specifically formulated to provide compatibility with also three dimensional solid elements. However, when they are used in conjunction with surrounding shell elements, computational errors can be introduced due to the incompatibility between shell and solid-like interface elements. To overcome this limitation, Reedy et al. (1997) developed a special 8-node hex interface element to connect opposing composite sublaminate shell elements. The interface element supplies the nodal forces and moments needed to make the two opposing shell elements act as a single element until a prescribed failure criterion is satisfied. Borg et al. (2004) presented a delamination CZM for shell elements. The thickness offset between shell elements was explicitly accounted for using an adhesive penalty contact formulation, in which fictitious beam elements were used to connect adjacent shell elements such that the rotational degrees of freedom of the shell elements could be included.

An objective of this dissertation is to derive a co-rotational isoparametric interface finite element for three dimensional crack propagation taking into consideration all the interfacial geometric nonlinearities in the consistent tangent stiffness matrix. The derivations stem from the discretization of the principle of virtual work equations for discontinuous structures. The details of the nonlinear interface finite element formulation are presented in Chapter 4.

3.3.3 Computational Issues

There are several relevant computational issues that arise when softening constitutive laws are used to model fracture process.

3.3.3.1 Numerical Integration Schemes in the Interface Elements

For numerical integration of continuum elements, the Gauss scheme is commonly used because of its accuracy. However, special care must be taken in choosing the integration scheme for the tangent stiffness matrix and the internal force vector of the cohesive interface elements as oscillations of the traction field may occur (Schellekens and de Borst, 1993; Mi et al., 1998). Schellekens and de Borst (1993) and Goncalves et al. (2000) used eigenmode analysis of the element stiffness matrices to demonstrate that the application of Gauss integration in evaluating the tangent stiffness matrix and the internal force vector of the interface elements leads to oscillatory traction profiles when large stress gradients are present over an interface element. The large stress gradients are as a result of the initial large stiffness of the softening constitutive law. With increasing mesh refinement, the element performance improves due to the decreasing stress gradients.

It was concluded by the above authors that for line interface elements and linear plane interface elements the performance can be improved by using either a nodal lumping scheme, Newton-Cotes, or Lobatto integration scheme. For quadratic interface elements, Newton-Cotes and Lobatto integration schemes produce smooth traction profiles when the displacement field over the element varies in only one direction. Oscillatory traction profiles may occur in other cases. However, this adverse effect is only significant for the central integration point, and it is less pronounced than the oscillations occurring when Gauss integration is used. If necessary, more refined meshes or linear elements can be used to reduce the magnitude of the stress oscillation.

Another relevant issue related to the integration of cohesive interface elements is the use of full integration schemes. Analyses of problems involving crack propagation and strain-softening behavior have shown that the use of full integration was superior to the use of reduced integration schemes (de Borst and Rots, 1989). Furthermore, because of the non-smooth profile of the stress in an element which is only partially delaminated, a high number of integration points might yield a more accurate estimation of the stiffness and of the residual forces. However, Alfano and Crisfield (2001) have shown that for fully integrated linear 4-node interface elements, increasing the number of Simpson integration points from 2 to 20, in order to improve the accuracy of the stiffness and the residual force vector, leads to a less robust solution algorithm and, therefore, to a reduction of the average increment size, whereas the spurious oscillations of the load-displacement curves due to a coarse mesh around the delamination front still remain.

3.3.3.2 Mesh Sensitivity

The softening constitutive law of the CZM relates tractions to separations and not to strains. Hence the method does not suffer from the well-known ‘loss-of-ellipticity’ problems associated with a continuum rather than a surface. Such problems have led to a range of non-local continuum models which require a length parameter, such as the crack band model as discussed in Section 2.4.3. However, the length parameter is not required in the CZM and it does not suffer from the severe mesh-sensitivity associated with softening stress-strain models or with strength-based models. Nonetheless, the CZM does require, as input, a strength as well as a critical fracture energy. Consequently, there is still some form of mesh sensitivity.

In particular, if the mesh is not sufficiently fine, the computed global load-displacement responses can be very non-smooth and exhibit a wide range of artificial 'snap-throughs' and 'snap-backs' that are purely artifacts of the mesh (Alfano and Crisfield, 2001). The reason for the non-smooth response is the inability of the coarse mesh to smoothly capture the correct strain field around the crack front as it propagates. In contrast to methods involving traditional fracture mechanics, with the CZM there is no precisely defined crack-tip and, instead, there is a softening 'process zone'. As a result of the latter there is no stress singularity. Nonetheless, particularly with high cracking strengths, there is a rapidly varying 'strain' field and, for a good solution, a fine mesh is required in the region around the process zone. In order to obtain a relatively smooth solution, it was suggested (Mi et al., 1998) that the mesh should be fine enough to include at least two interface elements in the cohesive zone located at the crack tip.

To circumvent non-convergence of the equilibrium iterations associated with using CZMs, analysts often resort to the device of artificially lowering the strengths. The improvement in convergence is due to the effect of increasing the cohesive zone ahead of the crack tip. The lower the interface strength, the larger will be the cohesive zone, and hence the smoother the solution. This method has been successfully used by Wisheart and Richardson (1998) in the simulation of DCB tests in composite laminates. The sensitivity of the CZM to the interface strength has also been investigated by Alfano and Crisfield (2001). It was reported that reducing the values of the maximum admissible tractions lighten the computational burden because it allows for a coarser mesh around the crack tip and an increased average increment size. However, too small values can result in a large underestimation of the maximum load and should be avoided. Other approaches involve adaptive remeshing to provide local fine mesh around the crack front in each load step. However, this method introduces special problems for implicit non-linear finite element analyses. In particular, even in the absence of history variables, once the displacements from one mesh have been interpolated to a new mesh, one may experience equilibrium jumps, which can impose severe difficulties for the non-linear solution procedure.

A more promising method is the use of local enrichment of the kinematics in the zone where a crack propagates (de Borst, 2003). This idea was put forward by Belytschko and co-workers in the XFEM as mentioned in Section 2.4.2. A similar approach has successfully been adopted by Crisfield and Alfano (2002) in conjunction with a CZM, using one-dimensional beam elements. In this work, polynomial hierarchical functions are used to adaptively enrich the finite-element interpolating spaces around the process zone. Hierarchical enrichment has been achieved by effectively changing the boundary conditions as the analysis proceeds and the cracks propagate. Enrichment is automatically provided ahead of the process zone and removed once the crack is fully open.

3.3.3.3 Nonlinear Solution Procedures

Even with a properly designed FE mesh and a good element integration scheme, the softening nature of the constitutive law of the CZM frequently causes convergence difficulties in the numerical solution. These are often related to the singularity of the tangent stiffness of the FE model. In dealing with this problem, Crisfield and coworkers have made a great effort and put forward several sophisticated and efficient procedures.

Crisfield et al. (1997) found that when using the Newton-Raphson method, under load (with the arc-length method) or displacement control, the iterative solutions often oscillated when a positive slope of the total potential energy was found, and therefore failed to converge. In order to obtain convergence, a 'line search' procedure with a negative step length was presented. The local softening interface relationship used often results in a global softening response of the structure. In these cases, arc-length methods, such as proposed by Riks (1975), are generally used to pass through limit points, which are typically present in the equilibrium path, by means of a constraint equation to relate the incremental load factor to the norm of the incremental displacement vector. Mi et al. (1998) and Qiu et al. (2001) proposed the use of a modified cylindrical arc-length method (Hellweg and Crisfield, 1998) to obtain converged solutions. This technique chooses between the two roots to the cylindrical arc-length equation for the iterative change of the load factor, selecting the one providing the minimum residual norm associated with the two values of the displacement vector. However, even with this new technique, the solution sometimes enters a cycle and oscillates between two points. The oscillation must be detected so that the increment size can be reduced.

In a very recent work, Alfano and Crisfield (2003) developed a more robust 'double-line-search' (DLS) method which is based on the combination of a local-control arc-length method and two types of line-search procedures. This method is particularly suited to the analysis of the delamination process using the CZM, in which strong nonlinearities are mainly related to a localized set of degrees of freedom. The control function is defined as a weighted sum of a localized set of relative-displacement parameters and, for each increment, these parameters are selected with a view to making the control function locally increase. The local-control method is more efficient than the modified cylindrical arc-length method but is also more unstable. The ‘lack of robustness’ is typically related to the extreme ‘non-smoothness’ of the problem and the use of line searches was considered as a remedy. When the classical ‘single-line-search’ (SLS) fails to compute an optimal step length, with the DLS method a different type of line search is performed in order to modify the iterative change of the load factor so as to obtain a ‘better’ iterative search direction. In general, the numerical results reported indicate that, although for some types of problems line searches may be not required at all, for some others it may be at least necessary to introduce conventional line searches through the SLS method, whereas in order to successfully complete the most difficult analyses the DLS method is needed.

Another alternative to overcome the difficulties of dealing with material softening when using cohesive interface elements is the use of explicit time integration for the FE formulation. Although explicit formulations are typically used to solve transient dynamic problems, they could also be used to address a problem involving quasi-static loading when the model contains a large number of elements, complex contact conditions, geometric instabilities, or material softening. The explicit time integration methods are conditionally stable because the minimum time step used for the explicit time integration of the governing equations depends on the highest eigenvalue in the mesh. Potential pitfalls such as ‘snap-back’ and ‘snap-through’ need no special treatment in a dynamic approach as opposed to path following algorithms used in a static approach. The explicit form of CZMs have been used to simulate delamination in composite structures by Reedy Jr. (1997) and Borg et al. (2001, 2002, 2004a, 2004b).

Hence, an additional objective of this dissertation is to investigate the aforementioned computational issues related to element integration schemes, mesh sensitivity, and nonlinear solution procedures in the development of the cohesive interface elements.

3.4 Summary

In this chapter, modeling of delamination in composite and sandwich structures are discussed. With the aim of efficiently simulating honeycomb sandwich facesheet-core delamination initiation and propagation, the cohesive crack modeling approach is adopted, directed to the implementation of a CZM as interface finite elements.

Chapter 4

Nonlinear Cohesive Interface Finite Element Formulation

In order to efficiently model delamination in composite and sandwich structures, interface elements based on CZMs can be effectively used. In this chapter, the framework of a three dimensional cohesive interface finite element will be described. To begin with, the principle of virtual work is given of solids containing cracks or discontinuous singular surfaces. The kinematics of the interfacial surface is developed next to describe correctly the finite deformation of the interface. In the third section, a linear-exponential softening traction-separation law, satisfying empirical mixed-mode fracture criteria, is proposed to represent progressive damage occurring in the interface during the fracture process. Section four is devoted to the detailed description of the three dimensional cohesive interface element formulations. In the last section, some typical nonlinear solution methods are discussed.

4.1 Principle of Virtual Work

Cracks in solids can be viewed as discontinuities which can be characterized as jumps in the displacement field across material lines or surfaces and have been termed as strong discontinuities (Simo et al., 1993). The presently available approaches to model displacement discontinuities can be classified into two main groups, namely the continuum mechanics approach and the fracture mechanics approach. Both families of approaches are developed from different departure points. The link between them has been established recently by Oliver et al. (2002). In this dissertation, the nonlinear (decohesive) fracture mechanics approach will be adopted based on the interfacial constitutive equations.

For discontinuous systems, the classical form of the principle of virtual work for a continuum has to be extended to include the description of interfacial displacement jumps, which has been done by Ortiz and Pandolfi (1999). Considering a body occupying an initial configuration $\Omega \subset R^3$, it undergoes a deformation under the body forces b_i (per unit volume) and surface tractions $\tilde{t}_i$ (per unit external surface area). The external virtual work δW_{ext} of the body forces and surface tractions is

$$\delta W_{ext} = \iint_{\partial\Omega} \tilde{t}_i \delta u_i dS + \iiint_{\Omega} b_i \delta u_i d\Omega \tag{4.1}$$

where $\partial\Omega$ is the entire surface area of the body. The prescribed surface tractions are acting on $\partial\Omega_\sigma$, and over the remaining part of the boundary, $\partial\Omega_u$, the displacement field is prescribed. Since $\delta u_i = 0$ on $\partial\Omega_u$, the surface integral in the external virtual work expression is extended to cover the entire surface $\partial\Omega = \partial\Omega_\sigma + \partial\Omega_u$. The boundary conditions are

$$\sigma_{ij} n_j = \tilde{t}_i \text{ on } \partial\Omega_\sigma \text{, and } u_i = \tilde{u}_i \text{ on } \partial\Omega_u \tag{4.2}$$

where n_j is the unit normal component of the external surface, and σ_{ij} are the Cauchy stress tensor components, and the tilde denotes the prescribed quantity. The internal virtual work due to the stress field σ_{ij} is

$$\delta W_{\text{int}} = \iiint_{\Omega} \sigma_{ij} \delta \varepsilon_{ij} d\Omega \tag{4.3}$$

where ε_{ij} are the infinitesimal strain tensor components. Using the elasticity equilibrium equations, it can be easily proved that if the stress field is statically admissible, the external virtual work in Equation (4.1) should be equal to the internal virtual work in Equation (4.3), i.e.

$$\iiint_{\Omega} \sigma_{ij} \delta \varepsilon_{ij} d\Omega = \iint_{\partial\Omega} \tilde{t}_i \delta u_i dS + \iiint_{\Omega} b_i \delta u_i d\Omega \tag{4.4}$$

Implementation of the principle of virtual work is to impose Equation (4.4) for every kinematically admissible displacement field to determine a statically admissible stress field.

Suppose now that the body is traversed by an interfacial surface S, Figure 4.1(a). Furthermore, orient S by choosing a unit normal $\hat{n}$. For simplicity, assume that the interfacial surface then partitions the body into two subbodies $\Omega^{\pm}$, lying on the upper and lower sides of S, denoted $S^{\pm}$ and oriented by unit normal $\hat{n}^{\pm}$, respectively (Figure 4.1(b)). The interfacial surface is an internal surface comprised of the upper and lower surfaces $S^{\pm}$. The traversing surface S in its undeformed configuration is denoted S^0. The surfaces S, S^+, and S^- are assumed to coincide with the reference surface S^0 in the undeformed configuration as shown in Figure 4.2. Thus, in the undeformed state, the interfacial surface is of zero thickness. The upper and lower surface $S^{\pm}$ can independently displace, stretch, and rotate. However, the motion of them is constrained by the material constitutive law used to describe the interfacial surface. In the context of a formed crack, S^{+} and S^{-} are the crack surfaces.

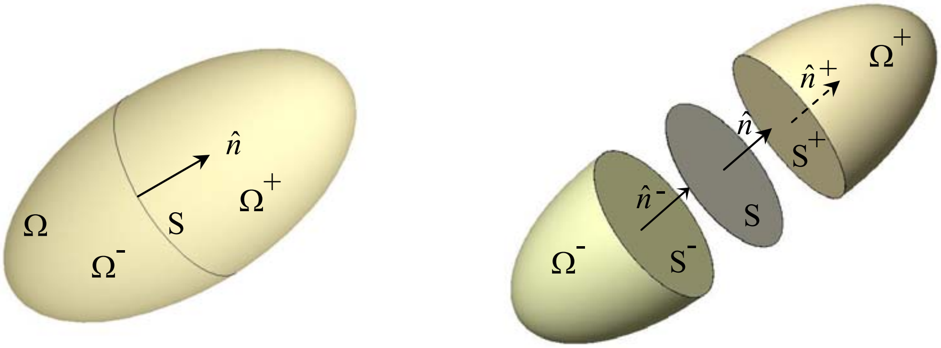

(a) Interfacial surface traversing a 3D body

(b) Upper and lower surfaces $S^{\pm}$ and interfacial surface S

Figure 4.1 A 3D body containing an interfacial surface.

Since the displacement are discontinuous across the interfacial surface, the principle of virtual work can only be written for each continuous subbody as

$$\begin{aligned}
\iiint_{\Omega^{+}} \sigma_{ij}\delta\varepsilon_{ij}\,d\Omega &= \iint_{S^{+}} t_i^{+}\delta u_i^{+}\,dS^{+} + \iint_{\partial\Omega^{+}} \tilde{t}_i\delta u_i\,dS + \iiint_{\Omega^{+}} b_i\delta u_i\,d\Omega \\
\iiint_{\Omega^{-}} \sigma_{ij}\delta\varepsilon_{ij}\,d\Omega &= \iint_{S^{-}} t_i^{-}\delta u_i^{-}\,dS^{-} + \iint_{\partial\Omega^{-}} \tilde{t}_i\delta u_i\,dS + \iiint_{\Omega^{-}} b_i\delta u_i\,d\Omega
\end{aligned} \tag{4.5}$$

where $t_i^{\pm}$ are the surface tractions acting on the upper and lower surface $S^{\pm}$. Although the stress components are not necessarily continuous, the resultants due to the traction components acting on any interior surface must be continuous by Newton's Third Law. Hence, the balance equation at the interfacial surface boundaries requires

$$t_i^+ dS^+ + t_i^- dS^- = 0 \quad \forall x_i^\pm \in S^\pm \tag{4.6}$$

Adding the equations in Equation (4.5) and replacing $t_i^- dS^-$ with $-t_i^+ dS^+$, we obtain

$$\iiint_\Omega \sigma_{ij} \delta\varepsilon_{ij} d\Omega - \iint_{S^+} t_i^+ \left(\delta u_i^+ - \delta u_i^-\right) dS^+ = \iint_{\partial\Omega} \tilde{t}_i \delta u_i dS + \iiint_\Omega b_i \delta u_i d\Omega \tag{4.7}$$

The behavior of the cohesive interfacial surface may be expected to differ markedly depending on whether the surface undergoes sliding or normal separation. This requires the continuous tracking of the normal and tangential directions to the surface; this task is compounded by the discontinuous behavior of the interfacial surface deformation. One scheme for identifying a unique deformed configuration of the cohesive interfacial surface is to introduce a midsurface $\overline{S}$ throughout the history of deformation. The midsurface is defined by the locus of the midpoints $\overline{P}$ of the line joining two points P^- and P^+ coincident in the undeformed configuration and located on S^- and S^+, respectively (Figure 4.3). The traversing surface S is assumed to coincide with the interfacial midsurface $\overline{S}$ throughout the history of deformations. Therefore, the normal and tangential components of the tractions and displacement jump vectors are determined by the local orientation of the midsurface $\overline{S}$, which is defined by its unit normal $\hat{n}$. Denote $\hat{t}_i$ the traction component acting on the midsurface along the direction of the global coordinate X_i. Thus, applying Newton's Third Law, the boundary equation for the surface traction $\hat{t}_i$ acting on the interfacial midsurface $\overline{S}$ is related to the internal surface tractions $t_i^\pm$ as follows

$$t_i^+ dS^+ = -t_i^- dS^- = -\hat{t}_i d\bar{S} \quad \forall x_i^\pm \in S^\pm \text{ and } \bar{x} \in \bar{S} \tag{4.8}$$

Therefore, the second term of the left side of the Equation (4.7) can be modified using Equation (4.8). This leads to the final form of the principle of virtual work equation for discontinuous systems

$$\iiint_\Omega \sigma_{ij}\delta\varepsilon_{ij} d\Omega + \iint_{\bar{S}} \hat{t}_i \delta [\![u_i]\!] d\bar{S} = \iint_{\partial\Omega} \tilde{t}_i \delta u_i dS + \iiint_\Omega b_i \delta u_i d\Omega \tag{4.9}$$

where $[\![u_i]\!]$ are the displacement jumps which play the role of a deformation measure with the tractions $\hat{t}_i$ furnishing the conjugate stress measure. Note that the displacement jump component $[\![u_i]\!]$ is measured along the global coordinate X_i. Defining a local midsurface coordinate system such that the basis vectors are normal and tangential to the midsurface, Equation (4.9) can be rewritten as

$$\iiint_\Omega \sigma_{ij}\delta\varepsilon_{ij} d\Omega + \iint_{\bar{S}} t_j R_{ij} \delta [\![u_i]\!] d\bar{S} = \iint_{\partial\Omega} \tilde{t}_i \delta u_i dS + \iiint_\Omega b_i \delta u_i d\Omega \tag{4.10}$$

where t_i are the interfacial traction components acting on a unit deformed interfacial midsurface area; R_{ij} is the rotation tensor relating the midsurface local coordinate system to the fixed global coordinate system. In this context, t_1 and t_2 are the tangential traction components, t_3 the normal traction component to the interfacial midsurface $\bar{S}$. Moreover, the displacement jumps Δ_1 and Δ_2 are defined as the sliding displacement jumps and Δ_3 as the opening displacement jump associated with traction components t_1, t_2, and t_3, respectively, as shown at a material point $\bar{P}$ in Figure 4.3.

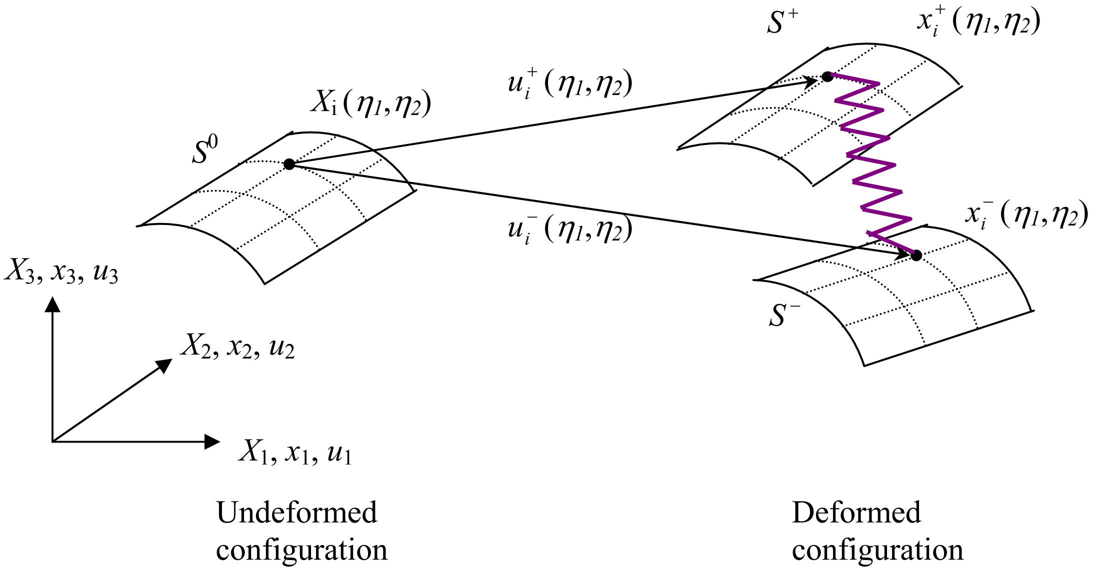

Figure 4.2 Interfacial surfaces in the deformed and undeformed configurations.

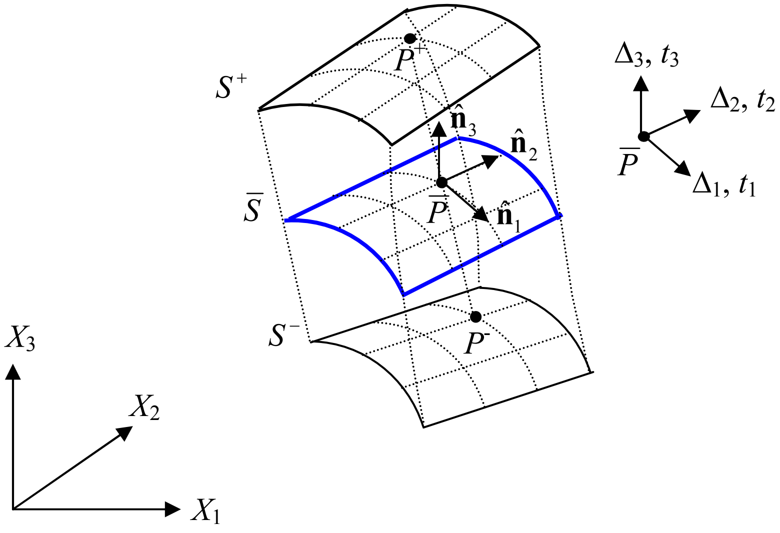

Figure 4.3 Interfacial midsurface with tractions and corresponding displacement jumps.

4.2 Kinematics of the Interfacial Surface

The fundamental problem introduced by the interfacial surface is the question of how to express the rotational tensor ***R*** in Equation (4.10) in terms of the upper and lower surface displacement $u_i^{\pm}$. The derivations of the kinematical relationships are based on relating the spatial coordinates to the surface curvilinear coordinates. As shown in Figure 4.2. Consider a three dimensional space with Cartesian coordinates X_i, $i = 1, 2, 3$, and let there be surface $S^{\pm}$ coincident with S^0 defined in this space by $X_i = X_i(\eta_1, \eta_2)$, where η_1, η_2 are curvilinear coordinates on the surface S^0. Let the Cartesian coordinates $x_i^{\pm} = x_i^{\pm}(\eta_1, \eta_2)$, $i = 1, 2, 3$ describe motion of the upper and lower surfaces $S^{\pm}$ in the deformed configuration. Any material point on $S^{\pm}$ in the deformed configuration is related to the same material point on S^0 through

$$x_i^{\pm} = X_i + u_i^{\pm} \tag{4.11}$$

where $u_i^{\pm}$ are displacement of a material point with respect to the fixed Cartesian coordinate system. The coordinates $\overline{x}_i = \overline{x}_i(\eta_1, \eta_2)$, $i = 1, 2, 3$ define the midsurface $\overline{S}$ as

$$\overline{x}_i = \frac{1}{2}\left(x_i^+ + x_i^-\right) = X_i + \frac{1}{2}\left(u_i^+ + u_i^-\right) \tag{4.12}$$

The surface $\overline{S}$ is coincident with S^0 in the undeformed configuration. As mentioned earlier, the components of the relative displacement vector are evaluated at the midsurface $\overline{S}$. Define the midsurface displacement gradients as

$$g_{i\alpha} = \frac{\partial \overline{x}_i}{\partial \eta_\alpha} \tag{4.13}$$

where $\alpha = 1, 2$. Thus, the local orientation of the tangential unit vectors to the midsurface $\overline{S}$ in terms of the displacement gradient is

$$\mathbf{n_1} = \{g_{11}, g_{21}, g_{31}\}^{\mathrm{T}} \tag{4.14}$$

$$\mathbf{n_2'} = \{g_{12}, g_{22}, g_{32}\}^{\mathrm{T}} \tag{4.15}$$

and the normal vector then is

$$\mathbf{n_3} = \mathbf{n_1} \times \mathbf{n_2'} \tag{4.16}$$

Hence, the magnitude of the differential midsurface area of the deformed configuration is expressed as

$$\begin{aligned} d\overline{S} &= \overline{A} d\eta_1 d\eta_2 = |\mathbf{n_3}| d\eta_1 d\eta_2 \\ &= \sqrt{\left(g_{21}g_{32} - g_{22}g_{31}\right)^2 + \left(g_{11}g_{32} - g_{12}g_{31}\right)^2 + \left(g_{11}g_{22} - g_{12}g_{21}\right)^2} d\eta_1 d\eta_2 \end{aligned} \tag{4.17}$$

In the undeformed configuration, the differential surface area is defined as

$$dS^0 = A d\eta_1 d\eta_2 \tag{4.18}$$

where A does not depend on the displacements. In general, the tangential vectors $\mathbf{n_1}$, $\mathbf{n_2'}$ are not orthogonal in a curvilinear coordinate system, so that, $\mathbf{n_2}$ vector is introduced that is orthogonal to $\mathbf{n}_3$ and $\mathbf{n_1}$ by

$$\mathbf{n}_2 = \mathbf{n}_3 \times \mathbf{n}_1 \tag{4.19}$$

For i = 1, 2, 3, the normal and tangential unit vectors to the surface $\overline{S}$ at a material point $\overline{P} \in \overline{S}$ are

$$\hat{\mathbf{n}}_\mathbf{i} = \frac{\mathbf{n}_\mathbf{i}}{\left|\mathbf{n}_\mathbf{i}\right|} \tag{4.20}$$

These unit vectors are the direction cosines of the local orthogonal coordinate system at a material point $\overline{P} \in \overline{S}$ and form the rotation tensor

$$\mathbf{R} = \left[\hat{\mathbf{n}}_1, \hat{\mathbf{n}}_2, \hat{\mathbf{n}}_3\right] \tag{4.21}$$

This orthogonal tensor relates the local coordinate system located at any point in the midsurface $\overline{S}$ to the fixed coordinate system. Using the rotation tensor, the normal and tangential components of the displacement jump vector expressed in terms of the displacement field are

$$\Delta_i = R_{ij} \left[\!\left[x_j \right]\!\right] = R_{ij}\left(x_j^+ - x_j^-\right) = R_{ij}\left(u_j^+ - u_j^-\right) \tag{4.22}$$

where R_{ij} are the components of the rotation tensor. Note that the rotation tensor depends only on the interfacial midsurface displacement gradients, i.e. **R** = **R** ($g_{i\alpha}$). From Equation (4.17), $\overline{A} = \overline{A}\left(g_{i\alpha}\right)$, which indicates that $\overline{A}$ is a function of the displacement gradients.

4.3 Constitutive Traction-Separation Laws

In the CZM, fracture is considered as a gradual phenomenon in which separation takes place across a cohesive zone resisted by cohesive tractions. The degradation of the material in the cohesive zone is represented by softening-type traction-separation laws which capture both strength-based bond weakening and fracture-based bond rupture from the viewpoint of the molecular theory of strength. In the following subsections, an exponential constitutive law is presented, which is then extended to explicit mixed-mode description with a linear-exponential form.

4.3.1 Exponential Constitutive Law

As mentioned earlier in Section 3.3.1, the exponential traction-separation law has been favored by many analysts and it was motivated by atomistic considerations following the work of Rose et al. (1981). The irreversible exponential constitutive law proposed by Ortiz and Pandolfi (1999) will be introduced next.

For isothermal conditions, the local traction (***t***) across the cohesive interfacial midsurface $\bar{S}$ derives from a free energy density function per unit undeformed area, $\phi(\boldsymbol{\Delta},\boldsymbol{q})$, in the form

$$\boldsymbol{t}=\frac{\partial\phi}{\partial\boldsymbol{\Delta}}(\boldsymbol{\Delta},\boldsymbol{q}) \tag{4.23}$$

where Δ represents the displacement jump across the interfacial midsurface, and $\boldsymbol{q}$ denotes a set of internal variables which describe the inelastic processes of decohesion.

Here, Δ vanishes when the body undergoes a rigid body translation. The internal variables, $\boldsymbol{q}$, evolve according to a set of kinetic relations in the form

$$\dot{\boldsymbol{q}} = f\left(\boldsymbol{\delta}, \boldsymbol{q}\right) \tag{4.24}$$

The potential structure of the cohesive law in Equation (4.23) follows as a consequence of the first and second laws of thermodynamics. The adoption of a potential structure reduces the formulation of the cohesive law from two independent functions, $\boldsymbol{t}(\Delta, \boldsymbol{q})$, to a single scalar function, $\phi\left(\boldsymbol{\Delta}, \boldsymbol{q}\right)$.

In a 3D setting, let Δ_n denote the opening displacement in the normal direction, Δ_s the sliding displacement in the shear direction. Corresponding work-conjugate tractions across the surfaces are t_n (normal) and t_s (shear). By assuming that resistance of the cohesive surfaces to (relative) sliding remains independent of the direction of sliding (i.e. isotropic), the free energy function has the simpler form

$$\phi = \phi\left(\delta_n, \delta_s, \boldsymbol{q}\right) \tag{4.25}$$

The cohesive law in Equation (4.23) then becomes

$$\boldsymbol{t} = \frac{\partial \phi}{\partial \Delta_n}\left(\Delta_n, \Delta_s, \boldsymbol{q}\right)\hat{\mathbf{n}} + \frac{\partial \phi}{\partial \Delta_s}\left(\Delta_n, \Delta_s, \boldsymbol{q}\right)\frac{\boldsymbol{\Delta}_s}{\Delta_s} = \boldsymbol{t}_n + \boldsymbol{t}_s \tag{4.26}$$

where $\hat{\mathbf{n}}$ is the unit normal of the interfacial surface; $\boldsymbol{\Delta}_s/\Delta_s$ is a unit vector in the direction of shear relative displacement resultant. The sliding displacement is composed of two fractions

$$\Delta_s = \|\mathbf{\Delta}_s\| = \sqrt{\Delta_{s1}^2 + \Delta_{s2}^2} \tag{4.27}$$

For shear traction, we also have

$$t_s = \|\boldsymbol{t}_s\| = \sqrt{t_{s1}^2 + t_{s2}^2} \tag{4.28}$$

By introduction of a scalar parameter, β, we can assign different weights to the sliding and the normal opening displacements. The effective opening displacement becomes:

$$\Delta = \sqrt{\Delta_n^2 + \beta^2 \Delta_s^2} \tag{4.29}$$

Then, the effective traction can also be expressed as

$$t = \sqrt{t_n^2 + \beta^{-2} t_s^2} \tag{4.30}$$

It's noteworthy that β also defines the relationship between maximum values of shear and normal tractions.

The free energy potential is chosen to be of an exponential form as

$$\phi = e\sigma_c \Delta_c \left[1 - \left(1 + \frac{\Delta}{\Delta_c} \right) e^{-\Delta/\Delta_c} \right] \tag{4.31}$$

where e = exp(1) and Δ_c denotes the peak value of Δ at $t = \sigma_c$; σ_c is the interfacial strength. Following an irreversible path with unloading always directed towards the origin (Figure 4.4), the relationship between the effective traction and effective opening displacement becomes, for loading and unloading,

$$t = \frac{\partial \phi}{\partial \Delta} = e\sigma_c \frac{\Delta}{\Delta_c} e^{-\Delta/\Delta_c}, \text{ if } \Delta = \Delta_{\max} \text{ and } \dot{\Delta} \geq 0, \text{ loading} \tag{4.32a}$$

$$t = \frac{t_{\max}}{\Delta_{\max}} \Delta, \qquad \text{if } \Delta < \Delta_{\max} \text{ or } \dot{\Delta} < 0, \text{ unloading} \tag{4.32b}$$

where $t_{\max}$ and $\Delta_{\max}$ are the maximum effective traction and relative displacement throughout a loading history. Under compression, in order to avoid penetration, a simple linear elastic behavior with a relatively high stiffness K_c is assumed to model the contact between the upper and lower interfacial surfaces.

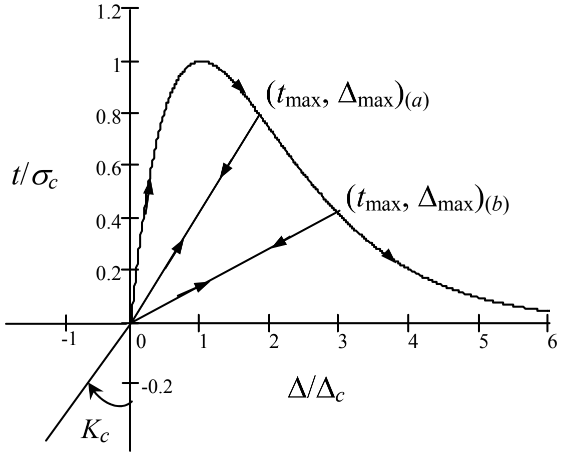

Figure 4.4 Irreversible exponential traction-separation law.

In nonlinear elastic materials, a standard application of the *J*-integral (Equation (1.9)) establishes the link between the critical energy release rate G_c for crack propagation and the cohesive law. Choosing a contour Γ for the evaluation of the *J*-integral which surrounds the cohesive zone gives

$$J = \int_0^r \mathbf{t} \cdot \mathbf{\Delta}_{,1} dx_1 = \int_0^r t\Delta_{,1} dx_1 = \int_0^r t d\Delta \tag{4.33}$$

where r is the cohesive zone length.

For brittle materials and for ductile materials under small scale yielding where plasticity effects are negligible, the J-integral can be expressed as the rate of decrease of potential energy with respect to the crack length a and is equivalent to the energy release rate, G,

$$J = -\frac{\partial \Pi}{\partial a} = G \tag{4.34}$$

where Π is the potential energy of the system. From Equation (4.33) and (4.34), and using Equation (4.32a), the fracture energy (G_c) is given by the area under the t-Δ curve

$$G_c = \int_0^\infty t\, d\Delta = e\sigma_c \Delta_c \tag{4.35}$$

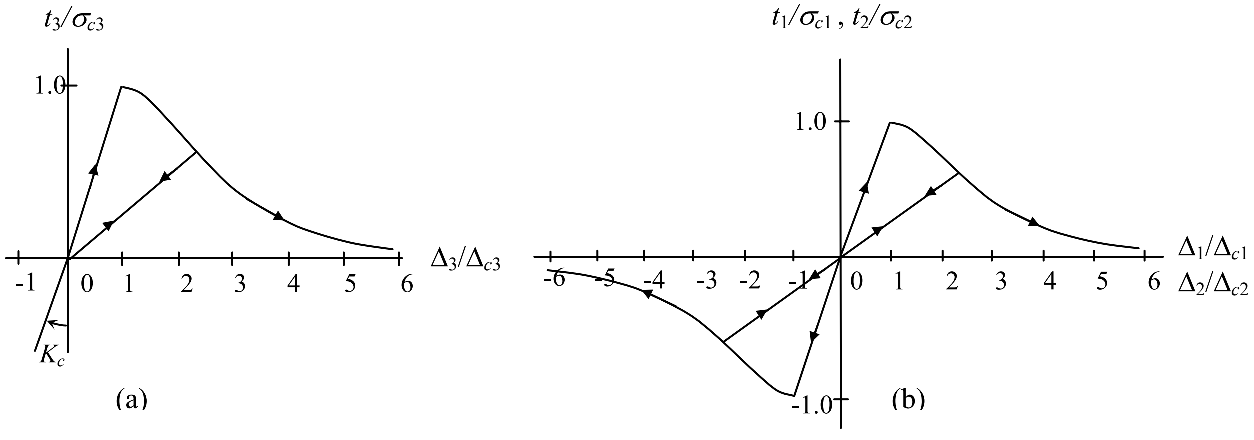

Figure 4.5 Irreversible linear-exponential traction-separation relationships for Mode I (a), Mode II and Mode III (b)

4.3.2 Mixed-Mode Linear-Exponential Constitutive Law

In the exponential traction-separation law described above, the interfacial strength and the fracture energy associated with Mode I, Mode II and Mode III fracture cannot be specified separately. Mode coupling was accounted for by the scalar parameter β as given before the analysis, which is inappropriate since the mode mixity is generally unknown *a priori* for different loading situations as the crack propagates. In order to circumvent this limitation, in this section, an irreversible linear-exponential constitutive law is proposed that incorporates mixed-mode fracture criteria.

4.3.2.1 Uncoupled Model

For the uncoupled model, linear-exponential relationships $t_i = t_i(\Delta_i)$ are assumed for the cases of a single-mode delamination as shown in Figure 4.5. For pure Mode I delamination, the traction-opening displacement relationship (Figure 4.5(a)) is

$$t_3 = \begin{cases} K_3 \Delta_3 & \text{if } \Delta_3 \le \Delta_{c3} \\ K_3 \Delta_3 e^{1-\Delta_3/\Delta_{c3}} & \text{if } \Delta_3 > \Delta_{c3} \end{cases} \tag{4.36}$$

In Equation (4.36) the penalty-like stiffness is $K_3 = \sigma_{c3}/\Delta_{c3}$; σ_{c3} is the peak traction, i.e. interfacial tensile strength; $e = \exp(1)$ and Δ_{c3} denotes the critical value of normal separation Δ_3 when $t_3 = \sigma_{c3}$. Under compression $\Delta_3 < 0$, and in order to avoid penetration, a relatively high stiffness K_c is assumed.

For pure Mode II or Mode III problem, the traction-sliding displacement relationship is depicted in Figure 4.5(b). For Δ_1, $\Delta_2 > 0$, it is the same as for mode I, whereas for Δ_1, $\Delta_2 < 0$ it is antisymmetric with respect to the origin. The analytical expression is

$$t_\alpha = \begin{cases} K_\alpha \Delta_\alpha & \text{if } |\Delta_\alpha| \le \Delta_{c\alpha} \\ K_\alpha \Delta_\alpha e^{1-\Delta_\alpha/\Delta_{c\alpha}} & \text{if } |\Delta_\alpha| > \Delta_{c\alpha} \end{cases} \tag{4.37}$$

where $K_\alpha = \sigma_{c\alpha} / \Delta_{c\alpha}, \alpha = 1, 2$; $\sigma_{c\alpha}$ are the interfacial shear strengths, and $\Delta_{c\alpha}$ are the critical shear separations.

The irreversibility of the interface damage can be taken into account by the following relation

$$t_i = \frac{(t_i)_{\max}}{(\Delta_i)_{\max}} \Delta_i \qquad \text{if } |\Delta_i| < (\Delta_i)_{\max} \text{ or } \dot{\Delta}_i < 0 \tag{4.38}$$

where $(t_\mathrm{i})_{\max}$ and $(\Delta_\mathrm{i})_{\max}$ are the maximum tractions and relative displacements throughout a loading history, $i = 1\text{-}3$. By Equation (4.38), cohesive surfaces are assumed to unload to the origin.

The areas under the traction-relative displacement curves are assumed to be equal to the critical energy release rates, namely, G_{cI}, G_{cII}, G_{cIII} which are characteristic parameters of the interface and can be measured separately by single-mode delamination tests.

$$\begin{gathered} G_{c\mathrm{I}} = \frac{1}{2}\sigma_{c3}\Delta_{c3} + \int_{\delta_{c3}}^{\infty} t_3 d\Delta_3 = 2.5\sigma_{c3}\Delta_{c3} \\ G_{c\mathrm{II}} = 2.5\sigma_{c1}\Delta_{c1}, G_{c\mathrm{III}} = 2.5\sigma_{c2}\Delta_{c2} \end{gathered} \tag{4.39}$$

4.3.2.2 Mixed-Mode Model

Following the approach by Crisfield and Alfano (2002), the mixed-mode delamination can be extended to three-dimensional cases for the single-mode linear-exponential traction-separation law described above. A scalar $\bar{\gamma}$ which accounts for the interactions between Mode I, Mode II and Mode III is defined as

$$\bar{\gamma}(\tau) = \max_{0 \le \tau' \le \tau} \gamma(\tau') \tag{4.40}$$

where

$$\gamma(t') = \left[\left(\frac{|\Delta_1(t')|}{\Delta_{c1}} \right)^{\alpha} + \left(\frac{|\Delta_2(t')|}{\Delta_{c2}} \right)^{\alpha} + \left(\frac{\langle \Delta_3(t') \rangle}{\Delta_{c3}} \right)^{\alpha} \right]^{1/\alpha} - 1 \tag{4.41}$$

with the scalar α being a material parameter, which will generally assume values between 2 and 4. For $\Delta_3 < 0$, since Mode I should not contribute to the damage process, the McCauley bracket $\langle \cdot \rangle$ is used as

$$\langle x \rangle = \begin{cases} x & \text{if } x \ge 0 \\ 0 & \text{if } x \le 0 \end{cases} \tag{4.42}$$

Before Δ_{ci} is reached, it is assumed that there are no interface damage and no coupling between different modes. The mixed-mode constitutive relationship is then given by

$$t_i = \begin{cases} K_i \Delta_i & \text{if } \bar{\gamma}(\tau) \le 0 \\ K_i \Delta_i e^{-\bar{r}} & \text{if } \bar{\gamma}(\tau) > 0 \end{cases} \tag{4.43}$$

where $i = 1, 2, 3$. It is easy to verify that relationships (4.40) – (4.43) specialize to (4.36) and (4.37) for a single-mode delamination problem. Note also that, as a consequence of the irreversibility of the damage, $\bar{\gamma}$ is a monotonic increasing function of τ.

With the above mixed-mode relationship, the following generalized ellipse fracture criterion can be fulfilled

$$\left(\frac{G_{\mathrm{I}}}{G_{c\mathrm{I}}} \right)^{\alpha/2} + \left(\frac{G_{\mathrm{II}}}{G_{c\mathrm{II}}} \right)^{\alpha/2} + \left(\frac{G_{\mathrm{III}}}{G_{c\mathrm{III}}} \right)^{\alpha/2} = 1 \tag{4.44}$$

For α = 2 and α = 4, a linear and a quadratic interaction criterion are recovered, respectively.

4.3.2.3 Proof of the Mixed-Mode Constitutive Law

In this section, the mixed-mode model proposed previously is shown to satisfy generalized ellipse fracture criterion in Equation (4.44) for the progression of delamination.

It is assumed that the relative displacement history is proportional, such that

$$\Delta_1 / z_1 = \Delta_2 / z_2 = \Delta_3 \tag{4.45}$$

where z is fixed during the delamination process.

Using Equation (4.35) and assuming that $\Delta_3 > 0$, from Equation (4.43) we can split the integral in two parts

$$G_{\mathrm{I}} = \int_0^{\infty} t_3 d\Delta_3 = \int_0^{\tilde{\Delta}_3} K_3 \Delta_3 d\Delta_3 + \int_{\tilde{\Delta}_3}^{\hat{\Delta}_3} e^{-\bar{\gamma}} K_3 \Delta_3 d\Delta_3 \tag{4.46}$$

The integration limits $\tilde{\Delta}_3$ and $\hat{\Delta}_3$ correspond to the beginning and to the end of the damage process, respectively. Without loss of generality we can assume a monotonic loading, and then we can write

$$\begin{aligned} \bar{\gamma} = \gamma &= \left[\left(\frac{|\Delta_1|}{\Delta_{c1}} \right)^{\alpha} + \left(\frac{|\Delta_2|}{\Delta_{c2}} \right)^{\alpha} + \left(\frac{\Delta_3}{\Delta_{c3}} \right)^{\alpha} \right]^{1/\alpha} - 1 \\ &= \Delta_3 \left[\left(\frac{|z_1|}{\Delta_{c1}} \right)^{\alpha} + \left(\frac{|z_2|}{\Delta_{c2}} \right)^{\alpha} + \left(\frac{1}{\Delta_{c3}} \right)^{\alpha} \right]^{1/\alpha} - 1 = \Delta_3 \beta_3 - 1 \end{aligned} \tag{4.47}$$

where

$$\beta_3 = \left[\left(\frac{|z_1|}{\Delta_{c1}} \right)^{\alpha} + \left(\frac{|z_2|}{\Delta_{c2}} \right)^{\alpha} + \left(\frac{1}{\Delta_{c3}} \right)^{\alpha} \right]^{1/\alpha} \tag{4.48}$$

Setting $\bar{\gamma} = 0$ related to the beginning of the damage process, we obtain

$$\tilde{\Delta}_3 = \frac{1}{\beta_3} \tag{4.49}$$

In addition, $\hat{\Delta}_3 = \infty$ at the end of the damage process for the proposed linear-exponential constitutive law. Hence, the evaluation of Equation (4.46) yields

$$\begin{aligned} G_{\mathrm{I}} &= \int_0^{1/\beta_3} K_3 \Delta_3 d\Delta_3 + \int_{1/\beta_3}^{\infty} e^{-\bar{\gamma}} K_3 \Delta_3 d\Delta_3 \\ &= K_3 \frac{1}{2\beta_3^2} + K_3 \frac{2}{\beta_3^2} = 2.5 \frac{K_3}{\beta_3^2} \end{aligned} \tag{4.50}$$

Since $G_{c\mathrm{I}} = 2.5\sigma_{c3}\Delta_{c3}$, we arrive at

$$\frac{G_{\mathrm{I}}}{G_{c\mathrm{I}}} = \frac{1}{\beta_3^2 \Delta_{c3}^2} \tag{4.51}$$

Analogous relationships can be obtained for Mode II and Mode III as

$$\frac{G_{\mathrm{II}}}{G_{c\mathrm{II}}} = \frac{1}{\beta_1^2 \Delta_{c1}^2}, \quad \frac{G_{\mathrm{III}}}{G_{c\mathrm{III}}} = \frac{1}{\beta_2^2 \Delta_{c2}^2} \tag{4.52}$$

where

$$\beta_1 = \left[\left(\frac{1}{\Delta_{c1}} \right)^{\alpha} + \left(\frac{|z_2|}{|z_1|\Delta_{c2}} \right)^{\alpha} + \left(\frac{1}{|z_1|\Delta_{c3}} \right)^{\alpha} \right]^{1/\alpha} \tag{4.53}$$

$$=\frac{1}{|z_1|}\left[\left(\frac{|z_1|}{\Delta_{c1}}\right)^{\alpha}+\left(\frac{|z_2|}{\Delta_{c2}}\right)^{\alpha}+\left(\frac{1}{\Delta_{c3}}\right)^{\alpha}\right]^{1/\alpha}=\frac{\beta_3}{|z_1|}$$

similarly

$$\beta_2=\frac{\beta_3}{|z_2|} \tag{4.54}$$

Accordingly, we get

$$\frac{G_{\mathrm{II}}}{G_{c\mathrm{II}}}=\frac{|z_1|^2}{\beta_3^2\Delta_{c1}^2},\frac{G_{\mathrm{III}}}{G_{c\mathrm{III}}}=\frac{|z_2|^2}{\beta_3^2\Delta_{c2}^2} \tag{4.55}$$

and then

$$\begin{aligned}\left(\frac{G_{\mathrm{I}}}{G_{c\mathrm{I}}}\right)^{\alpha/2}+\left(\frac{G_{\mathrm{II}}}{G_{c\mathrm{II}}}\right)^{\alpha/2}+\left(\frac{G_{\mathrm{III}}}{G_{c\mathrm{III}}}\right)^{\alpha/2}&=\left(\frac{1}{\beta_3^2\Delta_{c3}^2}\right)^{\alpha/2}+\left(\frac{|z_1|^2}{\beta_3^2\Delta_{c1}^2}\right)^{\alpha/2}+\left(\frac{|z_2|^2}{\beta_3^2\Delta_{c2}^2}\right)^{\alpha/2}\\&=\frac{1}{\beta_3^{\alpha}}\left[\left(\frac{1}{\Delta_{c3}}\right)^{\alpha}+\left(\frac{|z_1|}{\Delta_{c1}}\right)^{\alpha}+\left(\frac{|z_2|}{\Delta_{c2}}\right)^{\alpha}\right]=1\end{aligned} \tag{4.56}$$

which is coincident with Equation (4.44).

4.4 Interface Element Formulation

In this section, we formulate a general isoparametric interface element for the analysis of three dimensional crack propagation. At first, the basic nonlinear finite element equations are presented. Based on this, element matrices for the interface element are then derived.

4.4.1 Nonlinear Finite Element Solutions

The finite element equations for standard displacement based finite element analysis stem from the principle of virtual work given in Equation (4.10) as follows

$$\iiint_{\Omega} \sigma_{ij}\delta\varepsilon_{ij}d\Omega + \iint_{\bar{S}} t_j R_{ij}\delta[\![u_i]\!]d\bar{S} = \iint_{\partial\Omega} \tilde{t}_i\delta u_i dS + \iiint_{\Omega} b_i\delta u_i d\Omega \tag{4.57}$$

It is convenient to replace the expression of the internal virtual work with the integral over the reference volume Ω_0 as

$$\iiint_{\Omega_0} S_{ij}\delta E_{ij}d\Omega_0 + \iint_{\bar{S}} t_j R_{ij}\delta[\![u_i]\!]d\bar{S} = \iint_{\partial\Omega} \tilde{t}_i\delta u_i dS + \iiint_{\Omega} b_i\delta u_i d\Omega \tag{4.58}$$

where S_{ij} are the second Piola-Kirchhoff stress tensor components and E_{ij} are the Green-Lagrange strain tensor components. The displacement field u_i is interpolated with shape functions as

$$u_i = N_{ik}d_k \tag{4.59}$$

where N_{ik} is a component of an interpolation function matrix and d_k are the nodal displacements. The virtual displacement field δu_i then is

$$\delta u_i = N_{ik}\delta d_k \tag{4.60}$$

where δd_k are the virtual nodal displacements. The continuum variational statement in Equation (4.58) is approximated by a variation over a finite set δd_k. Substituting Equation (4.60) into Equation (4.58), we obtain

$$\delta d_k \left\{ \iiint_{\Omega_0} S_{ij} \frac{\partial E_{ij}}{\partial d_k} d\Omega_0 + \iint_{\bar{S}} t_j R_{ij} \frac{\partial [\![u_i]\!]}{\partial d_k} d\bar{S} - \iint_{\partial\Omega} \tilde{t}_i N_{ik} dS - \iiint_{\Omega} b_i N_{ik} d\Omega \right\} = 0 \tag{4.61}$$

Since δd_k are independent variables, we can choose each one to be nonzero and all others to be zero. Thus, for each δd_k there is an associated equation $f_k = 0$ with $k = 1, 2, \ldots, n$ given as follows

$$f_k = \iiint_{\Omega_0} S_{ij} \frac{\partial E_{ij}}{\partial d_k} d\Omega_0 + \iint_{\bar{S}} t_j R_{ij} \frac{\partial [\![u_i]\!]}{\partial d_k} d\bar{S} - \iint_{\partial\Omega} \tilde{t}_i N_{ik} dS - \iiint_{\Omega} b_i N_{ik} d\Omega = 0 \tag{4.62}$$

This system of equations forms the basis for the displacement finite element procedure which consists of n equations and n unknowns. Each equilibrium equation in Equation (4.62) obtained by discretizing the virtual work equation is written as follows

$$f_k\left(d_1, d_2, \cdots, d_n\right) = 0, \text{ or } f_k\left(d\right) = 0, \;\; k = 1, 2, \cdots, n \tag{4.63}$$

where (d) is equivalent to $(d_1, d_2, ..., d_n)$. In the most general form, the above equation is materially and geometrically nonlinear. The stress-strain and the traction-separation relations are nonlinear. Moreover, the strains and the separations are also nonlinear functions of the nodal displacements.

An iterative solution procedure such as Newton-Raphson is necessary to linearize and solve the nonlinear equilibrium equations in Equation (4.63). At iteration i, denote d^i the approximate displacement state. We assume that at the next iteration, i+1, with d^{i+1}, the equilibrium equations are exactly satisfied. Denote $h^i = d^{i+1} - d^i$ as the difference between the exact solution and the approximate solution. Then the nonlinear equilibrium equations can be written as

$$f_k\left(d^{i+1}\right)=f_k\left(d^i+h^i\right)=0 \tag{4.64}$$

Expanding the left side of the equation with a Taylor series expansion about the approximate solution d^i gives

$$f_k\left(d^i\right)+K_{kr}\left(d^i\right)h_r^i+K_{krs}\left(d^i\right)h_r^ih_s^i+\ldots=0 \tag{4.65}$$

where

$$K_{kr}\left(d^i\right)=\left[\frac{\partial f_k}{\partial d_r}\right]_{d=d^i} \quad \text{and} \quad K_{krs}\left(d^i\right)=\left[\frac{\partial^2 f_k}{\partial d_r \partial d_s}\right]_{d=d^i} \tag{4.66}$$

are the Jacobian and Hessian matrices, respectively. Since the magnitude of h^i is small, higher order terms in Equation (4.65) can all be neglected. It leads to the linearized system of equations

$$K_{kr}^i h^i=-f_k^i \tag{4.67}$$

At iteration i, h^i can be solved in Equation (4.67), and then the next approximate displacement state is $d^{i+1}=d^i+h^i$.

In the Newton-Raphson method, f_k is the residual load vector which defines the out-of-balance force vector. The iterative procedure is designed to drive the residual to zero. From Equation (4.62), the first two terms stemming from the internal virtual work is called the internal force vector denoted as

$$ {}^{\text{int}}f_k = \iiint_{\Omega_0} S_{ij} \frac{\partial E_{ij}}{\partial d_k} d\Omega_0 + \iint_{\bar{S}} t_j R_{ij} \frac{\partial [\![u_i]\!]}{\partial d_k} d\bar{S} \tag{4.68} $$

The last two terms stemming from the external virtual work is termed the external force vector denoted as

$$ {}^{ext}f_k = \iint_{\partial\Omega} \tilde{t}_i N_{ik} dS + \iiint_{\Omega} b_i N_{ik} d\Omega \tag{4.69} $$

Thus, the residual load vector can be rewritten as

$$ f_k = {}^{\text{int}}f_k - {}^{ext}f_k \tag{4.70} $$

Furthermore, the Jacobian matrix **K** is to be computed in Equation (4.67). It is also called the tangent stiffness matrix. We now discuss the contribution of each term in Equation (4.62) to the tangent stiffness matrix. The contribution from the first term is related to the bulk material

$$ {}^{a}K_{kr} = \iiint_{\Omega_0} S_{ij} \frac{\partial^2 E_{ij}}{\partial d_k \partial d_r} d\Omega_0 + \iiint_{\Omega_0} \frac{\partial S_{ij}}{\partial E_{mn}} \frac{\partial E_{mn}}{\partial d_r} \frac{\partial E_{ij}}{\partial d_k} d\Omega_0 \tag{4.71} $$

Similarly, the tangent stiffness matrix contribution from the second term is associated with the interfacial surface material and is obtained as

$$ \begin{aligned} {}^{b}K_{kr} = & \iint_{\bar{S}} \frac{\partial t_j}{\partial \Delta_m} \frac{\partial \Delta_m}{\partial d_r} R_{ij} \frac{\partial [\![u_i]\!]}{\partial d_k} d\bar{S} + \iint_{\bar{S}} t_j \frac{\partial R_{ij}}{\partial d_r} \frac{\partial [\![u_i]\!]}{\partial d_k} d\bar{S} \\ & + \iint_{\bar{S}} t_j R_{ij} \frac{\partial^2 [\![u_i]\!]}{\partial d_k \partial d_r} d\bar{S} + \iint_{\bar{S}} t_j R_{ij} \frac{\partial [\![u_i]\!]}{\partial d_k} \frac{1}{A_r} \frac{\partial A_r}{\partial d_r} d\bar{S} \end{aligned} \tag{4.72} $$

where $A_r = \left|d\overline{S}\right| / \left|dS^0\right| = \overline{A} / A$. The first term of the above equation vanishes since the displacement jump $[\![u_i]\!]$ is linearly related to the nodal displacement d_r. Thus, the tangent stiffness matrix contribution of the interfacial surface material is

$$ {}^{b}K_{kr} = \iint_{\overline{S}} t_j \frac{\partial R_{ij}}{\partial d_r} \frac{\partial [\![u_i]\!]}{\partial d_k} d\overline{S} + \iint_{\overline{S}} t_j R_{ij} \frac{\partial^2 [\![u_i]\!]}{\partial d_k \partial d_r} d\overline{S} + \iint_{\overline{S}} t_j R_{ij} \frac{\partial [\![u_i]\!]}{\partial d_k} \frac{1}{A_r} \frac{\partial A_r}{\partial d_r} d\overline{S} \tag{4.73} $$

The prescribed surface tractions and body forces may depend on the material deformation. Hence, in the most general form, the contribution of the external force vector from the last two terms in Equation (4.62) is

$$ {}^{c}K_{kr} = \iint_{\partial\Omega} \left(\frac{\partial \tilde{t}_i}{\partial d_r} N_{ik} + \tilde{t}_i N_{ik} \frac{1}{A_r} \frac{\partial A_r}{\partial d_r} \right) dS + \iiint_{\Omega} \left(\frac{\partial b_i}{\partial d_r} N_{ik} + b_i N_{ik} \frac{1}{J_r} \frac{\partial J_r}{\partial d_r} \right) d\Omega \tag{4.74} $$

where $J_r = \left|d\Omega\right| / \left|d\Omega^0\right|$. Thus, the tangent stiffness matrix **K** is obtained from Equations (4.71-4.74) as follows

$$ K_{kr} = {}^{a}K_{kr} + {}^{b}K_{kr} + {}^{c}K_{kr} \tag{4.75} $$

4.4.2 Three Dimensional Isoparametric Interface Element

In this subsection, a general three dimensional isoparametric interface element will be formulated. As we discussed in the preceding subsection, the main task is to derive the interface element tangent stiffness matrix **K** and the interface element internal force vector ${}^{\text{int}}\mathbf{f}$ as required in the nonlinear solution procedure. The expressions for **K** and ${}^{\text{int}}\mathbf{f}$ are complex due to the geometrical and material nonlinearities. The geometric nonlinearities are related to the stretching and rotation of the upper and lower surfaces of the interface element, while the material nonlinearity is caused by the nonlinear traction-separation constitutive law.

The element consists of an upper and lower surface $S^{\pm}$ with n nodes contained in each surface as shown in Figure 4.6. In the undeformed configuration, the upper and lower surfaces are coincident. The node numbering convention is such that the difference between the upper node number and the lower node number is n. The nodes of the lower surface are numbered first and those of the upper surface are numbered afterwards. Each node has three translational degrees of freedom.

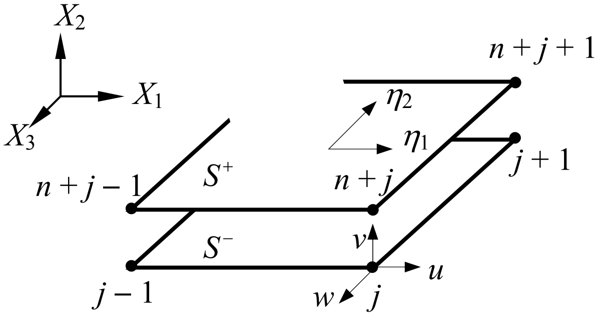

Figure 4.6 General three dimensional isoparametric interface element.

The global displacement for each node is (u, v, w) in the reference coordinate system (X_1, X_2, X_3). In the nodal displacement vector **d**, degrees of freedom corresponding to the displacement along the same direction are grouped together. In each group, the first n quantities correspond to the lower surface nodes and is represented with a '-' superscript; the following (n+1) ~ 2n ones correspond to the upper surface nodes and is denoted with a '+' superscript. Therefore, the nodal displacement vector **d** is

$$\mathbf{d}=\left\{u_1^+,\ldots,u_n^+,u_1^-,\ldots,u_n^-,v_1^+,\ldots,v_n^+,v_1^-,\ldots,v_n^-,w_1^+,\ldots,w_n^+,w_1^-,\ldots,w_n^-\right\}^{\mathrm{T}} \tag{4.76}$$

Using standard interpolation polynomials, in the natural coordinate system of the interface element (η_1, η_2) which is located in the interfacial midsurface, the continuous displacement field, $\mathbf{u} = \left(u^+, u^-, v^+, v^-, w^+, w^-\right)^{\mathrm{T}}$, on the upper and lower surfaces can be expressed in terms of the nodal displacements as

$$u_i = N_{ir} d_r \tag{4.77}$$

where N_{ir} is a component of the 6 × 6n shape function matrix $\mathbf{N}$ which contains the usual bilinear interpolation polynomials expressed in the natural coordinate system (η_1, η_2), $\mathcal{N}(\eta_1, \eta_2) : [N_1(\eta_1, \eta_2), N_2(\eta_1, \eta_2), \ldots, N_n(\eta_1, \eta_2)]$,

$$\mathbf{N} = \begin{bmatrix} \mathcal{N} & 0 & 0 & 0 & 0 & 0 \\ 0 & \mathcal{N} & 0 & 0 & 0 & 0 \\ 0 & 0 & \mathcal{N} & 0 & 0 & 0 \\ 0 & 0 & 0 & \mathcal{N} & 0 & 0 \\ 0 & 0 & 0 & 0 & \mathcal{N} & 0 \\ 0 & 0 & 0 & 0 & 0 & \mathcal{N} \end{bmatrix} \tag{4.78}$$

The global displacement jump can then be obtained as

$$[\![u_j]\!] = L_{ji} N_{ir} d_r \tag{4.79}$$

where L_{ji} is a component of the operator matrix

$$\mathbf{L} = \begin{bmatrix} +1 & -1 & 0 & 0 & 0 & 0 \\ 0 & 0 & +1 & -1 & 0 & 0 \\ 0 & 0 & 0 & 0 & +1 & -1 \end{bmatrix} \tag{4.80}$$

For computational purpose, $\llbracket u_j \rrbracket$ requires transformation from global coordinates to the local coordinate system (η_1, η_2) as given in Equation (4.22). Therefore, the displacement jump in the incremental form is

$$\delta\Delta_i = \delta R_{ji} \llbracket u_j \rrbracket + R_{ji}\delta\llbracket u_j \rrbracket = \llbracket u_j \rrbracket \frac{\partial R_{ji}}{\partial d_r}\delta d_r + R_{ji}\frac{\partial \llbracket u_j \rrbracket}{\partial d_r}\delta d_r \tag{4.81}$$

From the Equations (4.12), (4.13), and (4.77), the derivative of the rotation matrix with respect to the nodal displacement is obtained from the following variation

$$\delta R_{ji} = \frac{1}{2}\frac{\partial R_{ji}}{\partial g_{m\alpha}}\frac{\partial\left(L'_{ml}N_{lr}\right)}{\partial \eta_\alpha}\delta d_r \tag{4.82}$$

where L'_{mr} is a component of the operator matrix

$$\mathbf{L}' = \begin{bmatrix} +1 & +1 & 0 & 0 & 0 & 0 \\ 0 & 0 & +1 & +1 & 0 & 0 \\ 0 & 0 & 0 & 0 & +1 & +1 \end{bmatrix} \tag{4.83}$$

Substituting Equations (4.79) and (4.83) into Equation (4.82) gives

$$\delta\Delta_i = \left(\bar{B}_{ir} + \tilde{B}_{ir}\right)\delta d_r \tag{4.84}$$

where we have defined the following

$$\begin{gathered} \bar{B}_{ir} = \frac{1}{2}\frac{\partial R_{ji}}{\partial g_{m\alpha}}\frac{\partial\left(L'_{ml}N_{lr}\right)}{\partial \eta_\alpha}L_{jk}N_{ks}d_s \\ \tilde{B}_{ir} = R_{ji}L_{jk}N_{kr} \end{gathered} \tag{4.85}$$

Thus, the displacement jump/nodal displacement matrix is given as

$$\frac{\partial \Delta_i}{\partial d_r} = \bar{B}_{ir} + \tilde{B}_{ir} \tag{4.86}$$

The second term in Equation (4.68) is the interface element internal force vector which can be obtained using Equation (4.79) as follows

$$f_r = \iint_{\bar{S}} t_j R_{ij} \frac{\partial [\![u_i]\!]}{\partial d_k} d\bar{S} = \iint_{\bar{S}} t_j R_{ij} L_{ik} N_{kr} d\bar{S} = \iint_{\bar{S}} t_j \tilde{B}_{jr} d\bar{S} \tag{4.87}$$

The interface tangent stiffness matrix stems from the linearization of the internal force vector as discussed in the previous subsection. It consists of the contribution of the material tangent stiffness matrix and the geometric tangent stiffness matrix. From Equation (4.73), and the consistent linearization of the internal force vector in Equation (4.87) we obtain

$$K_{tw} = \frac{\partial f_t}{\partial d_w} = \iint_{\bar{S}} \tilde{B}_{jt} \frac{\partial t_j}{\partial \Delta_k} \frac{\partial \Delta_k}{\partial d_w} d\bar{S} + \iint_{S^0} \tilde{B}_{jt} t_j \frac{\partial A_r}{\partial d_w} dS^0 + \iint_{\bar{S}} \frac{\partial \tilde{B}_{jt}}{\partial d_w} t_j d\bar{S} \tag{4.88}$$

where $A_r = \left| d\bar{S} \right| / \left| dS^0 \right| = \bar{A} / A$.

The first term of Equation (4.88) is the material tangent stiffness matrix. Substituting Equation (4.86) into the first term we obtain

$$\iint_{\bar{S}} \tilde{B}_{jt} \frac{\partial t_j}{\partial \Delta_k} \frac{\partial \Delta_k}{\partial d_w} d\bar{S} = \iint_{\bar{S}} \tilde{B}_{jt} D_{jk} \left(\bar{B}_{kw} + \tilde{B}_{kw} \right) d\bar{S} \tag{4.89}$$

where $\bar{\mathbf{B}}$ and $\tilde{\mathbf{B}}$ were defined in Equation (4.85), and D_{jk} is a component of the 3 × 3 material tangent stiffness matrix **D**, and its computation is deferred to Section 4.3.3.4.

The second term of Equation (4.88) is the geometric tangent stiffness matrix due to the stretching of the midsurface, and it is obtained as

$$\iint_{S^0} \widetilde{B}_{jt} t_j \frac{\partial A_r}{\partial d_w} dS^0 = \frac{1}{2} \iint_{S^0} \widetilde{B}_{jt} t_j \frac{\partial A_r}{\partial g_{k\alpha}} \frac{\partial N_{kw}}{\partial \eta_\alpha} dS^0 \tag{4.90}$$

The third term of Equation (4.88) is also part of the geometric tangent stiffness matrix related to the rotation, and it is obtained as

$$\iint_{\bar{S}} \frac{\partial \widetilde{B}_{jt}}{\partial d_w} t_j d\bar{S} = \frac{1}{2} \iint_{\bar{S}} \frac{\partial R_{kj}}{\partial g_{l\alpha}} \frac{\partial N_{lw}}{\partial \eta_\alpha} N_{kt} t_j d\bar{S} \tag{4.91}$$

Substituting Equations (4.89) ~ (4.91) into Equation (4.88) gives the interface element tangent stiffness matrix

$$\begin{aligned} K_{tw} = & \iint_{\bar{S}} \widetilde{B}_{jt} D_{jk} \left(\overline{B}_{kw} + \widetilde{B}_{kw} \right) d\bar{S} + \frac{1}{2} \iint_{S^0} \widetilde{B}_{jt} t_j \frac{\partial A_r}{\partial g_{k\alpha}} \frac{\partial N_{kw}}{\partial \eta_\alpha} dS^0 \\ & + \frac{1}{2} \iint_{\bar{S}} \frac{\partial R_{kj}}{\partial g_{l\alpha}} \frac{\partial N_{lw}}{\partial \eta_\alpha} N_{kt} t_j d\bar{S} \end{aligned} \tag{4.92}$$

In the above equations, the partial derivatives of the rotation with respect to the midsurface displacement gradients are computationally expensive to calculate. In the Newton's method, the internal force vector needs to be computed accurately, but the tangent stiffness matrix may be computed approximately. Therefore, we could make the following approximations

$$\frac{\partial \overline{\mathbf{R}}}{\partial \mathbf{g}} \approx 0, \quad \frac{\partial \mathbf{R}}{\partial \mathbf{g}} \approx 0, \quad \frac{\partial A_r}{\partial \mathbf{g}} \approx 0 \tag{4.93}$$

From Equation (4.85), we also have $\overline{B}_{ir} = 0$. Thus, introducing these geometric approximations into Equation (4.92), we can obtain the final form of the tangent stiffness matrix as follows

$$K_{tw} = \iint_{\overline{S}} \widetilde{B}_{jt} D_{jk} \widetilde{B}_{kw} d\overline{S} \tag{4.94}$$

In summary, in matrix form, the internal force vector and the tangent stiffness matrix are given by

$$^{\text{int}}\mathbf{f} = \iint_{\overline{S}} \widetilde{\mathbf{B}}^{\mathrm{T}} \mathbf{t} d\overline{S} \tag{4.95}$$

and

$$\mathbf{K} = \iint_{\overline{S}} \widetilde{\mathbf{B}}^{\mathrm{T}} \mathbf{D} \widetilde{\mathbf{B}} d\overline{S} \tag{4.96}$$

4.4.3 Formulation of Eight-Node 3D Interface Element

Based on the previous discussion, the formulation of an eight-node 3D interface element will be given in this subsection. The interface element is a degenerate form of a 3D continuum element with initial zero-thickness as shown in Figure 4.7. This surface-like element consists of two four-node bilinear isoparametric surfaces, with nodes 1~4 lying on the lower surface of the element, and nodes 5~8 on the upper surface. In the model generation process, these cohesive interface elements are embedded between the surrounding solid or shell elements, and each pair of lower and upper surface nodes should be made coincident in the undeformed configuration.

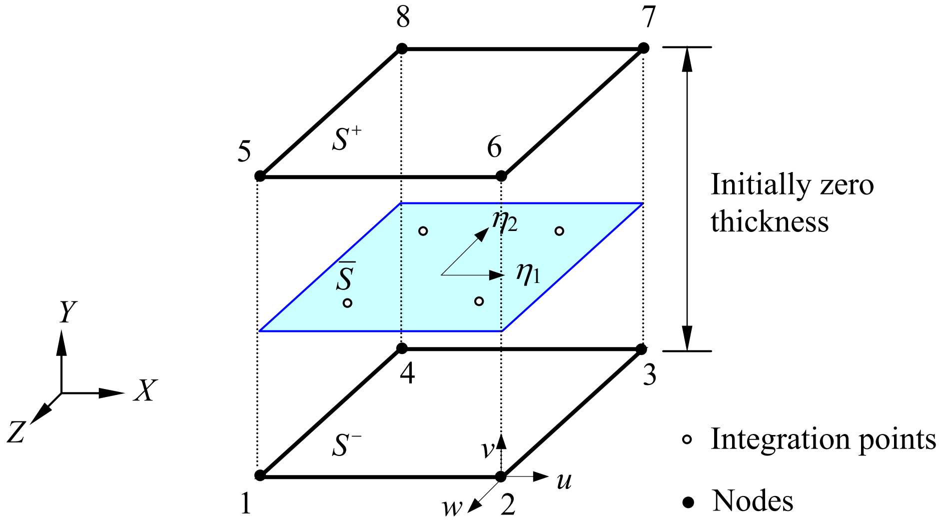

Figure 4.7 3D eight-node interface element.

The nodal displacement vector **d** in Equation (4.76) now is

$$\mathbf{d} = \{u_1^+, \ldots u_4^+, u_1^-, \ldots u_4^-, v_1^+, \ldots v_4^+, v_1^-, \ldots v_4^-, w_1^+, \ldots w_4^+, w_1^-, \ldots w_4^-\}^{\mathrm{T}} \qquad (4.97)$$

The displacement field is interpolated with the shape function matrix **N** as

$$\tilde{\mathbf{u}} = \mathbf{Nd} \qquad (4.98)$$

where $\tilde{\mathbf{u}} = \{u(\eta_1, \eta_2), v(\eta_1, \eta_2), w(\eta_1, \eta_2)\}^{\mathrm{T}}$; **N** is given in Equation (4.78), and $\mathcal{N}(\eta_1, \eta_2)$: $[N_1(\eta_1, \eta_2), N_2(\eta_1, \eta_2), \ldots, N_4(\eta_1, \eta_2)]$ is

$$N_1 = \frac{1}{4}(1-\eta_1)(1-\eta_2),\ N_2 = \frac{1}{4}(1+\eta_1)(1-\eta_2)$$
$$N_3 = \frac{1}{4}(1+\eta_1)(1+\eta_2),\ N_4 = \frac{1}{4}(1-\eta_1)(1+\eta_2) \tag{4.99}$$

The nodal coordinates of the undeformed interface element are contained in the vector **Q** which has the same structure as that of the nodal displacement vector **d**,

$$\mathbf{Q} = \{X_1^+,\ldots X_4^+,X_1^-,\ldots X_4^-,Y_1^+,\ldots Y_4^+,Y_1^-,\ldots Y_4^-,Z_1^+,\ldots Z_4^+,Z_1^-,\ldots Z_4^-\}^{\mathrm{T}} \tag{4.100}$$

where (*X*, *Y*, *Z*) is the global coordinate system. The same shape function matrix **N** is used to interpolate the material coordinate in the interior of the upper and lower surface

$$\widetilde{\mathbf{Q}} = \mathbf{NQ} \tag{4.101}$$

where $\widetilde{\mathbf{Q}} = \{X(\eta_1,\eta_2),Y(\eta_1,\eta_2),Z(\eta_1,\eta_2)\}^{\mathrm{T}}$.

Hence, from Equation (4.12), the material coordinates of the interface element midsurface is given by

$$\widetilde{\mathbf{q}} = \mathbf{NQ} + \frac{1}{2}\mathbf{L}^{'}\mathbf{Nd} \tag{4.102}$$

where $\widetilde{\mathbf{q}} = \{\bar{x}(\eta_1,\eta_2),\bar{y}(\eta_1,\eta_2),\bar{z}(\eta_1,\eta_2)\}^{\mathrm{T}}$; $\mathbf{L}^{'}$ is the operator matrix given in Equation (4.83). The tangent vectors to the interfacial midsurface are then obtained by

$$\mathbf{n}_\alpha = \frac{\partial\widetilde{\mathbf{q}}}{\partial\eta_\alpha} = \frac{\partial\mathbf{N}}{\partial\eta_\alpha}\mathbf{Q} + \frac{1}{2}\frac{\partial(\mathbf{L}^{'}\mathbf{N})}{\partial\eta_\alpha}\mathbf{d} \tag{4.103}$$

The normal vector to the interfacial midsurface is calculated as

$$\mathbf{n}_3 = \mathbf{n}_1 \times \mathbf{n}_2 = \frac{\partial \tilde{\mathbf{q}}}{\partial \eta_1} \times \frac{\partial \tilde{\mathbf{q}}}{\partial \eta_2} \tag{4.104}$$

The tangential vector $\mathbf{n}_2$ is redefined to ensure it is orthogonal to $\mathbf{n}_1$ as: $\mathbf{n}_2 = \mathbf{n}_3 \times \mathbf{n}_1$. The unit vectors are defined as $\hat{\mathbf{n}}_i = \mathbf{n}_i / |\mathbf{n}_i|$. The rotation tensor $\mathbf{R}$ is then given in Equation (4.21) as $\mathbf{R} = [\hat{\mathbf{n}}_1, \hat{\mathbf{n}}_2, \hat{\mathbf{n}}_3]$. Thus, from Equation (4.22), the displacement jumps are obtained by

$$\Delta = \mathbf{R}^{\mathrm{T}}\mathbf{LNd} \tag{4.105}$$

As we discussed previously, the derivative of the rotation tensor with respect to the nodal displacement vector is neglected. Then, $\tilde{\mathbf{B}}$ is given as

$$\tilde{\mathbf{B}} = \mathbf{R}^{\mathrm{T}}\mathbf{LN} \tag{4.106}$$

Finally, the internal force vector ${}^{\mathrm{int}}\mathbf{f}$ is obtained by Equation (4.95) as

$${}^{\mathrm{int}}\mathbf{f} = \int_{-1}^{1}\int_{-1}^{1} \tilde{\mathbf{B}}^{\mathrm{T}}\mathbf{t}\,|\mathbf{n}_3|\,d\eta_1 d\eta_2 \tag{4.107}$$

where $\mathbf{t}$ is the interfacial traction vector. The tangent stiffness matrix $\mathbf{K}$ is given by Equation (4.96) as

$$\mathbf{K} = \int_{-1}^{1}\int_{-1}^{1} \tilde{\mathbf{B}}^{\mathrm{T}}\mathbf{D}\tilde{\mathbf{B}}\,|\mathbf{n}_3|\,d\eta_1 d\eta_2 \tag{4.108}$$

where $\mathbf{D}$ is the interfacial material tangent stiffness matrix. Its computation is discussed in the following subsection. The integrations of the interface element internal force vector and tangent stiffness matrix are performed on the reference surface (midsurface). Different integration schemes could be used as we discussed in Chapter 3.

4.4.4 Interface Element Material Tangent Stiffness

Independently of the constitutive law, the components of the interface element material tangent stiffness matrix **D** are obtained from the following incremental expression

$$\delta t_i = \frac{\partial t_i}{\partial \Delta_j} \delta \Delta_j = D_{ij} \delta \Delta_j \tag{4.109}$$

The expressions for the cohesive constitutive laws include the exponential constitutive law as presented in Section 4.3.1, and the mixed-mode linear-exponential constitutive law as proposed in Section 4.3.2. Let us first consider the case in which no interpenetration occurs, i.e. $\Delta_3 > 0$.

For the exponential constitutive law, the derivation of the material tangent stiffness matrix **D** has already been given by Roy and Dodds (2001). Following Equation (4.26), the individual traction components can be expressed as

$$t_i = \frac{\partial \phi}{\partial \Delta} \frac{\partial \Delta}{\partial \Delta_i} = \phi' \frac{\partial \Delta}{\partial \Delta_i} = t \frac{\partial \Delta}{\partial \Delta_i} \tag{4.110}$$

Then, the material tangent stiffness matrix can be derived as

$$D_{ij} = \left(\phi'' + \phi' \right) \frac{\partial^2 \Delta}{\partial \Delta_j \partial \Delta_i} \tag{4.111}$$

From the above equation, it follows that $D_{ij} = D_{ji}$. Using Equation (4.29) and Equation (4.111), it gives

$$D_{ij} = c_{ij}\beta^2 \left\{ \delta_{ij}\frac{\phi'}{\Delta} + \frac{\beta^2 \Delta_i \Delta_j}{\Delta^2}\left[\phi'' - \frac{\phi'}{\Delta} \right] \right\} \tag{4.112}$$

where $i, j = 1, 2, 3$; δ_{ij} is the Kronecker delta; and c_{ij} is defined as

$$c_{ij} = \begin{cases} \dfrac{1}{\beta^2} & \text{if } i \text{ or } j = 3 \\ 1 & \text{if } i, j \in (1,2) \end{cases} \tag{4.113}$$

In addition,

$$t = \phi' = e\sigma_c \frac{\Delta}{\Delta_c} e^{-\Delta/\Delta_c}, \ \phi'' = \frac{\phi'}{\Delta}\left[1 - \frac{\Delta}{\Delta_c}\right], \ \text{for loading} \tag{4.114a}$$

$$\phi' = \frac{t_{\max}}{\Delta_{\max}}\Delta, \ \phi'' = \frac{t_{\max}}{\Delta_{\max}}, \qquad \text{for unloading} \tag{4.114b}$$

For the mixed-mode linear-exponential constitutive law, by differentiating (4.43) with respect to Δ_i, the material tangent stiffness matrix can be obtained as

$$\begin{aligned} D_{ij} &= \delta_{ij} K_i && \text{if } \bar{\gamma}(t) \le 0 \\ D_{ij} &= -\frac{e^{-\bar{\gamma}}}{(1+\bar{\gamma})^{\alpha-1}}\left[K_i \Delta_i \frac{\tilde{\Delta}_j^{\alpha-1}}{\Delta_{cj}^{\alpha}} - \delta_{ij} K_i (1+\bar{\gamma})^{\alpha-1} \right] && \text{if } \bar{\gamma}(t) > 0 \end{aligned} \tag{4.115}$$

where $i, j = 1, 2, 3$; $\alpha = 2 \sim 4$; δ_{ij} is the Kronecker delta; $\tilde{\delta}_1 = |\delta_1|$, $\tilde{\delta}_2 = |\delta_2|$, $\tilde{\delta}_3 = \langle \delta_3 \rangle$; and $K_i = \sigma_{ci} / \Delta_{ci}$, where σ_{ci} are the interfacial strengths, and Δ_{ci} are the critical separations. From the above equation, a non-symmetric material tangent stiffness matrix is produced unless $\alpha = 2$ and the same properties are used for Mode I, Mode II and Mode III.

For the case in which interpenetration occurs, i.e. when $\Delta_3 < 0$, the components $D_{13} = D_{31} = D_{23} = D_{32} = 0$, with the nonzero components D_{11}, D_{12}, D_{21}, D_{22} given by Equation (4.112) or (4.115), while $D_{33} = K_c = k\sigma_{c3} / \Delta_{c3}$ with the compression multiplier $k = \text{const.}$

The interface element can also be used as a frictionless contact-type element which is applicable for the initial crack region and for the cracked part when crack propagates. It is similar to the interface element involving interpenetration. All the components of the material tangent stiffness matrix are zero except that $D_{33} = k\sigma_{c3} / \Delta_{c3}$ with $k = \text{const.}$

4.5 Nonlinear Solution Procedures

The formulation of the cohesive interface element described above is implemented in the commercial finite element code ABAQUS (2001) via the user-defined element subroutine UEL. Modeling delamination with interface element of softening nature could induce highly nonlinear structural response. In this section, typical nonlinear solution methods are discussed, including Newton-Raphson method, line search method, and the constrained arc-length method.

4.5.1 Newton-Raphson Method

The Newton-Raphson method consists of iteratively solving Equation (4.67) for h_j^i at load increment step j as follows

$$h_j^i = -\left(K_{kr}^i\right)_j^{-1}\left(f_k^i\right)_j \tag{4.116}$$

where $\left(K_{kr}^i\right)_j^{-1}$ is the inverse of the tangent stiffness matrix and $\left(f_k^i\right)_j$ is the residual load vector at iteration i of increment j. The next approximate displacement state is obtained as $d_j^{i+1} = d_j^i + h_j^i$. The iteration continues until the following convergence criterion is reached,

$$\frac{\left\| {}^{ext}\mathbf{f} - {}^{\text{int}}\mathbf{f} \right\|_2}{\left\| {}^{ext}\mathbf{f} \right\|_2} < \varepsilon \tag{4.117}$$

where ε is the tolerance error usually taken as $\varepsilon = 10^{-3}$.

Within the FE analysis, the process of seeking a converged solution is demonstrated in Figure 4.8 using the Newton-Raphson incremental-iterative method. The external forces are applied at the first load step and an initial guess for the nodal displacements is assumed. As it is conventional in the FEM, the global internal force vector and tangent stiffness matrix are assembled from those values at the element level. Then the system of equilibrium equations is solved. We check if the convergence criterion is satisfied, if it is not, then the system is not in equilibrium which means that the nodal displacements need to be corrected. We correct the nodal displacements until they meet the convergence criterion. After the convergence criterion is satisfied, we proceed with the next load step by increasing the external load by a factor and use the previous nodal displacements as the initial guess. From here the procedure is repeated.

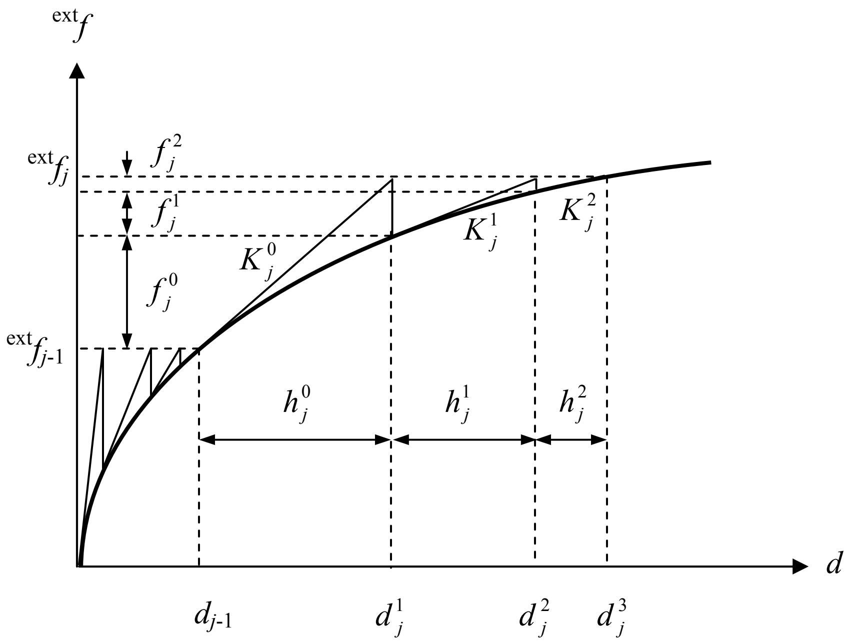

Figure 4.8 The Newton-Raphson incremental-iterative method.

With the Newton-Raphson method, a quadratic convergence rate can be achieved. But the solution to Equation (4.75) is computationally expensive and the tangent stiffness matrix has to be recalculated at each iteration. An alternative is the modified Newton-Raphson method, in which the tangent stiffness matrix is not updated at every iteration, but occasionally. That is, instead of calculating $\mathbf{K}^i$ at iteration i, we use $\mathbf{K}^i = \mathbf{K}^{i-1}$.

4.5.2 Line Search Method

The Newton-Raphson method has proved to be successful in tracing the equilibrium path beyond limit points in analyses of nonlinear structural problems under displacement control, if the displacement does not decrease after the limit point on the equilibrium path; i.e., if there is no snapback. However, the application of the Newton-Raphson method alone in highly nonlinear problems does not always lead to a converged solution. If the approximation to the solution is far from the radius of convergence, then the Newton-Raphson method fails to converge. To overcome this difficulty, Crisfield (1982) developed the line search method used in conjunction with the Newton-Raphson method to solve the highly nonlinear FE equations that stem from a problem involving concrete cracking.

The line search method can be derived from an energy basis. Suppose that the potential energy for a given structural system exists. A Taylor Series expansion of the total potential energy Π as a function of the displacement vector **d** gives

$$\Pi\left(\mathbf{d}^i + \mathbf{h}^i\right) = \Pi_0\left(\mathbf{d}^i\right) + \mathbf{f}\left(\mathbf{d}^i\right)\mathbf{h}^i + \frac{1}{2}\left(\mathbf{h}^i\right)^{\mathrm{T}}\mathbf{K}\left(\mathbf{d}^i\right)\mathbf{h}^i + \ldots \tag{4.118}$$

where

$$\mathbf{f}\left(\mathbf{d}^i\right) = \left(\frac{\partial \Pi}{\partial \mathbf{d}}\right)_{d=\mathbf{d}^i}, \quad \mathbf{K}\left(\mathbf{d}^i\right) = \left(\frac{\partial^2 \Pi}{\partial \mathbf{d}^2}\right)_{d=\mathbf{d}^i} \tag{4.119}$$

and i is the iteration number. Note that **K** is the tangent stiffness matrix and **f** is the residual force vector discussed previously. Thus, for equilibrium it is required that

$$\mathbf{f}\left(\mathbf{d}^i\right) = 0 \tag{4.120}$$

As with the Newton-Raphson method, we obtain **h** as

$$\mathbf{h} = -\mathbf{K}^{-1}\mathbf{f} \tag{4.121}$$

and then the nodal displacements are updated from

$$\mathbf{d}^{i+1} = \mathbf{d}^{i} + \mathbf{h}^{i} \tag{4.122}$$

In a more general form, it is

$$\mathbf{d}^{i+1} = \mathbf{d}^{i} + \vartheta \mathbf{h}^{i} \tag{4.123}$$

where the scalar ϑ is the iterative step length. With $\vartheta = 1$, the Newton-Raphson method is recovered. The line search method consists of obtaining ϑ such that the total potential is minimized. Note that $\mathbf{h}^{i}$ is obtained from Equation (4.121) and $\mathbf{d}^{i}$ is known from the previous iteration. Hence, the total potential energy Π only depends on ϑ. Expanding Π in a Taylor Series about the solution ϑ then gives

$$\Pi(\vartheta + \delta\vartheta) = \Pi_0(\vartheta) + \frac{\partial \Pi}{\partial \mathbf{d}} \frac{\partial \mathbf{d}}{\partial \vartheta} \delta\vartheta + \ldots \tag{4.124}$$

For the solution at ϑ to be stationary, we require the following condition

$$\frac{\partial \Pi}{\partial \mathbf{d}} \frac{\partial \mathbf{d}}{\partial \vartheta} = 0 \tag{4.125}$$

From Equations (4.119) and (4.122), the stationary condition reduces to

$$s(\vartheta) = \mathbf{h}^{\mathrm{T}} \mathbf{f}(\vartheta) = 0 \tag{4.126}$$

where s if the tangent to the total potential energy Π versus. the step length ϑ curve. Hence, the smallest ϑ with $0 \leq \vartheta \leq 1$ satisfying Equation (4.126) is the solution. Since the value ϑ need not to be exact, we use an interpolation method to determine ϑ. Let s_0 =

s ($\vartheta = 0$) and $s_j = s$ ($\vartheta = \vartheta_j$), we require $s_{j+1} = s$ ($\vartheta = \vartheta_{j+1}$) = 0. A linear interpolation to obtain ϑ_{j+1} gives the iteration scheme

$$\vartheta_{j+1} = \vartheta_j \frac{s_0}{s_0 - s_j} \tag{4.127}$$

with the following convergence criterion

$$\left| \frac{s_j}{s_0} \right| < \varepsilon \tag{4.128}$$

where ε is the line search tolerance within the range $0.7 \leq \varepsilon \leq 0.9$.

In summary, the procedure consists in solving Equation (4.121) for $\mathbf{h}^i$ at iteration i. Then, we seek the optimum step length ϑ through the iterative scheme in Equation (4.127) with s defined in Equation (4.126). When the convergence criterion in Equation (4.128) is satisfied, the displacements are updated with Equation (4.123). The Newton-Raphson method stops when the convergence criterion in Equation (4.117) is satisfied.

4.5.3 Constrained Arc-Length Method

Snap-through and snapback are two possible load-displacement structural responses involving limit points as shown in Figure 4.9. An example that involves snap-through is the buckling of shallow arches and an example involving snapback is the delamination of composite laminate. In Figure 4.9a for snap-through, under load control, an unstable dynamic response is expected at the limit point and the dynamic response will follow a path from A to B. Under displacement control the structural response is stable. In

Figure 4.9b for snapback, an unstable dynamic response occurs either under load or displacement control.

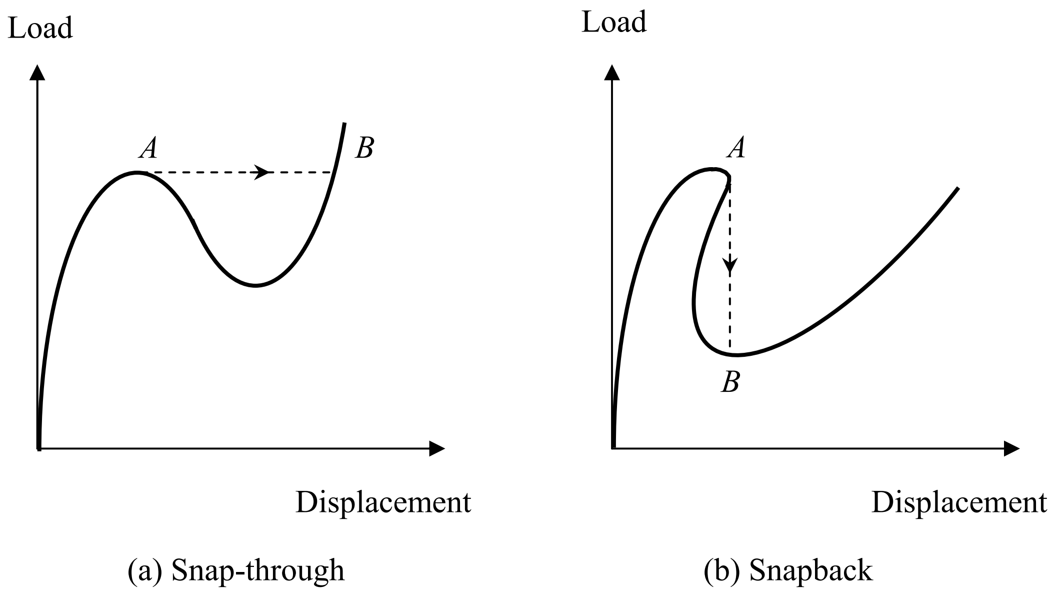

(a) Snap-through

(b) Snapback

Figure 4.9 Unstable structural response.

A major drawback of the Newton-Raphson method is that no limit points can be passed through under a load control procedure. When the specified load exceeds the load at the limit point the solution diverges. The divergence is characterized by growth of the residual forces. The response of structures undergoing a fracture process is highly nonlinear and sophisticated path following techniques have to be employed. The local softening associated with the cohesive constitutive law often results in global softening behavior of the structure and the load-displacement responses are usually characterized by snap-throughs or snapbacks. The Arc-length method originally introduced by Riks (1975) is intended to enable solutions to pass through limit points. In this method, both the load and displacement are unknowns and solved simultaneously. The incremental load is determined by a constraint equation which is a function of the nodal displacements and the load factor. The Newton-Raphson equilibrium iterations converge along an arc as shown in Figure 4.10, thereby preventing divergence even when the slope of the load versus displacement becomes zero or negative. The constraint equation is forced to be satisfied at each iteration.

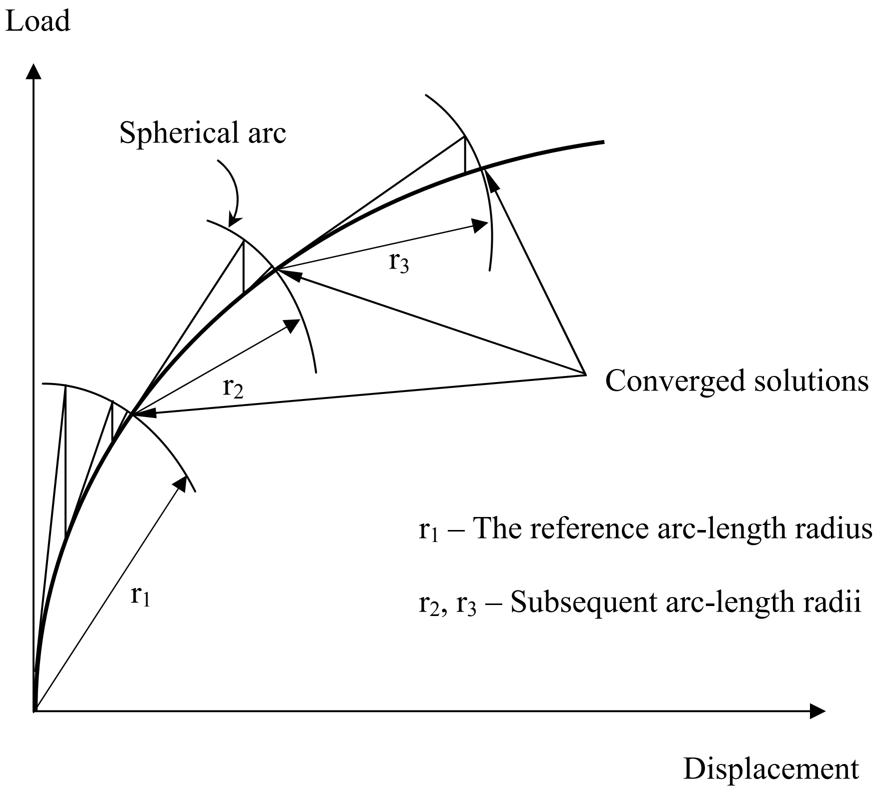

Figure 4.10 Path following arc-length method.

A typical arc-length method has four aspects (Crisfield, 1991): parameterization form, predictor phase, corrector phase, and step-length control. The possible parameterizations of a solution method are load control, displacement control, external work control, etc. But using either of these alone poses several problems in tracing the solution path. In the arc-length method, an adaptive parameterization is adopted in a more generalized form, which can be changed as required during the process of path following.

In the predictor phase, information that belongs to the point previously computed is used to compute a suitable starting value for the corrector phase. And in the corrector phase some numerical procedure is used to find out the solution of the constrained system of equations with the initial guess supplied by the predictor. The control of step size along the path is a crucial issue in the development of an arc-length method. Once the parameterization form, predictor and corrector strategies have been selected, it is expected that a step size control procedure can be achieved such that the desired solution path can be obtained at a minimum computational expense.

Chapter 5

Verification Examples and Computational Issues of Modeling with Interface Elements

The formulation of the cohesive interface element described in Chapter 4 is implemented in the commercial finite element code ABAQUS (2001) via the user-defined element subroutine UEL. Verification examples applying the developed interface element are given in this chapter with numerical simulations of standard fracture test configurations, including the double cantilever beam (DCB) test and the mixed mode bending (MMB) test. Among them, Mode I fracture occurs in the DCB specimen, Mode II and mixed-mode occurs in the MMB specimen. To assess the finite element modeling with the interface element, the response of the test configurations from the numerical simulation are compared to either the analytical solutions based on LEFM or experimental data available in the literature. Typical computational issues as previously mentioned in Chapter 3 will also be discussed. In the last section, delamination buckling of a laminated composite plate under in-plane compression is modeled to test the robustness of the CZM in simulating delamination coupled with highly nonlinear structural response.

5.1 Mode I Fracture Test of DCB Specimen

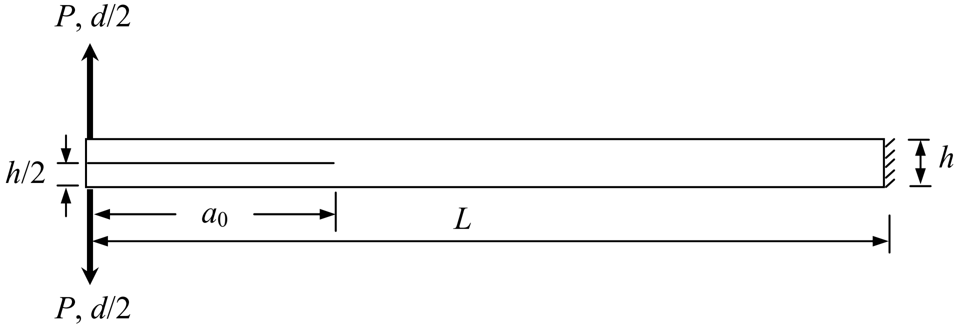

Figure 5.1 Configuration of the DCB specimen.

The DCB specimen is defined by ASTM as a standard test used to determine the Mode I interlaminar fracture toughness. The geometry and loading conditions of the DCB specimen are shown in Figure 5.1. The test is commonly performed on a unidirectional fiber-reinforced laminate with the fibers oriented parallel to the length of the initial delamination. The experiment consists of a displacement-controlled load that is applied at aluminum end blocks hinge-jointed to the DCB specimen. The initial delamination is achieved by incorporating a thin film at the midplane of the laminate layup near the loaded end prior to curing. There are issues pertaining to this conventional test specimen. First, with this specimen, the delamination front may not be straight due to the distribution of the energy release rate G across the width of the beam, which is caused by the anticlastic bending effect. This phenomenon is also called crack tunneling (James and Newman, 2003). It justifies the use of a 3D rather than 2D FE model which assumes a flat and straight crack front through the beam width. Secondly, the main delamination may branch into multiple cracks that may follow the fiber-matrix interfaces. This situation may lead to Mode II loading. In addition, the phenomenon of fiber bridging can also lead to variations of the critical energy release rate.

A complex fracture behavior involving fiber breakage, ply jumping, and fiber bridging often occurs when multidirectional laminates are used in the DCB specimen. The delamination branches to interfaces away from the midplane which leads to larger values of fracture toughness. Robinson and Song (1992) investigated if the complex fracture behavior is a function of the test rather than an intrinsic property of the material. They developed a modified DCB test specimen to suppress crack jumping and fiber bridging effects. To achieve pure Mode I delamination in a layup other than 0^0, the arms of the DCB specimen were designed such that these are balanced and symmetric so as to eliminate the stretching-shearing and stretching coupling effects. In addition, the layup of the angle ply laminate was designed to minimize the bending-twisting effects. The tests were designed to ensure there was no curvature or shear distortion of the laminate due to thermal stresses from curing.

The displacement $d/2$ is specified equal and opposite at the tip of the upper and lower arm of the DCB test specimen, respectively. The corresponding reaction force P is computed. The response is characterized by the load-deflection response P - d.

5.1.1 LEFM Analytical Solution of the DCB Specimen

The analytical solution has been given by Mi et al. (1998). For completeness, we present the derivation in this subsection based on the concepts of linear elastic fracture mechanics. We start with the potential energy of the DCB specimen which is given by

$$\prod = U - Pd \tag{5.1}$$

where U is the strain energy of the DCB; d is the applied tip opening displacement; and P is the corresponding reaction force opposite and equal at the upper and lower arm of the DCB. The free body diagram is shown in Figure 5.2. For a linear isotropic material, the strain energy due to bending of the DCB is simply

$$U = \int_0^a \frac{M_1^2}{2EI_1} dx + \int_0^a \frac{M_2^2}{2EI_2} dx + \int_0^L \frac{M_3^2}{2EI_3} dx \tag{5.2}$$

where M_i is the moment acting either in the upper or lower portion i shown in Figure 5.2; E is the elastic modulus assuming the beam made of isotropic material; and I_i is the moment of inertia of portion i. The moment of inertias for the specimen are related as: $I_1 = I_2 = I$ and $I_3 = 8I$. The respective moments acting in portion 1, 2, and 3 are

$$M_1 = Px\,,\ \ M_2 = Px\,,\ \ M_3 = 0 \tag{5.3}$$

Substituting Equation (5.3) into Equation (5.2) and performing the integrations one obtains the strain energy of the DCB specimen as

$$U = \frac{P^2 a^3}{3EI} \tag{5.4}$$

Substituting Equation (5.4) into Equation (5.1) and using Castigliano's theorem, the load tip deflection is obtained as

$$\frac{\partial \prod}{\partial P} = d\,,\ \ d = \frac{2Pa^3}{3EI} \tag{5.5}$$

Hence, considering each symmetric half (either upper or lower portion) of the specimen, the energy release rate is

$$G_{\mathrm{I}} = -\frac{1}{B}\frac{\partial \Pi}{\partial a} = \frac{P^2 a^2}{BEI} \tag{5.6}$$

where B is the width of the specimen. If $G_{\mathrm{I}} < G_{c\mathrm{I}}$, where $G_{c\mathrm{I}}$ is the Mode I critical energy release rate, then the crack is stationary and $a = a_0$. Thus, the initial response of the specimen is given by Equation (5.5) as

$$d = \frac{2Pa_0^3}{3EI} \tag{5.7}$$

where a_0 is the initial crack length. If $G_{\mathrm{I}} = G_{c\mathrm{I}}$ then the crack grows with $a > a_0$. Then, the response of the specimen is obtained by eliminating a in Equations (5.5) and (5.6) so that

$$d = \frac{2}{3}\frac{\left(BG_c EI\right)^{3/2}}{EIP^2} \tag{5.8}$$

Hence, the load-deflection response is given by the linear relationship in Equation (5.7) before the crack propagates, and by Equation (5.8) when the crack starts to grow. The above simplified solution neglects shear deformation and rotational effects at the crack tip.

5.1.2 Numerical Simulation of the DCB Specimen

The Mode I DCB specimen is modeled with the properties listed in Table 5.1, which were chosen in order to replicate the anisotropic properties of the ply layup in a test by Robinson and Song (1992). The loading and geometrical dimensions are shown schematically in Figure 5.2.

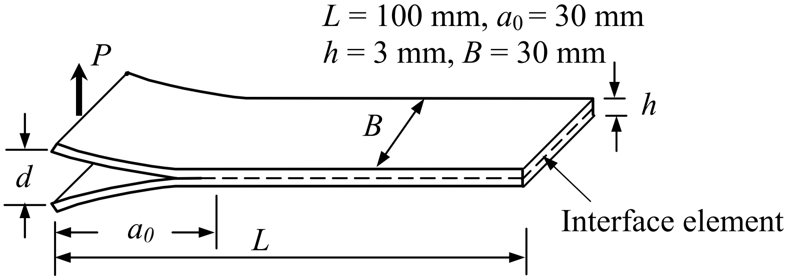

Figure 5.2 3D model of the DCB specimen.

Table 5.1 Mechanical properties of the fiber-reinforced laminate for the DCB specimen.

E_{11} (N/mm^2)	$E_{22} = E_{33}$ (N/mm^2)	$G_{12} = G_{13} = G_{23}$ (N/mm^2)	$\nu_{12} = \nu_{13} = \nu_{23}$
126,000	7,500	4, 981	0.263

The interface elements are positioned in the midplane where delamination is constrained to grow. Since the fracture in the specimen is under Mode I loadings, the exponential constitutive law is used in the formulation of the interface element. Two parameters are required, i.e. Mode I fracture toughness G_c and the interfacial tensile strength σ_c. Among them, G_c was experimentally obtained as 0.281 N/mm^2, while σ_c is chosen initially as 20 N/mm^2 according to similar tests in the literature. Due to symmetry, only one arm of the beam is modeled, and the lower surface of the interface element is constrained in the direction of the beam thickness. Moreover, the lower surface of the interface element is chosen as the reference surface and G_c is also halved accordingly. The ABAQUS finite element model in the deformed state is shown in Figure 5.3. The beam is modeled with C3D8I incompatible mode, 8-noded solid continuum element available in the ABAQUS library. The C3D8I elements are superior in bending to other 3D continuum elements. The beam is modeled using relatively fine mesh with two elements through the thickness, 65 elements along the length. To simulate the anticlastic effects, 15 elements are used across the width. The finite element model consists of 2700 elements, of which 750 are interface elements. The eight-node 3D isoparametric interface element is compatible with C3D8I element. In the initial undeformed configuration, each pair of upper and lower surface nodes are coincident.

An incremental-iterative approach should be used for the nonlinear finite element analysis as we discussed in Chapter 4. The Newton-Raphson method available in ABAQUS is used to trace the loading path of the DCB specimen with a displacement-control analysis. Gauss and Lobatto integration schemes are both applied. Since the bulk material is linear elastic, no pronounced distinction in the structural response is observed utilizing both integration schemes.

The finite element solutions are compared to the analytical solutions in Equations (5.7) and (5.8) with $E = E_{11}$. VCCT as introduced in Chapter 3 is also attempted assuming self-similar straight delamination. The load – deflection response of the DCB specimen is plotted in Figure 5.4. It can be seen that excellent agreement is obtained between the results from the FE analysis with interface element, and the solutions using VCCT, analytical solutions, and experimental data. A contour plot of the mean stress within deformed interface elements is shown in Figure 5.5. A top view of the delamination front region is plotted in Figure 5.5(b). The yellow strip is a region of low stress values, indicating that delamination has occurred. The brown strip is a region of intermediate stress values due to material softening. The red strip is the process zone with high stresses and it is the region where onset of delamination is occurring. The green strip is the location of the delamination front which is not straight across the width, since non-self-similar delamination growth occurs due to the free edge effect and the anticlastic bending effect.

In Figure 5.6, issues of mesh sensitivity, effects of step size and interfacial strength are investigated. Two mesh designs are used, 65 × 15 × 2 and 40 × 7 × 1 (number of elements along length × width × thickness of the beam). In the FE analysis with mesh design 65 × 15 × 2, the interfacial tensile strength = 20.0 N/mm^2. When larger step size is used, we get a less smooth solution during delamination propagation. As pointed out by Roy and Dodds (2001), large step sizes generally lead to satisfactory convergence of the global Newton iterations. However, the computed response might miss key features of the decohesion behavior and accumulate significant errors. If the bulk material involves plasticity, the peak stress attained in the cohesive zone would govern strongly the development of plasticity in the bulk material and consequently the overall specimen strength and ductility. Thus, with large step sizes, interface elements may pass from the pre-peak to post-peak side of the traction-separation curve without enforcing the peak stress level on adjacent bulk material. To eliminate these effects, the interface element could control the step sizes based on the maximum separations occurring in the element.

In the analysis with coarse mesh design 40 × 7 × 1, when the interfacial tensile strength = 20.0 N/mm^2, with Newton-Raphson method, converged solutions after delamination initiation could not be obtained, whereas using Riks arc-length method, the response shows sharp snapbacks and snap-throughs followed by numerical divergence. In this case, more sophisticated path-following methods, e.g. the modified cylindrical arc-length method (Hellweg and Crisfield, 1998), are needed to obtain converged solutions. Unfortunately, such local arc-length procedures are currently not available in ABAQUS. Nonetheless, when we lower the strength to 10.0 N/mm^2, good prediction of the response is achieved, although the maximum load is slightly underestimated. In addition, if more integration points are used, the predicative capability of the interface element could also be improved.

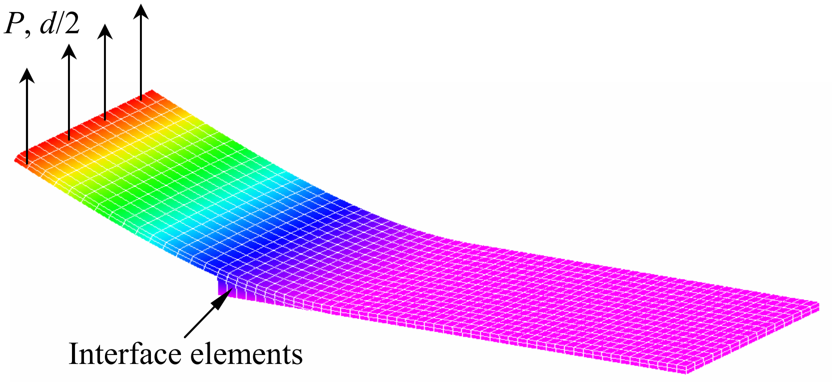

Figure 5.3 Finite element model of the DCB specimen.

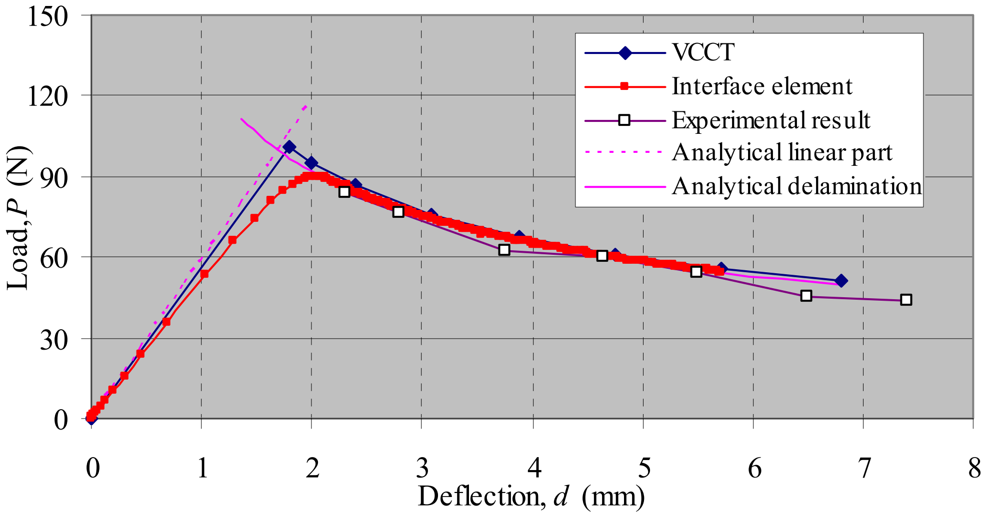

Figure 5.4 Load – deflection response of the DCB specimen.

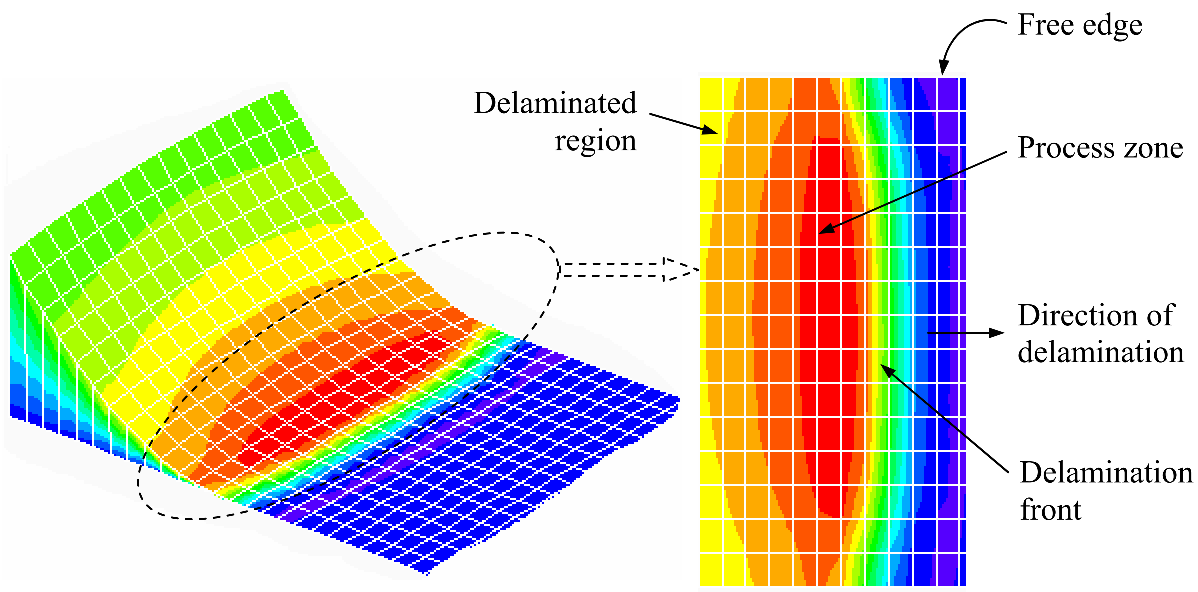

(a) Contour of mean stress within deformed interface elements

(b) Top view of the delamination front region

Figure 5.5 Contour plot of the mean stress within interface elements.

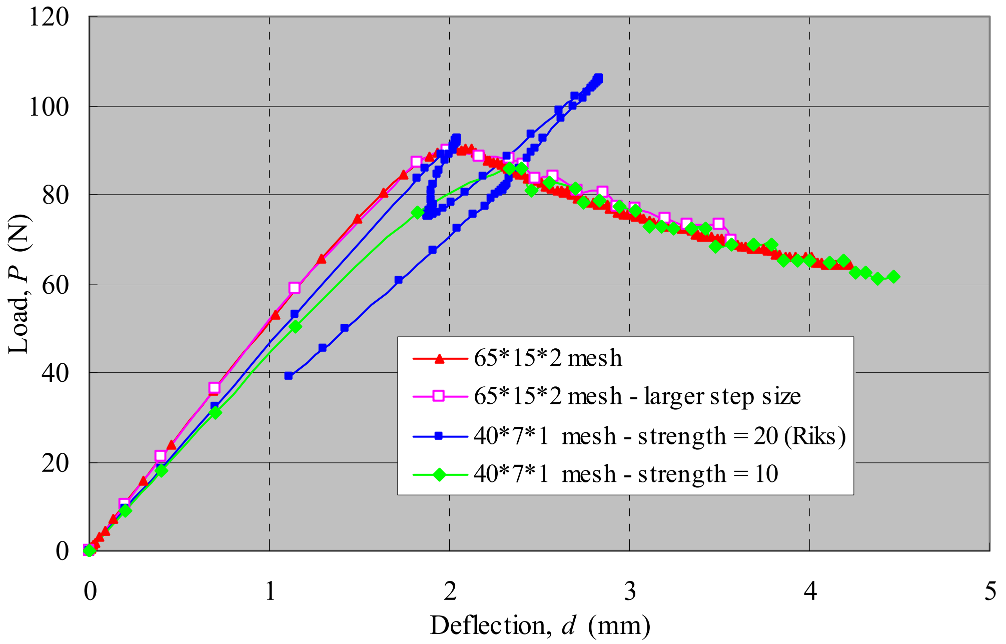

Figure 5.6 Mesh sensitivity, effects of step size and interfacial strength.

In summary, the global structural responses of the DCB specimen could be accurately simulated with the developed interface element. To obtain a relatively smooth solution, the mesh should be sufficiently fine in the evolving process zone at the delamination front. Slightly lowering the interfacial strength could reduce the burden on mesh refinement without sacrificing the accuracy of the prediction.

5.2 Mode II and Mixed-Mode Fracture Test of MMB Specimen

The mixed-mode bending (MMB) test specimen is generally used for the characterization of Mode I and Mode II fracture interaction. The MMB test configuration was proposed by Reeder and Crews (1990, 1991). The main advantage of this specimen is the possibility of using virtually the same configuration for fracture test spanning pure Mode I, mixed-mode, and pure Mode II by varying the mode ratio.

The experimental setup of the MMB test specimen is schematically shown in Figure 5.7. The specimen is simply supported with an initial crack length a_0 located at midplane. The load P_1 is applied at the left end of the upper arm and a load P_2 is applied at the middle of the specimen. The loads applied are $P_1 = P\, c/L$ and $P_2 = P\,(c/L + 1)$, where L is half length of the beam, c is the lever arm length, and P is the actual applied load. By varying the loading length c, different mode ratios can be achieved.

5.2.1 Analytical Solution of the MMB Specimen

The closed form solutions have been given by Allix et al. (1995) for Mode II, and extended by Mi et al. (1998) to include mixed-mode situations. The analytical solutions could also be derived based on LEFM as we did in Section 5.5.1 for Mode I fracture of the DCB specimen. For simplicity, we only give the final solutions next for pure Mode II and mixed-mode fracture.

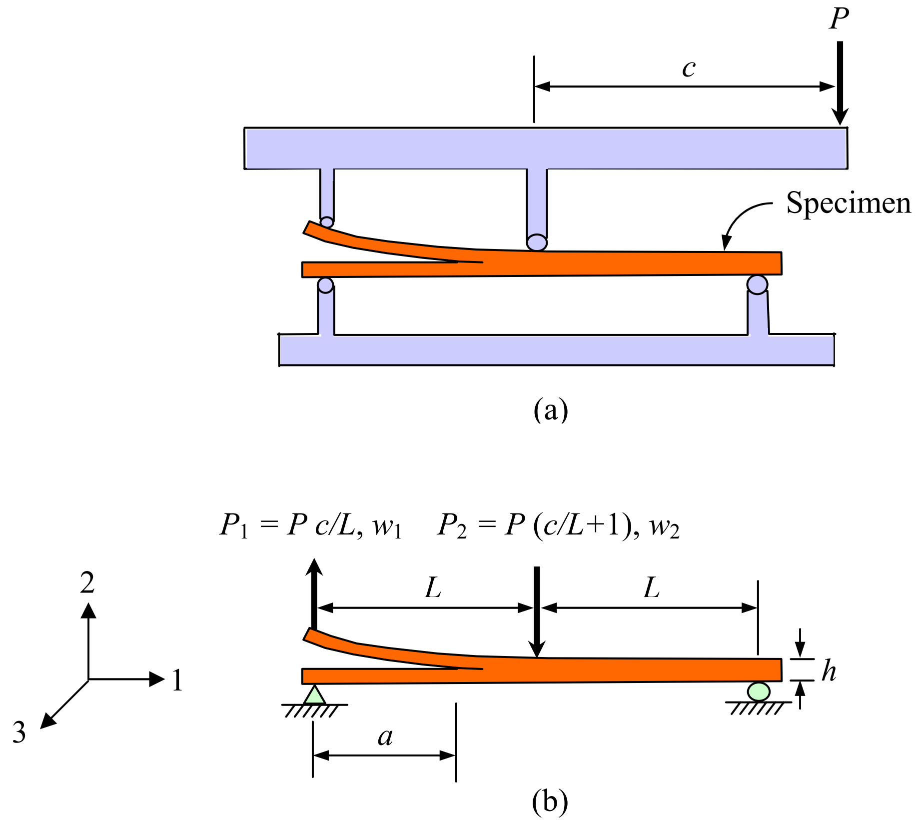

Figure 5.7 Mixed-Mode testing: a) experimental setup; b) loads applied to the specimen.

Mode II Fracture:

A pure Mode II fracture is resulted by setting c to zero, i.e. loading the beam at its center. There are three cases to be considered when the analytical solutions are sought: the initial loading response associated with an initial length of delamination, followed by the unloading path due to delamination growth when the delamination length $a < L$, and another loading response after the delamination grows such that $a > L$. Thus, the analytical solutions expressed as the load-midspan deflection (P-w_2) relationship include three parts. The first part related to the initial loading response is

$$w_2 = \frac{P\left(2L^3 + 3a_0^3\right)}{96EI} \tag{5.9}$$

where L is the half-length of the beam; I is the moment of inertia of one arm of the beam; and a_0 is the initial delamination length.

The second part corresponding to the unloading path ($a < L$) is

$$w_2 = \frac{P}{96EI}\left[2L^3 + \frac{\left(64G_{c\mathrm{II}}BEI\right)^{3/2}}{\sqrt{3}P^3}\right] \tag{5.10}$$

where $G_{c\mathrm{II}}$ is the critical energy release rate in Mode II; and B is the beam width.

The third part is the equivalent relationship when $a > L$ and is given by

$$w_2 = \frac{P}{24EI}\left[2L^3 - \frac{\left(64G_{c\mathrm{II}}BEI\right)^{3/2}}{4\sqrt{3}P^3}\right] \tag{5.11}$$

<u>Mixed-Mode Fracture</u>:

When the loading length $c \neq 0$, mixed-mode fracture occurs. As with pure Mode II fracture, analytical solutions to mixed-mode fracture also consist of three parts. Expressed as the load-specimen end deflection (P-w_1) relationship, the first part for the initial loading is

$$w_1 = \frac{2}{3}\left(\frac{3c - L}{4L}\right)\frac{Pa_0^3}{EI} \tag{5.12}$$

For the second and third parts, since fracture interaction is involved, different interaction criteria could be used to derive the analytical solutions. Let us define P_{I} and P_{II} as the loads associated with Mode I and Mode II respectively as

$$P_{\mathrm{I}} = \left(\frac{3c-L}{4L}\right)P, \quad P_{\mathrm{II}} = \left(\frac{c+L}{L}\right)P \tag{5.13}$$

Then if we assume the linear interaction criterion of Equation (3.1), the second part of the solution for $a < L$ is obtained as follows

$$w_1 = \frac{2P_{\mathrm{I}}}{3EI}\left(\frac{8BEI}{\frac{8P_{\mathrm{I}}^2}{G_{c\mathrm{I}}} + \frac{3P_{\mathrm{II}}^2}{8G_{c\mathrm{II}}}}\right)^{3/2} \tag{5.14}$$

When $a > L$, the third part of the solution has the same form as Equation (5.12), i.e.

$$w_1 = \frac{2}{3}\left(\frac{3c-L}{4L}\right)\frac{Pa^3}{EI} \tag{5.15}$$

However, the delamination length a is to be obtained by solving the following equation

$$\left(\frac{8P_{\mathrm{I}}^2}{G_{c\mathrm{I}}} + \frac{3P_{\mathrm{II}}^2}{8G_{c\mathrm{II}}} - \frac{8P_{\mathrm{I}}P_{\mathrm{II}}}{G_{c\mathrm{II}}}\right)a^2 - \left(\frac{3P_{\mathrm{II}}^2L}{2G_{c\mathrm{II}}} - \frac{8P_{\mathrm{I}}P_{\mathrm{II}}L}{G_{c\mathrm{II}}}\right)a + \frac{3P_{\mathrm{II}}^2L}{2G_{c\mathrm{II}}} - 8BEI = 0 \tag{5.16}$$

5.2.2 Numerical Simulation of the MMB Specimen

In this subsection, the MMB specimen as illustrated in Figure 5.7 is simulated with the interface finite element which is formulated with the mixed-mode linear-exponential constitutive law. The properties of the beam are listed in Table 5.2. The geometric dimensions are: L = 50 mm, a_0 = 30 mm, h = 3 mm, B = 1 mm; where h is the beam height.

Table 5.2 Mechanical properties for the MMB specimen.

E_{11} (N/mm^2)	$E_{22} = E_{33}$ (N/mm^2)	$G_{12} = G_{13} = G_{23}$ (N/mm^2)	$\nu_{12} = \nu_{13}$	ν_{23}
135,300	9,000	5,200	0.24	0.46

Finite element models with reasonable fine meshes are created as shown in Figure 5.8 for the deformed shape of the MMB specimen in pure Mode II fracture and mixed-mode situation. The beam is modeled using C3D8I elements available in the ABAQUS library, with 200 elements along the length, 2 elements along the beam width and 2 elements along the height of each arm. Interface elements are positioned at the midplane of the specimen, of which interface elements with contact properties are used for the initial crack length to prevent overlapping of the arms, and interface elements formulated with the mixed-mode linear-exponential constitutive law are positioned to simulate crack growth. The following properties are used for the interface elements: fracture toughness $G_{cI} = G_{cII} = G_{cIII} = 4.0$ N/mm, interfacial strengths $\sigma_{c1} = \sigma_{c2} = \sigma_{c3} = 57$ N/mm^2.

Firstly, we consider the pure Mode II fracture with the loading length c set to zero. Finite element analysis results of applied load versus midspan deflection (P - w_2) relationship are plotted against closed-form solutions in Figure 5.9. In the figure, there are three curves corresponding to the three parts of the analytical solutions in Equations (5.9) - (5.11), respectively: the linear part OB related to a cantilever with an initial crack length a_0, the unloading segment ABC for fracture with crack length $a < L$, and the loading curve DE valid for $a > L$. From the figure, we can observe that the finite element analysis agrees very well with the closed-form solutions. In highly nonlinear analysis, contact-type interface elements might lead to numerical instabilities which can be resolved in ABAQUS using **controls, analysis = discontinuous* to improve efficiency. Simulation without contact-type interface elements is also performed and the result is shown in Figure 5.9 in which the deflection is largely over-predicted. We demonstrate the snapback by considering a shorter initial crack length with a_0 = 15 mm. The only change to the closed form solution is that the initial loading curve *OB* becomes stiffer and so that when it meets the unloading curve *ABC*, a dynamic unstable crack growth will occur. In the finite element analysis, a converged solution has to be obtained with the Riks method available in ABAQUS. The result is shown in Figure 5.9 which closely follows the unloading path.

The mixed-mode case is then studied setting c to 41.5 mm so that $G_\mathrm{I}/G_\mathrm{II} = 1.0$. In Figure 5.10, load-deflection responses at the specimen end ($P_1 - w_1$) are shown from both the finite element analysis and closed-form solutions. As with the Mode II fracture case, three curves *OB*, *ABC*, and *DE* are plotted in the figure, which are related to the analytical solutions in Equations (5.12), (5.14) and (5.15), respectively. It can be seen that different mixed-mode interaction criteria, e.g., linear or quadratic criterion, would lead to distinguishable structural responses. Nevertheless, it is reported that most of the experimental results lie between these two limit cases (Reeder, 1992). The results from the finite element simulation are in good agreement with the closed-form solutions. However, large discrepancies exist for the portion of the response corresponding to stable crack growth when $a > L$. This is because the analytical solution does not take into account the geometrical nonlinear deformation of the beams while the numerical simulation does.

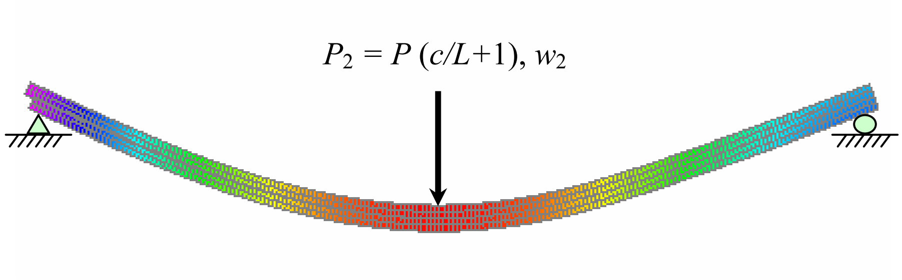

(a) MMB specimen in pure Mode II fracture

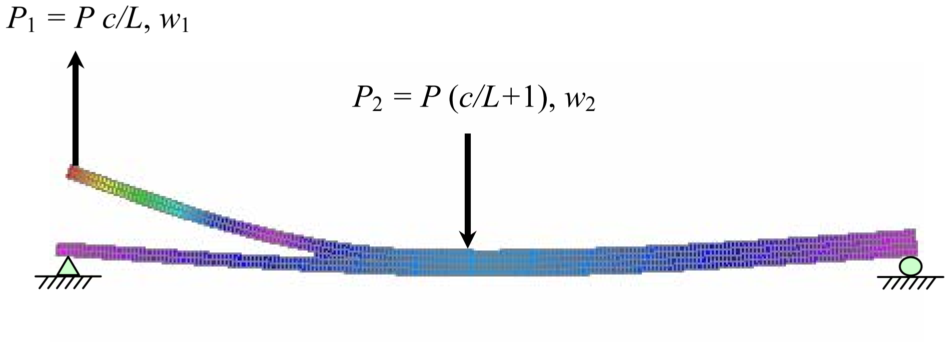

(b) Mixed-mode fracture

Figure 5.8 Finite element models of the MMB specimen.

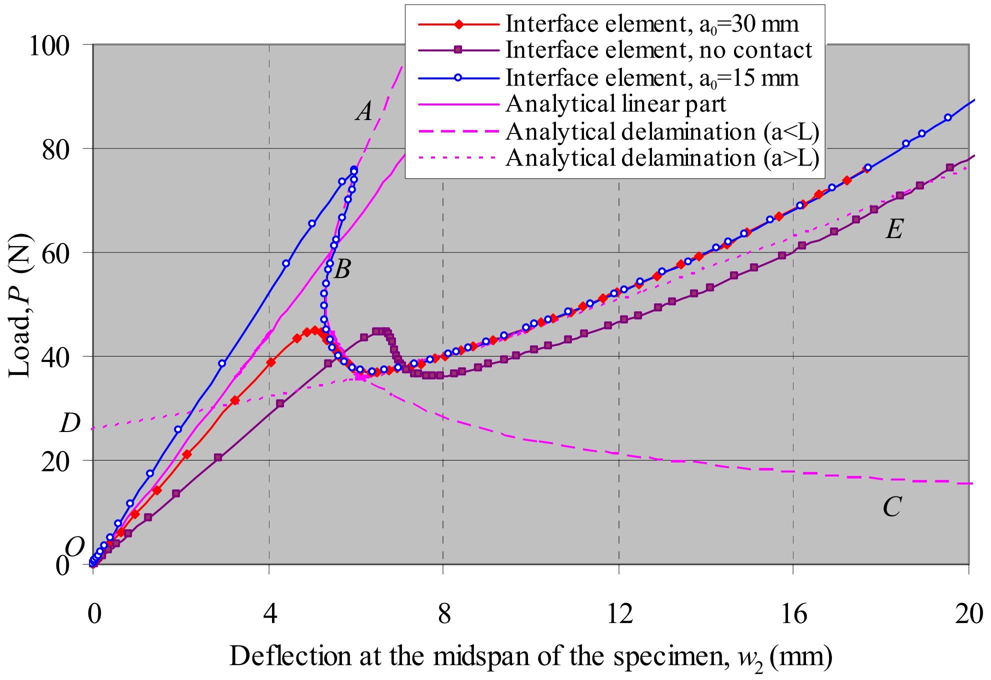

Figure 5.9 Load-deflection responses of the MMB specimen in pure Mode II fracture.

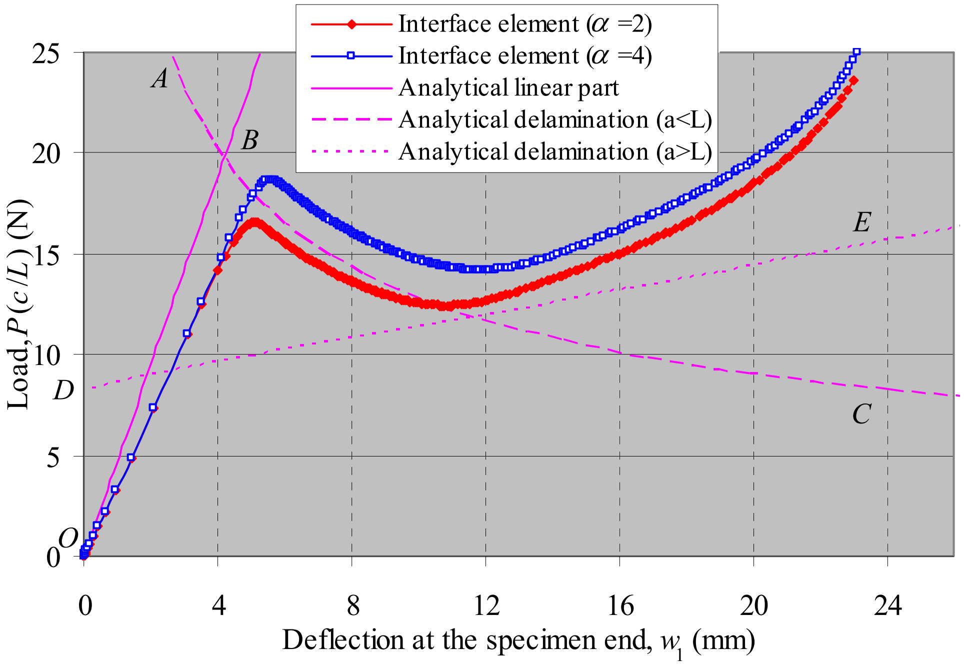

Figure 5.10 Load-deflection responses of mixed-mode fracture in the MMB specimen.

5.3 Delamination Buckling of Laminated Composite Plates

In this section, the phenomenon of buckling driven delamination growth in a compressively loaded laminated composite plate is analyzed. When the composite plate with an initial delamination is subjected to in-plane compression, the delaminated area may buckle and subsequently spread, thus causing a decrease in the load-carrying capacity of the structure. Hence, modeling of this phenomenon is of great practical importance.

In this study, we focus on a near-surface thin layer delaminated from the base laminate. In this case, the problem is much more complicated than the previous modeling of DCB and MMB specimens, since it involves complex interaction between delamination propagation and the response of the structure. As the buckling develops, large deformation may also occur in the delaminated area which could lead to progressive local fiber-matrix failure. Hence, the first part of this section will introduce the local fiber-matrix failure criteria suitable for the problem at hand. In the second part, applying the interface elements, finite element modeling of the buckling-driven delamination in a composite plate containing a single through-the-width delamination will be conducted incorporating local fiber-matrix failure.

5.3.1 Fiber-Matrix Failure Criteria

A set of failure criteria has been proposed by Hashin (1980) to predict failure modes in unidirectional fiber-reinforced composite materials. Four failure modes are considered in our case: fiber failure in tension, fiber failure in compression, matrix failure in tension, and matrix failure in compression. Failure criterion for each failure mode is introduced next. The stresses are computed in the principal material directions for each ply orientation and used in the failure criteria. For simplicity, only in-plane stress components, including σ_{11}, σ_{22}, and σ_{12}, are considered for shell elements used to model the delaminated thin layer. The in-plane shear strength is S_{cp} measured from cross-ply laminates. The strength perpendicular and parallel to the fiber direction is denoted as Y and X, respectively. The subscripts 't' and 'c' denote tension and compression.

Fiber failure:

The failure index for fiber failure in tension or in compression is

$$\begin{aligned} e_f^2 &= \left(\frac{\sigma_{11}}{X_t}\right)^2 + \left(\frac{\sigma_{12}}{S_{cp}}\right)^2, \text{ in tension } (\sigma_{11} > 0) \\ e_f^2 &= \left(\frac{\sigma_{11}}{X_c}\right)^2, \text{ in compression } (\sigma_{11} < 0) \end{aligned} \tag{5.17}$$

If the criterion is satisfied with $e_f \geq 1$ in any one of the plies in the laminate, then fiber failure occurs in that ply. Once failure occurs, material properties in the damaged area degrade. The property degradation model as proposed by Kutlu and Chang (1995b) is used here. If fiber failure occurs, ply longitudinal Young's modulus E_{11}, in-plane shear modulus G_{12}, and Poisson's ratio ν_{12} are reduced to zero within the damaged area.

Matrix failure:

The failure index for matrix failure in tension or in compression is

$$\begin{aligned} e_m^2 &= \left(\frac{\sigma_{22}}{Y_t}\right)^2 + \left(\frac{\sigma_{12}}{S_{cp}}\right)^2, \text{ in tension } (\sigma_{22} > 0) \\ e_m^2 &= \frac{\sigma_{22}}{Y_c}\left[\left(\frac{Y_c}{2S_{cp}}\right)^2 - 1\right] + \left(\frac{\sigma_{22}}{2S_{cp}}\right)^2 + \left(\frac{\sigma_{12}}{S_{cp}}\right)^2, \text{ in compression } (\sigma_{22} < 0) \end{aligned} \tag{5.18}$$

If the criterion is satisfied with $e_m \geq 1$ in any one of the plies in the laminate, then matrix cracking occurs in that ply. If matrix failure occurs, ply transverse Young's modulus E_{22}, and Poisson's ratio ν_{12} are reduced to zero within the damaged area of the layer.

The failure analysis presented above is implemented using the user subroutine USDFLD available in ABAQUS. The USDFLD invokes the material properties and the stresses of all the integration points of the elements. At each integration point, the failure criteria are evaluated and the material properties are degraded accordingly when any one of the modes of failure occurs.

5.3.2 Numerical Simulation of Buckling-Driven Delamination

The specimen under consideration is a 2 in. long and 1 in. wide, graphite-epoxy laminate (T300/976), consisting of 20, 0^0 plies with total thickness of 0.1 in. It is clamped at both ends and was tested in axial compression by Kutlu and Chang (1995b) as shown in Figure 5.11. The case of the specimen containing a single short initial through-the-width delamination is considered in this study. The delamination is located 0.02 in. from the top surface of the laminate at its center with length of 0.75 in. Very thin Teflon strips (0.001 in. thick) were placed at the designated interfaces during layups to introduce the initial delamination. In the test, the strain along the loading direction was recorded at the middle point of the delaminated region on the top of the specimen, which is referred to as front strain. The mechanical properties of the T300/976 graphite-epoxy laminate are listed in Table 5.3, and interlaminar strength and fracture toughness of the laminate are listed in Table 5.4.

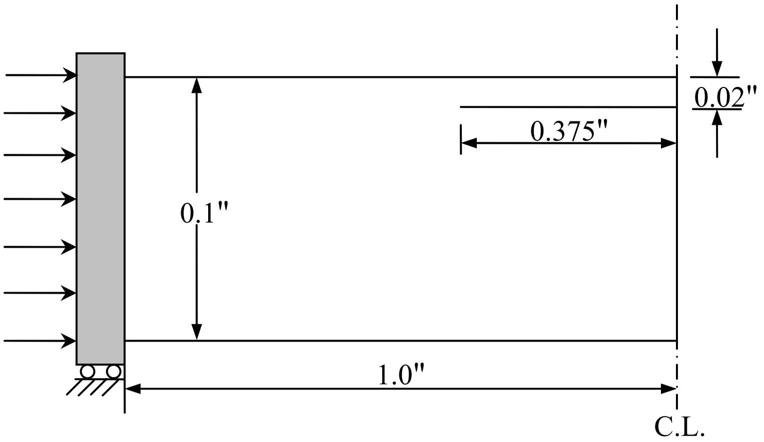

Figure 5.11 Laminated beam configuration.

Table 5.3 Mechanical properties of T300/976 graphite-epoxy.

E_{11} (msi)	$E_{22} = E_{33}$ (msi)	$G_{12} = G_{13}$ (msi)	G_{23} (msi)	$\nu_{12} = \nu_{13}$	ν_{23}
20.2	1.41	0.81	0.5	0.29	0.4

Table 5.4 Interlaminar strength and fracture toughness of T300/976 graphite-epoxy.

X_t (ksi)	X_c (ksi)	Y_t (ksi)	Y_c (ksi)	S_{cp} (ksi)	G_{cI} (lb./in.)	$G_{cII} = G_{cIII}$ (lb./in.)
220	231	6.46	36.7	15.5	0.5	1.8

Taking advantage of symmetry in geometry, loading conditions, and experimentally observed buckling shapes of the specimen, quarter-size finite element models are created. Two different types of models, here called Solid-Solid model and Solid-Shell model, are employed which are shown in Figure 5.12 in the deformed state.

Both models use C3D8I elements to model the thick base laminate; for the top thin layer involving delamination, the Solid-Solid model uses C3D8I elements while the Solid-Shell model uses S4 shell elements available in ABAQUS. Element S4 has four nodes with six degrees of freedom per node and it is transverse shear deformable. Interface elements formulated with the mixed-mode linear-exponential constitutive law are positioned at the interface between the top thin layer and the base laminate where potential delamination is constrained to develop.

Care must be taken to correctly perform the buckling analysis. If the loading on the structure is perfectly in-plane, i.e. membrane or axial stresses only, the out-of-plane deflections necessary to initiate buckling will not develop, and the analysis will fail to predict buckling behavior. To overcome this problem, apply a small out-of-plane perturbation, such as a modest temporary force or specified displacement, to begin the buckling response. A preliminary eigenvalue buckling analysis of the structure could be conveniently used as a predictor of the buckling mode shape, allowing to choose appropriate locations for applying perturbations to stimulate the desired buckling response. The perturbation or imperfection induced should match the location and size of that in the real structure since the structural response could be very sensitive to these parameters. In the present analysis, appropriate initial imperfections are introduced into the ‘perfect’ model to account for the presence of the thin Teflon strips using the first buckling mode shape extracted through a linear eigenvalue buckling analysis. The response of the specimen prove to be sensitive to the prescribed imperfection as shown in Figure 5.13 for the relationship of crack opening displacement (COD) at the center line versus in-plane compression load Consistent results yielded when using a scaling factor SF < 0.001, which also represents the actual thickness of the Teflon strips.

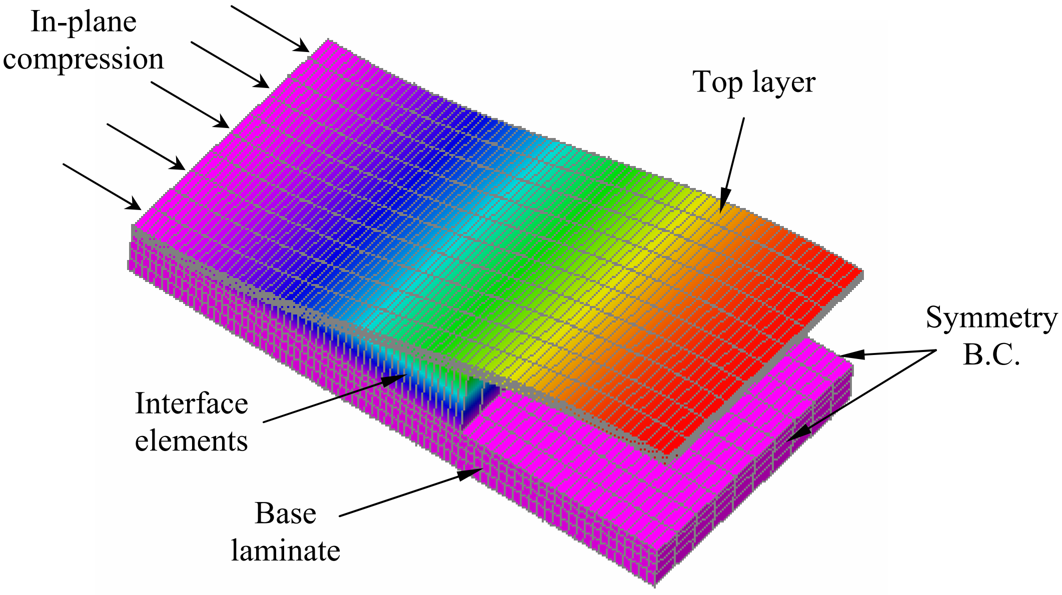

(a) Top thin layer modeled with solid elements in the Solid-Solid model.

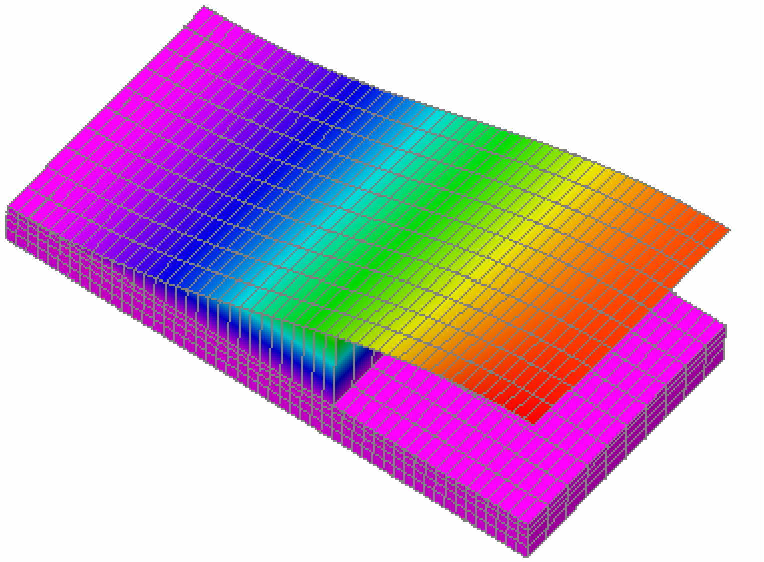

(b) Top thin layer modeled with shell elements in the Solid-Shell model.

Figure 5.12 Finite element models of the T300/976 graphite-epoxy laminate with buckling – driven delamination.

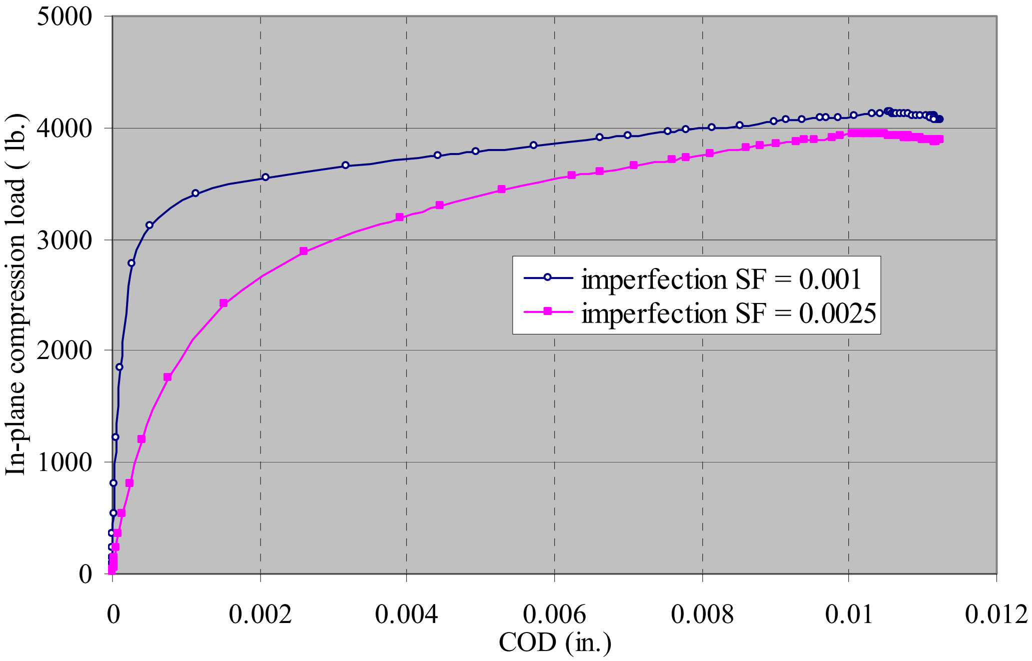

Figure 5.13 Imperfection – sensitivity of the response of COD vs. compression load.

Unlike the modeling of the DCB and MMB specimens previously, buckling – driven delamination analysis is very sensitive to the interfacial strength. Lowering the interfacial strength could significantly underestimate the failure load. In the present modeling, interfacial strengths $\sigma_{c1} = \sigma_{c2} = 9.3$ ksi,$\sigma_{c3} = 6.46$ ksi are used which are the same as those used by El-Sayed and Sridharan (2001) who also modeled the specimen applying a cohesive layer model. Sufficiently fine mesh should be used to obtain converged solutions when the delamination grows. The finest mesh size of 0.003125 in. for the interface elements is used.

Before presenting the detailed results of the analysis, typical loading history is examined in Figure 5.14 which depicts the variation of the front strain with in-plane compression load obtained from the finite element analysis using interface elements and the experimental data (Kutlu and Chang, 1995b). As shown in the figure, the loading history can be clearly divided into four stages. In the first initial loading stage, the strain varies linearly with load and remains compressive. In the second stage, the strain begins to decrease and shifts toward tension, indicating the buckling of the top thin layer and the beginning of the postbuckling phase. During postbuckling the strain becomes tensile. As the load continues to increase, the initiation of delamination growth is indicated by a sudden change in the slope of the load-strain curve. Unstable delamination growth is observed with dropping load in the finite element analysis, whereas snap-through occurred in the experiment. In the final stage, delamination grows stably until it reaches the supports that clamp the specimen.

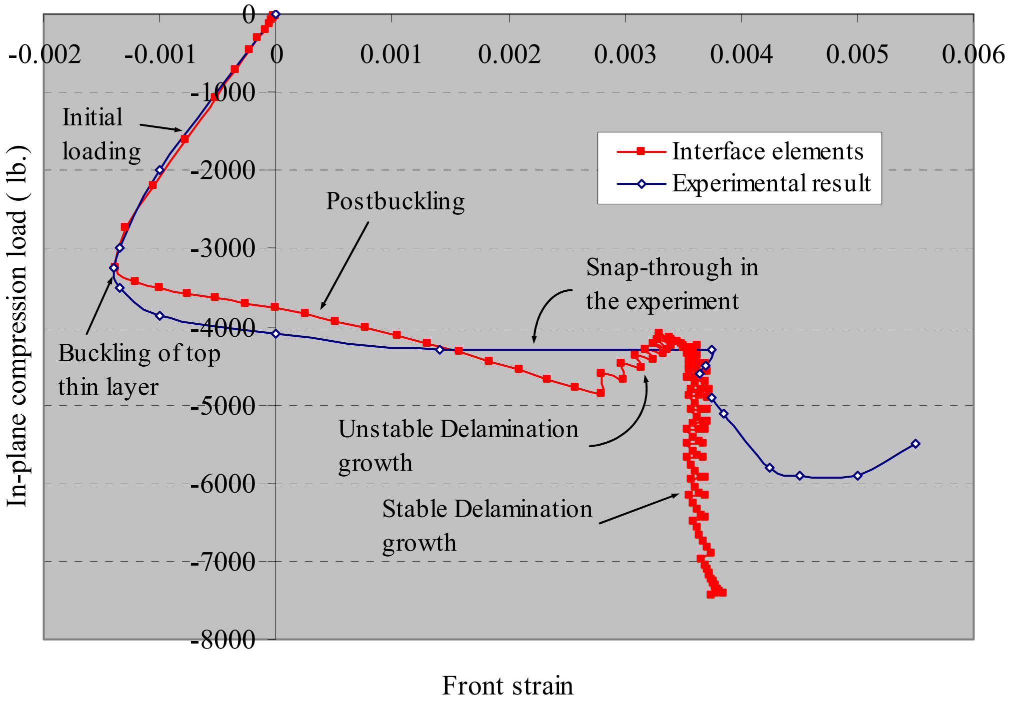

Figure 5.14 Typical loading history of the load vs. strain response.

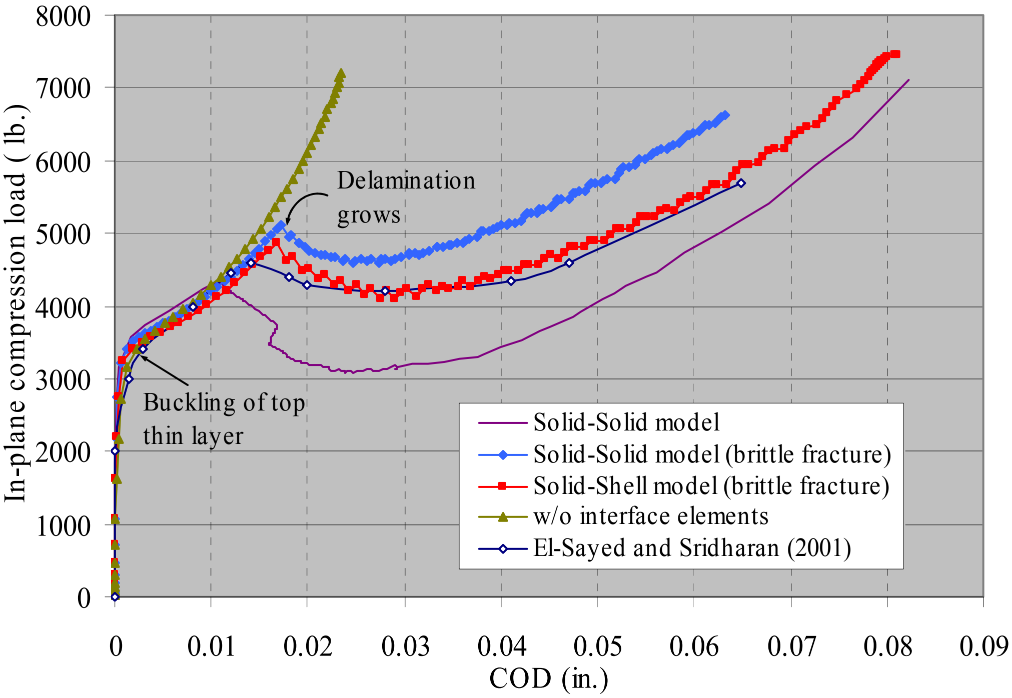

Figure 5.15 COD at the center line vs. in-plane compression load relationship.

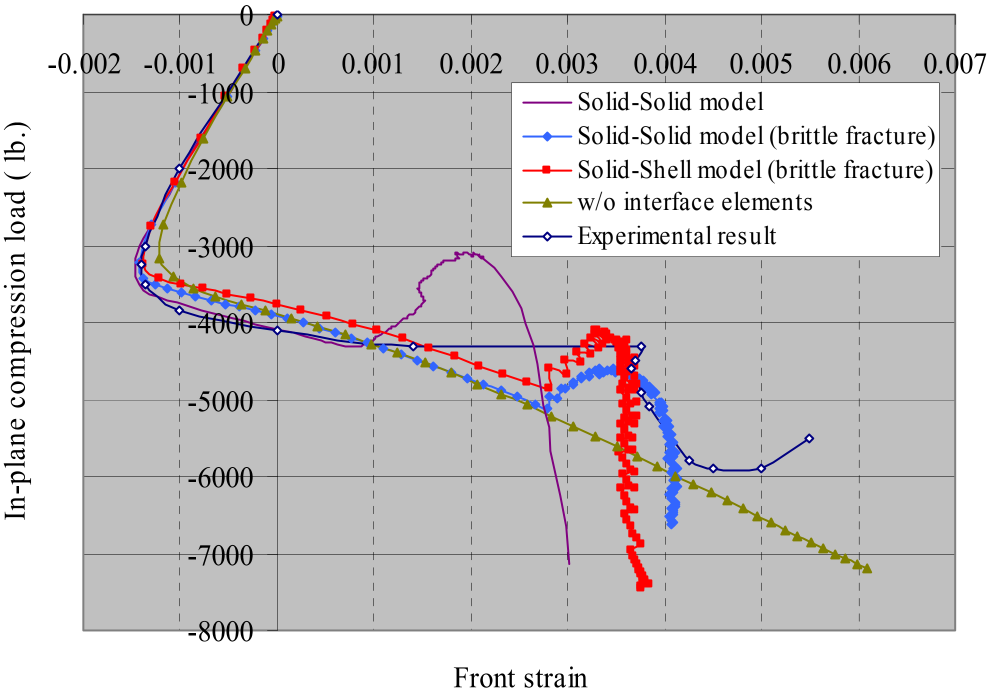

Figure 5.16 Variation of the front strain with in-plane compression load.

In Figure 5.15, finite element analysis results of the crack opening displacement (COD) at the center line versus in-plane compression load relationship are plotted together with the solution of El-Sayed and Sridharan (2001). Figure 5.16 depicts the variation of the front strain with in-plane compression load. In general, the Solid-Solid model and the Solid-Shell model produce similar results. Yet, no satisfactory results were obtained when compared to the experimental data (load-strain) and the solution of El-Sayed and Sridharan (2001) (load-COD). In Figure 5.15, the predicted load drops too much in the stage of unstable delamination growth. However, there is no explicit experimental evidence, since experimental data of COD versus in-plane compression load was not reported and snap-through occurred in the response of front strain versus compression load.

In order to use a relatively coarse mesh while maintain the actual interfacial strength, a different scheme was attempted in the formulation of the interface element. It is assumed that the interface element is damaged completely when the separation $\Delta > 1.1 \Delta_c$ instead of 6.0 Δ_c as originally postulated. Then the fracture toughness is $G_c = 0.55 \sigma_c \Delta_c$. With this formulation, a more brittle type of fracture is induced. Accordingly, stiffer responses are obtained as shown in Figures 5.15 and 5.16. Results from the Solid-Shell model are correlated well with those from the solution of El-Sayed and Sridharan (2001) and the experimental data. However, the Solid-Solid model overestimates the compression load in the postbuckling stage. One way to verify the usage of reasonable parameters for the interface element is to compare the structural responses in the linear range from both models with and without interface elements. For the traction-separation softening law, the linear range of the curve should model the global linear response of the structure, so correct penalty stiffness, $K_c = \sigma_c / \Delta_c$, should be used. From Figures 5.15 and 5.16, it is observed that the structural linear responses are captured accurately with the chosen interfacial strength. Material damage within the top thin layer in the delaminated region, i.e. fiber failure or matrix failure, is accounted for in the Solid-Shell model applying the method discussed in Section 5.3.1. However, no local failure is induced in the top thin layer, which is the reason why the finite element analysis did not predict well the final stage of the strain – load response. Thus, more sophisticated failure analysis is desired for the accurate prediction of the final failure load, which is, however, out of the scope of the current study.

Chapter 6

Facesheet-Core Interface Delamination in HFRP Sandwich Panels

As we already discussed in previous chapters, delamination in composite sandwich structures is an important failure mode. Although the problem of a facesheet delaminated from a solid core has been extensively investigated, the failure mechanism of delamination of a facesheet from a honeycomb core is far from fully understood. The robustness of the cohesive zone model (CZM) implemented as interface element has been verified in Chapter 5 in modeling of standard fracture test configurations and buckling-driven delamination in composite laminates. Application of CZM to study facesheet-core interface delamination of honeycomb sandwich structures is rare. To our best knowledge, only one research of this kind was reported by Han et al. (2002) in which buckling induced delamination propagation of a hexagonal core honeycomb sandwich panel was addressed using a cohesive element method. The composite sandwich panels studied typically have relatively small cells of 3/16 in. and shallow cores, which are mainly used as airframe in commercial aircraft industries. Moreover, the core was homogenized and not explicitly modeled, which could be justified since the core cell is small compared to other geometric dimensions. In our case, however, the use of sinusoidal core HFRP sandwich panels for highway bridge application is a fairly new concept, with large honeycomb cell openings (≈ 4" × 2") leading to different failure mechanisms at the facesheet-core interface.

In this chapter, the developed cohesive interface element is applied to investigate facesheet-core interface delamination in HFRP sandwich panels. For this purpose, the interfacial properties, i.e. interface fracture toughness G_c and interfacial strength σ_c need to be acquired first. Extensive experiments were performed to measure the Mode-I interface fracture toughness ($G_{c\mathrm{I}}$) for the HFRP sandwich panels using contoured double cantilever beam (CDCB) specimens. The interface tensile and shear strengths were also measured experimentally. To provide guidelines for the optimized practical design, the effects of such parameters as facesheet bonding layers and core-wall thickness were investigated. Hence, this chapter is organized as follows. The first part presents the experimental results. In the second part, numerical simulation of the HFRP sandwich panels are conducted using the cohesive interface element.

6.1 Experimental Investigation of Interfacial Properties

In this section, experiments are conducted to measure the interfacial properties, G_c and σ_c. Among them, Mode I interface fracture toughness ($G_{c\mathrm{I}}$) is obtained using CDCB specimens; interfacial tensile and shear strength σ_{cI}, σ_{cII} (or σ_{cIII}) are determined by flatwise tension (FWT) and shear tests, respectively.

6.1.1 Configuration and Properties of HFRP Sandwich Panels

At first, for completeness, the configuration and material properties of HFRP sandwich panels are introduced. For more detailed description, one is referred to the original work by Davalos et al. (2001). The HFRP sandwich panel for bridge deck applications considered in this study was developed by Kansas Structural Composites (Plunkett, 1997). The geometry of the sandwich structure is intended to improve stiffness and buckling response by the continuous support of core elements with the face laminates (or facesheets). Originated from the basic concept of sandwich structures, two faces composed of FRP laminates are co-cured with the core as shown in Figure 6.1. The core geometry consists of closed honeycomb-type FRP cells. It is noteworthy that the thermosetting property of resin distinguishes honeycomb cores from their metal counterparts in both manufacturing and consequent corrugated shapes. Unlike traditional honeycomb sandwich structures, the shape of the FRP corrugated cell wall is defined by a sinusoidal function in the plane. The combined flat and waved FRP cells are produced by sequentially bonding a flat sheet to a corrugated sheet, which is similar to the processing of the paper resin sandwich panel. The assembled cellular core is then co-cured with the upper and bottom facesheets to build a sandwich panel (see Figure 1.2).

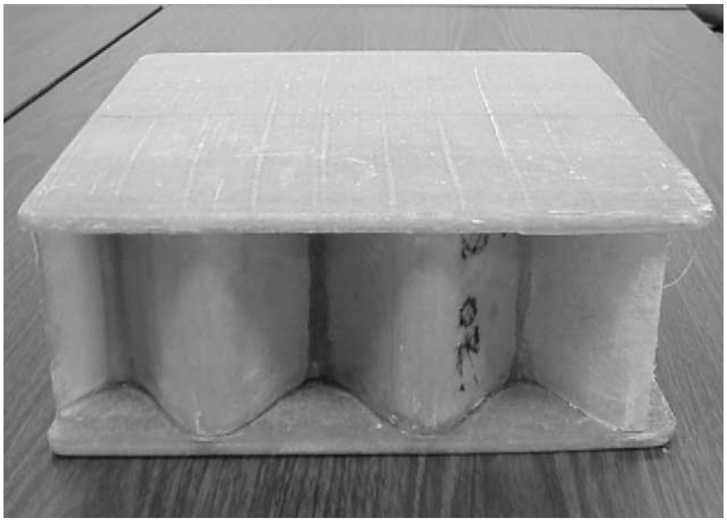

Figure 6.1 HFRP sandwich panel.

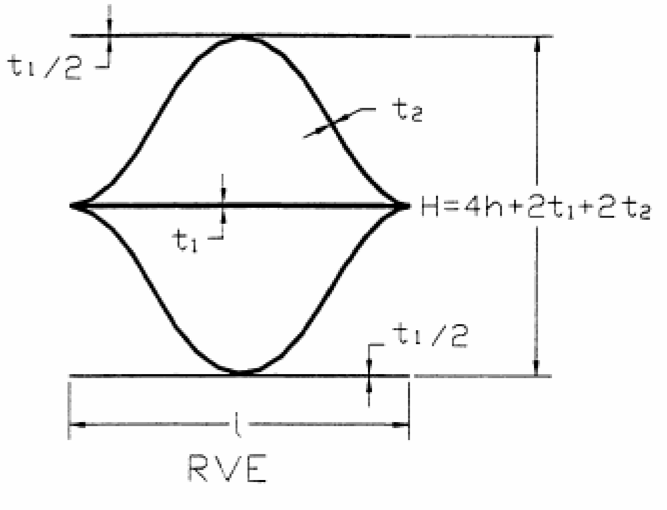

Figure 6.2 Representative volume element (RVE) of honeycomb core.

The waved flutes of core elements are produced by forming FRP sheets onto a corrugated mold. As shown in Figure 6.2, the distance of adjoining crests represents the wavelength l, and the interval between two adjoining flats gives the amplitude $2h$. In the coordinate system of Figure 6.2, the wave function of the corrugated core wall can be defined as

$$y = h\left(1 - \cos\frac{2\pi x}{l}\right) \tag{6.1}$$

In the current study, HFRP sandwich panels with the following dimensions are used: h = 1 in. and l = 4 in. The constituent materials used for the facesheets and the core consist of E-glass fibers and polyester resin, and their properties are listed in Table 6.1.

A typical facesheet may include the following three types of fiber layers (Figure 6.3): (1) Chopped Strand Mat (ChopSM), which is made of short fibers randomly oriented resulting in nearly isotropic in-plane properties. This layer is placed in the inner side of the facesheet and provides a uniform and resilient bond between the facesheet and the core; (2) bidirectional Stitched Fabrics (SF) with balanced off-angle unidirectional fibers (e.g. $0^0/90^0$ or $\pm 45^0$); and (3) unidirectional layer of fiber bundles or rovings. In general, the fiber architecture of upper and bottom facesheets is symmetric about the midsurface plane of the sandwich panel, while each facesheet may exhibit some extensional-bending coupling effect due to the presence of the ChopSM bonding layer. In the current study, the fiber system of the facesheet (Figure 6.3) includes two layers of specified bi-ply combination mat (CS-3208) consisting of a $0^0/90^0$ SF and a ChopSM layer, nine layers of unidirectional combination mat (UM-1810) consisting of a unidirectional layer and a ChopSM layer, and two bonding layers of ChopSM. The resin used is polyester (UN1866). The layer properties of the facesheets are given in Table 6.2. The stiffness of each ply can be obtained using micromechanics models. Based on the assumption that the material is isotropic in the plane, the stiffness properties of the ChopSM layer was evaluated by an averaging procedure for randomly oriented composites. The elastic constants for each individual layer and the core material are listed in Table 6.3.

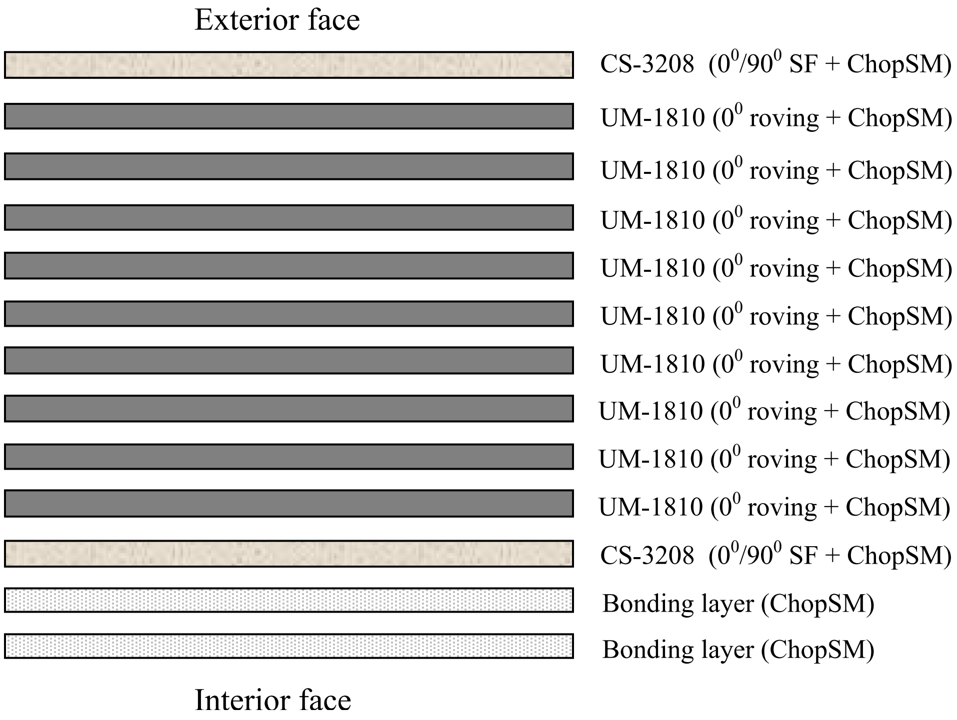

Figure 6.3 Lay-up of facesheets.

Table 6.1 Properties of the constituent materials.

Material	E (ksi)	G (ksi)	ν	ρ (lb/in.^{3})
E-glass fiber	10501	4177	0.255	0.092
Polyester resin	734	236	0.300	0.041

Table 6.2 Layer properties of facesheets.

Material	Ply type	Nominal weight (oz/ft^2)	Thickness, t_f (in.)	Fiber volume fraction
Bonding layer	ChopSM	3.0	0.06	0.235
CS 3208	0^0	1.75	0.0215	0.382
	90^0	2.0	0.0245	0.383
	ChopSM	0.85	0.01	0.399
UM 1810	0^0	2.0	0.02	0.469
	ChopSM	1.0	0.01	0.469

Table 6.3 Layer stiffness properties.

Ply name	Orientation	E_1 (ksi)	E_2 (ksi)	G_{12} (ksi)	G_{23} (ksi)	ν_{12}	ν_{23}
Bonding layer	Random	1705	1705	608	342	0.402	0.400
CS 3208	0^0 or 90^0	4404	1249	484	451	0.293	0.385
	Random	2522	2522	894	467	0.410	0.383
UM 1810	0^0	5265	1488	509	543	0.287	0.371
	Random	2905	2905	1030	543	0.289	0.371
Core mat	Random	4404	1249	484	451	0.293	0.385

Note: For unidirectional layer: $G_{13} = G_{12}$; for random layer: $G_{13} = G_{23}$.

6.1.2 Mode I Interface Fracture Toughness

The conventional method for determining the interface fracture toughness under Mode I loading is by testing double cantilever beam (DCB) specimens. The critical strain energy release rate, $G_{c\mathrm{I}}$, which is a measure of the Mode I fracture toughness of an interface bond, is given by

$$G_{c\mathrm{I}} = \frac{P_c^2}{2b}\frac{dC}{da} \tag{6.2}$$

where, P_c = critical load, b = width of the DCB specimen, and dC/da = rate of change of compliance with respect to crack length a, also called the compliance gradient. The difficulty involved in measuring the crack length can be circumvented by contouring the DCB specimen such that dC/da is a constant. The specimen is known as the contoured double cantilever beam (CDCB) which was described in detail in (Davalos et al., 1997).

In order to avoid discontinuities that may occur in evaluating the interface fracture toughness, the honeycomb core of the CDCB specimen consists of evenly spaced vertical panels instead of the actual sinusoidal wave configurations. The spacing distance is about 0.25" resulting in five or six vertical panels along the width of the specimen. Moreover, the facesheets are reduced to only include one layer of unidirectional combination mat (UM-1810) and the ChopSM bonding layer(s), since the bonding layer and the core-wall thickness are expected to be the dominant parameters influencing the interface properties. In the UM-1810, the ContSM layer was placed on the outside face (see Figure 6.4), and the surfaces of the facesheets were sanded for bonding purposes.

The profile of the CDCB specimen is shown in Figure 6.5. It has length of 22", and width of 1.75". The upper and lower contours were cut out of a single board of Yellow Poplar Laminated Veneer Lumber (LVL). These wood contours were bonded onto the surfaces of the upper and lower facesheets. Polyurethane premium construction adhesive was used as the bonding agent. The specimen has an initial sawed crack with length a_0 = 4" positioned at the interface between the lower facesheet and the core where the crack is expected to propagate under opening load at the right end of the specimen. Along this crack line, the specimen could be divided into two parts: the upper part consisting of the upper LVL contour, the upper facesheet and the honeycomb core; the lower part consisting of the lower facesheet and the lower LVL contour. By appropriately designing the shapes of the wood contours, the CDCB specimen is made symmetric about the crack line such that the stiffness of the upper and lower parts are equal, and thus a pure Mode I fracture is achieved. To ensure such symmetric condition, compliance calibrations of the specimen should be performed, which will be described in detail later.

As previously mentioned, for the purpose of optimal practical design, the number of bonding layers and the core-wall thickness t_c were varied to study the effects of these parameters on the interface properties. In fact, for the bonding layer, 1 or 2 layer(s) were used, thus the total facesheet thickness $t_f = 0.0382 + n \times 0.082$ inch, where the thickness of the UM–1810 layer is 0.0382", the thickness of one bonding layer is 0.082", and n is the number of bonding layer(s). With regard to the core-wall thickness, three types of honeycomb core were used, each with thickness of 0.06", 0.09", and 0.12", respectively. Therefore, there are six types of specimens to be examined, each with different combinations of bonding layer(s) and core-wall thickness. For convenience, here we use the following naming convention to distinguish each class of specimen:

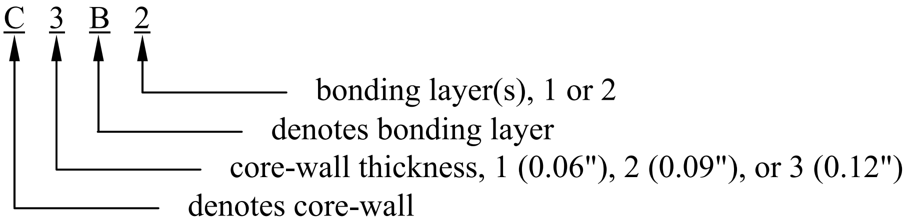

For example, C2B2 is a specimen with core-wall thickness of 0.09", and has two bonding layers.

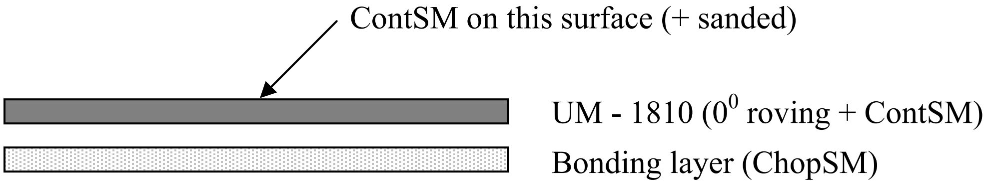

Figure 6.4 Facesheet lay-up of specimens for measuring interface properties.

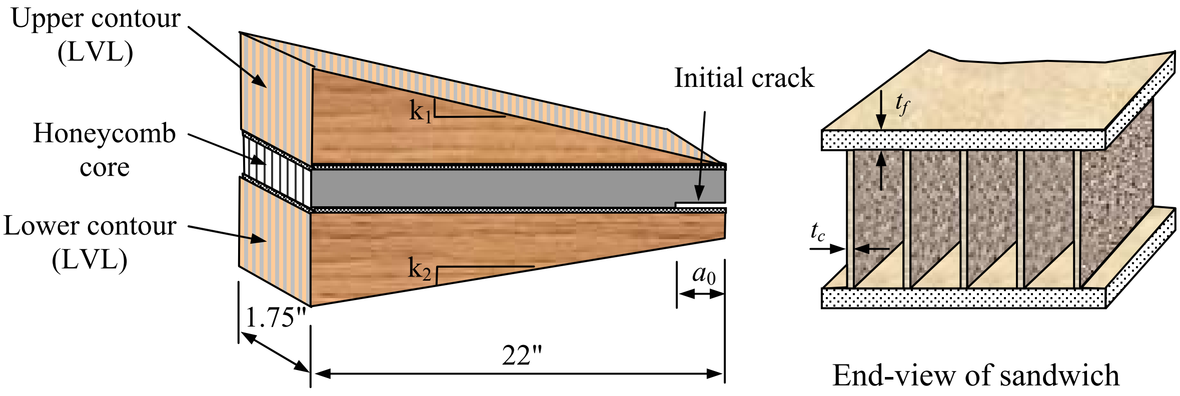

Figure 6.5 Profile of the CDCB specimen.

Compliance Calibrations:

From Equation (6.2), it is evident that the accuracy of measuring the interface fracture toughness G_{cI} is restricted by the precision with which the compliance gradient, *dC/da*, is determined. Therefore, much effort was devoted to investigating this fundamental parameter prior to any fracture test. A systematic experimental compliance calibration program involving six distinct types of specimens aforementioned was sequentially conducted. The main task of performing the compliance calibration test is to design the shapes of the upper and lower wood contours, such that the specimen maintains a symmetric geometry about the crack line located at the interface between the core and the lower facesheet (see Figure 6.5). Instead of elaborating about the specific compliance calibration process of each class of specimen, we present next the design of a representative contour shape and the calibration test for the C1B1 specimen type.

In the initial design of contour shapes, we applied the modified beam theory which was originally developed by Qiao et al. (2003) to predict constant values of tapered DCB specimens involving hybrid interface bonds. In this analytical approach, the uncracked region of the specimen is modeled as a tapered beam on a generalized elastic foundation while taking into account relative translations and rotations of the crack tip. Based on the analytical solutions, the slopes of the upper and lower contours are determined as $k_1 = 0.17$ and $k_2 = 0.16$, respectively. It results in the shape of the specimen as shown in Figure 6.6 with heights of each contour H_1 = 3.74", H_2 = 4.735", and h_0 = 1.215". With such design, the compliance gradient, *dC/da*, remains approximately constant for crack length a = 4" ~ 19" as observed in Figure 6.7.

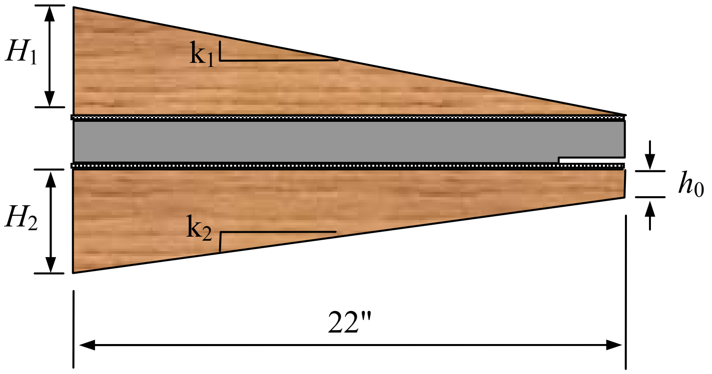

Figure 6.6 Wood contour shapes for the CDCB specimen.

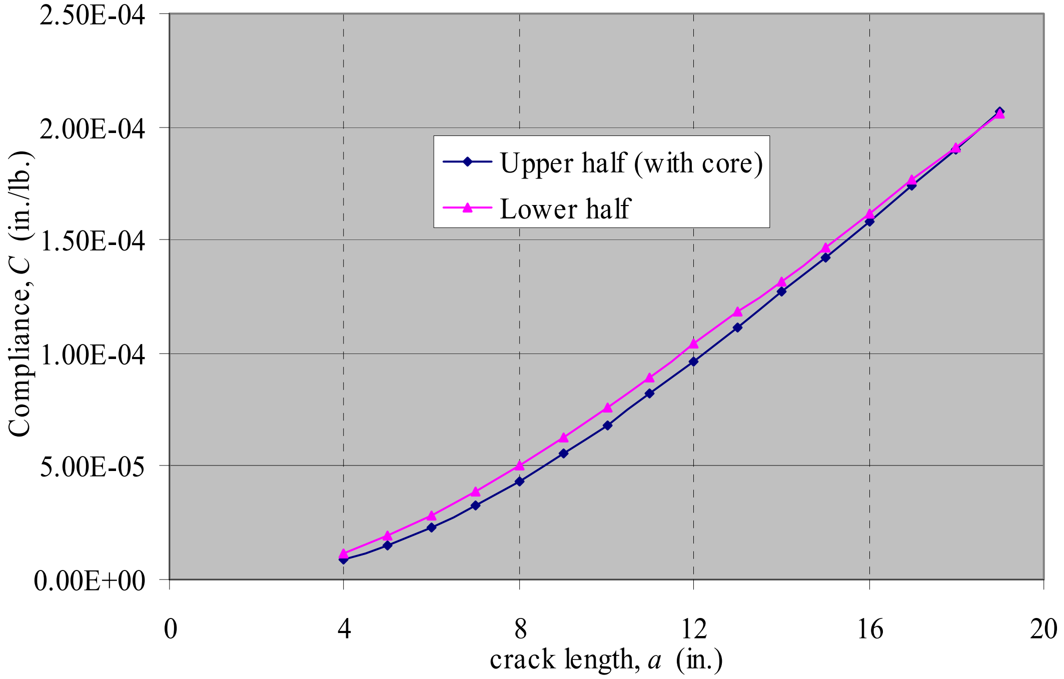

Figure 6.7 Theoretical compliance vs. crack length relationship for C1B1 specimen.

A finite element analysis is also carried out to verify the initial design. A 3D finite element model is created in ABAQUS (Figure 6.8). The properties of the specimen are listed in Table 6.4. Solid elements C3D8 are used for the LVL contours, and shell elements S4 are used for the facesheets and the core. Surface-based tie constraints are used to couple the displacements of the LVL contours, the facesheets, and the core. Node release method is used to simulate the crack propagation along the facesheet-core interface, and a unit tip-load is applied as shown in Figure 6.8. From the analysis, the tip displacement where the load is applied yields the specimen compliance for a given crack length. From a linear regression of the compliance versus crack length plot, we obtained $dC/da = 7.1 \times 10^{-5}$ (lb^{-1}) for crack length a = 4.4" ~ 14.3".

Table 6.4 Properties of LVL, facesheets and core for C1B1 specimens.

Property	LVL	Facesheet	Core
E_{11} (ksi)	1200	1870	1710
$E_{22} = E_{33}$ (ksi)	80	1500	1710
$G_{12} = G_{13} = G_{23}$ (ksi)	65	530	611
$\nu_{12} = \nu_{13} = \nu_{23}$	0.3	0.387	0.4
Thickness (in.)	---	0.12	0.06

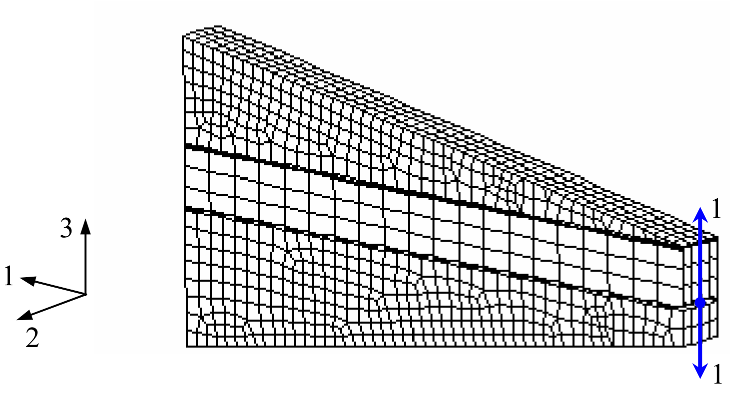

Figure 6.8 Finite element model of the CDCB specimen.

As pointed out by Boyajian (2002), although both analytical and finite element approaches offer a good reference point from which the contour shapes might be arrived at, these methods are based on certain approximations, and thus should not be solely relied upon in the determination of the *dC/da* value. Instead, the parameter *dC/da* should always be determined experimentally through compliance calibrations.

The experimental calibrations were performed on an MTS servo hydraulic testing machine (458.10 MicroConsole/418.91 MicroProfiler) operating under a displacement-control mode with a loading rate of 0.001 in./sec. Load is applied through a pair of steel straps attached to the right end of the specimen (see Figure 6.9). During the calibrations, the applied load and displacement were continuously recorded by the MTS machine. Simultaneously, another pair of load-displacement data was acquired externally, i.e. the load was obtained from the output of a two-kip load cell and the opening displacement at the loading end was measured using a highly sensitive extensometer. The extensometer unit is an MTS model 632.03 clip-on gage which can give accurate readings sensitive to 0.00001". It possesses a double cantilever configuration with slot-grooved free-ended deflecting arms that affix to the specimen through a pair of knife-edges. Two small pieces of wood were bonded to the loading end of the specimen to accommodate these knife-edges (see Figure 6.9b).

For each type of specimen, two calibration tests were conducted. The specimen typically has an initial crack length $a_0 = 4"$. Various crack lengths had to be simulated to determine the compliance versus crack length relationship. These crack lengths were produced by sawing the interface to specified lengths. Nine crack locations in the range of 4" ~ 20" were created, each with crack length advancing by 2" incrementally. By definition, the compliance can be found as the inverse of the ratio of the applied load and its corresponding displacement. Experimentally, this was determined by applying a monotonically increasing load within the linear elastic range (typically up to about 150 lbs.) and collecting corresponding tip displacement data. The collected displacement-load data was then plotted and a best-fit curve, i.e. a straight line in this case, was found using linear regression. The slope of this line is thus the experimental compliance of the specimen corresponding to the current crack position. For each crack length, the procedure just outlined was repeated twice and the final compliance value was found as the average of these two compliance values. As such, nine pairs of data points in terms of compliance versus crack length were obtained from each calibration test. The *dC/da* parameter is then found from the slope of the linear regression performed on these data points. In order to effectively determine the slope of the regressed line, out of the nine data points, only five or six were used to determine the *dC/da* parameter. The decision to omit other data points is mainly due to the ‘hinging action’ as discussed by Boyajian (2002). It arises from a change in the constraint condition as the location of the crack approaches the end of the specimen, resulting in a relaxed fixity condition for the contoured cantilever beam. Thus, it yields a much larger value of compliance than the otherwise expected linear trend. As a matter of fact, the *dC/da* values of the calibrated specimens were computed by restricting the crack length range to the interval from 4" to 14", corresponding to the linear portion of the experimental curve. More importantly, this is also the region in which major cracks were observed to occur during the fracture test performed later.

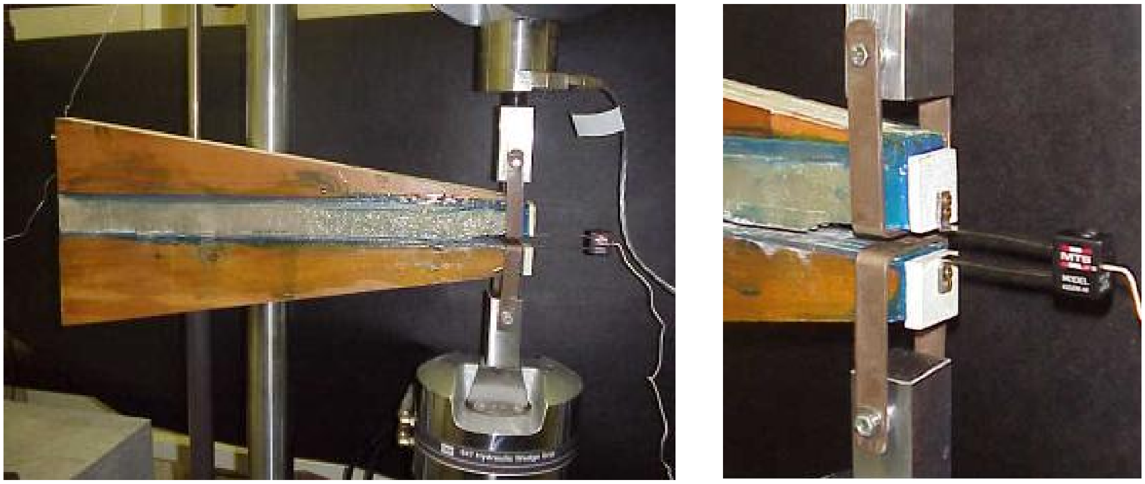

(a) Side-view of the CDCB specimen (b) Details of load straps and clip-on gage

Figure 6.9 Calibration test of the CDCB specimen.

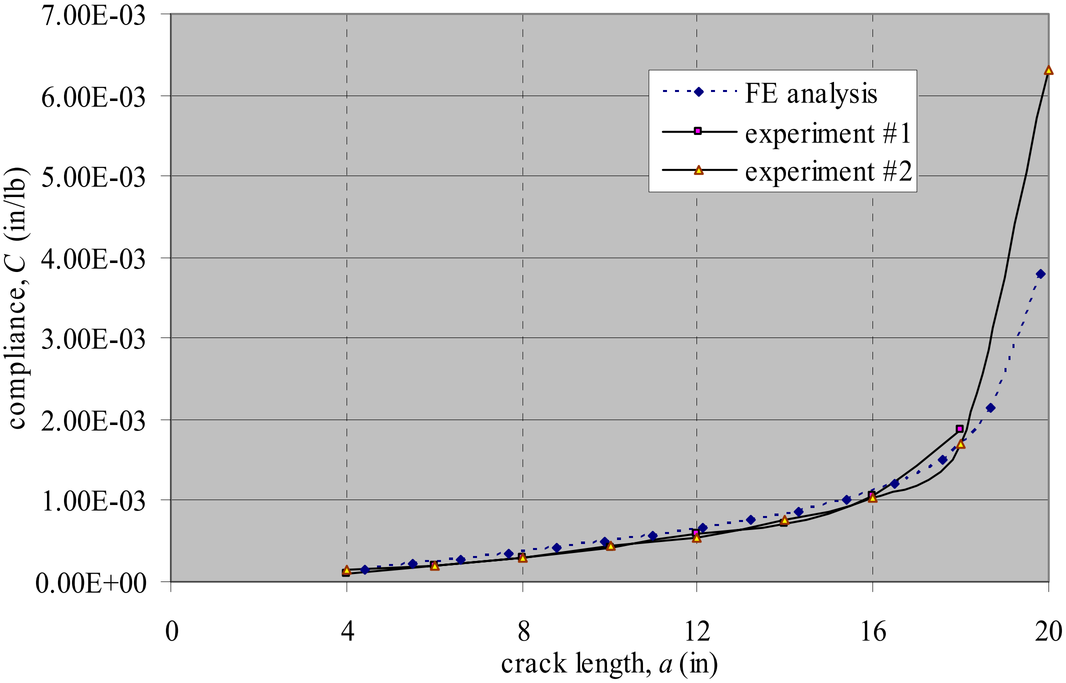

Figure 6.10 Compliance vs. crack length relationship from finite element analysis and calibration tests of the CDCB specimen.

The compliance versus crack length values for C1B1 specimen is shown in Figure 6.10, which agrees very well with the results from finite element analysis. It also clearly shows the ‘hinging action’ effects aforementioned after certain value of crack length is reached. The calibration results for each class of specimen are reported next.

Calibration Results:

Wood contours for each class of specimen are similar in shape, i.e. all have the same width B = 1.75", and height of lower contour H_2 = 4.735", h_0 = 1.215". The differences arise from upper contour height H_1 with different design for each class of specimen. The *dC/da* values from finite element analyses and experimental calibrations are reported together within the crack range 4 - 14" and the corresponding r^2 values. The r^2 value is a statistical measure of the preciseness of the actual data approaching the curve-fitted line in linear regression. Thus, the closer this parameter is with respect to unity, the greater is the degree to which the actual data matches the curve-fitted line. A percentage difference comparison made between the experimental and finite element results is also included. All of these results are summarized in Table 6.5. It is revealed that the finite element analysis can provide a good estimation of the *dC/da* value.

Table 6.5 Compliance calibration results of the CDCB specimens.

Specimen type	H_1 (in.)	dC/da ($\times 10^{-5}$ lb^{-1})		Percentage difference
		Experiment (r^2)	FE (r^2)	
C1B1	3.74	6.97 (0.983)	7.34 (0.993)	- 5.3 %
C1B2	2.86	8.95 (0.983)	8.11 (0.992)	9.4 %
C2B1	2.82	7.11 (0.906)	7.80 (0.993)	- 9.7 %
C2B2	2.82	7.61 (0.935)	7.58 (0.992)	0.4 %
C3B1	2.0	7.18 (0.980)	8.36 (0.990)	- 16.4 %
C3B2	2.0	---	8.44 (0.992)	---

Fracture Tests:

Mode I facesheet-core interface fracture test results, as achieved by use of the CDCB specimens, are presented in this section.

The fracture tests were performed using the same specimens as utilized in the compliance calibration tests. During fracture testing, simultaneous load and crack opening displacements (COD) are recorded at every 0.2 seconds by a data acquisition system, with a loading rate of 0.0003 in./sec. The measured maximum load P_c is substituted into Equation (6.2). With the calibrated value of dC/da, the Mode I fracture toughness, G_{Ic}, could then be obtained for each class of specimen.

As discussed by Boyajian (2002), there are essentially two types of cracking associated with adhesively bonded or jointed structures, namely, stable and unstable cracks. Generally, all structural adhesive systems display a form of elastic behavior prior to crack initiation. At this stage, the crack remains stationary with no measurable inelastic flow until a critical value, G_{Ic}, is reached. Once this critical value is exceeded, differences in cracking behaviors between adhesive systems are evident. For some systems, cracking extends at a nearly constant value of strain energy release rate, so that materials displaying this sort of 'cracking-stability' are classified as being strain rate insensitive. This behavior is generally characterized by a flat plateau in the structural response of load versus displacement curve in the cracking region, as shown in Figure 6.11a. Other material systems display an unstable cracking behavior as shown in Figure 6.11b. The high load at the first peak, also known as the (first) crack-initiation load, typically corresponds to the critical load, P_c, which is used in computing the fracture toughness value of Equation (6.2). Once the crack initiates, the required force to advance the crack decreases, thus resulting in the saw-toothed appearance of Figure 6.11b. The crack is only reinitiated when the load level once again reaches a critical initiation value, P_c.

The ideal adhesive bonding is the one requiring high crack initiation energy and producing stable crack growth. However, in reality, fracturing often occurs as a combination of unstable and stable crack growth. In the facesheet-core interface fracturing tests, a typical plot of the relationship of the measured load versus COD is shown in Figure 6.12. Initially, there is a linear elastic region prior to the onset of cracking. Following this, are a series of regions in which cracking initiates and arrests. At last, testing is terminated in an abrupt manner with the complete fracturing of the interface, as described by a sudden drop in load. Unstable crack growth is mainly due to various defects in fabricating of the specimens, such as a non-uniform bonding layer, as observed in Figure 6.13 showing the specimen after tested.

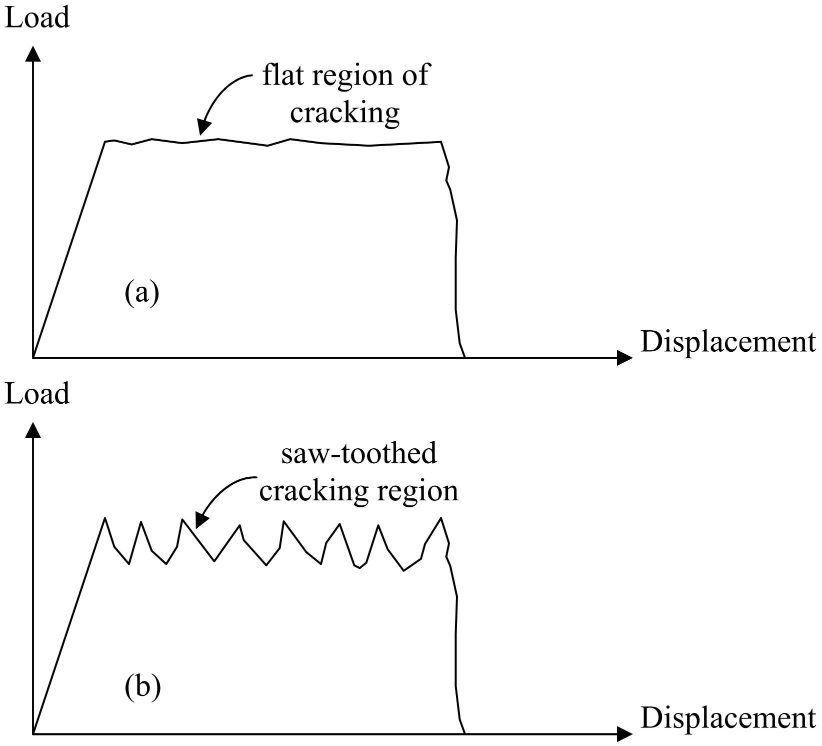

Figure 6.11 Schematic load vs. displacement curves of (a) a rate insensitive material with a flat region of cracking indicating stable cracking and (b) a rate sensitive material with a region of saw-toothed cracking indicating unstable cracking (Boyajian, p. 114, 2002).

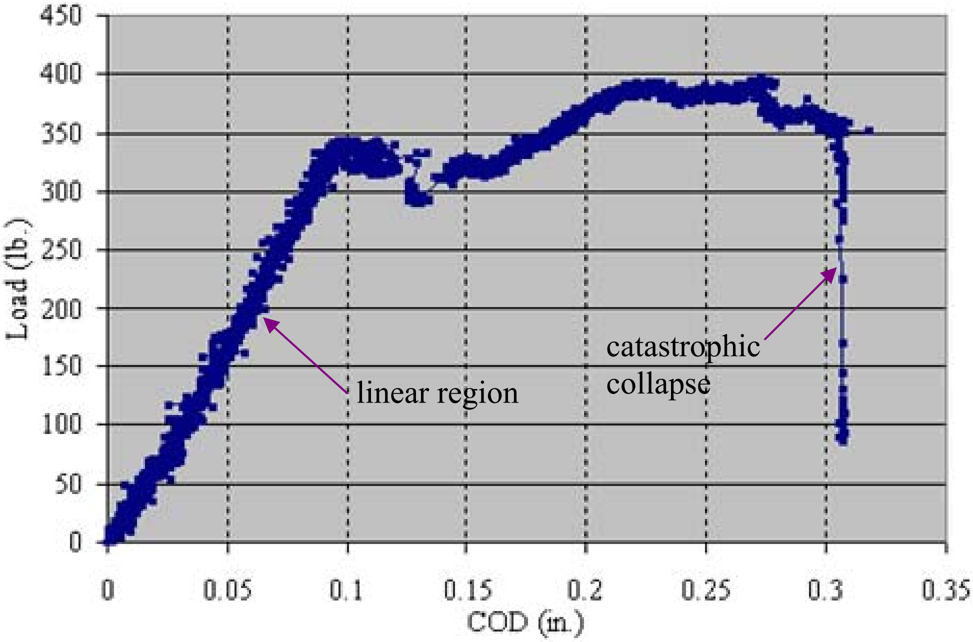

Figure 6.12 Typical fracturing behavior of facesheet-core interface.

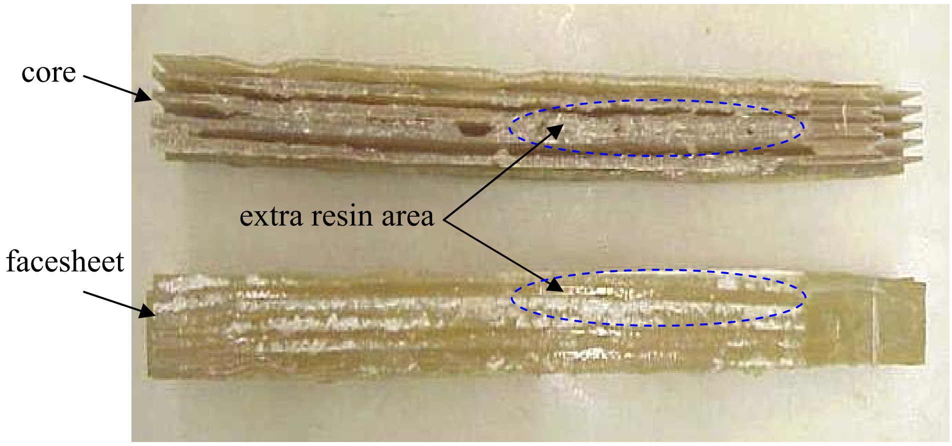

Figure 6.13 Fractured facesheet-core interface after test.

The relationship of load versus COD from the fracturing tests of facesheet-core interface for each class of specimen is shown in Figure 6.14. Three to five samples were tested in each class of specimen, from which the critical load, P_c, is determined as the average of the maximum loads attained in every sample. The Mode I fracture toughness, $G_{\mathrm{I}c}$, is then obtained by substituting the critical load and the calibrated value of dC/da into Equation (6.2). It is noteworthy that when applying Equation (6.2), the width b should be the total thickness of the core panels across the width of the specimen. All of these results are summarized in Table 6.6. Obviously, more tests are needed before a definite conclusion can be drawn from the current experimental data. However, some preliminary observations can be made regarding the effects of facesheet bonding layers and core-wall thickness: (1) adding bonding layers can significantly increase the interface fracture toughness ($G_{\mathrm{I}c}$ of C1B2 is two times larger than that of C1B1); (2) increasing core-wall thickness cannot achieve a pronounced improvement of the interface fracture toughness.

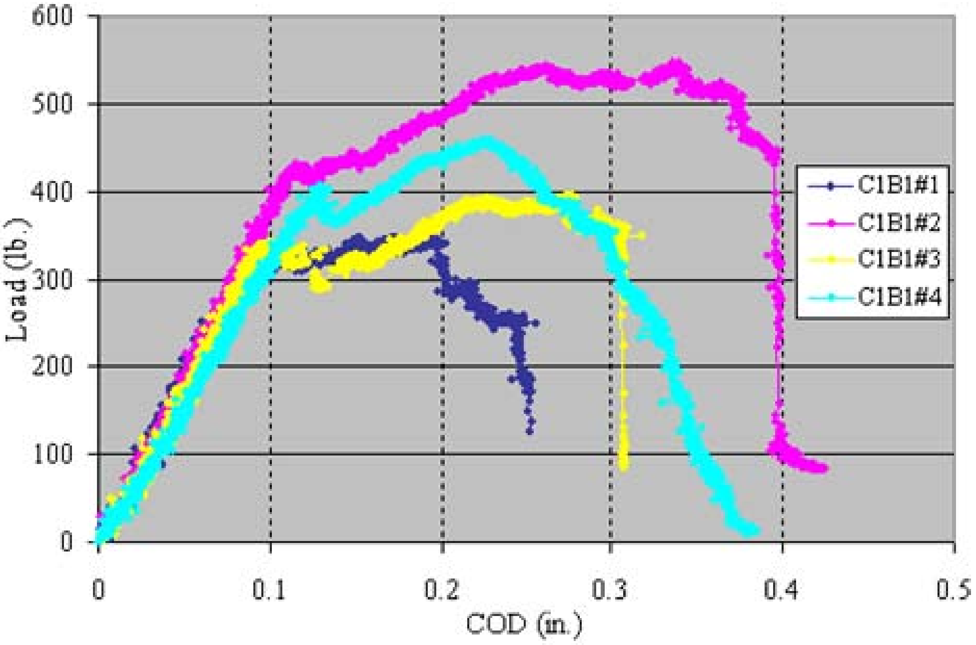
Load (lb.)
COD (in.)
0
100
200
300
400
500
600
0.1
0.2
0.3
0.4
0.5
C1B1#1
C1B1#2
C1B1#3
C1B1#4

(a)

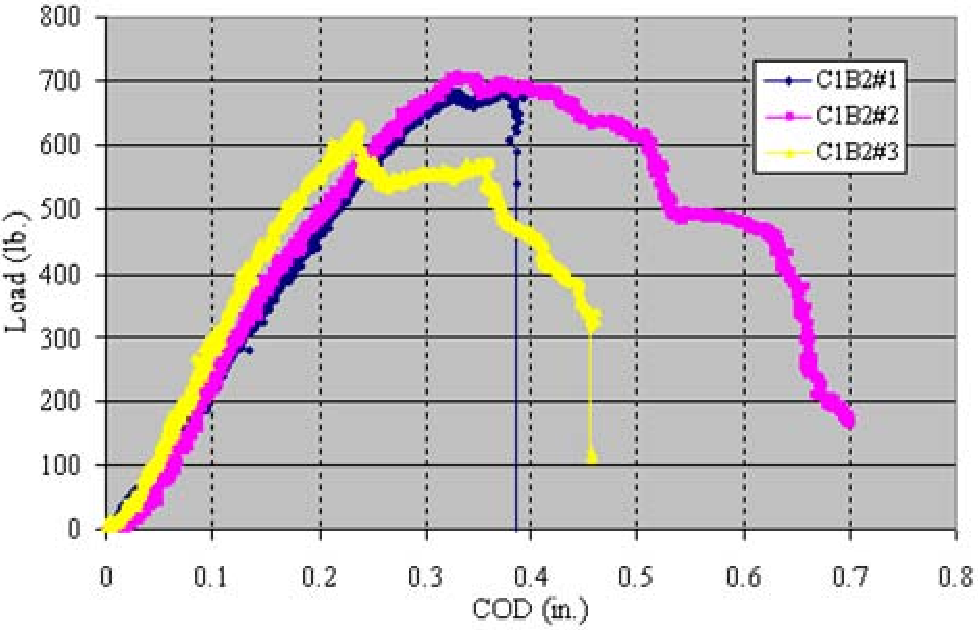
Load (lb.)
COD (in.)
0
100
200
300
400
500
600
700
800
0.1
0.2
0.3
0.4
0.5
0.6
0.7
0.8
C1B2#1
C1B2#2
C1B2#3

(b)

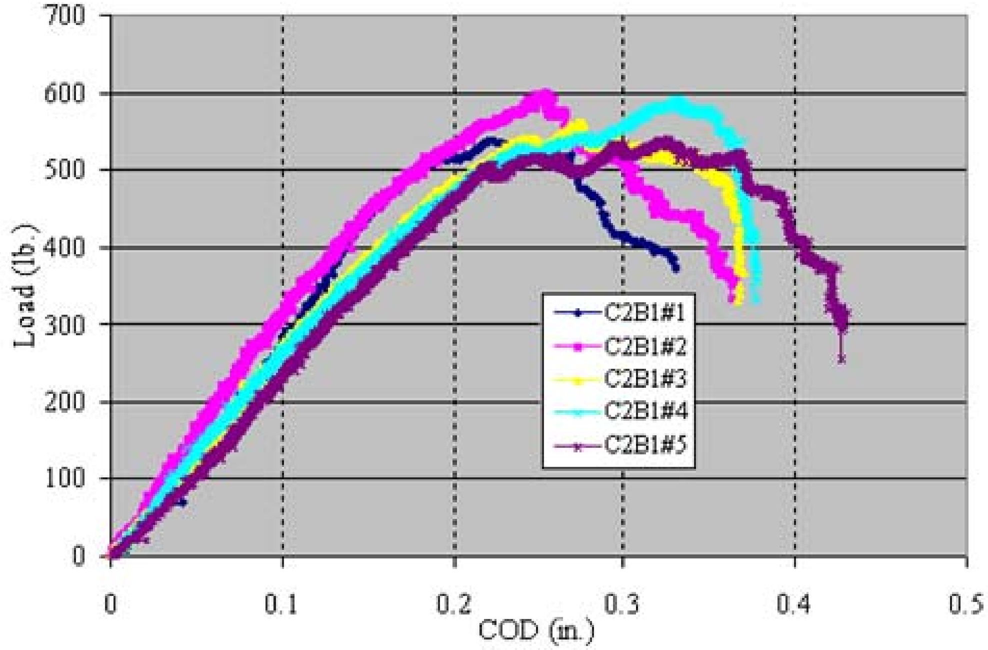
700
600
500
400
300
200
100
0
Load (lb.)
0
0.1
0.2
0.3
0.4
0.5
COD (in.)
C2B1#1
C2B1#2
C2B1#3
C2B1#4
C2B1#5

(c)

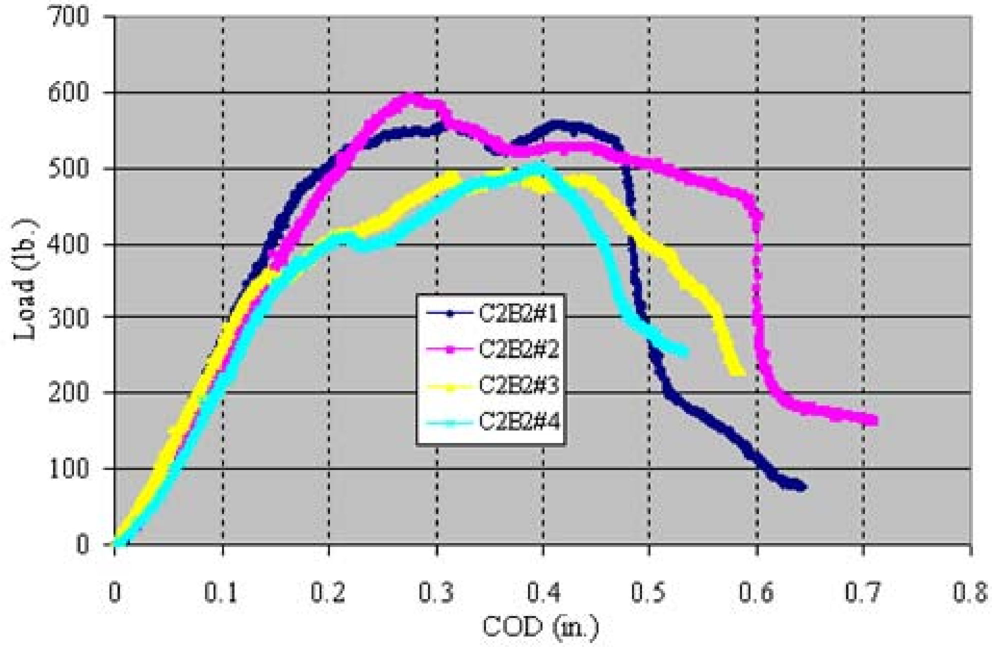
700
600
500
400
300
200
100
0
Load (lb.)
0
0.1
0.2
0.3
0.4
0.5
0.6
0.7
0.8
COD (in.)
C2B2#1
C2B2#2
C2B2#3
C2B2#4

(d)

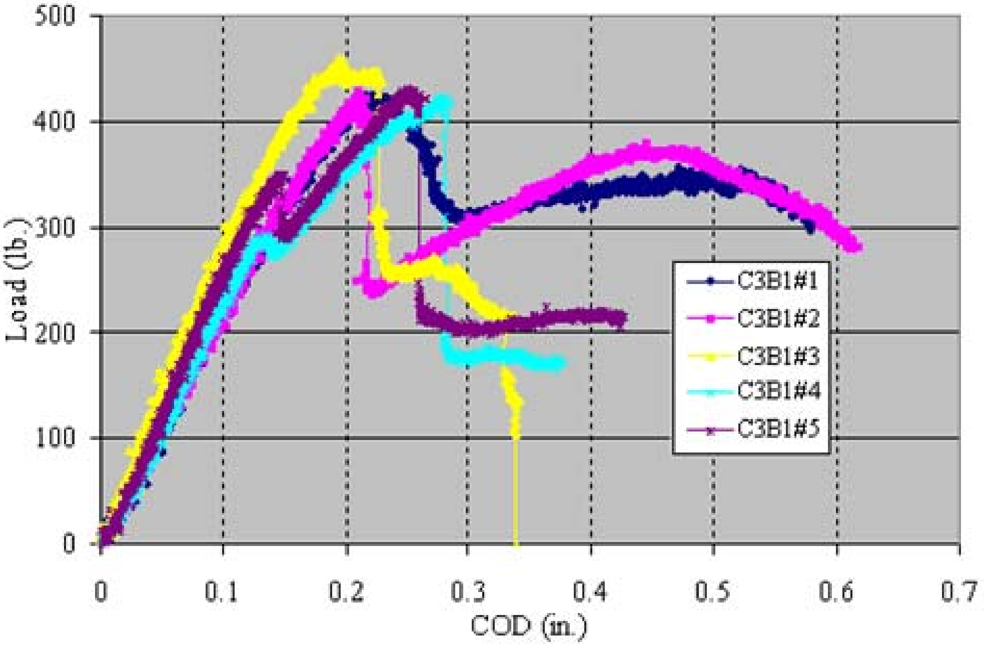

(e)

Figure 6.14 The relationship of load vs. COD from fracturing tests of facesheet-core interface for specimen types (a) C1B1, (b) C1B2, (c) C2B1, (d) C2B2, and (e) C3B1.

Table 6.6 Mode I facesheet-core interface fracture toughness values.

Specimen type	b (in.)	dC/da ($\times 10^{-5}$ lb^{-1})	P_c (lb.)	G_{Ic} (lb./in.)
C1B1	0.36	6.97	438.0	18.6
C1B2	0.36	8.95	675.8	56.8
C2B1	0.45	7.11	565.6	25.3
C2B2	0.45	7.61	537.1	24.4
C3B1	0.6	7.18	432.8	11.2

6.1.3 Interfacial Strength

Before applying the developed CZM, another interfacial property need to be evaluated, i.e. the interfacial strength, including interfacial tensile strength and interfacial shear strength. Testing methods and results are presented in this section.

The Flatwise Tension (FWT) test (ASTM C 297-94, 1999) is often adopted to measure interfacial tensile strength for honeycomb sandwich structures with main applications in aerospace and automotive industries. For the newly developed sinusoidal core HFRP sandwich panels, this standard test has to be modified for actual application. The dimensions of the specimen is 4" × 4" (width × length) with an RVE of honeycomb core as shown in Figure 6.2. Two steel plates with dimensions of 6" × 8" × 0.25" (width × length × thickness) are bonded to the facesheets for applying loading (see Figure 6.15a). The specimen was tested on the MTS machine with a loading rate of 0.001 in./sec. (see Figure 6.15b). Fracture occurred only on one side due to the fabrication process of the material (see Figure 6.15c). Typical response of the FWT test is depicted in Figure 6.16 which describes an almost linear elastic behavior followed by a sudden failure with the facesheet-core interface fully debonded. The interfacial tensile strength is calculated as

$$\sigma_c = \frac{T_c}{A} \tag{6.3}$$

where T_c is the critical load, A is the area of the core considering the actual core-wall thickness. As in the fracture tests, three to five samples were tested for each type of specimen, from which the critical load, T_c, is determined as the average of the maximum loads attained in every sample. The test results are summarized in Table 6.7.

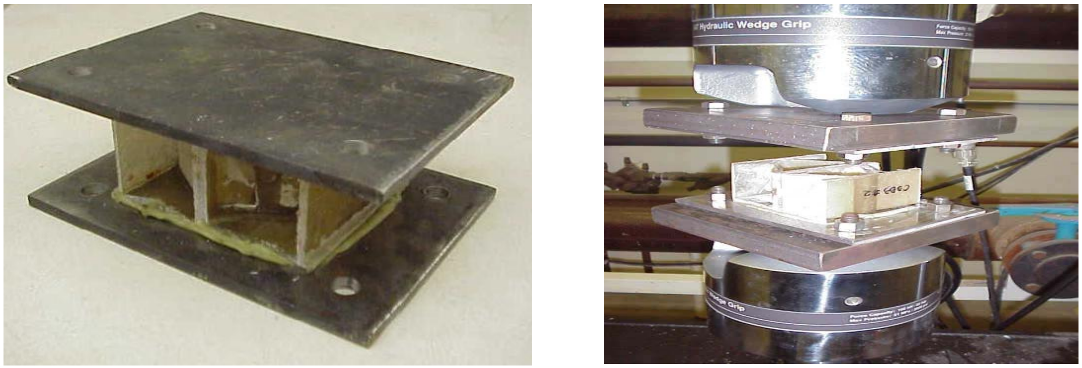

(a) before test (b) during test

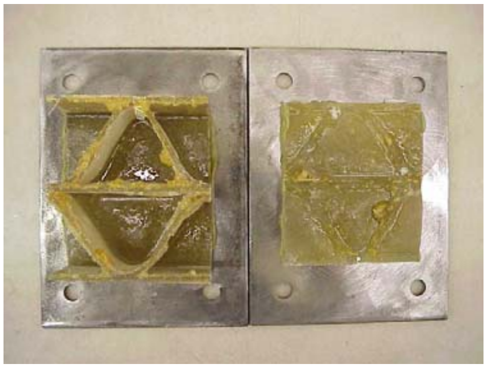

(c) after test

Figure 6.15 FWT test of the HFRP sandwich specimen with an RVE of honeycomb core.

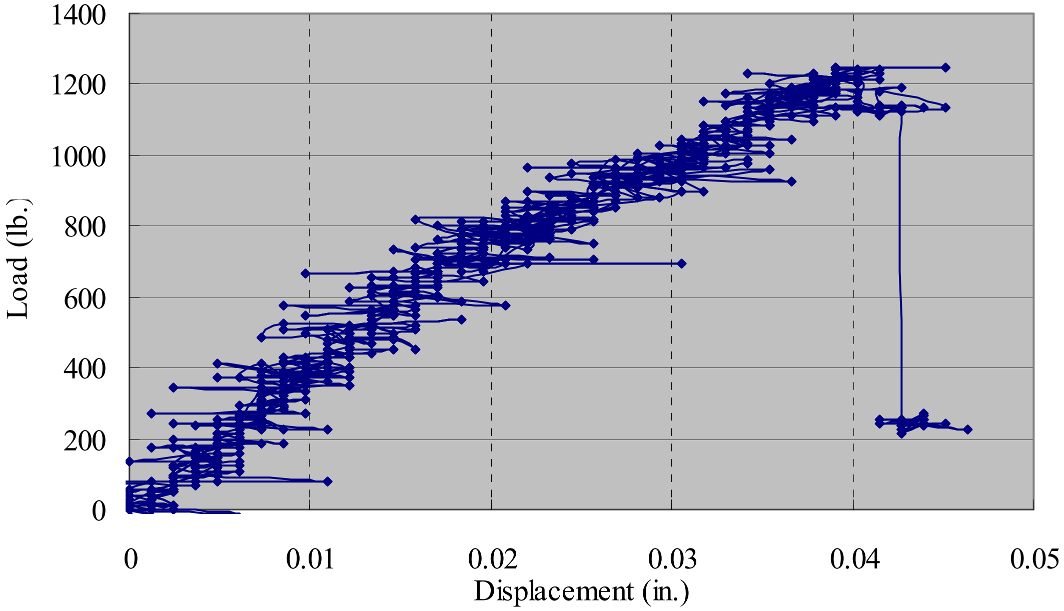

Figure 6.16 Typical response of the FWT test.

There is no standard test for measuring interfacial shear strength. The testing configuration as shown in Figure 6.17 is used in this study. It consists of two rectangular steel plates and two L-shape steel plates with the geometries and dimensions schematically shown in the figure. The sandwich specimen consists of evenly spaced vertical panels as used in the fracture tests. An initial notch was created to induce desirable cracking in the facesheet-core interface. LORD 7542A/B urethane adhesive was used to bond the specimen to the rectangular steel plates. The specimen was tested on the MTS machine with a loading rate of 0.001 in./sec. (see Figure 6.18a). Due to bending effects, a pure shear fracture couldn't be achieved. For most tests, the fracture propagated into the facesheet. Only two tests were performed successfully and the desirable fracture type was obtained as shown in Figure 6.18b. As with the FWT test, the measured critical load is substituted into Equation (6.3) to determine the interfacial shear strength. The test results are summarized in Table 6.8.

Table 6.7 Facesheet-core interfacial tensile strength.

Specimen type	A (in.^{2})	T_c (lb.)	σ_{c3} (psi)
^{1}C1B2	1.44	964	670
C1B3	1.423	1217	855
C2B1	2.134	1937	908
C2B2	2.134	1524	714
C2B3	2.134	1790	839
^{1}C3B2	2.40	1405	585

Note: ^{1} parallel core used.

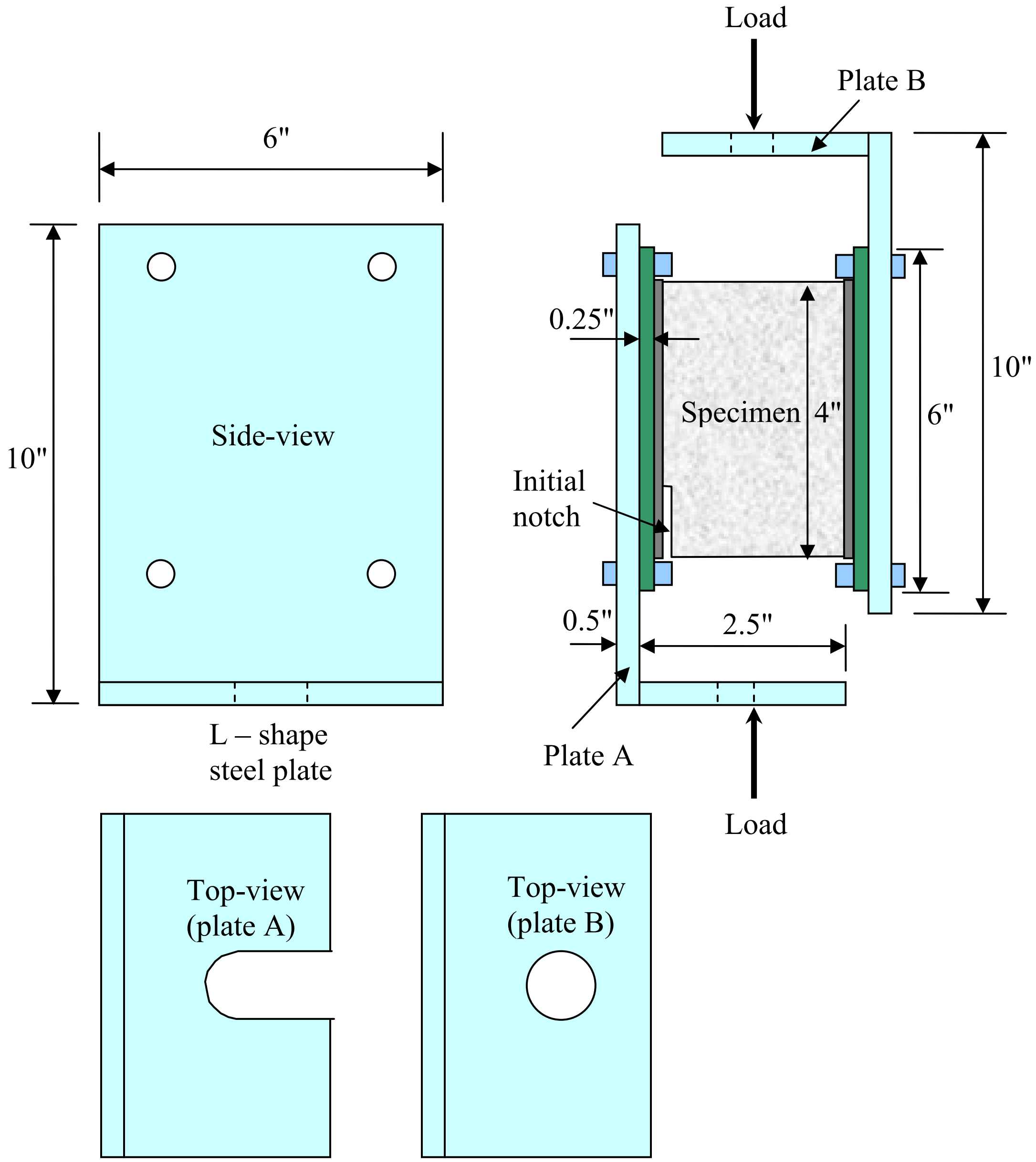

Figure 6.17 Testing configuration for measuring the interfacial shear strength.

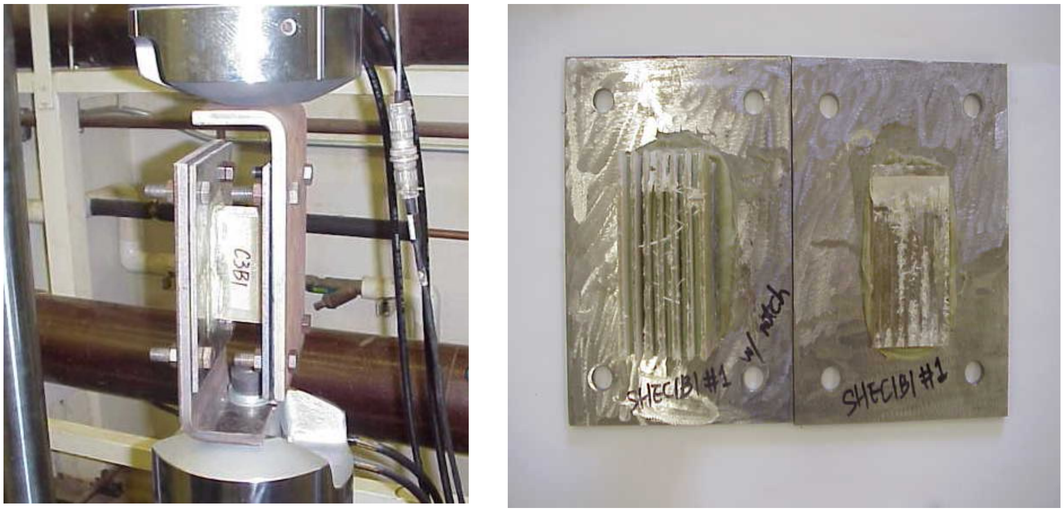

(a) during test (b) after test

Figure 6.18 Testing configuration for measuring interfacial shear strength.

Table 6.8 Facesheet-core interfacial shear strength.

Specimen type	A (in.^{2})	T_c (lb.)	$\sigma_{c1} = \sigma_{c2}$ (psi)
C1B1	1.26	2207	1752

In spite of the limited experimental data, from Table 6.7, it can be concluded that when facesheet bonding layers and core-wall thickness are varied, there is no drastic change of the interfacial tensile strength which falls in the range of 400 psi ~ 1000 psi. On the other hand, although more shear tests of specimens with stronger facesheets should be performed, it is expected that similar to the FWT tests, the interfacial shear strength value of 1752 psi for C1B1 can give a good estimation of the overall interfacial shear strength. As a matter of fact, it will be demonstrated in the subsequent section that the response of the HFRP sandwich panel involving facesheet-core interface delamination propagation is mainly controlled by the interface fracture toughness, while the interfacial strength has a relatively small effect. As such, the interfacial strength value need not be measured precisely.

6.2 Simulation of the CDCB Specimen Using CZM

In this section, simulation of the CDCB specimen used in the fracture test is attempted with the above measured interfacial properties. The test specimen C1B1#1 is simulated here as a representative example.

Basically, the finite element model is similar to that used to simulate the compliance calibrations (see Figure 6.8). The same geometries and material properties as listed in Table 6.4 are used. The only difference is related to the facesheet-core interface modeling. The core is modeled with shell elements except that near the interface along which the delamination is expected to propagate, solid elements are used. Shell-to-solid transition in the core is implemented using multi-point constraint **MPC SS Linear* available in ABAQUS. The developed cohesive interface elements formulated with the mixed-mode linear-exponential constitutive law are then inserted between facesheet shell elements and core solid elements to simulate the progressive material damage occurring in the interface during delamination propagation. The finite element model is shown in Figure 6.19 in the deformed configuration. It consists of 2984 solid elements, 2024 shell elements, and 216 interface elements.

The peak load in the test C1B1#1 was 340.0 lbs, hence Mode I fracture toughness is obtained as $G_{c\mathrm{I}}$ = 11.2 lb./in. Without the actual experimental data of fracture toughness for Mode II and Mode III, it is assumed that $G_{c\mathrm{II}} = G_{c\mathrm{III}} = 3\ G_{c\mathrm{I}}$. Since the fracture is Mode I dominant, this assumption is relatively reasonable and would not considerably influence the results. The interfacial properties for the specimen are listed in Table 6.9.

Table 6.9 Fracture toughness and interfacial strength for the C1B1 specimen.

$G_{c\mathrm{I}}$	$G_{c\mathrm{II}} = G_{c\mathrm{III}}$	σ_{c3}	$\sigma_{c1} = \sigma_{c2}$
11.2 lb/in.	33.6 lb/in.	400 psi	1750 psi

The results from the finite element simulation using interface elements are compared to the experimental data of the CDCB specimen. The load versus COD relationships at the loaded end is shown in Figure 6.20. It can be seen that excellent correlations are obtained. Nonetheless, appropriate stiffness, K_c, for the interface element under compression should be used to avoid interfacial penetration. It is shown in the figure that when K_c is equal to ten times the tension stiffness of the interface element, i.e. compression multiplier (cm) = 10, the postcracking response of the specimen could be accurately captured. Mesh convergence study is also performed with four times finer mesh size near the interface. Almost the same results yields which shows the advantage of using the CZM.

Results of analyses with different interfacial tensile strength σ_{c3} are compared in Figure 6.21. The load versus COD relationships are plotted for σ_{c3} = 400 psi and σ_{c3} = 800 psi, while $G_{c\mathrm{I}}$ = 11.2 lb./in. It is observed that the main difference between the two cases is the delamination initiation load, but the influence of changing σ_{c3} is relatively small, since the delamination load was increased by only 10% when σ_{c3} was increased by 100% from 400 psi to 800 psi, while $G_{c\mathrm{I}}$ was kept constant. So, we can conclude that delamination propagation is not sensitive to σ_{c3} when $G_{c\mathrm{I}}$ remains constant. Likewise, analyses with different values of $G_{c\mathrm{I}}$ while σ_{c3} is kept constant are depicted in Figure 6.22. It can be seen that $G_{c\mathrm{I}}$ is a very sensitive parameter since 100% increase in $G_{c\mathrm{I}}$ induced 34% increase in the delamination load, which is a significant change compared with the effect of changing σ_{c3}. These results suggest that the fracture mechanics-based approach is more appropriate for the study of interface delamination propagation of HFRP sandwich panels as opposed to a strength-based approach (Wang and Davalos, 2003).

Mode-mixity in the CDCB specimen is investigated regarding the validity of measuring Mode I fracture toughness with the specimen. Variation and percentage difference of energy release rate in Mode I and Mode II as the delamination propagates are shown in Figure 6.23. It is evident that the delamination process is truly Mode I dominant with Mode II contribution less than 8% within the measuring crack range.

In Figure 6.24, contours of maximum principal stresses as the delamination propagates are plotted. It clearly shows the evolution of the fracture process zone where highest stresses are present in the red region of the figure. There is no distinguishable crack front in the facesheet-core interface since fracture occurs in the whole process zone in various forms, e.g. fiber bridging.

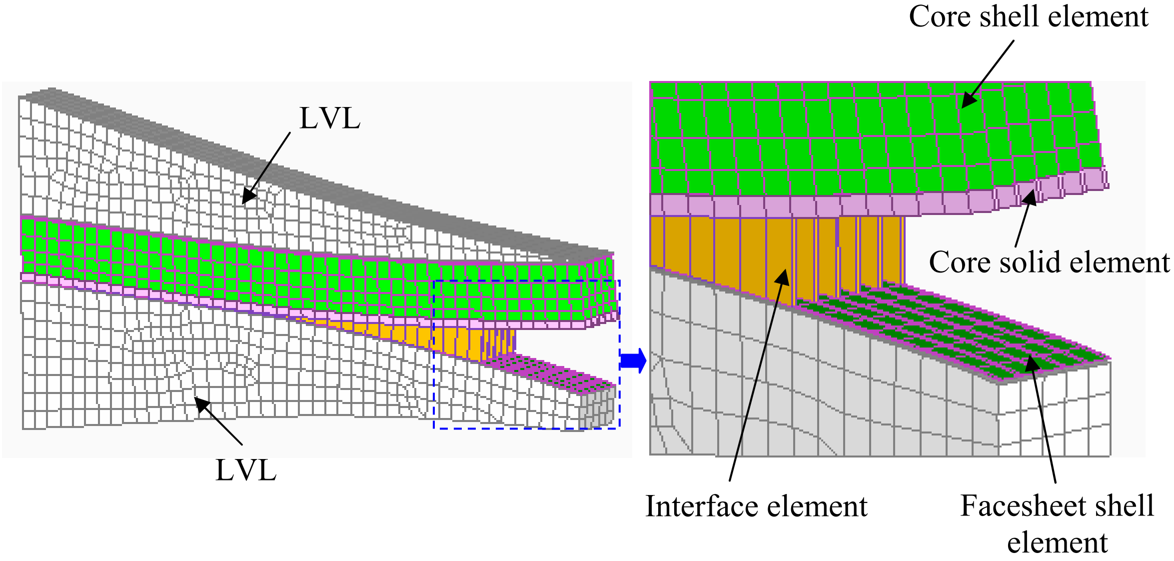

Figure 6.19 Finite element simulation of the CDCB specimen.

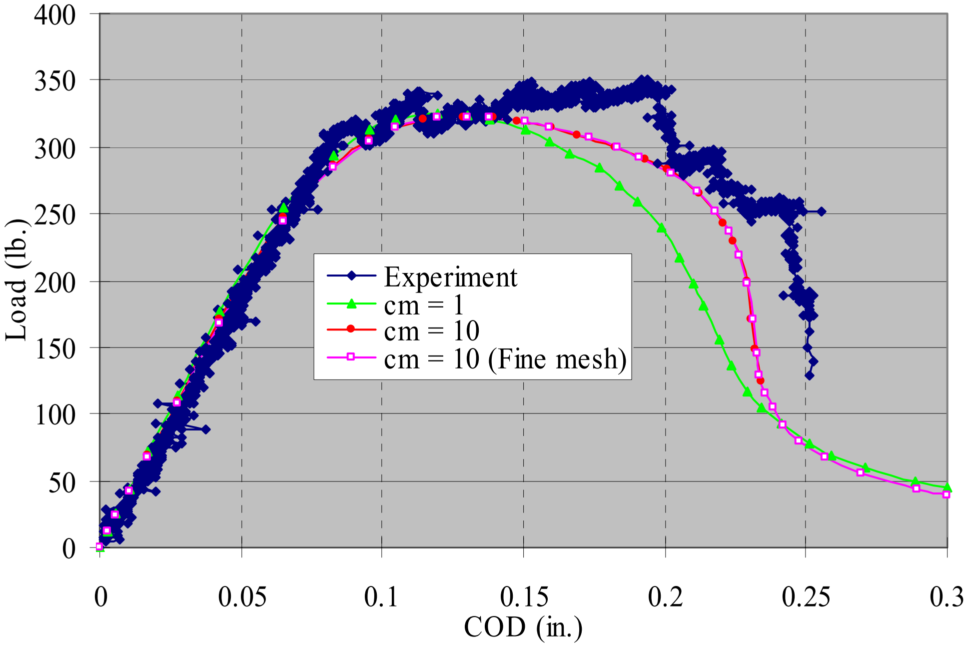

Figure 6.20 Results of COD vs. load relationship from finite element simulation compared to experimental data of the CDCB specimen.

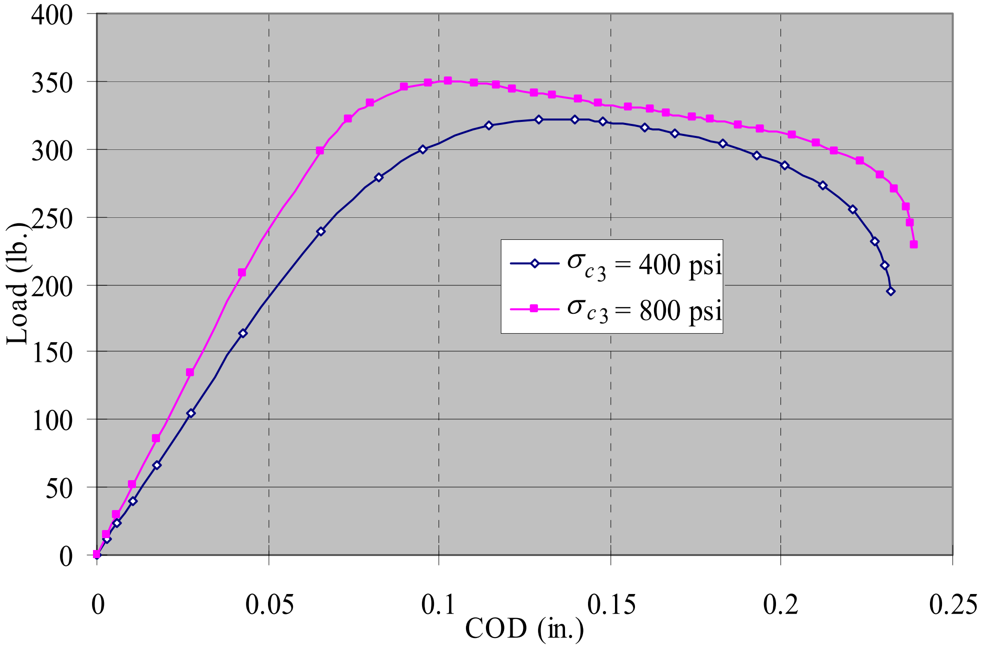

Figure 6.21 Sensitivity to interfacial strength (G_{cI} = 11.2 lb./in.).

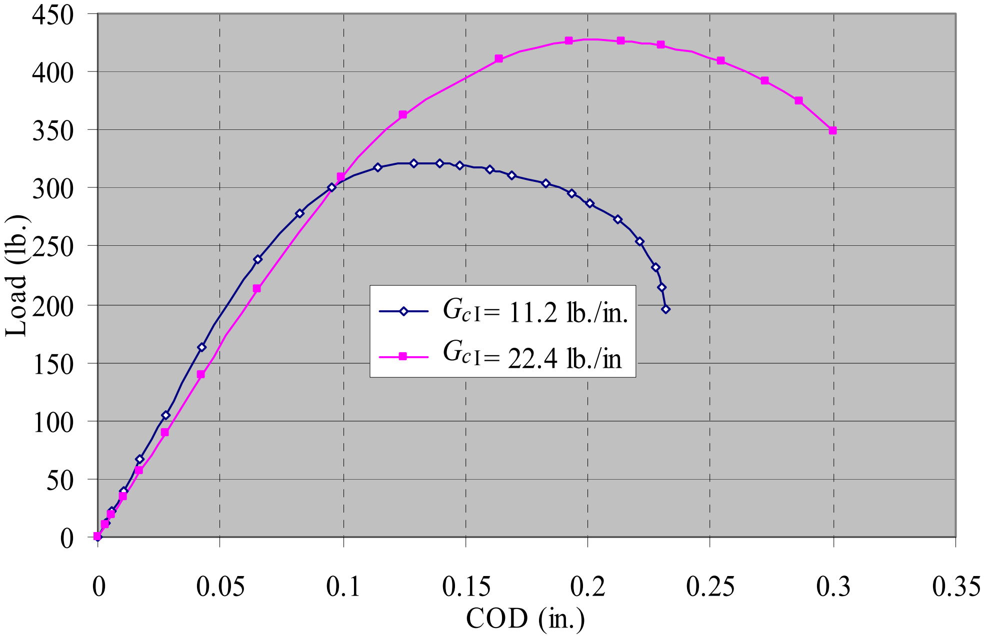

Figure 6.22 Sensitivity to fracture toughness (σ_{c3} = 400 psi).

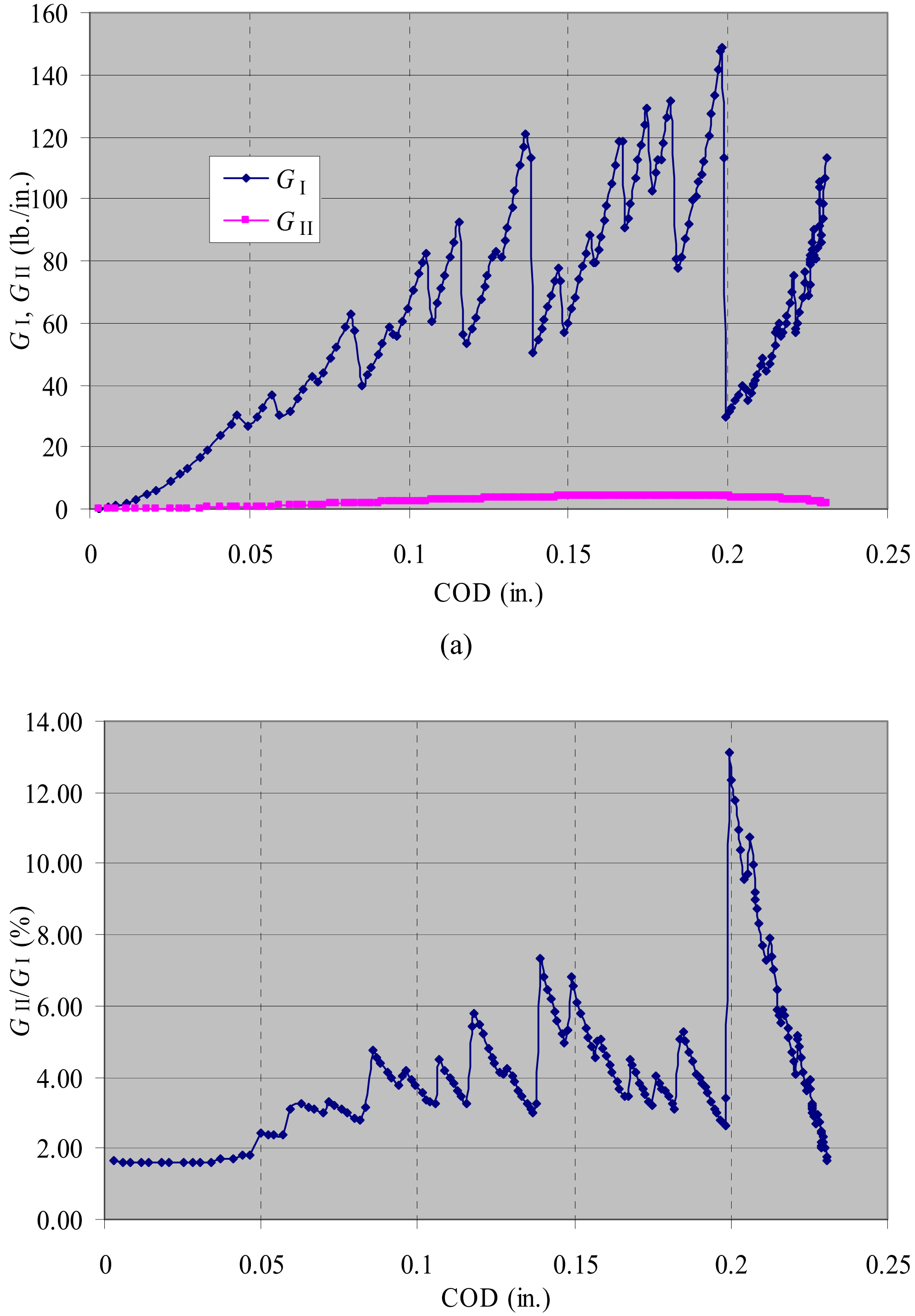

(a)

(b)

Figure 6.23 Mode-mixity in the CDCB specimen: (a) variation and (b) percentage difference of energy release rate in Mode I and Mode II as the delamination propagates.

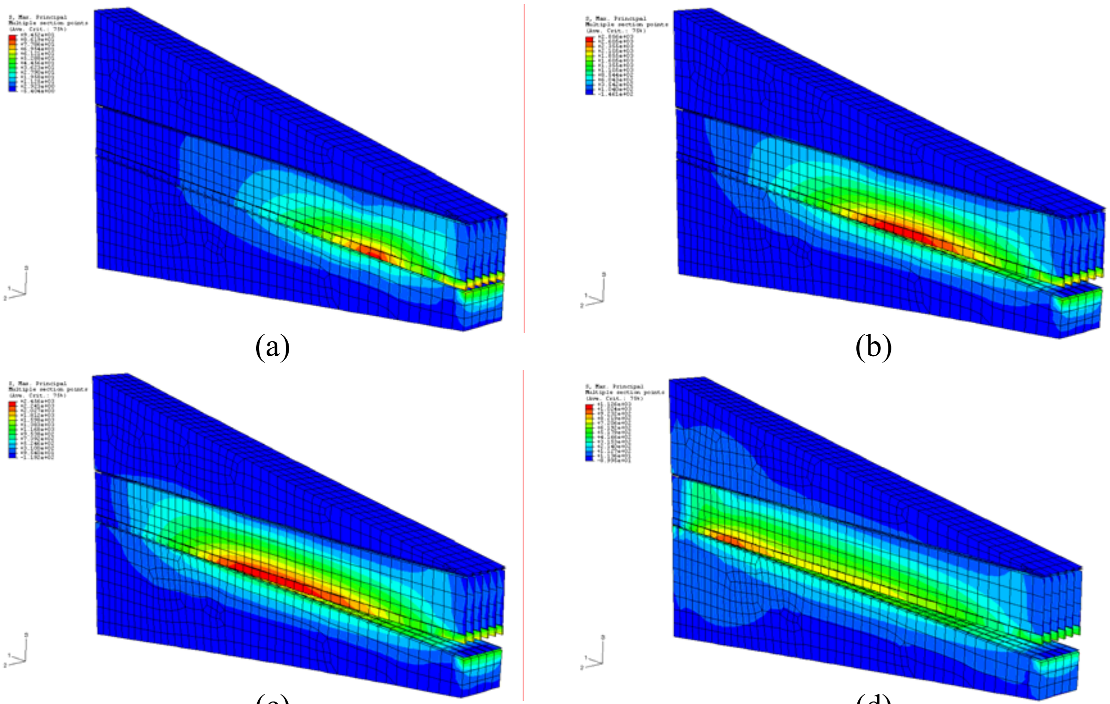

(a) (b)

(c) (d)

Figure 6.24 Contours of maximum principal stresses as the delamination propagates.

6.3 Peeling Delamination Test of HFRP Sandwich Panel

A peeling delamination test of an HFRP sandwich panel was conducted to verify the predictive capability of the developed CZM to simulate the facesheet-core interface delamination propagation in HFRP sandwich panels with actual sinusoidal wave core configuration. A longitudinal HFRP sandwich panel including only one core cell in the transverse direction was attached to a steel plate and loaded under tension at one end through a piano hinge as shown in Figure 6.25a. The specimen has dimensions of 28" × 4.5" × 5" (length × width × height), while the top facesheet has an additional length of 2" to accommodate the piano hinge. The sinusoidal wave core has a configuration of RVE as shown in Figure 6.2 with h = 1", l = 4", and core-wall thickness = 0.09". The facesheet lay-up is shown in Figure 6.3 and layer properties are listed in Tables 6.2 and 6.3. An initial interfacial delamination with length of 7.5" was sawed to induce progressive delamination in the interface. The disbonded length was long enough to avoid undesirable damage within the facesheet. Open holes were drilled in the outside flat panels of the core in order to bolt the bottom facesheet to the steel plate. The specimen was tested on the MTS machine with a loading rate of 0.0003 in./sec. Upon loading, the initial delamination propagated slowly through the facesheet-core interface until peeling of the entire top facesheet occurred, leaving a cleanly delaminated interface as shown in Figure 6.25b.

Finite element modeling of the peeling delamination test is performed applying the developed CZM with the mixed-mode linear-exponential constitutive law. The interfacial properties used in the finite element simulation are listed in Table 6.10; these values are based on the former experimental measurements. Due to lack of experimental data for fracture toughness of Mode II and Mode III, it is assumed that $G_{c\mathrm{II}} = G_{c\mathrm{III}} = 3\ G_{c\mathrm{I}}$.

Table 6.10 Fracture toughness and interfacial strength for the peeling delamination test.

$G_{c\mathrm{I}}$	$G_{c\mathrm{II}} = G_{c\mathrm{III}}$	σ_{c3}	$\sigma_{c1} = \sigma_{c2}$
24.4 lb/in.	73.2 lb/in.	700 psi	1800 psi

A 3D finite element model is created with ABAQUS. The facesheets are modeled with shell elements, and the core is modeled entirely with solid elements using finer mesh near the interface of the top facesheet and the core. The developed cohesive interface elements are embedded between the top facesheet shell elements and core solid elements to model the material degradation within the interface during delamination propagation.

The bottom facesheet is fixed and directly connected to the core without embedding interface elements since delamination didn’t occur in this interface. Open holes in the flat panels of the core are not considered because their influences on the overall structural response are expected to be negligible. The finite element model is shown in Figure 6.26 in the deformed state. It consists of 3024 solid elements, 3364 shell elements, and 372 interface elements.

In Figure 6.27, the finite element results of COD versus applied load are compared to experimental data of the peeling delamination test. Evidently, the delamination initiation load is accurately predicted. In the region of delamination propagation, the experimental curve displays a combination of stable and unstable delamination growth due to the non-uniform bonding layer as observed in Figure 6.25b showing the specimen after being tested. Nonetheless, the global response of the specimen in this region is captured with a reasonable accuracy.

Mode-mixity in this test is evaluated as shown in Figure 6.28. Against the initial speculation, Mode II influence is negligible compared to that of Mode I with only 0.27% contribution at most. Thus, the peeling delamination in this test is basically in pure Mode I and fracture toughness values of Mode II and Mode III need not to be specified exactly.

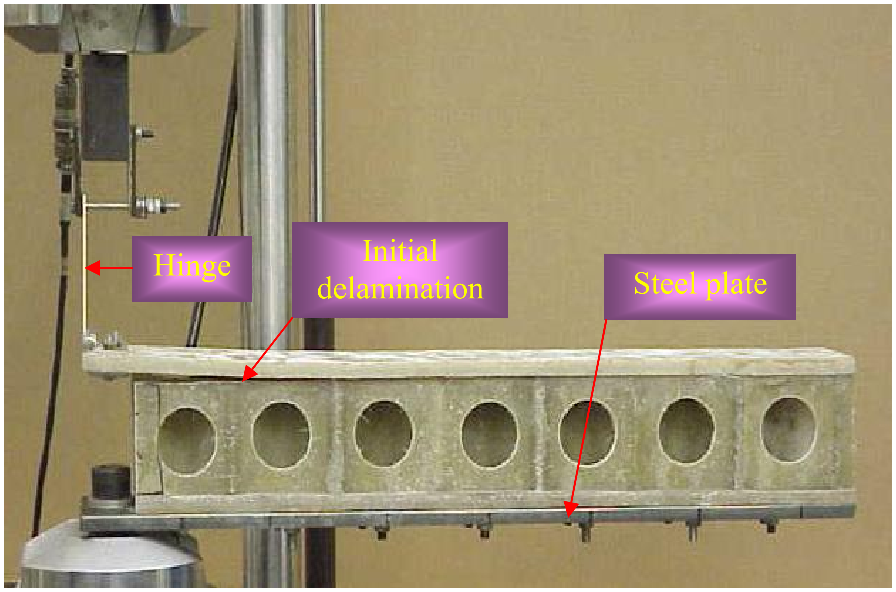

(a) experimental set-up.

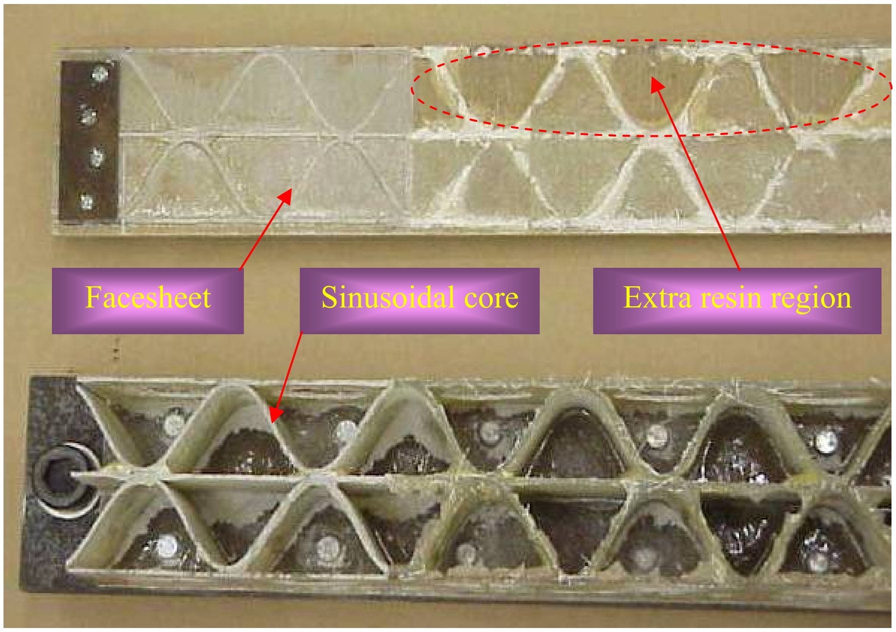

(b) detached interface after test.

Figure 6.25 Peeling delamination test of an HFRP sandwich panel with sinusoidal core wave configuration: (a) experimental set-up; (b) detached interface after test.

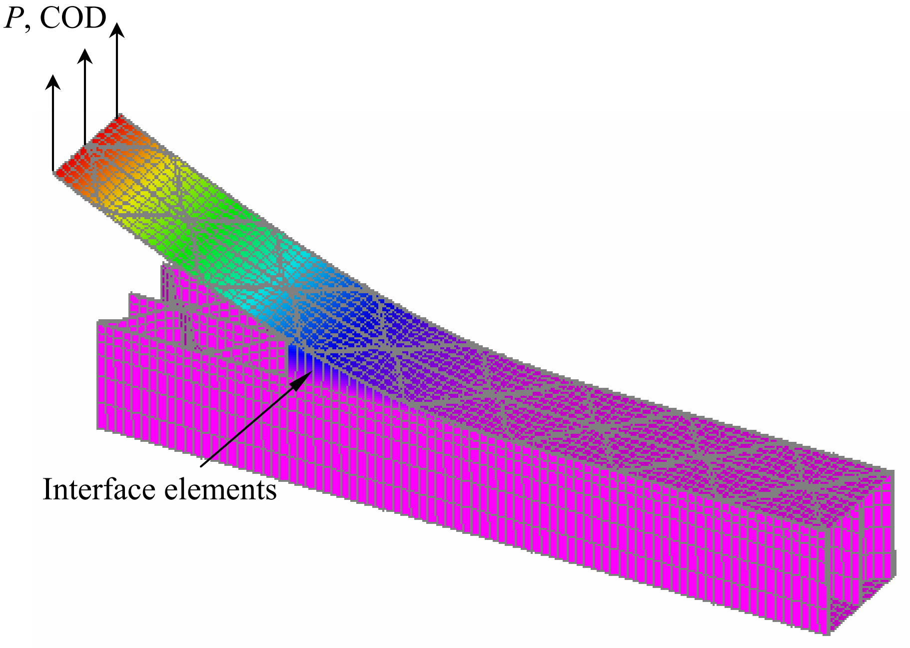

Figure 6.26 Finite element model of the peeling delamination test of an HFRP sandwich panel with sinusoidal wave core configuration.

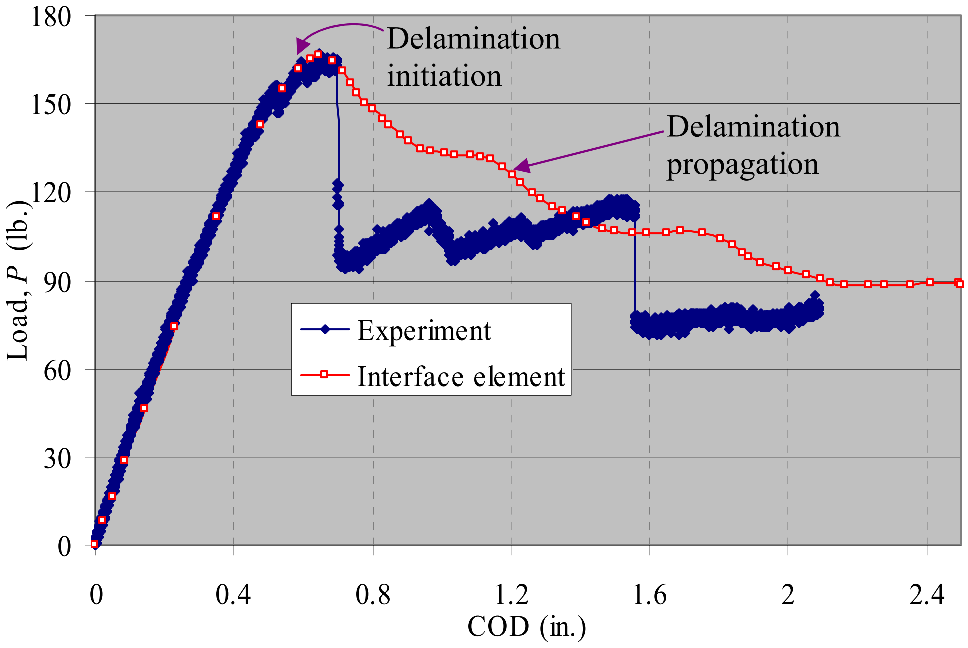

Figure 6.27 Finite element results compared to experimental data of the peeling delamination test.

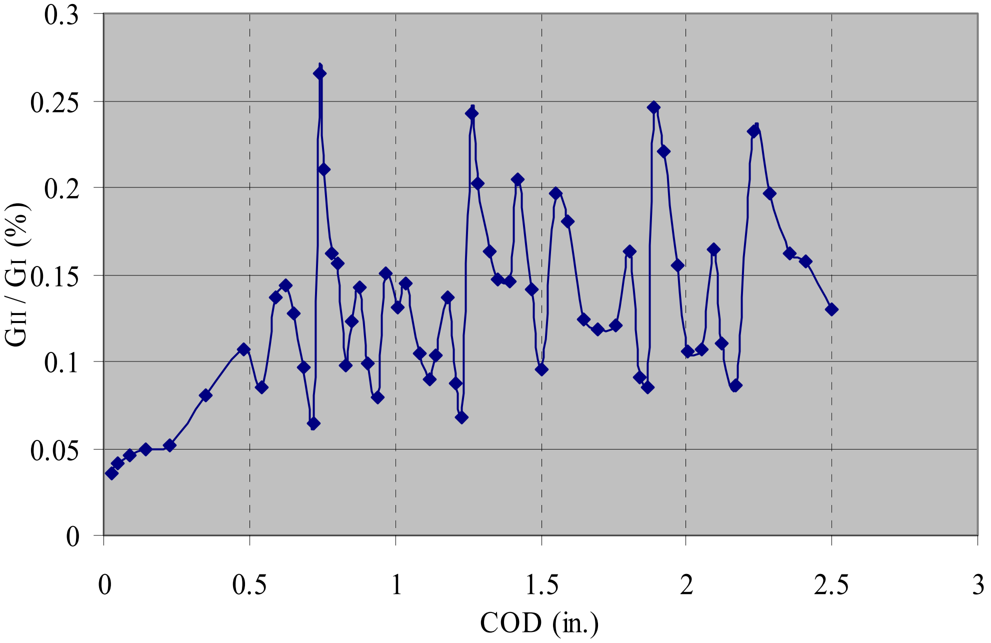

Figure 6.28 Mode-mixity in the peeling delamination test: percentage difference of energy release rate in Mode I and Mode II as the delamination propagates.

6.4 Four-Point Bending Test of HFRP Sandwich Panel

In this section, numerical simulation is attempted for a four-point bending test of the HFRP sandwich panel with sinusoidal wave core geometry.

The test was conducted by Chen and Davalos (2003). The dimensions of the specimen are 28" × 4.5" × 2" (length × width × height). There are seven single core cells along the longitudinal direction and one single core cell in the transverse direction. The sinusoidal wave core has a configuration of RVE as shown in Figure 6.2 with h = 1", l = 4", and core-wall thickness = 0.09". The facesheet lay-up is shown in Figure 6.4 with one bonding layer, and related layer properties are listed in Tables 6.2 and 6.3. The test was carried out in an MTS machine according to ASTM standards (ASTM C 393-00, 2000).

Figure 6.29 shows schematically the testing configuration, where L = 24", a = 12", b = 4.5", and h = 2". The experimental set-up is displayed in Figure 6.30a. The applied load was recorded using an external load cell placed between the loading block and the specimen. Midspan deflection was measured using LVDTs. The test was performed with a loading rate of 0.001 in./sec. Four specimens were tested with the final failure exclusively attributed to facesheet delamination in the shear loading section as shown in Figure 6.30b.

Finite element modeling of the four-point bending test is performed applying the developed CZM with the mixed-mode linear-exponential constitutive law. The interfacial properties for the cohesive interface element, as listed in Table 6.11, are based on previous experimental measurements. Without experimental data for fracture toughness of Mode II and Mode III, it is assumed that $G_{c\mathrm{II}} = G_{c\mathrm{III}} = 3\ G_{c\mathrm{I}}$.

Table 6.11 Fracture toughness and interfacial strength for the four-point bending test.

$G_{c\mathrm{I}}$	$G_{c\mathrm{II}} = G_{c\mathrm{III}}$	σ_{c3}	$\sigma_{c1} = \sigma_{c2}$
25 lb/in.	75 lb/in.	800 psi	1500 psi

A 3D finite element model is created with ABAQUS. Due to symmetry, only half of the sandwich beam is modeled. The facesheets are modeled with shell elements, and the core is modeled entirely with solid elements. Material degradation within the facesheet-core interfaces during delamination propagation is modeled by embedding cohesive interface elements between the facesheet shell elements and core solid elements. The finite element model is shown in Figure 6.31 in the deformed state. It consists of 1512 solid elements, 1624 shell elements, and 504 interface elements.

In this simulation, the major difference with all the previous numerical modeling solutions is that no initial delamination is present in the specimen. As discussed in chapter 3, traditional fracture mechanics methods are invalid for this case. However, with resorting to CZMs, crack initiation and growth could still be successfully predicted. As shown in Figure 6.31, the delaminated region is found to be located in the shear loading section of the beam which is consistent with the observation in the experiments. In Figure 6.32, the finite element result of midspan deflection versus applied load is compared to experimental data of the four-point bending test. We can observe that the failure load due to facesheet delamination is accurately predicted. In the numerical simulation, severe snapback is induced right after delamination initiation, which could not be captured in the experiment when delamination propagated very quickly leading to catastrophic sudden collapse of the specimen. Because of lack of more sophisticated numerical solution methods, the finite element analysis was terminated prematurely, since the global response was successfully captured.

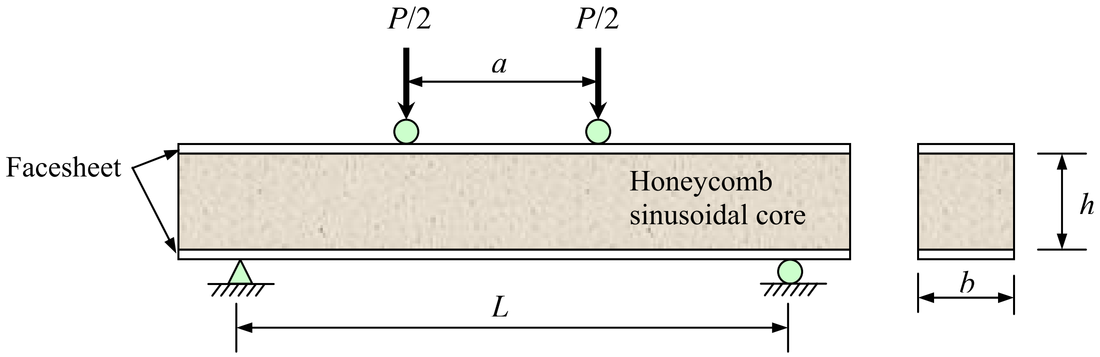

Figure 6.29 Four-point bending test configuration.

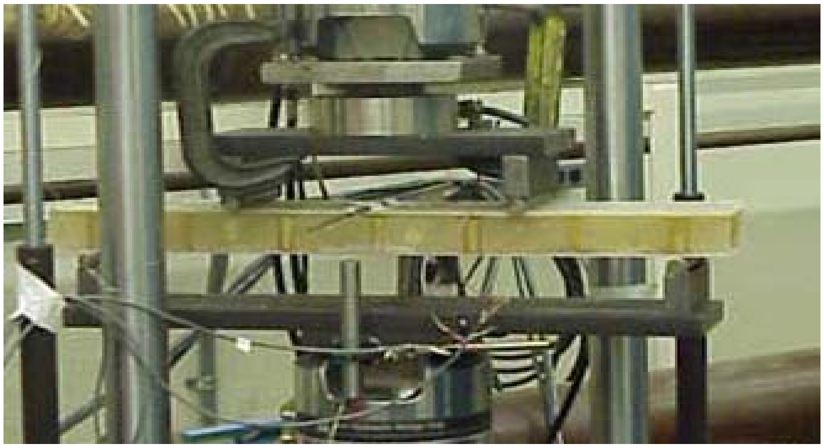

(a)

(b)

Figure 6.30 Four-point bending test: (a) experimental set-up; (b) specimen after being tested showing delamination failure.

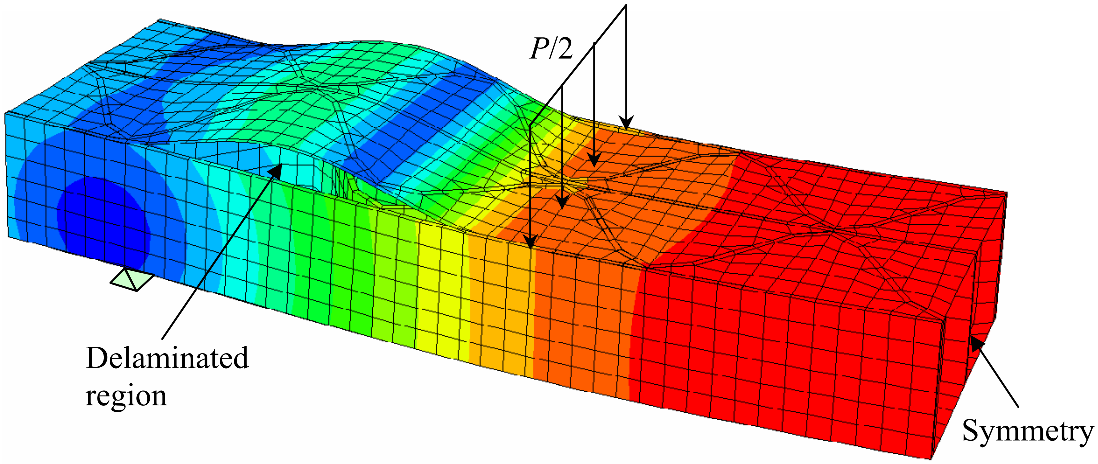

Figure 6.31 Finite element model of the four-point bending test of an HFRP sandwich panel with sinusoidal wave core configuration.

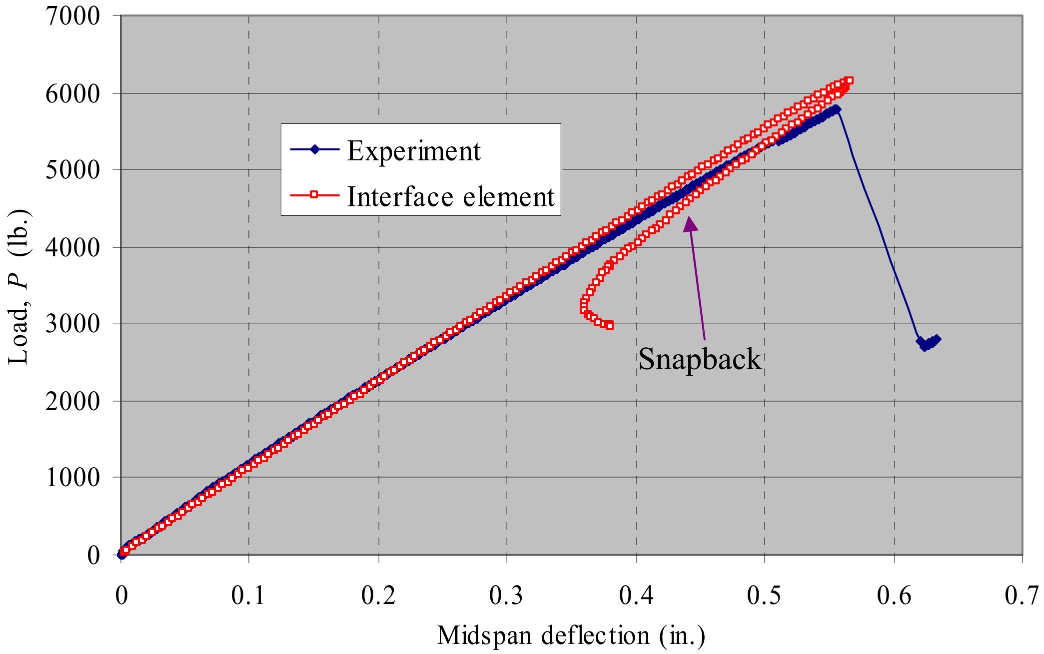

Figure 6.32 Finite element results compared to experimental data of the four-point bending test.

Chapter 7

Concluding Remarks

In this dissertation, our attention has been focused on developing efficient modeling techniques to study facesheet-core interface delamination in HFRP sandwich panels. For this purpose, a CZM is proposed and implemented as interface elements through a user-defined element subroutine within the commercial general purpose finite element code ABAQUS. The predictive capability of the developed CZM is thoroughly verified through simulations of standard fracture test configurations and experiments available in the literature for laminated composites. The applicability of the CZM to simulating facesheet delamination in HFRP sandwich panels is investigated. In this chapter, major findings and conclusions are presented, followed by suggestions for future work.

7.1 Cohesive Crack Modeling Technique

Delamination problems are usually treated from a fracture mechanics point of view. However, interface delamination is generally very complex in nature and difficult to solve, because it involves not only geometric and material discontinuities, but also the inherently coupled Mode I, II and III fracture in layered material systems attributed to the well-known oscillatory singularity nature of the stress and displacement field in the vicinity of the delamination crack tip. One of the key issues in this research is to determine the best way to characterize interface delamination within the framework of continuum mechanics rather than using ad hoc methods just to facilitate numerical implementations, e.g. springs in finite element methods.

Through a comprehensive literature review in Chapter 2-3, it is found that requiring assumptions of an initial crack and self-similar progression of cracks, traditional fracture mechanics approaches are inappropriate for modeling interface delamination. To circumvent these difficulties, five most relevant nonlinear crack models are reviewed and compared. It is concluded that unifying strength-based crack initiation and fracture-based crack progression, the cohesive crack modeling approach has distinct advantages compared to other global methods.

7.2 Nonlinear Cohesive Interface Finite Element Development

In this dissertation, a CZM with linear-exponential irreversible softening traction-separation law, fulfilling empirical mixed-mode fracture criteria, is proposed to represent progressive damage occurring within the interface during the fracture process. The CZM is implemented as cohesive interface elements through the user-defined element subroutine UEL within ABAQUS. The framework and formulation of a three dimensional interface element are presented. Two sets of parameters are required for application of the developed interface element, namely, interfacial strength and fracture toughness. The initiation of fracture is determined by the interfacial strength and the progression of fracture is determined by the interface fracture toughness. The surface-like interface element consists of an upper and a lower face with initially zero thickness in the undeformed configuration. In the finite element modeling, these interface elements are positioned within the interface where potential delamination propagation is expected. Contact-type interface element is also developed to simulate contact behaviors in the delaminated region.

7.3 Interface Element Modeling Verification

Verification examples applying the developed interface element are presented with numerical simulations of standard fracture test configurations, namely DCB and MMB specimens, under Mode I, Mode II, or mixed-mode loading conditions. For all the simulations, the finite element solutions are in excellent agreement with either the LEFM analytical solutions or experimental data available in the literature. Non-self-similar delamination growth or a curved delamination front due to anticlastic bending effect in the DCB specimen is captured numerically.

Typical computational issues related to modeling with interface elements are discussed. It is shown that no pronounced distinction in the structural response is observed using Gauss or Lobatto integration schemes since the bulk material is linear elastic. Nonetheless, if more integration points are used, the predicative capability of the interface element can be improved. Issues of mesh sensitivity, effects of interfacial strength and step size are investigated. Generally, cohesive zone modeling does not require very fine mesh near the crack front since no singularity is present. However, in order to obtain a relatively smooth solution, the mesh should be sufficiently fine in the evolving process zone at the delamination front. Slightly lowering the interfacial strength can reduce the burden on mesh refinement without sacrificing the accuracy of the prediction. It is found that when larger step size is used, it leads to a less smooth solution during delamination propagation, and the response of interface elements may 'jump' from the pre-peak to post-peak side of the traction-separation curve without enforcing the peak stress level on adjacent bulk material. To eliminate these effects, the step size is automatically adjusted within the interface element based on the maximum separations attained. In addition, interface interpenetration should be carefully handled by appropriately amplifying the compressive stiffness without causing ill-conditioning of the overall material tangent stiffness matrix.

To test the robustness of the CZM in simulating delamination coupled with highly nonlinear structural response, delamination buckling of a laminated composite plate under in-plane compression is simulated. In order to lessen the burden of using fine mesh, slight modification of the formulation of the interface element is made resulting in more brittle fracture behavior within the interface. The powerful predictive capability of the interface element modeling is demonstrated by producing numerical results that compare well with experimental data and similar simulation result available in the literature. Material damage within the thin layer in the delaminated region is accounted for using Hashin's failure criteria. However, more sophisticated failure analysis is desired for the accurate prediction of the final failure load.

7.4 Facesheet Delamination in HFRP Sandwich Panels

Delamination in composite sandwich structures is an important failure mode. Although the problem of a facesheet delaminated from a solid core has been extensively investigated, the failure mechanism of delamination of a facesheet from a honeycomb core is far from fully understood. Application of CZM to study facesheet-core interface delamination of honeycomb sandwich structures is rare. In this research, facesheet delamination in HFRP sandwich panels is addressed with the developed cohesive interface element.

The interfacial properties, i.e. interfacial strength and fracture toughness, are measured through a systematic experimental program. Effects of such parameters as facesheet bonding layers and core-wall thickness are investigated. Although more tests are needed before a definite conclusion can be drawn from the current experimental data, some preliminary observations can be made regarding the effects of facesheet bonding layers and core-wall thickness: (1) adding bonding layers could significantly increase the interface fracture toughness (G_{Ic} of C1B2 is two times larger than that of C1B1); (2) increasing core-wall thickness cannot achieve a pronounced improvement of the interface fracture toughness. On the other hand, in spite of the limited experimental data, it is concluded that when facesheet bonding layers and core-wall thickness are varied, there is no drastic change of the interfacial tensile strength which falls in the range of 400 psi ~ 1000 psi. Although more shear tests of specimens with stronger facesheets should be performed, it is expected that similar to the FWT tests, the interfacial shear strength value of 1752 psi for C1B1 can give a good estimation of the overall interfacial shear strength. In fact, it is demonstrated that the response of the HFRP sandwich panel involving facesheet-core interface delamination propagation is mainly controlled by the interface fracture toughness, while the interfacial strength has a relatively small effect. As such, the interfacial strength value need not be measured precisely.

Simulation of the CDCB specimen is successfully performed with the measured interfacial properties. It is verified that in the fracture test, Mode II contribution is negligible, showing the validity of using the CDCB specimen for measurement of Mode I interface fracture toughness. A peeling delamination test of an HFRP sandwich panel is successfully modeled, demonstrating the predictive capability of the developed CZM to simulate the facesheet-core interface delamination propagation in HFRP sandwich panels with actual sinusoidal wave core configuration. Against the initial speculation, Mode II influence is negligible compared to that of Mode I with only 0.27% contribution at most. Finally, simulation of a four-point bending test of the HFRP sandwich panel is attempted. Without assuming an initial delamination, the cohesive zone modeling approach using the interface element successfully predicts the delaminated region observed in the experiments.

7.5 Suggestions for Future Work

Although the developed cohesive zone modeling technique has proven to be simple and robust in many applications involving interface delamination, the current formulation of the CZM is still to be refined and extended. Further investigations in the following directions are suggested.

Under mixed-mode loading, delamination initiation may occur before each traction component reaches its maximum interfacial strength. Thus, a multi-axial stress criterion could be incorporated for more accurate prediction of the onset of delamination. Subsequent to delamination, friction between the delaminated surfaces could also be considered using the classical Coulomb friction model.

The softening nature of the constitutive law of the CZM frequently causes convergence difficulties in the numerical solution, especially in cases of short cracks and coarse finite element mesh. The robustness of the CZM could be enhanced either by developing a more sophisticated path-following technique than what is available in ABAQUS, or by implementing the CZM in the explicit version of ABAQUS through the user-defined material subroutine VUMAT.

The strength of the CZM lies in its capability of accounting for the irreversibility of the material degradation during crack growth, which is especially suitable for fatigue life prediction when delamination is involved as demonstrated by the study of Roe and Siegmund (2003). Fatigue life prediction is crucial in evaluating the performance of the HFRP sandwich panels for highway bridge applications. Hence, fatigue crack growth simulation is practically important and should be investigated in the future study.

Continuing experimental investigations should be performed to evaluate the interfacial properties. In order to obtain consistent results, special care should be taken in fabricating the specimens. Interfacial shear strength could be measured using the same experimental set-up as in the current study, but stronger facesheet should be fabricated to avoid undesirable damage within the facesheet. Mode II interface fracture toughness could be measured using either the cracked sandwich beam (CSB) specimen (Carlsson,

1991) or the tapered end-notched flexure (TENF) specimen (Wang and Qiao, 2003). Mode interaction could be studied using a carefully designed test rather than the peeling delamination test.

References

ABAQUS (2001), *ABAQUS/Standard User's Manual, Version 6.2*, Hibbitt, Karlsson, and Sorensen, Inc., Pawtucket, RI.

Adan, M., Sheinman, I. and Altus, E. (1994), "Buckling of multiply delaminated beams," *Journal of Composite Materials*, v 28, pp. 77-90.

Alfano, G. and Crisfield, M.A. (2001), "Finite element interface elements for the delamination analysis of laminated composite structures: mechanical and computational Issues," *International Journal for Numerical Methods in Engineering*, v 50, pp. 1701-1736.

Allen, H.G., *Analysis and design of structural sandwich panels*, Pergamon Press, London, 1969.

Allix, O., Ladeveze, P. and Corigliano, A. (1995), "Damage analysis of interlaminar fracture specimens," *Composite Structures*, v 31, pp. 61-74.

Allix, O. and Corigliano, A. (1999), "Geometrical and interfacial nonlinearities in the analysis of delamination in composites," *International Journal of Solids and Structures*, v 36, pp. 2189-2216.

Armanios, E.A., Sriram, S. and Badir, A.M. (1991), "Fracture analysis of transverse crack-tip and free-edge delamination in laminated composites," *Composite Materials: Fatigue and Fracture (Third Volume)*, ASTM STP 1110, pp. 269-286.

ASTM C 297-94 (1999), "Standard test method for flatwise tensile strength of sandwich constructions," In: *Annual Book of ASTM Standards*, v 03.01, American Society for Testing and Materials.

ASTM D 5528-94a (2000), "Standard test method for mode I interlaminar fracture toughness of unidirectional fiber-reinforced polymer matrix composites," In: *Annual Book of ASTM Standards*, v 15.03, American Society for Testing and Materials.

ASTM C 393-00 (2000), "Standard test method for flexural properties of sandwich constructions," In: *Annual Book of ASTM Standards*, v 03.01, American Society for Testing and Materials.

Avery, J.L. (1998), *Compressive failure of delaminated sandwich composites*, MS thesis, University of Florida, Gainesville, Florida.

Avery, J.L. and Sankar, B.V. (2000), "Compressive failure of sandwich beams with debonded face-sheets," *Journal of Composite Materials*, v 34, n14, pp. 1176-1199.

Barenblatt, G.I. (1962), "The mathematical theory of equilibrium cracks in brittle fracture," *Advances in Applied Mechanics*, VII, pp. 55-129.

Bažant Z.P. (1976), "Instability, ductility and size effect in strain-softening concrete," *Journal of Engineering Mechanics*, v 102, pp. 331-344.

Bažant Z.P. (1990), "Smeared-tip superposition method for nonlinear and time-dependent fracture," Mechanics Research Communications, v 17, n 5, pp. 343-351.

Bažant Z.P. and Planas, J., *Fracture and size effect in concrete and other quasibrittle materials*, CRC Press, 1997.

Bažant Z.P. and Cedolin, L. (1979), "Blunt crack band propagation in finite element analysis," *Journal of Engineering Mechanics*, v 105, pp. 297-315.

Bažant Z.P. and Cedolin, L. (1980), "Fracture mechanics of reinforced concrete," *Journal of Engineering Mechanics*, v 106, pp. 1257-1306.

Bažant Z.P. and Cedolin, L. (1983), "Finite element modeling of crack band propagation," *Journal of Structural Engineering*, v 109, pp. 69-92.

Beer, G. (1985), "An isoparametric joint/interface element for the finite element analysis," *International Journal for Numerical Methods in Engineering*, v 21, pp. 585-600.

Begley, J.A. and Landes, J.D. (1972), "The *J*-integral as a fracture criterion," *Fracture Toughness*, ASTM STP 514, American Society for Testing and Materials, Philadelphia, pp. 1-20.

Belytschko, T. and Black, T. (1999), "Elastic crack growth in finite elements with minimal remeshing," *International Journal for Numerical Methods in Engineering*, v 45, pp. 601-620.

Belytschko, T., Moës, N., Usui, S. and Parimi, C. (2001), "Arbitrary discontinuities in finite elements," *International Journal for Numerical Methods in Engineering*, v 50, pp. 993-1013.

Beuth, J.L. (1996), "Separation of crack extension modes in orthotropic delamination models," *International Journal of Fracture*, v 77, pp. 305-321.

Borg, R., Nilsson, L. and Simonsson, K. (2001), "Simulation of delamination in fiber composites by the use of a discrete cohesive-failure model," *Composites Science and Technology*, v 61, pp. 667-77.

Borg, R., Nilsson, L. and Simonsson, K. (2002), "Modeling of delamination using a discretized cohesive zone and damage formulation," *Composites Science and Technology*, v 62, pp. 1299-1314.

Borg, R., Nilsson, L. and Simonsson, K. (2004a), "Simulating DCB, ENF and MMB experiments using shell elements and a cohesive zone model," *Composites Science and Technology*, v 64, pp. 269-278.

Borg, R., Nilsson, L. and Simonsson, K. (2004b), "Simulating of low velocity impact on fiber laminates using cohesive zone based delamination model," *Composites Science and Technology*, v 64, pp. 279-288.

Bottega, W.J. (1983), "A growth law for propagation of arbitrarily shapes delaminations in layered plates," *International Journal of Solids and Structures*, v 19, pp. 1009-1017.

Bottega, W.J. and Maewal, A. (1983), "Delamination buckling and growth in laminates," Journal of Applied Mechanics, v 50, pp. 184-189.

Boyajian, D.M. (2002), "Mode I fracture and durability of the CFRP-concrete interface bond," Ph.D. dissertation, West Virginia University, Morgantown, WV.

Brewer, J.C. and Lagace, P.A. (1988), "Quadratic stress criterion for initiation of delamination," *Journal of Composite Materials*, v 22, pp. 1141-1155.

Burdekin, F.M. and Stone, D.E.W. (1966), "The crack opening displacement approach to fracture mechanics in yielding materials," *Journal of Strain Analysis*, v 1, pp. 145-153.

Burton, W.S. and Noor, A.K. (1997), "Structural analysis of the adhesive bond in a honeycomb sandwich panels," *Finite Elements in Analysis and Design*, v 26, pp. 213-227.

Camacho, G.T. and Ortiz, M. (1996), "Computational modelling of impact damage in brittle materials," International Journal of Solids and Structures, v 33, pp. 2899-2938.

Carlsson, L.A., Sendlein, L.S. and Merry, S.L. (1991), "Characterization of face sheet/core shear fracture of composite sandwich beams," *Journal of Composite Materials*, v 25, pp. 101-116.

Carlsson, L.A. (1991), "On the design of the cracked sandwich beam (CSB) specimen," *Journal of Reinforced Plastics and Composites*, v 10, pp. 434-444.

Carpinteri, A., editors, *Nonlinear crack models for nonmetallic materials*, Kluwer Academic Publishers, 1998.

Carpinteri, A., Cornetti, P., Barpi, F. and Valente, S. (2003), "Cohesive crack model description of ductile to brittle size-scale transition: dimensional analysis vs. renormalization group theory," *Engineering Fracture Mechanics*, v 70, pp. 1809-1839.

Chaboche, L.J., Girard, R. and Schaff, A. (1997), "Numerical analysis of composite systems by using interphase/interface models," *Computational Mechanics*, v 20, pp. 3-11.

Chai, H., Babcock, C.D. and Knauss, W.G. (1981), "One dimensional modeling of failure in laminated plates by delamination buckling," *International Journal of Solids and Structures*, v 17, n 11, pp. 1069-1083.

Chai, H. and Babcock, C.D. (1985), "Two dimensional modeling of compressive failure in delaminated laminates," *Journal of Composite Materials*, v 19, n 11, pp. 67-98.

Chandra, N., Li, H., Shet, C. and Ghonem, H. (2002), "Some issues in the application of cohesive zone models for metal-ceramic interfaces," International Journal of Solids and Structures, v 39, pp. 2827-2855.

Charalambides, P.G., Lund, J., Evans, A.G., and McMeeking, R.M. (1989), "Test specimen for determining the fracture resistance of bimaterial interfaces," *Journal of Applied Mechanics*, v 56, pp. 77-82.

Chatterjee, S., Dick, W. and Pipes, R. (1986), "Mixed-mode delamination fracture in laminated composites," *Composites Science and Technology*, v 25, pp. 49-67.

Chattopadhyay, A. and Gu, H. (1994), "New higher order plate theory in modeling delamination buckling of composite laminates," *AIAA Journal*, v 32, pp. 1709-1716.

Chen, A. and Davalos, J.F. (2003), "Bending strength of honeycomb FRP sandwich beams with sinusoidal core geometry," *Proceedings of the fourth Canadian-International Composites Conference, CANCOM 2003,* Ottawa, Canada, August 19-22, 2003.

Chen, H.P. (1993), "Transverse shear effects on buckling and postbuckling of laminated and delaminated plates," *AIAA Journal*, v 30, pp. 163-169.

Chen, S.H., Lin, C.C. and Wang, J.T.S. (1997), "Local buckling of delaminated sandwich beams using continuous analysis," *International Journal of Solids and Structures*, v 34, n 2, pp. 275-288.

Cho, S.B., Lee, K.R. and Choy, Y.S. (1992a), "A further study of two-dimensional boundary element analysis in anisotropic or orthotropic materials," *Engineering Fracture Mechanics*, v 43, n 4, pp. 589–601.

Cho, S.B., Lee, K.R., Chou, Y.S. and Yuuki, R. (1992b), "Determination of stress intensity factors and boundary element analysis for interface cracks in dissimilar anisotropic materials," *Engineering Fracture Mechanics*, v 43, n 4, pp. 603–614.

Comminou, M. (1977a), "The interface crack," *Journal of Applied Mechanics*, v 44, pp. 631-636.

Comminou, M. (1977b), "Interface crack with friction in the contact zone," *Journal of Applied Mechanics*, v 44, pp. 780-781.

Crisfield, M.A., Hellweg, H.B. and Davies, G.A.O. (1997), "Failure analysis of composite structures using interface elements," *Proceedings of the NAFEMS Conference on Application of Finite Elements to Composite Materials*, v 1-4, London, U.K.

Cui, W. and Wisnom, M. (1993), "A combined stress-based and fracture-mechanics-based model for predicting delamination in composites," *Composites*, v 24, n 6, pp. 467-474.

Davalos, J.F., Madabhusi-Raman, P. and Qiao, P. (1997), "Characterization of Mode-I fracture of hybrid material interface bonds by contoured DCB specimens," *Engineering Fracture Mechanics*, v 58, n 3, pp. 173-192.

Davalos, J.F., Qiao, P., Xu, F.X., Robinson, J. and Barth, K.E. (2001), "Modeling and characterization of fiber-reinforced plastic honeycomb sandwich panels for highway bridge applications," *Composite Structures*, v 52, pp. 441-452.

Davidson, B.D. (1995), "Prediction of energy release rate for edge delamination using a crack tip element approach," *Composite Materials: Fatigue and Fracture* (Fifth Volume), ASTM STP 1230, R.H. Martin, Ed., American Society for Testing and Materials, pp. 155-175.

Davidson, B.D., Hu, H. and Schapery, R.A. (1995a), "An analytical crack tip element for layered elastic structures," *Journal of Applied Mechanics*, v 62, n 6, pp. 243-253.

Davidson, B.D., Krueger, R., and König, M. (1995b), "Three dimensional analysis and resulting design recommendations for unidirectional and multidirectional end-notched flexure Tests," *Journal of Composite Materials*, v 29, n 16, pp. 2108-2133.

Davidson, B.D., Fariello, P.L., Hudson, R.C. and Sundararaman, V. (1997), "Accuracy assessment of the singular field-based mode mix decomposition procedure for the prediction of delamination," *Composite Materials: Testing and Design* (Thirteenth volume), ASTM STP 1242, S.J. Hooper, Ed., American Society for Testing and Materials, pp. 109-128.

Davidson, B.D., Gharibian, S.J. and Yu, L. (2000), "Evaluation of energy release rate-based approaches for predicting delamination growth in laminated composites," *International Journal of Fracture*, v 105, pp. 343-365.

de Borst, R. and Rots, J.G. (1989), "Occurrence of spurious mechanisms in computation of strain-softening solids," *Engineering Computations*, v 6, pp. 272-280.

de Borst, R. (2003), "Numerical aspects of cohesive-zone models," Engineering Fracture Mechanics, v 70, pp. 1743-1757.

de-Andres, A., Perez, J.L. and Ortiz, M. (1999), "Elasto-plastic finite element analysis of three-dimensional fatigue crack growth in aluminum shafts subjected to axial loading," *International Journal of Solids and Structures*, v 36, pp. 2231-2258.

de Moura, M., Gonçalves, J., Marques, J. and de Castro, P. (1997), "Modeling compression failure after low velocity impact on laminated composites using interface elements," *Journal of Composite Materials*, v 31, n 15, pp. 1462-1479.

Donaldson, S.L. (1987), "The effect of interlaminar fracture properties on the delamination buckling of composite materials," *Composite Science and Technology*, v 28, pp. 33-44.

Dugdale, D.S. (1960), "Yielding of steel sheets containing slits," *Journal of the Mechanics and Physics of Solids*, v 8, pp. 100-108.

Dundurs, J. (1969), "Edge-bonded dissimilar orthogonal elastic wedges under normal and shear loading," *Journal of Applied Mechanics*, v 36, pp. 650-652.

Elices, M., Guinea, G.V., Gómez, J. and Planas, J. (2002), "The cohesive zone model: advantages, limitations and challenges," *Engineering Fracture Mechanics*, v 69, pp. 137–163.

El-Sayed, S. and Sridharan, S. (2001), "Predicting and tracking interlaminar crack growth in composites using a cohesive layer model," *Composites: Part B*, v 32, pp. 545-553.

El-Sayed, S. and Sridharan, S. (2002), "Cohesive layer models for predicting delamination growth and crack kinking in sandwich structures," *International Journal of Fracture*, v 117, pp. 63-84.

England, A.H. (1965), "A crack between dissimilar media," *Journal of Applied Mechanics*, v 32, pp. 400-402.

Erdogan, F. (1965), "Stress distribution in bonded dissimilar materials with cracks," *Journal of Applied Mechanics*, v 32, pp. 403-410.

Erdogan, F. and Gupta, G.D. (1971), "Layered composites with an interface flaw," *International Journal of Solids and Structures*, v 7, pp. 1089-1107.

Fairbairn, W., *An account of the construction of the Britannia and Conway tubular bridges*, John Weale *et al.*, London, 1849.

Falk, L. (1994), "Foam core sandwich panels with interface disbonds," *Composite Structures*, v 28, n 4, pp. 481–490.

Finot, M., She, Y.-L., Needleman, A. and Suresh, S. (1994), "Micro-mechanical modelling of reinforcement fracture in plastic-reinforcement metal-matrix composites," Metallurgical Transactions, v 254, pp. 2403-2420.

Frostig, Y. (1992), "Behavior of delaminated sandwich beams with transversely flexible core-high order theory," *Composite Structures*, v 20, n 1, pp. 1–16.

Frostig, Y., Baruch, M., Vilnai, O. and Sheinman, I. (1992), "High-order theory for sandwich-beam bending with transversely flexible core," *Journal of Engineering Mechanics*, v 118, n 5, pp. 1026–1043.

Frostig, Y. and Baruch, M. (1992), "Localized load effects in high order bending of sandwich panels with flexible Core," *Journal of Engineering Mechanics*, v 122, n 11, pp. 1069–1076.

Garg, A.C. (1988), "Delamination – a damage in composite structures," *Engineering Fracture Mechanics*, v 29, n 5, pp. 557-584.

Gautesen, A.K. and Dundurs, J. (1987), "The interface crack in a tension field," *Journal of Applied Mechanics*, v 54, pp. 93-98.

Gautesen, A.K. and Dundurs, J. (1988), "The interface crack under combined loading," *Journal of Applied Mechanics*, v 55, pp. 580-586.

Goncalves, J., de Moura, M., de Castro, P.M.S.T. and Marques, A. (2000), "Interface element including point-to-surface constraints for three-dimensional problems with damage propagation," *Engineering Computations*, v 17, n 1, pp. 28-47.

Goodier, J.N. and Field, F.A. (1963), *Fracture of Solids*, D.C. Drucker and J.J. Gilman Wiley, New York, pp. 103-118.

Griffith, A.A. (1920), "The phenomena of rupture and flow in solids," *Philosophical Transactions of the Royal Society*, Series A, v 221, pp. 163-198.

Han, T.S., Ural, A., Chen, C.S., Zehnder, A.T., Ingraffea, A.R. and Billington, S.L. (2002), "Delamination buckling and propagation analysis of honeycomb panel using cohesive element approach", *International Journal of Fracture*, v 115, n 2, pp. 101-123.

Hashin, Z. (1980), "Failure criteria for unidirectional fiber composites," Journal of Applied Mechanics, v 47, pp. 329-334.

He, M.Y. and Hutchinson, J.W. (1989), "Kinking of a crack out of an interface," *Journal of Applied Mechanics*, v 56, pp. 270-278.

Hellweg, H.B. and Crisfield, M.A. (1998), "A new arc-length method for handling sharp snap-backs," *Computers and Structures*, v 66, n 5, pp. 705-709.

Herrmann, J.M. (1989), "An asymptotic analysis of finite deformations near the tip of an interface crack," *Journal of Elasticity*, v 21, pp. 227-269.

Hillerborg, A., Modéer, M. and Petersson, P.E. (1976), "Analysis of crack formation and crack growth in concrete by means of fracture mechanics and finite elements," *Cement and Concrete Research*, v 6, pp. 773-782.

Huang, R., Prévost, J.H., Huang, Z.Y. and Suo, Z. (2003), "Channel-cracking of thin films with the extended finite element method," *Engineering Fracture Mechanics*, v 70, pp. 2513-2526.

Hutchinson, J.W. (1968), "Singular behavior at the end of a tensile crack in a hardening material," *Journal of the Mechanics and Physics of Solids*, v 16, pp. 13-31.

Hutchinson, J.W. and Paris, P.C. (1979), *Elastic-plastic fracture*, ASTM STP 668, In: Landes, J.D., Begley, J.A., Clarke, G.A., editors, American Society for Testing and Materials, Philadelphia, pp. 37-64.

Hutchinson, J.W. and Suo, Z. (1992), "Mixed mode cracking in layered materials," *Advances in Applied Mechanics*, v 29, Academic Press, New York, pp. 63-191.

Hwang, S.F. and Mao, C.P. (2001), "Failure of delaminated carbon/epoxy composite plates under compression," *Journal of Composite Materials*, v 35, n 18, pp. 1634-1653.

Hwu, C. and Hu, J.S. (1992a), "Stress intensity factors and energy release rates of delaminations in composite laminates," *Engineering Fracture Mechanics*, v 42, n 6, pp. 977-988.

Hwu, C. and Hu, J.S. (1992b), "Buckling and postbuckling of delaminated composite sandwich beams," *AIAA Journal*, v 30, n 7, pp. 1901-1909.

Hwu, C., Kao, C.J. and Chang, L.E. (1995), "Delamination fracture criteria for composite laminates," *Journal of Composite Materials*, v 29, n 15, pp. 1962-1987.

Ingraffea, A., TerMaath, S. and Ferguson, K. (1997), "An investigation into damage tolerance of honeycomb structural members," Final Report to Boeing Commercial Airplane Company, Purchase Contract Numbers ZA0079 and JG7634.

Irwin, G.R. (1948), "Fracture dynamics," *Fracturing of Metals*, American Society for Metals, Cleveland, pp. 147-166.

Irwin, G.R. (1957), "Analysis of stresses and strains near the end of a crack traversing a plate," *Journal of Applied Mechanics*, v 24, pp. 361-364.

Irwin, G.R., "Fracture," In: Flügge S, editor, *Encyclopedia of Physics*, VI – elasticity and plasticity, Springer, Berlin, 1958, pp. 551-590.

Ingraffea, A.R. (2003), FRANC, http://www.cfg.cornell.edu/software.htm.

James, M.A. and Newman, J.C. (2003), "The effect of crack tunneling on crack growth: experiments and CTOA analyses," *Engineering Fracture Mechanics*, v 70, pp. 457-468.

Johnson, W. (editor) (1985), *Delamination and Debonding of Materials*, ASTM STP 876, Philadelphia.

Johnson,W.S. and Mangalagiri, P.D. (1987), "Influence of the resin on the interlaminar mixed-mode fracture," Toughened Composites, ASTM STP 937, ed. W.S. Johnson, American Society for Testing and Materials, pp. 295-315.

Jurf, R. and Pipes, R. (1982), "Interlaminar fracture of composite materials." *Journal of Composite Materials*, v 16, pp. 386-394.

Kachanov, L.M. (1976), "Separation of composite materials," *Mekh. Polim.*, v 5, pp. 918-922.

Kachanov, L.M. (1988), *Delamination Buckling of Composite Materials*, Kluwer Academic Publishers, Dordrecht.

Kardomateas,G.A. (1993), "The initial post-buckling and growth behavior of internal delaminations in composite plates," *Journal of Applied Mechanics*, v 60, pp. 903-910.

Kardomateas,G.A. and Huang, H.Y. (1993), "An asymptotic solution for the response of face-sheet delamination/debonds under compression," *Mechanics of Sandwich Structures*, Eds. Y.D.S. Rajapakse, G.A. Kardomateas and V. Birman, AD-Vol. 62, American Society of Mechanical Engineers, New York.

Kim, W.C. and Dharan, C.K.H. (1992), "Facesheet debonding criteria for composite sandwich panels under in-plane compression," *Engineering Fracture Mechanics*, v 42, n 4, pp. 643-652.

Klug, J.C. (1994), "Efficient modeling of postbuckling delamination growth in composite laminates using plate elements," MS thesis, Purdue University, West Lafayette, Indiana.

Knowles, J.K. and Sternberg, E. (1983), "Large deformations near a tip of an interface-crack between two Neo-Hookean sheets," *Journal of Elasticity*, v 13, pp. 257-293.

König, M., Krueger, R., and Rinderknecht, S. (1995), "Numerical simulation of delamination buckling and growth," *Proceedings of the 10th International Conference on Composite Materials (ICCM-10)*, Whistler, Canada, August 14-18, pp. 269-276.

Krueger, R., and O'Brien, T.K. (2001), "A Shell/3D Modeling Technique for the Analysis of Delaminated Composite Laminates," *Composites Part A*: *Applied Science and Manufacturing*, v 32, n1, pp. 25-44.

Krueger, R. (2002), "The virtual crack closure technique: history, approach and applications," NASA/CR-2002-211628, *ICASE Report* No. 2002-10.

Krueger, R., Minguet, P.J. and O'Brien, T.K. (2003), "Implementation of interlaminar fracture mechanics in design: an overview," *Proceedings of the 14th International Conference on Composite Materials (ICCM-14)*, San Diego, July 14-18.

Kutlu, Z. (1991), "Compressive response of laminated composite panels containing multiple delaminations," Ph.D. Thesis, Stanford University.

Kutlu, Z. and Chang, F.K. (1992), "Modeling compression failure of laminated composites containing multiple through-width delaminations," *Journal of Composite Materials*, v 26, pp. 350-387.

Kutlu, Z. and Chang, F.K. (1995a), "Composite panels containing multiple through-the-width delaminations and subjected to compression. Part I: analysis," *Composite Structures*, v 31, pp. 273-296.

Kutlu, Z. and Chang, F.K. (1995b), "Composite panels containing multiple through-the-width delaminations and subjected to compression. Part II: experiments & verification," *Composite Structures*, v 31, pp. 297-314.

Kyoung, W.M. and Kim, C.G. (1995), "Delamination buckling and growth of composite laminated plates with transverse shear deformation," *Journal of Composite Materials*, v 29, pp. 2047-2068.

Landes, J.D. and Begley, J.A. (1972), "The effect of specimen geometry on J_{Ic}," *Fracture Toughness*, ASTM STP 514, American Society for Testing and Materials, Philadelphia, pp. 24-29.

Lee, S.M. (1993), "An edge crack torsion method for Mode III delamination fracture testing," *Journal of Composites Technology & Research*, v 15, n 3, pp. 193-201.

Levy, A.J. (1994), "Separation at a circular interface under bi-axial loading," *Journal of Mechanics and Physics in Solids*, v 42, pp. 1087-1104.

Li, J., Lee, S.M., Lee, E.W., and O'Brien, T.K. (1997), "Evaluation of the edge crack torsion ECT test for Mode III interlaminar fracture toughness of laminated composites," *Journal of Composites Technology and Research*, v 19, pp. 174-183.

Liu, S., Kutlu, Z. and Chang, F.K. (1993), "Matrix cracking-induced delamination propagation in Graphite/Epoxy laminated composites due to a transverse concentrated load," *Composite Materials: Fatigue and Fracture (Fourth Volume)*, ASTM STP 1156, pp. 86-101.

Malyshev, B.M. and Salganik, R.L. (1965), "The strength of adhesive joints using the theory of crack," *International Journal of Fracture Mechanics*, v 1, pp. 114-128.

Martin, R.H. (1991), “Evaluation of the split cantilever beam for Mode III delamination testing,” *Composite Materials: Fatigue and Fracture (Third Volume)*, ASTM STP 1110, pp. 243-266.

Martin, R.H. and Davidson, B.D. (1999), “Mode II fracture toughness evaluation using a four point bend end notched flexure test,” *Plastics, Rubber and Composites*, v 28, pp. 401-406.

Mi, Y., Crisfield, M.A., Davies, G.A.O. and Hellweg, H.B. (1998), “Progressive delamination using interface elements,” *Journal of Composite Materials*, v 32, pp. 1246-1273.

Moës, N. and Belytschko, T. (2002), “Extended finite element method for cohesive crack growth,” *Engineering Fracture Mechanics*, v 69, pp. 813-833.

Moës, N., Dolbow, J. and Belytschko, T. (1999), “A finite element method for crack growth without remeshing,” *International Journal for Numerical Methods in Engineering*, v 46, pp. 131-150.

Mukherjee, Y., Xie, Z. and Ingraffea, A. (1991), “Delamination buckling of laminated plates,” *International Journal for Numerical Methods in Engineering*, v 32, pp. 1321-1337.

Mukherjee, Y.X., Gulrajani, S.N., Mukherjee, S. and Netravali, A.N. (1994), “A numerical and experimental study of delaminated layered composites,” *Journal of Composite Materials*, v 28, n 9, pp. 837-870.

Mushkhelishvili, N.I., *Some basic problems in the mathematical theory of elasticity*, Nordhoff, The Netherlands, 1954.

Narayan, S.H. and Beuth, J.L. (1998), “Designation of mode mix in orthotropic composite delamination problem,” *International Journal of Fracture*, v 90, pp. 383-400.

Narayanan, M. (1999), *Finite element analysis of debonded sandwich beams under compression*, MS thesis, University of Florida, Gainesville, Florida.

Needleman, A.(1987), “A continuum model for void nucleation by inclusion debonding,” *Journal of Applied Mechanics*, v 54, pp. 25–531.

Needleman, A. (1990), “An analysis of tensile decohesion along an interface,” *Journal of Mechanics and Physics of Solids*, v 38, pp. 289–324.

O’Brien, T.K. (1982), “Characterization of delamination onset and growth in a composite laminate,” *Damage in Composite Materials*, ASTM STP 775, pp. 140-167.

O'Brien, T.K. (1998a), “Interlaminar fracture toughness: the long and winding road to standardisation,” *Composites-Part B*, v 29, pp. 57-62.

O'Brien, T.K. (1998b), "Composite interlaminar shear fracture toughness, G_{IIC}: shear measurement of sheer myth?" *Composite Materials: Testing and Design (Seventh Volume)*, ASTM STP 1330, American Society for Testing and Materials, pp. 3-18.

Oliver, J., Huespe, A.E., Pulido, M.D.G. and Chaves, E. (2002), "From continuum mechanics to fracture mechanics: the strong discontinuity approach," *Engineering Fracture Mechanics*, v 69, pp. 113-136.

Orowan, E. (1948), "Fracture and strength of solids," *Reports on Progress in Physics*, XII, pp. 185.

Pagano, N. (editor) (1989), *Interlaminar Response of Composite Materials*, Composite Materials Series, v 5, Elsevier, Amsterdam.

Patzák, B. and Jirásek, M. (2003), "Process zone resolution by extended finite elements," *Engineering Fracture Mechanics*, v 70, pp. 957-977.

Petersson, P.E. (1981), "Crack growth and development of fracture zone in plain concrete and similar materials," Report No. TVBM-1006, Division of Building Materials, Lund Institute of Technology, Lund, Sweden.

Petrossian, Z. and Wisnom, M.R. (1998), "Prediction of delamination initiation and growth from discontinuous plies using interface elements," *Composites: Part A*, v 29, pp. 503-515.

Planas, J. and Elices, M. (1991), "Nonlinear fracture of cohesive materials," *International Journal of Fracture*, v 51, pp. 139-157.

Planas, J. and Elices, M. (1992), "Asymptotic analysis of a cohesive crack: 1. theorectical background," *International Journal of Fracture*, v 55, pp. 153-177.

Plantema, F.J., *Sandwich construction: the bending and buckling of sandwich beams, plates and shells*, John Wiley and sons, New York, 1966.

Plunkett, J.D., "Fiber-reinforcement polymer honeycomb short span bridge for rapid installation," IDEA Project Report, November, 1997.

Qiao, P.Z., Wang, J.L. and Davalos, J.F. (2003), "Tapered beam on elastic foundation model for compliance rate change of TDCB specimen," *Engineering Fracture Mechanics*, v 70, n 2, pp. 339-353.

Qiu, Y., Crisfield, M.A. and Alfano, G. (2001), "An interface element formulation for the simulation of delamination with buckling," *Engineering Fracture Mechanics*, v 68, pp. 1755-1776.

Qu, J. and Bassani, J.L. (1993), "Interfacial fracture mechanics for anisotropic bimaterials," *Journal of Applied Mechanics*, v 60, pp. 422-431.

Rabinovitch, O. and Frostig, Y. (2002), “High-order behavior of fully bonded and delaminated circular sandwich plates with laminated face sheets and a ’soft’ core,” *International Journal of Solids and Structures*, v 39, pp. 3057-3077.

Rahul-Kumar, P., Jagota, A., Bennison, S., Saigal, S. and Muralidhar, S. (1999), “Polymer interfacial fracture simulations using cohesive elements,” *Acta Metallurgica*, v 47, n 15, pp.4161-4169.

Rahul-Kumar, P., Jagota, A., Bennison, S. and Saigal, S. (2000), “Interfacial failures in a compressive shear strength test of glass/polymer laminates,” *International Journal of Solids and Structures*, v 37, pp. 7281-7305.

Raju, I.S. (1987), “Calculation of strain-energy release rates with higher order and singular finite elements,” *Engineering Fracture Mechanics*, v 28, pp. 251-274.

Raju, I.S., Crews, J.H. Jr. and Aminpour, M.A. (1988), “Convergence of strain energy release rate components for edge-delaminated composite laminates,” *Engineering Fracture Mechanics*, v 30, n 3, pp. 383-396.

Rashid, Y.R. (1968), “Analysis of prestressed concrete pressure vessels,” *Nuclear Engineering and Design*, v 7, n 4, pp. 334-355.

Ravichandran, G. and Knauss. W.G. (1989), “A finite elastostatic analysis of bimaterial interface cracks,” *International Journal of Fracture*, v 39, pp. 235-253.

Razi, H., Sergeev, B., Shkarayev, S. and Madenci, E. (1999), “Analysis of sandwich panels with multiple-site damage,” *Engineering Fracture Mechanics*, v 64, pp. 255-268.

Reeder, J.R. and Crews, J.H. (1990), “Mixed-mode bending method for delamination testing,” AIAA Journal, v 28, pp.1270-1276.

Reeder, J.R. and Crews, J.H. (1991), “Nonlinear analysis and redesign of the mixed-mode bending delamination test,” NASA TM 102777.

Reeder, J.R. (1992), “An evaluation of mixed-mode delamination failure criteria,” NASA TM 04210.

Reeder, J.R. (1993), “A bilinear failure criterion for mixed-mode delamination,” *Composite Materials: Testing and Design (Eleventh Volume)*, ASTM STP 1206, E.T. Camponeschi, Jr., Ed., American Society for Testing and Materials, pp. 303-322.

Reedy Jr., E.D., Mello, F.J. and Guess, T.R. (1997), “Modeling the initiation and growth of delaminations in composite structures,” *Journal of Composite Materials*, v 31, pp. 812-831.

Rice, J.R. and Sih, G.C. (1965), “Plane problems of cracks in dissimilar media,” *Journal of Applied Mechanics*, v 32, pp. 418-423.

Rice, J.R. (1968), “A path independent integral and the approximate analysis of strain concentration,” *Journal of Applied Mechanics*, v 35, pp. 379-386.

Rice, J.R. and Rosengren, G.F. (1968), “Plane strain deformation near a crack tip in a power law hardening materials,” *Journal of the Mechanics and Physics of Solids*, v 16, pp. 1-12.

Rice, J.R. (1988), “Elastic fracture mechanics concepts for interfacial cracks,” *Journal of Applied Mechanics*, v 55, pp. 98-103.

Riks, E. (1975), “An incremental approach to the solution of snapping and buckling problems,” *International Journal of Solids and Structures*, v 15, pp. 529-551.

Rinderknecht, S. and Kröplin B. (1994), “Delamination Growth Simulation with a Moving Mesh Technique,” In: *Advances in Non-Linear Finite Element Methods*, B. H. V. Topping and M. Papadrakakis, Eds., pp. 187-197.

Rinderknecht, S. and Kröplin B. (1995), “A finite element model for delamination in composite plates,” *Mechanics of Composite Materials and Structure*, v 2, pp. 19-47.

Robinson, P. and Song, D.Q. (1992), “A modified DCB specimen for Mode I testing of multidirectional laminates,” *Journal of Composite Materials*, v 26, pp. 15-54.

Robinson, P. and Song, D.Q. (1994), “Development of an improved mode III delamination test for composites,” *Composites Science and Technology*, v 52, pp. 217-233.

Rose, J.H., Ferrante, J. and Smith, J.R. (1981), “Universal binding energy curves for metals and bimetallic interfaces,” *Physical Review Letters*, v 47, n 9, pp. 675–678.

Roy, Y.A. and Dodds, R.H. (2001), “Simulation of ductile crack growth in thin aluminum panels using 3-D surface cohesive elements,” *International Journal of Fracture*, v 110, pp. 21-45.

Rybicki, E.F. and Kanninen, M.F. (1977), “A finite element calculation of stress intensity factors by modified crack closure integral,” *Engineering Fracture Mechanics*, v 9, pp. 931-938.

Sankar, B.V., Narayanan M. and Avery, J.L. (1999), “Post-buckling behavior of debonded sandwich composite beams under compression,” Paper No. AIAA-99-1295, *AIAA SDM Conference*, St. Luis, MO.

Saouma, V.E. (2003), MERLIN, http://ceae.colorado.edu/~saouma/computer/merlin.

Schellekens, J.C.J. and de Borst, R. (1993), "On the numerical integration of interface elements," *International Journal for Numerical Methods in Engineering*, v 36, pp. 43-66.

Shahwan, K.W. and Waas, A.M. (1997), "Non-self-similar decohesion along a finite interface of unilaterally constrained delaminations," *Proceedings of the Royal Society of London*, v 453, pp. 515-550.

Shih, C.F. and Asaro, R.J. (1988), "Elastic-plastic analysis of cracks on bimaterial interfaces: Part I – small-scale yielding," *Journal of Applied Mechanics*, v 55, pp. 299-316.

Shih, C.F. and Asaro, R.J. (1989), "Elastic-plastic analysis of cracks on bimaterial interfaces: Part II – structures on small-scale yielding fields," *Journal of Applied Mechanics*, v 56, pp. 763-779.

Shih, C.F. (1991), "Cracks on bimaterial interfaces: elasticity and plasticity aspects," *Materials Science and Engineering*, v A143, pp. 77-90.

Siegmund, T. and Needleman, A. (1997), "Numerical simulation of fast crack growth in brittle solids," *Journal of Mechanics and Physics in Solids*, v 42, pp. 1397-1434.

Sih, G.C. (1973), "Some basic problems in fracture mechanics and new concepts," *Engineering Fracture Mechanics*, v 5, pp. 365-377.

Sih, G.C. and Macdonald, B. (1974), "Fracture mechanics applied to engineering problems – strain energy density fracture criterion," *Engineering Fracture Mechanics*, v 5, pp. 361-386.

Simitses, G.J., Sallam, S. and Yin, W.L. (1985), "Effect of delamination on axially loaded homogeneous laminated plates," *AIAA Journal*, v 23, pp. 1437-1444.

Simo, J., Oliver, J. and Armero, F. (1993), "An analysis of strong discontinuities induced by strain-softening in rate-independent inelastic solids," Computational Mechanics, v 12, pp. 277-296.

Somers, M., Weller, T. and Abramovich, H. (1991), "Influence of predetermined delaminations on buckling and postbuckling behavior of composite sandwich beams," *Composite Structures*, v 17, n 4, pp. 295–329.

Sprenger, W., Gruttmann, F. and Wagner, W. (2000), "Delamination growth analysis in laminated structures with continuum-based 3D-shell elements and a viscoplastic softening model," *Computer Methods in Applied Mechanics and Engineering*, v 185, pp. 123-139.

Sukumar, N., Moës, N., Moran, B. and Belytschko, T. (2000), "Extended finite element method for three-dimensional crack modeling," *International Journal for Numerical Methods in Engineering*, v 48, pp. 1549-1570.

Sukumar, N., Srolovitz, D.J., Baker, T.J. and Prévost, J.H. (2003a), "Brittle fracture in polycrystalline microstructures with the extended finite element method," *International Journal for Numerical Methods in Engineering*, v 56, pp. 2015-2037.

Sukumar, N., Huang, Z., Prevost, J.H. and Suo, Z. (2003b), "Partition of unity enrichment for bimaterial interface cracks," *International Journal for Numerical Methods in Engineering*, in press.

Sun, C.T. and Jih, C.J. (1987), "On strain energy release rates for interfacial cracks in bi-material media," *Engineering Fracture Mechanics*, v 28, n 1, pp. 13-20.

Sun, C.T. and Manoharan, M.G. (1989), "Strain energy release rates of an interfacial crack between two orthotropic solids," *Journal of Composite Materials*, v 23, pp. 460-478.

Suo, Z. and Hutchinson, J.W. (1989), "Sandwich test specimens for measuring interface crack toughness," *Materials Science and Engineering*, A107, pp. 135-143.

Suo, Z. (1990), "Singularities, interfaces and cracks in dissimilar anisotropic media" *Proceedings of the Royal Society of London*, A427, pp. 331-358.

Suo, Z., Ortiz, M. and Needleman, A. (1992), "Stability of solids with interfaces," *Journal of Mechanics and Physics in Solids*, v 40, pp. 613-640.

TerMaath, S.C., Ingraffea, A.R. and Wawrzynek. P.A. (1999), "A computational fracture mechanics approach for the analysis of facesheet-from-core disbond of honeycomb core sandwich panels", *Fatigue and Fracture Mechanics (Thirtieth Volume)*, ASTM STP 1360, Paris, P.C. and Jerina, K.L., Eds., American Society for Testing and Materials, pp. 169-182.

Tijssens, M.G.A., van der Giessen, E. and Sluys, L.J. (2000), "Simulation of mode I crack growth in polymers by crazing," *International Journal of Solids and Structures*, v 37, n 48, pp. 7307-7327.

Triantafillou, T. and Gibson, L. (1987), "Failure mode maps for foam core sandwich beams," *Materials Science and Engineering*, v 95, pp. 37-53.

Triantafillou, T. and Gibson, L. (1989), "Debonding in foam-core sandwich panels," *Materials and Structures*, v 22, pp. 64-69.

Trakas, K. and Kortschot, M.T. (1997), "The relationship between critical strain energy release rate and fracture mode in multidirectional Carbon-Fiber/Epoxy laminates," *Composite Materials: Fatigue and Fracture (Sixth Volume)*, ASTM STP 1285, pp. 283-304.

Tvergaard, V. and Hutchinson, J.W. (1992), "The relation between crack growth resistance and fracture process parameters in elastic–plastic solids," *Journal of Mechanics and Physics of Solids*, v 40, pp. 1377–97.

Tvergaard, V. and Hutchinson, J.W. (1992), "Effect of T -stress on mode I crack growth resistance in a ductile solid," *International Journal of Solids and Structures*, v 31, pp. 823–33.

Tvergaard, V. and Hutchinson, J.W. (1994), "Effect of T -stress on mode I crack growth resistance in a ductile solid," *International Journal of Solids and Structures*, v 31, pp. 823–33.

Ural, A., Han, T., Chen, C., Zehnder, A., Ingraffea, A. and Wawrzynek, P. (1999), "Continuing investigations into damage tolerance of honeycomb structural members," Final Report to Boeing Commercial Airplane Company, Purchase Contract Numbers ZA0079 and JG7634.

Vinson, J.R., *The behavior of sandwich structures of isotropic and composite materials*, Technomic Publishing Co., USA, 1999.

Vizzini, A.J. and Lagace, P.A. (1987), "The buckling of a delaminated sublaminate on an elastic foundation," *Journal of Composite Materials*, v 21, pp. 1106-1117.

Wagner, W., Gruttmann, F. and Sprenger, W. (2001), "A finite element formulation for the simulation of propagation delaminations in layered composite structures," *International Journal for Numerical Methods in Engineering*, v 51, pp. 1337-1359.

Wang, J.T.S., Cheng, S.H. and Lin, C.C. (1995), "Local buckling of delaminated beams and plates using continuous analysis," *Journal of Composite Materials*, v 29, pp. 1374-1402.

Wang, J.T.S., Pu, H.N. and Lin, C.C. (1997), "Buckling of beam-plates having multiple delaminations," *Journal of Composite Materials*, v 31, pp. 1002-1025.

Wang, S.S. (1983), "Fracture mechanics for delamination problems in composite materials," *Journal of Composite Materials*, v 17, pp. 210-223.

Wang, W.Q. and Davalos, J.F. (2003), "Numerical/experimental study of facesheet delamination for honeycomb FRP sandwich panels," Proceedings of Composites in Constructions International Conference (Paper #162), Cosenza, Italy, Sept. 16-19.

Wells, A.A. (1961), "Unstable crack propagation in metals: cleavage and fast fracture," *Proc. Crack Propagation Symposium*, v 1, paper 84.

Wells, G.N. and Sluys, L.J. (2001), "A new method for modelling cohesive cracks using finite elements," *International Journal for Numerical Methods in Engineering*, v 50, pp. 2667-2682.

Westergaard, H.M. (1939), "Bearing pressures and cracks," *Transactions of the American Society of Mechanical Engineers*, v 61, pp. A49-A53.

Whitcomb, J.D. (1981), "Finite element analysis of instability related delamination growth," *Journal of Composite Materials*, v 15, pp. 403-426.

Whitcomb, J.D. (1989), "Three-dimensional analysis of a postbuckled embedded delamination," *Journal of Composite Materials*, v 23, pp. 862-889.

Whitcomb, J.D. (1992), "Analysis of a laminate with a postbuckled embedded delamination, including contact effects," *Journal of Composite Materials*, v 26, n 10, pp. 1523-1535.

Williams, J.H., Lee, S.S. and Kousiounelos, P.N. (1981), "Dynamic crack propagation and arrest in orthotropic DCB fiber composite specimens," *Engineering Fracture Mechanics*, v 14, pp. 427-438.

Williams, M.L. (1959), "The stress around a fault or crack in dissimilar media," *Bulletin of the Seismological Society of America*, v 49, pp. 199-204.

Wisheart, M. and Richardson, M.O.W. (1998), "The finite element analysis of impact induced delamination in composite materials using a novel interface element," *Composites: Part A*, v 28, pp. 301-313.

Xu, X.P. and Needleman, A. (1993), "Void nucleation by inclusion debonding in a crystal matrix," *Modeling and Simulation in Materials Science and Engineering*, v 1, n 2, pp. 111-132.

Xu, X.P. and Needleman, A. (1994), "Numerical simulation of fast crack growth in brittle solids," *Journal of the Mechanics and Physics of Solids*, v 42, pp.1397-1434.

Xu, X.P. and Needleman, A. (1995), "Analysis of ductile crack growth by means of a cohesive damage model," *International Journal of Fracture*, v 81, pp. 99-112.

Xu, X.P. and Needleman, A. (1996), "Numerical simulation of dynamic crack growth along an interface," International Journal of Fracture, v 74, pp. 289-324.

Yang, Y. and Shih, C.F. (1990), "Fracture along an interface," Technical Report, Division of Engineering, Brown University, Providence, R.I.

Yeh, M.K. and Tan, C.M. (1994), "Buckling of elliptically delaminated composite plates," *Journal of Composite Materials*, v 28, pp. 36-52.

Yin, W.L., Sallam, S. and Simitses, G.J. (1986), "Ultimate axial load capacity of a delaminated beam-plate," *AIAA Journal*, v 24, n 1, pp. 123-128.

Zenkert, D., *An introduction to sandwich construction*, Chameleon Press, London, 1995.